Hyperon Interaction in Free Space and Nuclear Matter Within a SU(3) Based Meson Exchange Model

Dissertation

zur Erlangung des Grades eines

Doktors der Naturwissenschaften

(Dr. rer. nat.)

Madhumita Dhar

aus Cooch-Behar, Indien

JUSTUS-LIEBIG-
UNIVERSITÄT
GIESSEN

Institut für Theoretische Physik

Justus-Liebig-Universität

Gießen, Germany

June, 2016

Dekan: Prof. Dr. Bernhard Mühlherr

Betreuer: Prof. Dr. Horst Lenske

Erstgutachter: Prof. Dr. Horst Lenske

Zweigutachter: Prof. Dr. Christian Fischer

To my parents

"It always seems impossible until its done."

Nelson Mandela

Abstract

To establish the connection between free space and in-medium hyperon-nucleon interactions is the central issue of this thesis. The guiding principle is flavor SU(3) symmetry which is exploited at various levels. In first step hyperon-nucleon and hyperon- hyperon interaction boson exchange potential in free space are introduced. A new parameter set applicable for the complete baryon octet has been derived leading to an updated one-boson- exchange model, utilizing SU(3) flavor symmetry, optimizing the number of free parameters involved, and revising the set of mesons included. The scalar, pseudoscalar, and vector SU(3) meson octets are taken into account. T-matrices are calculated by solving numerically coupled linear systems of Lippmann-Schwinger equations obtained from a 3-D reduced Bethe-Salpeter equation. Coupling constants were determined by χ^2 fits to the world set of scattering data. A good description of the few available data is achieved within the imposed SU(3) constraints.

Having at hand a consistently derived vacuum interaction we extend the approach next to investigations of the in-medium properties of hyperon interaction, avoiding any further adjustments. Medium effect in infinite nuclear matter are treated microscopically by recalculating T-matrices by an medium-modified system of Lippmann-Schwinger equations. A particular important role is played by the Pauli projector accounting for the exclusion principle. The presence of a background medium induces a weakening of the vacuum interaction amplitudes. Especially coupled channel mixing is found to be affected sensitively by medium. Investigation on scat-

tering lengths and effective range parameters are revealing the density dependence of the interaction on a quantitative level.

Abstrakt

Der zentrale Aspekt dieser Arbeit ist es die Beziehung zwischen der Hyperon-Nukleon Wechselwirkung im Vakuum und Medium herzustellen. Das Leitprinzip ist die SU(3) flavour Symmetrie die auf verschiedenen Levels Verwendung findet. In einem ersten Schritt werden die Bosonenaustauschpotentiale der Hyperon-Nukleon und Hyperon-Hyperon Wechselwirkung eingeführt. Ein neuer Parametersatz, welcher für das gesamte Baryon-Oktett anwendbar ist wurde bestimmt, was unter Benutzung der SU(3) flavour Symmetrie, Optimierung der Anzahl beteiligter freier Parameter und Überarbeitung des einbezogenen Satzes an Mesonen zu einem aktualisierten Einbosonaustausch-Modell führt. Die skalaren, pseudoskalaren und vektoriellen SU(3) Meson-Oktetts sind berücksichtigt. T-Matrizen sind durch das numerische Lösen gekoppelter, linearer Systeme von Lippmann-Schwinger-Gleichungen, erhalten aus einer dreidimensionalen reduzierten Bethe-Salpeter-Gleichung, berechnet. Kopplungskonstanten wurden durch einen χ^2-Fit an den weltweiten Satz an Streudaten bestimmt. Eine gute Beschreibung der wenigen, verfügbaren Daten ist innerhalb der auferlegten SU(3) Bedingungen erreicht.

Mit einer konsistent bestimmten Vakuumwechselwirkung zur Hand, erweitern wir den Ansatz, unter Vermeidung irgendwelcher weiterer Anpassungen zu Untersuchungen der Mediumseigenschaften der Hyperonwechselwirkung. Mediumseffekte in unendlicher Kernmaterie sind mikroskopisch durch die Neuberechnung der T-Matrizen durch ein mediumsmodifiziertes System von Lippmann-Schwinger-Gleichungen behandelt. Eine besonders wichtige Rolle spielt der Pauli-Projektor, welcher das Ausschlussprinzip berücksichtigt. Das Vorhandensein eines Hintergrundmediums be-

wirkt eine Abschwächung der Vakuumswechselwirkungsgamplituden. Es stellt sich heraus, dass insbesondere die Mischung gekoppelter Kanäle durch das Medium empfindlich beeinflusst ist. Die Untersuchungen von Streulängen und Parametern der effektiven Reichweite enthüllen die quantitative Dichteabhängigkeit der Wechselwirkung.

Contents

1 Introduction **19**
- 1.1 Strong Interaction . . . 19
  - 1.1.1 Properties of Nuclear Forces . . . 20
- 1.2 Pathway to Hyperon Interaction . . . 22
- 1.3 Current Approaches . . . 24
  - 1.3.1 Lattice QCD approaches . . . 24
  - 1.3.2 Meson Exchange Models . . . 25
  - 1.3.3 Chiral (χ) Effective Field Theory . . . 26
  - 1.3.4 Quark Cluster Model . . . 26
- 1.4 Framework Used in This Thesis . . . 27

2 Interaction Model Description **29**
- 2.1 $SU_f(3)$ Flavor Symmetry . . . 30
  - 2.1.1 Baryon and Meson Representations in $SU_f(3)$ . . . 33
- 2.2 Interaction Lagrangian . . . 35
  - 2.2.1 Field Theoretical Description . . . 36
  - 2.2.2 Meson Exchange Forces . . . 36
- 2.3 Effective Model Parameters . . . 40
  - 2.3.1 Meson Masses . . . 40
  - 2.3.2 Coupling Constants . . . 42
  - 2.3.3 Octet-Octet and Octet-Singlet Interaction . . . 44
  - 2.3.4 $SU_f(3)$ Baryon-Baryon-Meson vertices . . . 45
  - 2.3.5 Free Parameters . . . 48
- 2.4 Comparison with Contemporary Models . . . 50
- 2.5 Summary of the model . . . 52

3 Scattering Theory and Formalism **53**
- 3.1 Kinematics . . . 54
  - 3.1.1 Relativistic kinematics of Two-particle Scattering . . . 54
- 3.2 Scattering Equations . . . 57
  - 3.2.1 Bethe-Salpeter Equation . . . 57
  - 3.2.2 Lippmann-Schwinger Equation . . . 60
- 3.3 Isospin Basis . . . 61
- 3.4 Coupled Channel Formalism . . . 64

3.5 Formation of the Potential . . . 68
3.5.1 OBEP Amplitudes . . . 69
3.5.2 Potential Matrix in Isospin Basis . . . 78
3.6 Introduction to Particle Basis . . . 79

4 Numerical Methods 85
4.1 R-Matrix . . . 85
4.2 Representation in Partial Wave Basis . . . 86
4.2.1 Partial Wave Amplitude . . . 87
4.2.2 Partial Wave Projection of Potential Elements . . . 91
4.2.3 Partial Wave Integral Equation . . . 92
4.3 Numerical Formalism for R-matrix Solution . . . 94
4.3.1 Extraction of T-matrix from R-matrix . . . 97
4.4 Determination of Observables . . . 99
4.4.1 Cross Section . . . 99
4.4.2 Phase Shift . . . 100
4.4.3 Low-Energy (LE) Parameters . . . 101

5 Vacuum Hyperon-Baryon Interactions 105
5.1 Sensitivity of Parameters . . . 105
5.1.1 Fitting Procedure . . . 107
5.2 Result of Fit . . . 116
5.3 Free Space Result . . . 121
5.3.1 S = 0 Results . . . 122
5.3.2 S = -1 Results . . . 126
5.3.2.1 Uncoupled Channels . . . 127
5.3.2.2 Coupled Channels . . . 128
5.3.3 S = -2 Results . . . 139
5.4 Dependence of the LE Parameters on the Coupling Constants . . . 141
5.5 Summary of Free Space Interaction . . . 142

6 In-Medium Effect 147
6.1 Baryon-Baryon Interaction in Infinite Nuclear Matter . . . 148
6.1.1 In-Medium Bethe-Goldstone Equation . . . 148
6.1.2 Pauli Projector Operator . . . 150
6.1.3 Transformation to Center-of-Mass Frame . . . 151
6.2 Hyperon Mean Fields . . . 155
6.3 In-medium Phase Shift and Cross Section . . . 156
6.4 In-medium Low-Energy Parameters . . . 161
6.5 Medium Effect vs. Parameter Variation . . . 166
6.6 Conclusion . . . 167

7 Summary and outlook 171

Appendices 175

A Coupling Constant Values 177

B Partial Wave Potential Matrix Elements **179**

C LSJM Representation Operators **183**

D Partial Wave Decomposition of NN **187**

E Helicity State Basis Decomposition **189**

Bibliography **192**

Preface

"Not only is the Universe stranger than we think, it is stranger than we can think. "

Werner Heisenberg

About a century ago, microscopic physics started with the demand of understanding atomic spectra. That effort gave rise to the invention of quantum mechanics, the key science of our time. From the present day's point of view, theoretical as well as experimental studies of atoms and molecules have become standard work, reaching even deep into the industrial and commercial sectors. That is because those systems exist under the action of the meanwhile well known electromagnetic laws of force.

In nuclear and hadron physics, however, we have not yet reached a comparable state of knowledge. In addition to the complexities of quantum mechanics, nuclear physics is governed by the strong force which in its low energy realization is a highly complicated non-perturbative phenomenon. While the nuclear sector has taken a large step forward to produce a good number of successful, realistic, high-precision models [10, 11, 55, 62, 64, 110] utilizing a rich data set available with simultaneous computational progress, the strange nuclear physics is still far behind. The main constraint is the lack of even a sufficient number of experimental data that makes it difficult to have a unique understanding. There are several attempts made to construct to construct an unique interaction, in both relativistic and non-

relativistic framework, however the combined effort failed to close the open problem on hyperons. This being one scenario, the oner is more compelling for physicists to take this issue under re-investigation.

The present available interaction models include the meson exchange approaches of the groups from Nijmegen [49, 50](NSC, ESC) and Jülich [46–48], respectively, the Kyoto-Niigata model based on the quark cluster framework (Fss2) [105], the Lattice QCD descriptions [44, 45] using numerical simulations based on Quantum Chromo Dynamics (QCD), and the latest addition to this list is chiral perturbation theory extended to the SU(3) flavor sector, also known as chiral effective field theory (χEFT) [100], which is accounting for QCD symmetries and applying a systematic order-by-order scheme on the diagrammatic level. However, most of the results are in contradiction to one another in many key points and as of now none of the framework can deal simultaneously from S = 0 to S = -4 strangeness sector without extra modifications accounting for the the complexities introduced by higher strangeness involved. Sophisticated approaches like χEFT [100] and Lattice QC [44, 45] are still under construction for the higher strangeness channels to a satisfactory level.These issues emphasizes that to construct a single line theory for the hyperon interactions is a demanding task. The special characteristics of hyperon-related problems is multi-channel physics which is an important aspect goes much beyond the level of complexity encountered in the Nucleon-Nucleon (NN) case.

Recent observation of different exotic systems such as ${}^{6}\Lambda_{H}$ [1], unexpected short-lifetime of hypertriton [2], strong indication towards the existence of only-charge neutral $nn\Lambda$ bound state [3], also supported by recent hyper-nuclear and hyper-matter results from RHIC and LHC [4, 5] are not yet being understood under the present hyperon interaction framework available. On the other hand, a number of strangeness experiments has been planned to perform in near future in J-PARC (Japan), CLAS12 at J-LAB (USA), PANDA (Germany) , KaoS at MAMI (Germany) and FINUDA and DAΦNE (Italy) that will require of course a realistic hyperon interaction scheme for proper interpretation. The hyper physics program leading by Take Saito et. al ar FRS at GSI that is upgraded to SUPERFRS at FAIR in the upcoming facility will also be an important laboratory for hyper-nuclear physics.

All these together demand for a reconsideration of the existent models, with a more elaborate frame work. We therefore decided to take this issue as our research topic with attention to the unsolved problems. Therefore, we will construct a revised vacuum interaction model for hyperons in this thesis that can be applied to investigate all the above mentioned phenomena in a consistent manner.

While vacuum interaction information is fundamental, to complete the knowledge base, there is additional requirement towards investigation of in-medium hyperon interaction as well. The major drawback for obtaining experimental data for hyperons is their short-lifetime that make is impossible to make a hyperon beam. Only possible option to have hyperons are therefore as by-product from other processes. High energy hadronic reactions are one such tool that provides the opportunity to have hyperons as final fragments. On the contrary to beam-target type accelerator experiments, these kind of production method come up with a large background. For the heavy ion collisions the background is mainly nuclear medium. The recent two solar mass neutron star [89, 90] observation started the present day discussed "*hyperon puzzle*" of neutron stars. The high mass limit sets a strong con-

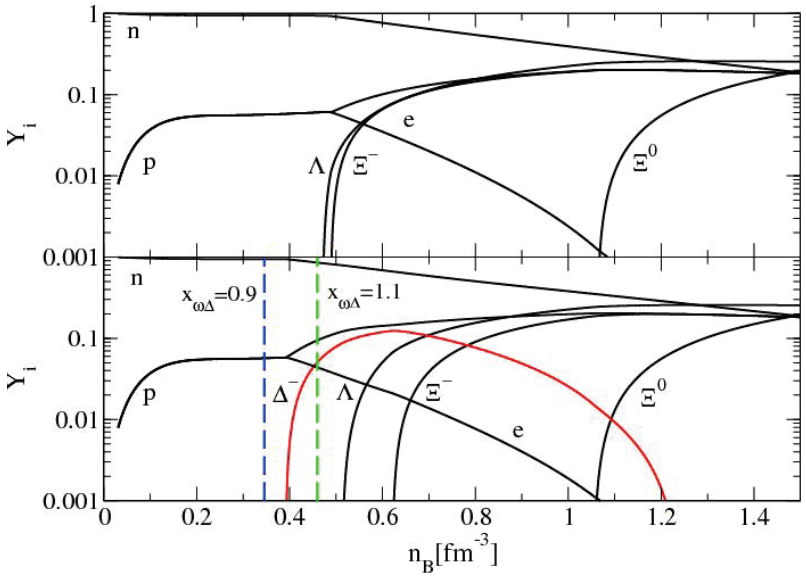

Figure 1: Baryon particle fraction as a function of baryon density. Figure taken from [91]

straint on the type of equation of state (EoS) being able to reproduce neutron stars the highest observed masses. The inclusion of hyperons softens the EoS, making it difficult to reach the two-solar-mass region at least with the standard parameter sets

[7]. An additional uncertainty is introduced by the open question if in the interior of a neutron star a transitions into a new quark matter phase occurs. However, there is still not a full proof answer to the question of whether hyperon degrees of freedom are present inside neutron stars or not. The puzzle arises since at such high densities hyperons are most likely to be present in neutron star core as shown for example in the baryon particle fraction plot as a function of density, taken from [91], although the result is model dependent, however it does give an idea that hyperons are most likely to appear already well below neutron star typical densities, which is about 5 times nucleon saturation density. Thus, inclusion of hyperons not producing two-solar-mass is emerging as the *hyperon puzzle*.

This created a quest for hyperon interaction at high baryon densities within a realistic interaction framework. A number of phenomenological approaches have pointed towards ad-hoc vector meson exchange [94], multi pomeron exchange [95], even in particular adjusting the Λ-nucleon three-body interaction [41]. More systematic investigation is therefore mandatory to solve this puzzle. In this thesis, we, therefore considered the medium effect study of hyperon bare interaction as our second part of work.

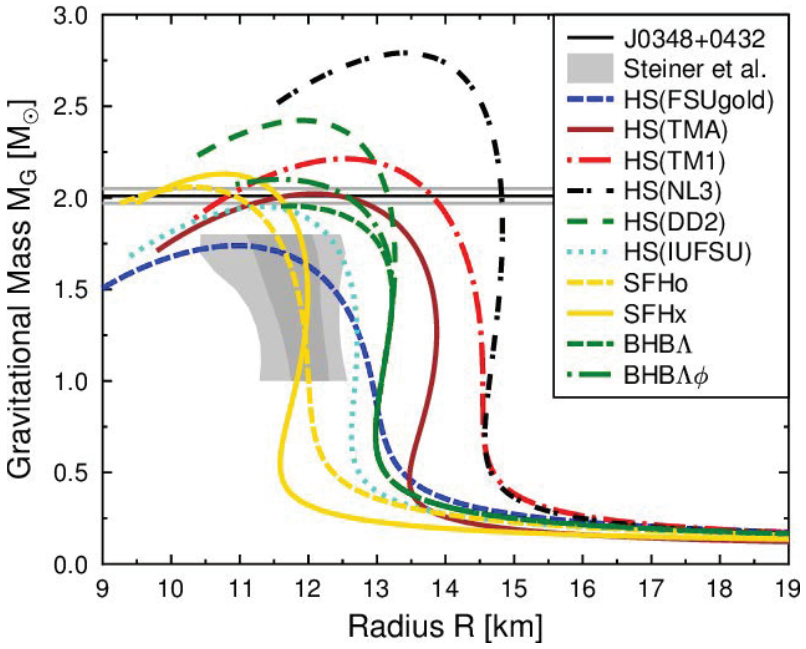

Figure 2: Mass-Radius diagram of different neutron star models. Only steep EoS can reach up to two solar masses. Figure taken from [92]

There exists a number of methods like Dirac-Brueckner Hartree-Fock calculation [32], G-matrix calculation [19], density functional theory [34, 35] etc. for investigating the medium effect. Most of these methods are based in mean-filed frame work, relativistic [108, 109], or non-relativistic [86]. The mean-field framework does not need information about the bare interaction. For a microscopic in-medium interaction, on the other hand, the in-medium effect is applied on the free space interaction, by Brueckner theory. Brueckner theory is largely used for nuclear sector already. Extension of the same to include hyperons was done first in the nineties by [87, 88]. The advantage of a microscopic theory over these mean field models is obvious, providing more insights already from the bare interaction level. With the aim of constructing a consistent realistic free space hyperon interaction as first task, we can readily study in-medium properties with necessary modification microscopically. Thus, our investigation is divided in to two parts: first we will present a realistic hyperon interaction for vacuum, which then we will use for investigating hyperon in-medium property research. In this thesis, we restrict ourselves at this stage up to nuclear matter densities for in-medium effect study of the bare interaction, pointing out the possibility to extend to other exotic systems with relevant mechanism.

Some of the results presented in this thesis are published in:

"Exotic nuclear matter", Horst Lenske, Madhumita Dhar, Nadja Tsoneva, Jonas Willhelm, EPJ Web Conf. 107 (1026) 10001;

"Hyperon Interaction in Free Space and Nuclear Matter", The 12th International Conference on Hypernuclear and Strange Particle Physics (HYP2015) Conference Proceedings, 7-11 September, 2015, Sendai, Japan, [arXiv:1603.00298];

"Hyperon Interaction in Nuclear matter and Neutron Star", GSI Scientific Report 2014;

"SU(3) Approach to Hypernuclear Interactions and Spectroscopy", Horst Lenske, Madhumita Dhar, Theodoros Gaitanos, submitted to Nuclear Physics A for publication, [arXiv:1602.08917],

and the rest of the results are in preparation.

The thesis is organized as follows:

- Chapter 1: A general review of strong interaction is given. The contemporary

models and theories for hyperon interaction are reviewed briefly. Finally the need of a revised approach is explained in connection with this work.

- Chapter 2: The interaction model used in this work is explained in detail.
- Chapter 3: This chapter contains information about two- body scattering theory. The two-body covariant Bethe-Salpeter equation is discussed in connection to hyperon interaction. One-boson-exchange potential amplitudes used in this work are described in detail. Various representation basis schemes of baryon-baryon scattering channels are also a part of discussion of the chapter.
- Chapter 4: This chapter deals about numerical formalism of our research. A description of the partial wave decomposition of scattering equation is given, followed by the numerical methods adopted to solve the scattering equation is explained first, finishing with a description on determination of relevant scattering observables numerically.
- Chapter 5: Results for the vacuum baryon-baryon interaction is presented.
- Chapter 6: The effect of nuclear - medium on the vacuum interaction is shown.
- Chapter 7: A brief summary and future outlook are the topics of this chapter.

Chapter 1

Introduction

"The important thing is to not stop questioning. Curiosity has its own reason for existence."

Albert Einstein

In this chapter, a general review about strong hyperon interaction has been given. In Section 1 the aspects of strong interaction is described, which must be followed by hyperon interaction. Section 2 is devoted to describe the known properties of nuclear force. In Section 3 few words on hyperon discovery and the properties observed till date are mentioned. The various interaction models active in this field that are mentioned briefly in Section 4. In Section 5 reasons for deriving a revised a vacuum interaction approach has been highlighted.

1.1 Strong Interaction

Both hyperons and nucleons belong to the same group of particles: the *baryons*. Both of the particles are part of the baryon octet and strongly interacting particles. This ensures a basic similarity must lie between their interactions with of course a bit of difference owing to the strange and non-strange quark presence. There are a large number of non-strange stable nuclei available that allows to do nucleon scattering experiments. On the other hand, hyperon scattering experiments are very difficult due to the short life time of hyperons. This makes hyper nuclear physics as the most

difficult branch of nuclear physics. In order to proceed, one can use the information obtained from the nucleon scattering experiments, which effectively helped to gain an understanding about the basic features of the strong interaction, in particular the nuclear force.

1.1.1 Properties of Nuclear Forces

Nuclear force is what holds the nucleons together inside the nucleus. There are three types of nuclear interactions: strong, weak and electro magnetic. As far as strong interaction is concerned, the force between two nucleons is the most prominent example on this front. Over the last century there has been a great number of theoretical and experimental research that adds up to the understanding of strong interaction properties. The basic properties of the nuclear forces that are known until today are compiled in many papers [20]. The nature of nuclear forces is studied by analyzing the properties of the nuclei. The empirical features of nuclear force are listed as the followings:

1. **Short range**: Nuclear force is of short range nature. Rutherford's famous alpha particle scattering experiment showed the range of nuclear force to be of the order of 10^{-15} m. The range is usually upto 1-2 fm. The nearly constant values of the binding energy per nucleon (Fig. 1.1) and the density supports the finite short range behavior. This is also evident from the fact that the interactions between nuclei in a molecule are entirely described by Coulomb force.

2. **Stronger than Coulomb force at short distances**: The strength of the force is stronger than the Coulomb force at this order, otherwise it would not have been possible to keep the protons together in presence of the Coulomb repulsion among them.

3. **Short range repulsion**: The short range repulsion part of the strong force is the most interesting yet challenging one. This is usually is referred as the 'repulsive core' or simply 'hard core'. The repulsive core is usually over the distance 0.5 fm. This means the nucleons cannot go closer beyond that.

4. **Intermediate range attraction**: Outside the repulsive core, nuclear force must be attractive in nature otherwise one can not have nucleus. Nucleon-nucleon (NN) scattering experiments showed positive S-wave phase shifts (implying attraction) for low energies as a proof of this.

5. **Saturation**: The saturation property is coming from the fact of nearly constant binding energy per nucleon ($B.E/A$) $\simeq$ 8.5 MeV for nuclei above $A > 4$ [Fig. 1.1].

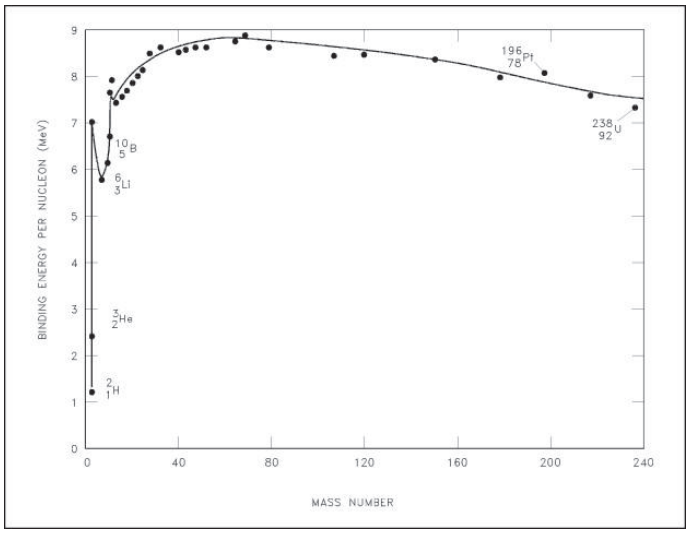

Figure 1.1: Binding Energy per Nucleon vs mass number plot. Binding energy per nucleon clearly shows a saturation behavior. Figure copyright [6].

6. **Spin dependence**: For deuteron, only spin 1 state is bound. Different isospin states of spin 0 shows different phase shift. To conclude, nuclear force depends both on spin and isospin.

7. **Non - central tensor force**: The deuteron has a non-zero magnetic and quadrupole moment, which implied the shape being not spherical. This fact can be explained by postulating deuteron as an admixture of S-state and D-state. Tensor force hence come into play a role here as the tensor operator defined in coordinate space here as

$$S_{12} = 3(\sigma_1 \cdot \hat{r}_{12})(\sigma_2 \cdot \hat{r}_{12}) - (\sigma_1 \cdot \sigma_2) \tag{1.1}$$

can mix states with different orbital angular momentum (**L**) where σ_1 and σ_2 are the spins of particle 1 and 2 respectively and $\hat{r}_{12}$ is the unit vector along the direction of relative distance between particle 1 and 2.

8. **Spin - orbit force**: Nuclear spectra showed evidence on the dependence of nuclear force on spin-orbit (**L**.**S**) force.

9. **Charge independence**: Nuclear force is charge symmetric. This implies that if one exchange the overall number of protons with neutrons and vice-versa, the force will remain unaltered. The similarity in the excitation spectra of the mirror nuclei also is a consequence of the charge symmetry of strong force.

10. **Exchange of charge** : Nuclear force can exchange charge. From neutron-proton scattering experiments, a forward as well as a backward peak has been seen. The backward peak is interpreted as actually a neutron being converted to a proton being scattered. Beta-decay is also another example of the charge -exchange reaction.

11. **Symmetry principles**: Lastly the force must follow the basic invariance principles: translation, Galilei, rotation, parity, and time -reversal.

1.2 Pathway to Hyperon Interaction

In 1947, Rochester and Butler reported the appearance of forked tracks due to associated production of a pair of unstable particles [122]. These tracks were experimentally soon discovered as referring to pair production of particles, K-meson and Λ. This was the first discovery of a strange particle and marked the beginning of strangeness era in physics. These new particles were termed 'strange' due to the two peculiar behaviors of their tracks: these particles were always observed to be produced in 'pairs' by 'fast' strong interaction processes, and found to decay by a 'slow' process. The puzzle at that time was why the particles which were produced by strong interaction, always decayed by weak interaction, later indebted as the characteristics of particles carrying the new quantum number S for strangeness.

If that was the beginning of strange particle physics, hypernuclear physics was born in 1953 when Danysz and Pniewski [8] observed a stack of photographic emulsions appeared when studying the cosmic radiation at about 26 km from Earth's surface. Collision between a high energy proton with a nuclear emulsion created the appearance of several nuclear fragments among which one observed to decay, pointing towards unstability, now known was due to Λ hyperon. These are termed as hyperfragments in today's time. This was the first discovery of a hypernucleus.

It is the same year when the new quantum number 'strangeness' (S) was introduced by Gell-Mann to solve the strange particle puzzle, postulating strangeness as a conservation for strong and electromagnetic interaction, not weak. In the 1950s several new mesons and baryons were discovered enriching the '*particlezoo*'. Gell-Mann and Ne'eman in 1961 independently proposed the eight -fold way as a classification scheme of the particles, distributed in an eight-member isospin multiplet. To describe the formation, in 1964, the 'quark model' was introduced by Gell-Mann and Zweig depicting hadrons as quark bound states.

The strangeness created another puzzle when the nature of K^0 and $\bar{K^0}$ mesons were studied. The decay properties of these two differing only by strangeness number, revealed the charge-conjugation-parity (CP) symmetry violation of the kaons [123]. The discovery of this violation is playing an important role in strangeness physics as a display of the features of flavor physics. The violation is crucial to point out the violation of matter and antimatter symmetry.

Studies on hypernuclear production processes require knowledge about in-medium hyperon interaction to set proper conditions for the formation or non-existence of bound states. Searches in the direction for hypernuclear bound states are of special interest here. As of now a good number of Λ-hypernuclei are known [124] and a few double-Λ, there are still ambiguity for Σ and Ξ hypernuclei. For example the separation energies of known S = -1 single Λ-hypernuclei are shown in Fig. 1.2 as a function of mass number to the power $-\frac{2}{3}$. For more detailed information of on this subject one can look at [129, 130].

Thus to conclude, in addition to the properties of Section 1, there are many more not yet understood phenomenon like the experimental detection of the exotic

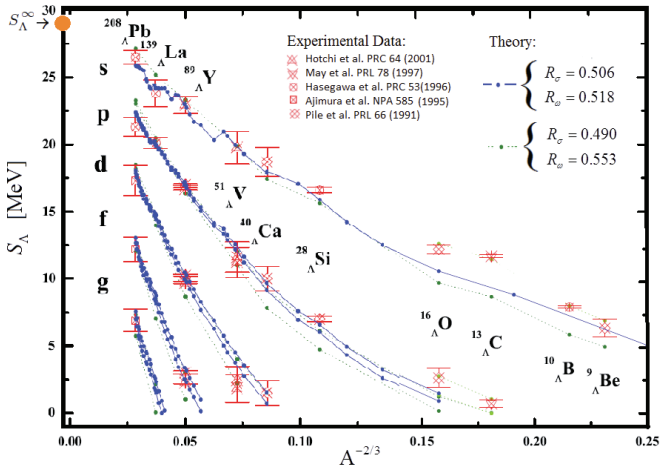

Figure 1.2: Separation energies of known S = -1 single Λ-hypernuclei as a function of mass number to $A^{-\frac{2}{3}}$. Figure taken from [129]

hyperon systems, short life-time, multi-channel transfer reactions, effect on highly dense objects like neutron star on hyperon physics, which are typical to hyperon physics. To conclude, there are still many open questions in this subject that is worth attempting for investigations with a consistent hyperon interaction framework.

1.3 Current Approaches

Before introducing our interaction model, we first briefly summarize the till date existent models or frameworks aiming to calculate hyperon-baryon interactions. There are mainly four approaches used to treat this problem: Lattice QCD (Quantum Chromo Dynamics) [44, 45], meson-exchange models [46–50], chiral effective field theory, (χEFT) [100, 101, 106], and quark -cluster models [105]. In the following we highlight the key aspects of these frameworks.

1.3.1 Lattice QCD approaches

Quantum Chromodynamics (QCD) is the fundamental theory of strong interaction governing the interaction of baryons. However, field theoretical description of the baryon interaction should start from quark degrees of freedom as the QCD Lagrangian needs description of quark-gluon dynamics. The non-perturbative nature of QCD at hadron degrees of freedom therefore makes the solution of QCD Lagrangian very much involved, making the analytical solution technique impossible.

Lattice QCD framework provides an alternative simulation technique to this. The QCD path integral is calculated in a finite four-dimensional discretized Euclidean or Minkowski box with a shortest length scale, known as the lattice-spacing, thus discretizing space and time to evaluate the integral in a finite volume. Quantum Monte Carlo integration is used to perform the path integral. At present only simulations with fairly large quark masses, small volumes, and large lattice spacings are achievable for full QCD due constraint coming from computer computation limit. Due to the excessive time consuming calculations, the progress in lattice QCD sector is rather slow compared to other effective frameworks involved.

Different type of QCD simulations like quenched and (2+1)-flavor has been carried out by HAL-QCD [44] and NPLQCD [45] collaborations for ΛN and ΣN systems already, with preliminary calculations for S = -2 by [44]. Extension to higher strangeness channels are in progress. However, the present pion mass used in this calculations is still far from physical point usually of the order of 300-400 MeV. In any event, simulation results from lattice QCD play an important role in providing additional constraints in hyperon physics with large ambiguity.

1.3.2 Meson Exchange Models

Days since Yukawa predicted meson exchange theory, meson exchange has been employed extensively to construct baryon potentials. The exchanged mesons in meson-exchange models playing the same role as photons in electrodynamics. The meson-exchange potentials has been proven to be very successful for phenomenological determination of nuclear forces [10, 11, 55, 64]. The high-precision Bonn nuclear potential has been successfully extended to include hyperons by the Jülich group in the late eighties [46], further modified to two more versions [47, 48] all utilizing SU(6) symmetry of quarks. The Jülich has their last version applicable for S = -1 sector with no more further advancement provided from the authors.

The Nijmegen nucleon potential is modified to include hyperons using SU(3)-flavor symmetry with mass breaking effects explicitly included. Different version available from Nijmegen groups differing on the core interaction , hard or soft one [49, 50]. One specific feature if Nijmegen group of potentials is their inclusion of

fictitious particle pomeron in their models. The Nijmegen strange potentials has different versions, with a large set of variation within their own framework both published and unpublished with a version available for complete baryon octet [49] with many other versions available as applied versions to S = -1, S = -2 [50, 51].

1.3.3 Chiral (χ) Effective Field Theory

An alternative theory in nuclear physics is discovered recently in the last decade, namely the chiral effective field theory. The framework is based on a modified Weinberg power counting incorporating the QCD symmetries explicitly into the scheme. Similar to meson-exchange models, the EFT framework too assumes the validity of SU(3)-flavor symmetry for the hyperon-nucleon interaction. The framework has the option of systematic improvements by including higher order terms by perturbative expansion, known as leading order (LO), next-to-leading-order (NLO) and so on. The Jülich-Bonn-Munich [100, 101, 106] group is extensively working on this subject. The diagrams contributing for EFT theory are calculated analytically first by power counting. For higher order the number of diagrams increases, hence making the task quite cumbersome. The short-range part on the interaction in χEFT is attributed by four-baryon contact terms, that are fixed by fit to data. The contact terms derived here are imposed with SU(3)-flavor constraints to reduce free parameters. For the LO version [106], the long-range part consists of one-pseudo-scalar meson exchange and for NLO [101], two-pseudo scalar meson exchange diagrams are also included. At present S = -2, -3, -4 results are available up to LO [100] and only S = -1 extended up to NLO [101]. The results obtained are pretty good in describing the hyperon-nucleon data with uncertainty involved equivalent to the present meson-exchange models. Thus, the EFT scheme is a good alternative theory to study the hyperon-interaction in general.

1.3.4 Quark Cluster Model

In quark cluster model [105] valence quarks are the force mediators. The Hamiltonian here consists of three parts: quark kinetic energy, quark confinement potential,

and residual quark-quark interactions. The short- range core here is derived from the color-magnetic gluon exchange and the quark anti-symmetrization in the valence quark dynamics. In a hybrid version of the model, low-lying mesons were also included to describe the long-range interaction part. In this framework, contrary to meson-exchange picture, the mesons can also interact with the quarks inside baryons. The meson-baryon couplings used for the calculations are usually taken from Nijmegen potential. The results obtained from this scheme in many cases differ from the other three mentioned earlier and in general not preferred for further application.

1.4 Framework Used in This Thesis

In this work, we will follow the conventional meson-exchange scheme to construct our own bare interaction model. Due to the present uncertainty in the level of OBE parameter sets used by the OBE hyperon models, increasing strangeness leads to change in the parameters involved for better quantitative analysis of the observables. Moreover, the two groups differ in their preference in symmetry consideration as discussed earlier. With this being the case, we are interested in a qualitative study of the validity of SU(3)-flavor symmetry in the baryon-baryon octet sector. As a consequence we do not want to not include any other mesons as mediators other than octet ones. With all these modifications, our aim is to achieve a single parameter set for whole baryon-baryon interaction in the SU(3) limit.

In next step of this work, we will use the constructed version of the 'revised' meson model to study in-medium properties within a microscopic framework via Brueckner theory [57]. The motivation here is that a theoretical investigation of baryon-baryon interaction well constrained by SU(3) will help to understand the extent up to which SU(3) is actually followed in nature which is still not yet discussed. More information on this will in turn help in treating the breaking if necessary to get an accurate quantitative analysis. Therefore, we believe, a work based on the SU(3) symmetry will help the whole community as a whole and show directions in which point one needs to pay attention to get the 'correct' interaction. And next, as our another major focus of this thesis, we will extensively investigate the effect of nuclear medium on bare hyperon- interaction that is important for hyper-nuclear structure

studies to astrophysical exotic objects like neutron stars, as already pointed put in last Chapter.

Chapter 2

Interaction Model Description

> "The laws of nature are constructed in such a way as to make the universe as interesting as possible."
>
> Freeman Dyson

In this thesis we want to study hyperon (Y)-nucleon (N) and hyperon (Y)-hyperon (Y), in general baryon (B)-baryon (B) in-medium interactions. In order to find the in-medium behavior, it is necessary to understand the vacuum interaction first. Our main interest is to have a qualitative idea of the BB interaction in presence of nuclear-medium. Therefore, instead of a phenomenological model or quantitative one, we are more interested in building a qualitative model using SU(3) symmetry that, if required, can also be modified to make it more accurate quantitatively.

The main problem with hyperons compared to nucleons is the lack of experimental data which makes hyperon sector a long-standing theoretical problem. Due to scarce data set, unlike many successful phenomenological NN models [10, 11, 55, 62], hyperon interaction models are mainly developed using the underlying $SU(3)$-flavor symmetry (here after as $SU_f(3)$). Following the common practice, our model is also based on $SU_f(3)$ symmetry.

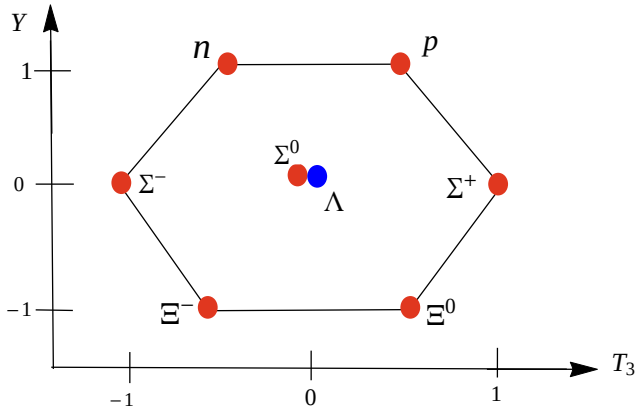

Figure 2.1: $J^P = \frac{1}{2}^+$ Baryon Octet

In the following*, we first briefly discuss about the SU(3) flavor symmetry in section 2. In section 3, the effective interaction Lagrangian used in this work will be introduced using one-boson-exchange (OBE) forces. Section 4 is devoted on describing the parameters of the model and the method used to determine them. In section 5, a comparative discussion between our model with other existing hyperon OBE models has been presented. The chapter ends summarizing the key points of the model in section 6.

2.1 $SU_f(3)$ Flavor Symmetry

The basic idea of our model relies on the well known quark model. It is an established fact that baryons interact via strong interaction. In the sixties, after strange particles were discovered, the strangeness quantum number (S) was introduced. This was utilized in arranging the eight $J^P = \frac{1}{2}^+$ baryons in a hexagon pattern as shown in Fig. 2.1 in a two dimensional plane of third component of isospin (I_3) and hyper charge (Y), Y being the sum total of baryon number B and S. The mesons has also this eight-fold degeneracies as shown in Fig. 2.2.

This so called "Eight-fold Way" was discovered as well as named in 1961 by Murray Gell-Mann [12] and independently by Yuval Ne'eman [13]. This introduced the $SU_f(3)$ symmetry as an internal symmetry of the baryons. The eight-fold way is

*The work presented in this chapter is based on the works [12, 14, 56]

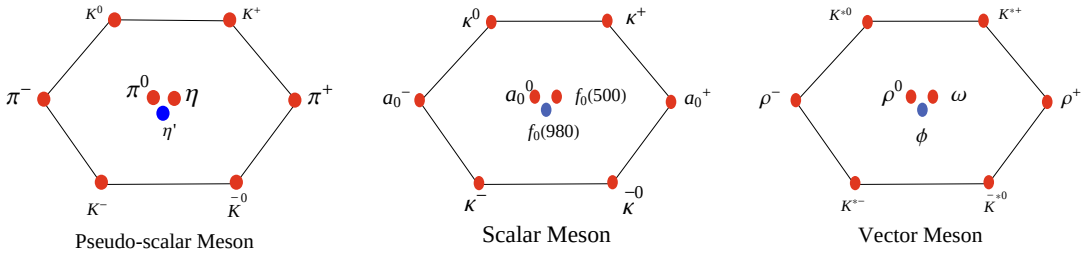

Figure 2.2: Meson nonets

a theory that organized the hadrons in terms of an octet. In mathematical language this is like organizing the particles in 'groups of eight' as in abstract group algebra. The major break through was achieved in 1964 when Gell-Mann [14] and Zweig [15] (independently) proposed the quark model to explain the classification of various hadron multiplets, marking their names into the 1969 Nobel prize in physics.

Baryon	Mass[MeV]
n	938.56
p	1877.27
Λ	1115.68
Σ^+	1189.37
Σ^-	1197.44
Σ^0	1192.55
Ξ^-	1321.71
Ξ^0	1314.86

Table 2.1: Octet Baryons and their Masses

The benchmark of the 'quark model' was to postulate hadrons as quark bound states: baryons as three quark bound state and mesons as a bound state of quark and anti-quark pair that can describe the formation of hadrons correctly. The $SU_f(3)$ symmetry includes SU(2) isospin symmetry (up-down quark flavor symmetry) as a subgroup. In the quark model, the SU(3) multiplets then can be explained by considering the flavor SU(3) group with the three quark flavors: up (u), down (d), and strange (s), forming the fundamental representation (here represented by short-

hand notation **3**) of $SU_f(3)$ known usually as the triplet (say, q^i).

$$\mathbf{3} = \begin{pmatrix} u \\ d \\ s \end{pmatrix} \quad \bar{\mathbf{3}} = \begin{pmatrix} \bar{u} \\ \bar{d} \\ \bar{s} \end{pmatrix} \tag{2.1}$$

The corresponding anti-quarks form the representation, known as anti-triplet (say $\overline{q^i}$. The corresponding weight diagram is shown in Fig. 2.3

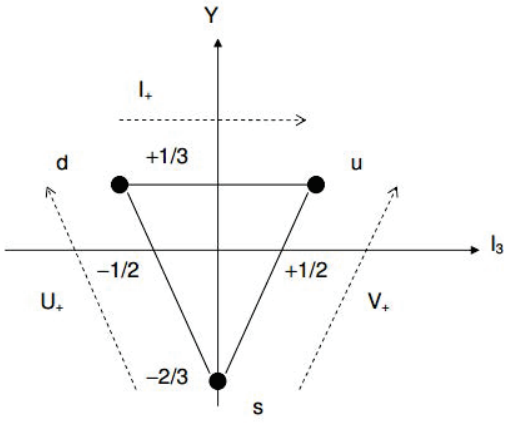

Figure 2.3: Weight Diagram or triplet representation

The baryons and mesons can be formed now by constructing the appropriate higher-dimensional representations. A third-order tensor ($q^iq^jq^k$), the baryons, in SU(3) has four types of representations,

$$\mathbf{3} \otimes \mathbf{3} \otimes \mathbf{3} = \mathbf{1}_B \oplus \mathbf{8}_B \oplus \mathbf{8}_B \oplus \mathbf{10}_B \tag{2.2}$$

where $\mathbf{1}_B$: totally antisymmetric, $\mathbf{8}_B$: mixed symmetry , $\mathbf{10}_B$: totally symmetric. Here $\mathbf{8}_B$ represents the eight-fold degenerate baryons, called octet baryons (Fig. 2.3), where as $\mathbf{10}_B$ corresponds to the $J^P = \frac{3}{2}^+$ decuplet baryons (Fig. 2.4). The SU(3) flavor singlet uds state is forbidden by Fermi statistics.

In this thesis, we are dealing with the lowest order the $J^P = \frac{1}{2}^+$ baryon octet represented by $\mathbf{8_B}$ as listed in Table 3.1. The formation of mesons is explained by combining a quark and anti-quark ($q^i\bar{q^j}$) producing various meson ($J^P = 0^-, 0^-, 1^-$)

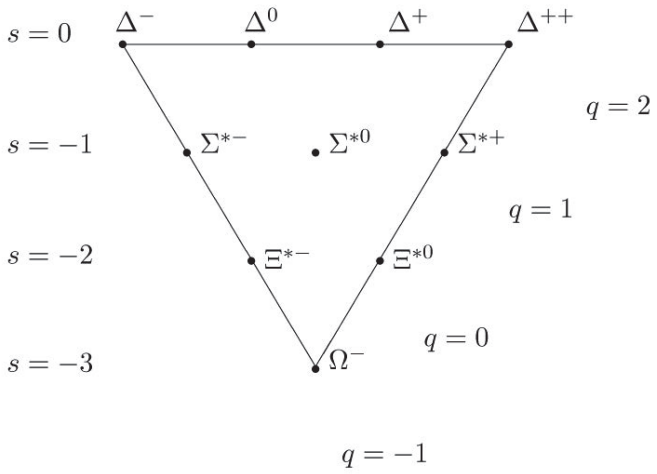

Figure 2.4: Baryon decuplet

nonets (octet $\mathbf{8}_M$ and singlet $\mathbf{1_M}$ together).

$$\mathbf{3} \otimes \bar{\mathbf{3}} = \mathbf{8}_M \oplus \mathbf{1}_M \tag{2.3}$$

It should be mentioned here that SU(3) symmetry is not exact but broken weakly. However, the breaking is small compared to the baryon mass scale providing SU(3) as one of the most fundamental symmetries to follow in baryon sector. We will discuss on this aspect in sec. 3.1 in more detail.

2.1.1 Baryon and Meson Representations in $SU_f(3)$

In order to derive the interaction we need to first define the baryon octet $\mathbf{8_B}$, meson octet $\mathbf{8_M}$ and singlet $\mathbf{1_M}$ irreducible representations and the necessary parameters required.

The irreducible representation $J^P = \frac{1}{2}^+$ baryon octet can be represented as the following $SU_f(3)$ invariant traceless matrix following the phase convention as in [56]

$$\mathcal{B} = \frac{1}{\sqrt{2}} \sum_{a=1}^{8} \lambda^a B^a = \begin{pmatrix} \frac{\Sigma^0}{\sqrt{2}} + \frac{\Lambda}{\sqrt{6}} & \Sigma^+ & p \\ \Sigma^- & -\frac{\Sigma^0}{\sqrt{2}} + \frac{\Lambda}{\sqrt{6}} & n \\ -\Xi^- & \Xi^0 & -\frac{2\Lambda}{\sqrt{6}} \end{pmatrix} \tag{2.4}$$

Here λ^a's are the eight Gell-Mann matrices. The irreducible representations for the

pseudoscalar (ps) ($J^P = 0^-$) , scalar (s) ($J^P = 0^+$), and vector (v) ($J^P = 1^-$) meson octets can be represented in a similar fashion as following

$$\mathcal{M}_8^{ps} = \frac{1}{\sqrt{2}} \sum_{a=1}^{8} \lambda^a \phi_{ps}^a = \begin{pmatrix} \frac{\pi^0}{\sqrt{2}} + \frac{\eta_8}{\sqrt{6}} & \pi^+ & K^+ \\ \pi^- & -\frac{\pi^0}{\sqrt{2}} + \frac{\eta_8}{\sqrt{6}} & K^0 \\ K^- & \bar{K}^0 & -\frac{2\eta_8}{\sqrt{6}} \end{pmatrix} \tag{2.5}$$

$$\mathcal{M}_8^{s} = \frac{1}{\sqrt{2}} \sum_{a=1}^{8} \lambda^a \phi_{s}^a = \begin{pmatrix} \frac{a_0^0}{\sqrt{2}} + \frac{f_0}{\sqrt{6}} & a_0^+ & \kappa^+ \\ a_0^- & -\frac{a_0^0}{\sqrt{2}} + \frac{f_0}{\sqrt{6}} & \kappa^0 \\ \kappa^- & \bar{\kappa}^0 & -\frac{2f_0}{\sqrt{6}} \end{pmatrix} \tag{2.6}$$

$$\mathcal{M}_8^{v} = \frac{1}{\sqrt{2}} \sum_{i=1,3} \sum_{a=1}^{8} \lambda^a \phi_{v}^a = \begin{pmatrix} \frac{\rho^0}{\sqrt{2}} + \frac{\omega}{\sqrt{6}} & \rho^+ & K^{*+} \\ \rho^- & -\frac{\rho^0}{\sqrt{2}} + \frac{\omega}{\sqrt{6}} & K^{*0} \\ K^{*-} & \bar{K}^{*0} & -\frac{2\omega}{\sqrt{6}} \end{pmatrix} \tag{2.7}$$

While the irreducible representation of the pseudoscalar (ps) singlet meson is the following 3 dimensional square diagonal matrix

$$\mathcal{M}_1^{ps} = \frac{1}{\sqrt{3}} \begin{pmatrix} \eta_1 & 0 & 0 \\ 0 & \eta_1 & 0 \\ 0 & 0 & \eta_1 \end{pmatrix} \tag{2.8}$$

Similar matrices exists for scalar (s) and vector (v) singlet meson representations. The meson nonet is obtained by simply combining the octet and singlet as given below

$$\mathbf{3} \otimes \bar{\mathbf{3}} = \mathbf{8}_M \oplus \mathbf{1}_M \tag{2.9}$$

$$\mathcal{M}^{ps,s,v} = \mathcal{M}_8^{ps,s,v} + \mathcal{M}_1^{ps,s,v} \tag{2.10}$$

As a consequence of broken SU(3) symmetry, the physical η, φ, and ϵ are observed to be an odd mixtures of the respective octet and singlet particles. The octet-singlet mixing is represented in terms of the respective meson mixing angles. For example, the physical η and η' mesons are represented in terms of the pseudoscalar mixing

angle θ_{ps} as

$$\eta' = \sin\theta_{ps}\ \eta_8 + \cos\theta_{ps}\ \eta_1$$
$$\eta = \cos\theta_{ps}\ \eta_8 - \sin\theta_{ps}\ \eta_1 \tag{2.11}$$

Similar relations exists for physical ϕ and ϵ as a function of $(\theta_v, \omega_8, \varphi_1)$ and (θ_s, a_0, f_0) respectively We will discuss in chapter 5 about the uncertainty in the value of the mixing angle and the consequences.

Channel	Meson	Mass [MeV]
0^-	π	138.03
0^-	η	547.86
0^-	$K^{0,+}$	497.64
0^+	ϵ	760.0
0^+	δ	983.0
0^+	κ	880.0
1^-	ω	782.65
1^-	ρ	775.26
1^-	K^*	891.66

Table 2.2: Various mesons and their masses as used as input for this work.

2.2 Interaction Lagrangian

The next step is to define an interaction for the hyperons. As discussed in Sec. 2.1, SU(3) flavor symmetry is an underlying global symmetry of the hadrons. Therefore, it is important for any interaction model to satisfy this condition. This means the interaction Lagrangian should be a SU(3) flavor singlet.

Here in this thesis, we want to address the hyperon-baryon scattering problem. From the nucleon sector it is well established [10, 11, 18, 21, 22, 62] that the free-space two-body interaction serves as the lowest order contribution but the dominant one. Therefore, we will focus on the two- particle vacuum interaction here that can be used for further applications to study many-body effects. The derived two-body interaction we are going to use then as an input in our in-medium scattering equation (Chap. 2) to study the many-body effect. For works related to few- body hyperon calculations one may look at the ref. [23–25, 27] and for a many body

description see ref. [28–32, 32, 34, 35, 38, 39, 41, 43]. However, the two-body interaction is the fundamental baryon-baryon interaction that one should understand to have a complete knowledge of the baryon interactions. Many of the above approaches make use of the available two-body interactions as input for their higher order calculations [36, 37, 40, 41] while others determine the interaction by direct many-body treatments like mean field theory [38, 39], Brueckner-Hartree-Fock approximation [42] , Dirac-Bruckner-Hartree-Fock model [32] , density functional theory [34, 35], quantum Monte Carlo simulations [41, 43]. Nevertheless, due to the short-range nature of the strong force, two-body interactions are the most dominant ones and hence can be well sufficient to describe the two-body scattering problem in a satisfactory manner.

2.2.1 Field Theoretical Description

We want to develop an effective "interacting" Lagrangian consisting of non-zero two-particle baryon interaction and of course the higher ones which we will neglect in our work as already discussed earlier.

Let us consider Ψ is the complex baryon field of mass M_B. The free field baryon Lagrangian ($\mathcal{L}_B$) containing the kinetic energy and the mass term is given by

$$\mathcal{L}_B = i\overline{\Psi}_B\gamma^\mu\partial_\mu\Psi_B - M_B\overline{\Psi}_B\Psi_B \tag{2.12}$$

The baryons are "free" here, i. e., moving independently, neither interacting with each other. Now let the baryons interact with each other however with only one at a time: not with other fields, that leads to the concept of two-body interaction.

2.2.2 Meson Exchange Forces

For a scalar field, the interaction picture is simple. Baryons being a complex field and provided the known facts about hyperon is insufficient, we need to tackle this interaction problem carefully. The first principle of strong interaction, QCD being complex to handle in hyperon scale, an effective model is a handy tool to fulfil the gap. Being effective in nature, most of the available nuclear models are mainly

phenomenological. The successful high-precision one-boson-exchange effective nuclear models [10, 11, 62] are trying to circumvent the gap by providing a possible choice aiming to "reproduce" the well-known nuclear properties making use of the rich scattering data available for the nucleon sector as well as serving as a good predicting tool. Following this successful high-precision NN potential models and their counter parts as an extension including hyperons [46–50], we too will build our model based on the pioneering idea of Hideki Yukawa [52], quoting his own words:

> "The interactions of elementary particles are described by considering a hypothetical quantum which has the elementary charge and the proper mass and which obeys Bose's statistics.[52]"

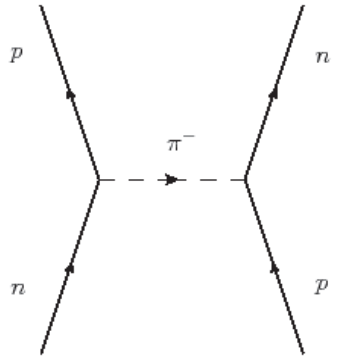

Figure 2.5: Yukawa Feynman Diagram

Although baryons are no more having the 'elementary particle' status, still the meson exchange models are serving as a good approximations compensating the non-perturbative QCD regime. Yukawa first introduced the idea in terms of a scalar meson mediator (remember at this time pion was not discovered). The Lagrangian for this scalar Yukawa Theory is given by

$$\begin{aligned} \mathcal{L}_M &= \frac{1}{2}\partial_\mu\Phi\partial^\mu\Phi - \frac{1}{2}m^2\Phi^2 \\ \mathcal{L}^s_{int} &= -g_{BB's}\bar{\Psi}_{B'}\Psi_B\Phi^s \\ \mathcal{L}_Y &= \mathcal{L}^f_B + \mathcal{L}^f_M + \mathcal{L}^s_{int} \end{aligned} \tag{2.13}$$

Here $\mathcal{L}_M$ represents the meson free field Lagrangian and $\mathcal{L}^s_{int}$ is the baryon (B)-

baryon (B)- scalar meson (s)- vertex (2.6) coupling constant "$g_{BB's}$".

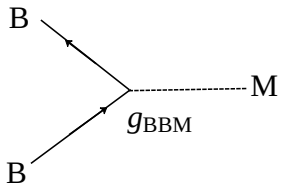

Figure 2.6: Baryon-Baryon-Meson vertex

The Yukawa Lagrangian $\mathcal{L}_Y$ failed to reproduce the 'proper' nucleon potential specially in the short ranges (as it is known now that pion is responsible for the long range part). Physicists tried to overcome the problem by considering multi-pion exchange models but that too could not solve the problem and the idea of meson exchange forces were discarded for further use. It was in the 60's when the discovery of the other heavy mesons, $\sigma(600)$, $\rho(770)$, $\omega(782)$ etc. opened the possibility of reviving the Yukawa theory by now including other mesons (bosons) exchange channels. In the 70's refined sophisticated 'one-boson-exchange' theories were introduced for the nucleon sector by several groups [10, 62]. The Nijmegen group [11] entered the picture with more precise treatment. Until then a number of good high-precision NN one-boson-exchange potentials [54, 55, 64] are discovered and still in use. The main essence of these models is the inclusion of not only scalar

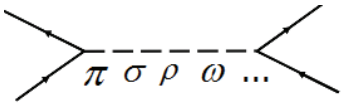

Figure 2.7: One-boson-exchange baryon - baryon -meson vertex

but also pseudo - scalar and vector mesons channels. The new Lagrangian is then takes the form as given below

$$\mathcal{L}_{Full} = \mathcal{L}_B + \mathcal{L}_M + \mathcal{L}_{int} \tag{2.14}$$

In One–boson–exchange models, the interaction have three different terms, limited to meson with masses less than 1 GeV, the scalar, the pseudo-scalar, and vector

meson baryon vertices

$$\mathcal{L}_{MB} = \mathcal{L}^{s}_{int} + \mathcal{L}^{ps}_{int} + \mathcal{L}^{v}_{int} \tag{2.15}$$

Eq. 2.15 defines the interaction Lagrangian used in this thesis. The explicit Lagrangian forms of the three interactions are given here

$$\mathcal{L}^{ps}_{int} : -g_{\mathcal{B}\mathcal{B}'ps}\bar{\Psi}_{\mathcal{B}'} i\gamma_5 \Psi_B \Phi^{ps} \tag{2.16}$$

$$\mathcal{L}^{s}_{int} : +g_{\mathcal{B}\mathcal{B}'s}\bar{\Psi}_{\mathcal{B}'} \Psi_{\mathcal{B}} \Phi^{s} \tag{2.17}$$

$$\mathcal{L}^{v}_{int} : -\left[g_{\mathcal{B}\mathcal{B}'v}\bar{\Psi}_{\mathcal{B}'}\gamma^{\mu}\Psi_{\mathcal{B}}\left(\tau \cdot \Phi^{v}_{\mu}\right) - \frac{f_{\mathcal{B}\mathcal{B}'v}}{M_{\mathcal{B}} + M_{\mathcal{B}'}}\bar{\Psi}_{\mathcal{B}'}\sigma^{\mu\nu}\Psi_{\mathcal{B}}F^{v}_{\mu\nu}\right] \tag{2.18}$$

Here $g_{\mathcal{B}\mathcal{B}'ps}$, $g_{\mathcal{B}\mathcal{B}'s}$, and $g_{\mathcal{B}\mathcal{B}'v}$ are the pseudoscalar, scalar, and vector meson-baryon coupling constants, $\tau = \sum_{i=1}^{3}\tau^{i}$ represents the three Pauli matrices, and $F_{\mu\nu}$ is the field strength tensor given by

$$F_{\mu\nu} = \left(\partial_{\mu} - \partial_{\nu}\right)\left(\tau \cdot \Phi^{v}_{\mu}\right) \tag{2.19}$$

The above mentioned couplings gave rise to the *effective* interaction for the baryons. There exists also gradient coupling of the nucleons by the pseudo-vectors (pv) with the Lagrangian of form

$$\mathcal{L}^{pv}_{int} : -\frac{f_{BB'pv}}{m_{pv}}\bar{\Psi}_{\mathcal{B}'}\gamma_5\gamma^{\mu}\Psi_{\mathcal{B}}\partial_{\mu}\Phi^{ps} \tag{2.20}$$

The pseudo-scalar and pseudo-vector coupling constants, $g_{\mathcal{B}\mathcal{B}'ps}$ and $f_{BB'pv}$, are equivalent on-mass-shell condition provided they satisfy the following relation

$$f_{BB'pv} = g_{\mathcal{B}\mathcal{B}'ps}\left(\frac{m_{ps}}{M_{\mathcal{B}} + M_{\mathcal{B}'}}\right) \tag{2.21}$$

The meson free field Lagrangian is now redefined as

$$\mathcal{L}_{\mathcal{M}} = \frac{1}{2}\sum_{i=ps,s,v}\left(\partial_{\mu}\Phi^{\mu}_{i}\Phi_{i} - m^{2}_{\Phi_i}\Phi^{2}_{i}\right) - \frac{1}{2}\sum_{\mathcal{M}=V}\left(\frac{1}{2}F^{(\mathcal{M})^2} - m^{2}_{\mathcal{M}}V^{2}_{\kappa}\right) \tag{2.22}$$

2.3 Effective Model Parameters

The effective interactions defined in Eq. 2.16, 2.18, 2.17 are characterized by three factors:

1. ***The value and sign of the coupling strength of the interaction vertex (g)***:
   + sign : attractive interaction (e.g: scalar)
   - sign : repulsive interaction (e.g: pseudo-scalar, vector, pseudo-vector)

2. ***Mass of the meson (m)***: Determines the range of baryon-baryon interaction the meson is responsible for.

3. ***Type of meson (J^P)***: Determines the Lorentz structure of the vertex and hence the Lagrangian as shown in Eq. 2.16, 2.18, 2.17.

Among these three, the critical ones are are the first two. In the following, we discuss these two factors in detail.

2.3.1 Meson Masses

Pure SU(3) symmetry demand the multiplets to be mass degenerate. However as already found by in the early decades of quark model discovery [12, 14] that this is not the case and the physical mass values are different. These mass difference is coming out of the *explicit symmetry breaking* due to strange quark (s) being slightly heavier than the up (u) and down (d) ones. The observed particles are called as the 'physical' ones. Therefore, for any SU(3) model to be realistic, one must study these physical particles. We, in this work, incorporate this breaking by using the physical mass values of the particles.

In Table 2.3 the physical mesons are listed with their spin (J), isospin (I), mass reported by Particle Data Group [16], and the full width of the particles in the complex plane. From the table it can be noticed that except for the strange $K^{-,+}$ pseudo-scalar meson, which has a two close bump structure (see Fig. 2.10), the pseudo-scalar and vector mesons are easy to identify as particles due to sharp peak in

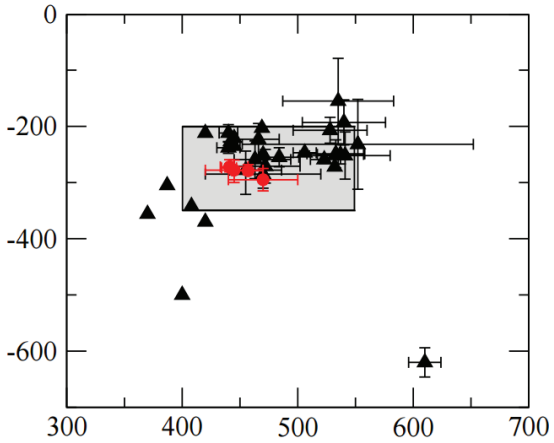

Figure 2.8: $f_0(500)$ scalar meson pole positions in complex energy plane. Figure taken from [126]

Meson	Spin (J^P)	Isospin (I^G)	Mass [MeV]	Full Width [MeV]
$\pi^{\pm}$	0^-	1^-	139.57018	0
π^0	0^-	1^-	134.97660	0
η	0^-	0^+	547.86000	.00131
η'	0^-	0^+	957.78000	0.198
$K^{0,+}$	0^-	$\frac{1}{2}$	497.64000	–
ϵ	0^+	0^+	760.00000	400-700
a_0 (δ)	0^+	1^-	983.00000	50-100
κ	0^+	$\frac{1}{2}$	880.00000	547
ω	1^-	0^-	782.65000	8.49
ρ	1^-	1^+	775.26000	149.1
K^*	1^-	$\frac{1}{2}$	891.66000	–

Table 2.3: Meson masses

the complex energy plane, but for scalar mesons it is an ongoing problem, thus arising the so-called ***'meson puzzle.'***. In fact, there is long debate among different groups

Type	Meson	Resonances as in [16]	Total
Pseudo-scalars	η	$\eta(1295)$,$\eta(1405)$,$\eta(1475)$,$\eta(1760)$,$\eta(2225)$	5
Scalar	f_0	f_0 (500),f_0 (980),f_0 (1370),f_0 (1500), f_0 (1710),f_0 (2020),f_0 (2100),f_0 (2200),f_0 (2330)	9
Scalar	a_0	$a_0(980)$,a_0 (1450)	2
Vector	ω	$\omega(782)$,$\omega(1420)$,$\omega(1650)$	3

Table 2.4: Different resonances available for mesons

whether the respective resonances for the scalar mesons are actually representing a

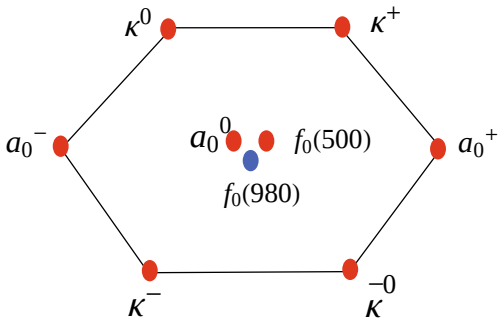

Figure 2.9: Scalar meson octet.

single particle (read scalar meson) or resonances between two other light particles. This discrepancy has lead many physicists to discard the scalar meson sector and approaching the problem as two or multi-particle resonances, for example, the latest Jülich hyperon model [48] considers the scalar-isoscalar σ meson interactions as $\pi\pi$.

Moreover, a look at the PDG listing of particles, one can find a long list of particles with same nomenclature but with different resonances or pole positions, for all types of mesons, making it difficult to position the particle in the particle plane. Particularly for the scalar mesons the determination of the width is very model dependent. For example the Fig. 2.8 one can see various pole positions of the $f_0(500)$ scalar meson as reported in [16]. The mesons used in this thesis and their corresponding PDG listed particle identifiers are reported in Table. 2.5. An scalar-isoscalar meson ϵ (or σ) is used to provide intermediate- range interaction as done by [11, 49, 50, 62], to make the model realistic. For the mass we choose a value of 760 MeV, following ESC group [49].

2.3.2 Coupling Constants

In order to use the effective Lagrangian (Eq. 2.15), the required input is the correct coupling strengths of the meson-baryon vertices. The more precise the values are, the larger the predictive power of the model will be. There are few possible way outs for determining the coupling:

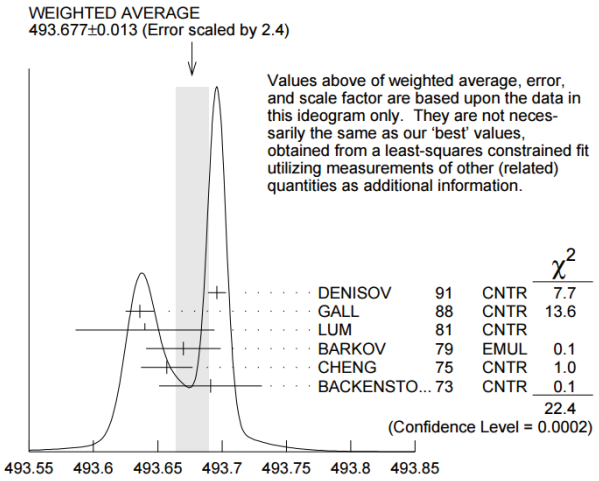

Figure 2.10: $K^{-,+}$ pseudo-scalar meson pole positions in complex energy plane. This figure is taken from [16].

Meson	PDG2012 listed particle identifier	Mass [MeV]
$\pi^{\pm}$	$\pi^{\pm}$	139.57018
π^0	π^0	134.9766
η	η	547.86
$K^{0,+}$	$K^{0,+}$	497.64
ϵ	$f_0(500)$	760.0
a_0	$a_0(980)$	983.0
κ	$K_0^*(800)$	880.0
ω	$\omega(782)$	782.65
ρ	$\rho(770)$	775.26
K^*	$K^*(892)$	891.66

Table 2.5: Meson used in this model listed according to the PDG identifiers [16].

- Phenomenological method: treating them as parameters and fix the values then by fit to approximately chosen experimental values. This is how the nucleon meson-nucleon coupling constants are fixed [10, 11, 54, 62, 64]

- Theoretical method: Fix the values by theory. Usually by symmetry or other relevant physical constraints the theory demands. In the future, results from lattice QCD (LQCD) could be used.

- The 'hybrid' method: A mixture of all the above, e.g., use theoretical relations to eliminates the number of free parameters and determine only a subset by phenomenology.

As far as hyperons are concerned, phenomenology is ruled out due to few data points compared to the number of channels. Therefore, the usual practice here is to fix the values by theory, here it is SU(3). However, since SU(3) is not exact, many groups use the third approach, for example the various models of Nijmegen groups differ by the choice of coupling strengths [49, 50] as well as for the Jülich model also have varied the coupling strength values in their different versions [46–48]. The one-boson-exchange potential will be discussed in more detail in the next chapter.

Here in this thesis, we will constraint ourselves to SU(3) symmetry. However, we will use the physical particle masses to make the model realistic and allowing this explicit breaking. Our aim is to have a qualitative understanding of the baryon-baryon octet interactions. One of our major application of the free space interaction is to find the medium effect on it. For this reason, we, at this moment, do not indulge on the complexities involved in countering the breaking involved. In the next section, we discuss how the coupling constants are determined in our case using SU(3) symmetry.

2.3.3 Octet-Octet and Octet-Singlet Interaction

We have already discussed in Sec. 3.1 that baryons are observed to have the octet structure represented as $\mathbf{8_B}$ (Fig. 2.1). SU(3) symmetry demands the Lagrangian to be SU(3) invariant,i.e., SU(3) scalar. This means all our interaction terms defined in the previous section (Eq. 2.16-2.18) should be SU(3) singlet. We have already

defined our interaction vertices as baryon-baryon-meson (BB'M) one. In terms of group theory, this means we need to construct SU(3) scalar with the meson nonets $(\mathbf{8_M}, \mathbf{1_M})$ and the baryon current $\mathbf{8_B} \otimes \mathbf{8_B}$. This has been worked out completely by J.J. de Swart [56] in 1965. In the following, we describe the method of determining g's from SU(3) considerations.

The baryon current yields the following six representations

$$\mathbf{8_B} \otimes \mathbf{8_B} = \mathbf{27} \oplus \mathbf{10} \oplus \mathbf{10^*} \oplus \mathbf{8_1} \oplus \mathbf{8_2} \oplus \mathbf{1} \tag{2.23}$$

$\mathbf{8_1}$ and $\mathbf{8_2}$ corresponds two distinct octet representations of same dimension. $\mathbf{8_1}$ is symmetric under the exchange of the coupled basis elements, while $\mathbf{8_2}$ is the antisymmetric under same condition. The reason why these two are named distinctly is that these results in two different types of coupling:

- D- coupling : Results from the coupling between symmetric baryon multiplet $\mathbf{8_1}$ with meson octet $\mathbf{8_M}$ with strength $\mathbf{g_D}$
- F- coupling :Results from the coupling between anti-symmetric baryon octet $\mathbf{8_2}$ with meson octet $\mathbf{8_M}$ with strength $\mathbf{g_F}$

There are now two ways in which now one can construct a SU(3) scalar out of a baryon–baryon–meson coupling, namely

1. Octet-octet coupling : $\mathbf{8_B} \otimes \mathbf{8_B} \otimes \mathbf{8_M}$
2. Octet-singlet coupling: $\mathbf{8_B} \otimes \mathbf{8_B} \otimes \mathbf{1_M}$

2.3.4 $SU_f(3)$ Baryon-Baryon-Meson vertices

In eqs. 2.4-2.7 the SU(3) invariant traceless baryon and octet matrices has been shown. The available SU(3) invariant combinations using these matrices are the following

$$\mathrm{Tr}\,(\bar{\mathcal{B}}\mathcal{M}\mathcal{B}),\ \mathrm{Tr}\,(\bar{\mathcal{B}}\mathcal{B}\mathcal{M}),\ \mathrm{Tr}\,(\bar{\mathcal{B}}\mathcal{B})\,\mathrm{Tr}\,(\mathcal{M})$$

The definition of the anti-symmetric (F), symmetric (D) , and singlet(S) SU(3) scalars are then

$$\begin{aligned}
[\bar{\mathcal{B}}\mathcal{B}\mathcal{M}]_F &= \mathrm{Tr}\,(\bar{\mathcal{B}}\mathcal{M}\mathcal{B}) - \mathrm{Tr}\,(\bar{\mathcal{B}}\mathcal{B}\mathcal{M}) \\
&= \mathrm{Tr}\,(\bar{\mathcal{B}}\mathcal{M}_8\mathcal{B}) - \mathrm{Tr}\,(\bar{\mathcal{B}}\mathcal{B}\mathcal{M}_8) \\
&= \mathrm{Tr}\,([\bar{\mathcal{B}},\mathcal{B}]\mathcal{M}_8) \qquad (2.24) \\
[\bar{\mathcal{B}}\mathcal{B}\mathcal{M}]_D &= \mathrm{Tr}\,(\bar{\mathcal{B}}\mathcal{M}\mathcal{B}) - \mathrm{Tr}\,(\bar{\mathcal{B}}\mathcal{B}\mathcal{M}) - \frac{2}{3}\mathrm{Tr}\,(\bar{\mathcal{B}}\mathcal{B})\,\mathrm{Tr}\,(\mathcal{M}) \\
&= \mathrm{Tr}\,(\bar{\mathcal{B}}\mathcal{M}_8\mathcal{B}) + \mathrm{Tr}\,(\bar{\mathcal{B}}\mathcal{B}\mathcal{M}_8) \\
&= \mathrm{Tr}\,(\{\bar{\mathcal{B}},\mathcal{B}\}\,\mathcal{M}_8) \qquad (2.25) \\
[\bar{\mathcal{B}}\mathcal{B}\mathcal{M}]_S &= \mathrm{Tr}\,(\bar{\mathcal{B}}\mathcal{B})\,\mathrm{Tr}\,(\mathcal{M}) \\
&= \mathrm{Tr}\,(\bar{\mathcal{B}}\mathcal{B})\,\mathrm{Tr}\,(\mathcal{M}_1) \qquad (2.26)
\end{aligned}$$

Here $[\bar{\mathcal{B}},\mathcal{B}]$ represents the $\bar{\mathcal{B}},\mathcal{B}$ commutator and $\{\bar{\mathcal{B}},\mathcal{B}\}$ is the corresponding anti-commutator. Now we can re-define our same interaction Lagrangian 2.15 in terms of these SU(3) flavor invariants. The SU(3) interaction Lagrangian is a linear combinations of the F,D, and S scalars defined above

$$\mathcal{L}_{MB}^{SU(3)} = -g_8\sqrt{2}\left\{\alpha\left[\overline{\mathcal{B}}\mathcal{B}\mathcal{M}_8\right]_F + (1-\alpha)\left[\overline{\mathcal{B}}\mathcal{B}\mathcal{M}_8\right]_D\right\} - g_S\sqrt{\frac{1}{3}}\left[\overline{\mathcal{B}}\mathcal{B}\mathcal{M}_1\right]_S \qquad (2.27)$$

Here a new constant α, known as the $\frac{F}{F+D}$-ratio, is introduced with the definition

$$\alpha = \frac{g_F}{g_F + g_D} \qquad (2.28)$$

where g_8 and g_1 are the octet and singlet coupling constant respectively. Apart from SU(3), another important feature of the Lagrangian is isospin symmetry. The Lagrangian should also be isospin invariant. Let us define the following baryon (N,Λ, Σ, Ξ) and meson (K, K_c, π) isospin multiplets

$$N = \begin{pmatrix} n \\ p \end{pmatrix}, \Lambda = \Lambda, \quad \Sigma = \begin{pmatrix} \Sigma^+ \\ \Sigma^0 \\ \Sigma^- \end{pmatrix}, \Xi = \begin{pmatrix} \Xi^0 \\ \Xi^- \end{pmatrix} \qquad (2.29)$$

$$\pi = \begin{pmatrix} \pi^+ \\ \pi^0 \\ \pi^- \end{pmatrix}, K = \begin{pmatrix} K^+ \\ K^0 \end{pmatrix}, K_c = \begin{pmatrix} \overline{K^0} \\ -K^- \end{pmatrix} \tag{2.30}$$

As has been worked out by [56], the most general isospin invariant meson octet Lagrangian (shown for π as an example) is of the following form

$$\begin{aligned} m_\pi \mathcal{L}^8_{MB} &= -g_{NN\pi}(\overline{N}\Gamma\tau N)\cdot\pi + ig_{\Sigma\Sigma\pi}(\overline{\Sigma}\times\Gamma\Sigma)\cdot\pi \\ &- g_{\Lambda\Sigma\pi}(\overline{\Lambda}\Gamma\Sigma + \overline{\Sigma}\Gamma\Lambda)\cdot\pi - g_{\Xi\Xi\pi}(\overline{\Xi}\Gamma\tau\Xi)\cdot\pi \\ &- g_{\Lambda NK}\left[(\overline{N}\Gamma K)\Lambda + \overline{\Lambda}\Gamma(\overline{K}N)\right] \\ &- g_{\Xi\Lambda K}\left[(\overline{\Xi}\Gamma K_c)\Lambda + \overline{\Lambda}\Gamma(\overline{K_c}\Xi)\right] \\ &- g_{\Sigma NK}\left[\overline{\Sigma}\cdot\Gamma(\overline{K}\tau N) + (\overline{N}\Gamma\tau K)\cdot\Sigma\right] \\ &- g_{\Xi\Sigma K}\left[\overline{\Sigma}\cdot\Gamma(\overline{K_c}\tau\Xi) + (\overline{\Xi}\Gamma\tau K_c)\cdot\Sigma\right] \\ &- g_{NN\eta_8}(\overline{N}\Gamma N)\eta_8 - g_{\Lambda\Lambda\eta_8}(\overline{\Lambda}\Gamma\Lambda)\eta_8 \\ &- g_{\Sigma\Sigma\eta_8}(\overline{\Sigma}\cdot\Gamma\Sigma)\eta_8 - g_{\Xi\Xi\eta_8}(\overline{\Xi}\Gamma\Xi)\eta_8. \end{aligned} \tag{2.31}$$

with the singlet interaction of the form

$$m_\pi \mathcal{L}^1_{MB} = \left[g_{NN\eta_1}(\overline{N}N) + g_{\Lambda\Lambda\eta_1}(\overline{\Lambda}\Lambda) + g_{\Sigma\Sigma\eta_1}(\overline{\Sigma}\cdot\Sigma) + g_{\Xi\Xi\eta_1}(\overline{\Xi}\Xi)\right]\eta_1 \tag{2.32}$$

We follow the *de Swart* [56] phase convention that defines the inner product of the isovector Σ- baryon and π-meson in the following form

$$\mathbf{\Sigma}\cdot\pi = \Sigma^+\pi^- + \Sigma^0\pi^0 + \Sigma^-\pi^+ \tag{2.33}$$

$g_{NN\pi} = g_8^{ps}$	$g_{NN\eta_8} = \frac{1}{\sqrt{3}}(4\alpha_{ps} - 1)g_8^{ps}$	$g_{\Lambda NK} = -\frac{1}{\sqrt{3}}(1 + 2\alpha_{ps})g_8^{ps}$
$g_{\Xi\Xi\pi} = -(1 - 2\alpha_{ps})g_8^{ps}$	$g_{\Xi\Xi\eta_8} = -\frac{1}{\sqrt{3}}(1 + 2\alpha_{ps})g_8^{ps}$	$g_{\Xi\Lambda K} = \frac{1}{\sqrt{3}}(4\alpha_{ps} - 1)g_8^{ps}$
$g_{\Lambda\Sigma\pi} = \frac{2}{\sqrt{3}}(1 - \alpha_{ps})g_8^{ps}$	$g_{\Sigma\Sigma\eta_8} = \frac{2}{\sqrt{3}}(1 - \alpha_{ps})g_8^{ps}$	$g_{\Sigma NK} = (1 - 2\alpha_{ps})g_8^{ps}$
$g_{\Sigma\Sigma\pi} = 2\alpha_{ps}g_8^{ps}$	$g_{\Lambda\Lambda\eta_8} = -\frac{2}{\sqrt{3}}(1 - \alpha_{ps})g_8^{ps}$	$g_{\Xi\Sigma K} = -g_8^{ps}$

Table 2.6: Pseudo-scalar meson-baryon coupling constants

Incorporating the SU(3) invariance conditions to the isospin invariance, the pseudoscalar meson coupling constants need to satisfy the following relations (Tab. 2.6). Similar relations for the vector and scalar mesons are given in Tab. 2.3.5. The singlet mesons couples universally with baryons (Table 3.4).

ps	$g_{NN\eta_1} = g_{\Lambda\Lambda\eta_1} = g_{\Sigma\Sigma\eta_1} = g_{\Xi\Xi\eta_1} = g_1^{ps}$
v	$g_{NN\phi} = g_{\Lambda\Lambda\phi} = g_{\Sigma\Sigma\phi} = g_{\Xi\Xi\phi} = g_1^{v}$
s	$g_{NN\sigma_1} = g_{\Lambda\Lambda\sigma_1} = g_{\Sigma\Sigma\sigma_1} = g_{\Xi\Xi\sigma_1} = g_1^{s}$

Table 2.7: Singlet meson-baryon coupling constants

2.3.5 Free Parameters

From the relations above, it is clear that three parameters are governing the coupling of a particular type of meson (ps,s,v) with baryons

1. the octet coupling strength (g_8)
2. the $\frac{F}{F+D}$-ratio (α)
3. the singlet coupling strength (g_1)

So considering three types of mesons we have in total 9 parameters. However, there is one extra parameter that need to be taken into account to incorporate the octet-singlet mixing: the mixing angle (θ) already defined in eq. 2.11. In addition, there is the standard set of OBE model parameters containing meson masses and form factor parameters. These will add to the count and in total our parameters are summarized in Table. 2.10.

$g_{NN\rho} = g_8^v$	$g_{NN\omega_8} = \frac{1}{\sqrt{3}}(4\alpha_v - 1)g_8^v$	$g_{\Lambda NK^*} = -\frac{1}{\sqrt{3}}(1 + 2\alpha_v)g_8^v$
$g_{\Xi\Xi\rho} = -(1 - 2\alpha_v)g_8^v$	$g_{\Xi\Xi\omega_8} = -\frac{1}{\sqrt{3}}(1 + 2\alpha_v)g_8^v$	$g_{\Xi\Lambda K^*} = \frac{1}{\sqrt{3}}(4\alpha_v - 1)g_8^v$
$g_{\Lambda\Sigma\rho} = \frac{2}{\sqrt{3}}(1 - \alpha_v)g_8^v$	$g_{\Sigma\Sigma\omega_8} = \frac{2}{\sqrt{3}}(1 - \alpha_v)g_8^v$	$g_{\Sigma NK^*} = (1 - 2\alpha_v)g_8^v$
$g_{\Sigma\Sigma\rho} = 2\alpha_v g_8^v$	$g_{\Lambda\Lambda\omega_8^v} = -\frac{2}{\sqrt{3}}(1 - \alpha_v)g_8^v$	$g_{\Xi\Sigma K^*} = -g_8^v$

Table 2.8: Vector meson-baryon coupling constants

There is an additional parameter too, namely the form factor, that needs to be multiplied with each $\mathcal{B}\mathcal{B}'\mathcal{M}$ vertex to regularize the high-momentum behavior. We will discuss about this later in detail. The model we will use is a low-energy effective

$g_{NNa_0} = g_8^s$	$g_{NN\epsilon} = \frac{1}{\sqrt{3}}(4\alpha_s - 1)g_8^s$	$g_{\Lambda N\kappa} = -\frac{1}{\sqrt{3}}(1 + 2\alpha_s)g_8^s$
$g_{\Xi\Xi a_0} = -(1 - 2\alpha_s)g_8^s$	$g_{\Xi\Xi\epsilon} = -\frac{1}{\sqrt{3}}(1 + 2\alpha_s)g_8^s$	$g_{\Xi\Lambda\kappa} = \frac{1}{\sqrt{3}}(4\alpha_s - 1)g_8^s$
$g_{\Lambda\Sigma a_0} = \frac{2}{\sqrt{3}}(1 - \alpha_s)g_8^s$	$g_{\Sigma\Sigma\epsilon} = \frac{2}{\sqrt{3}}(1 - \alpha_s)g_8^s$	$g_{\Sigma N\kappa} = (1 - 2\alpha_s)g_8^s$
$g_{\Sigma\Sigma a_0} = 2\alpha_s g_8^s$	$g_{\Lambda\Lambda\epsilon} = -\frac{2}{\sqrt{3}}(1 - \alpha)g_8^s$	$g_{\Xi\Sigma\kappa} = -g_8^s$

Table 2.9: Scalar meson-baryon coupling constants

theory. Therefore, there is a certain limit up to which the model will give realistic result. This is taken into account by the form factor. In higher energy regime, many other degrees of freedom will enter the system which is not treated in our model. Here we use a dipole form factor having the following form

$$\mathcal{F}^2(\vec{k}) = \left(\frac{\Lambda_c^2 - m^2}{\Lambda_c^2 + k^2}\right)^2 \tag{2.34}$$

Λ_c is called the cut-off. Here $\vec{k}$ is the relative momenta between the initial and final baryon. "m" is the mass of the meson involved as a force carrier. Λ_c has the dimension of mass usually chosen as 500- 600 MeV higher than the meson. The value of Λ_c fixes the higher momentum domain of the calculation. For massive mesons (σ), Λ_c is much higher than lighter ones (π). As it is found out, the value of Λ_c also effects the behavior of the model [46, 47, 49, 50]. The Nijmegen-Tokyo group [50] uses each vertex cut-off as a parameter. In our case, we have fixed the value of the cut-off for the whole meson octet that reduced the number of parameter significantly. Table 1.8 summarizes the parameters used in this thesis. In Table. 2.10 the *free parameters* of the model are listed, total 15 in number. These parameters are fixed by preferably by fitting to the scattering data available However, due to a limited number of data set that is insufficient to fix the parameters with desired accuracy, some of the parameters are fixed from theoretical aspect. The details of the fitting procedure will be discussed in Chapter 5. We will keep updating this parameter list

Meson	Parameters	Total Parameter (Meson Octet)
pseudo-scalar	$g_8^{ps}, g_1^{ps}, \alpha_{ps}, \Lambda_c^{ps}, \theta_{ps}$	5
vector	$g_8^v, g_1^v, \alpha_v, \theta_v, \Lambda_c^v$	5
scalar	$g_8^s, g_1^s, \alpha_s, \theta_s, \Lambda_c^s$	5
Total Model Parameter: 15		

Table 2.10: Parameters of the model.

as we start discussing the results to minimize the parameter even more by putting constant values to the less sensitive ones.

2.4 Comparison with Contemporary Models

There exists few more hyperon models based on OBE, namely the Jülich models, Extended-soft-core (ESC) models (known as Nijmegen models too). The basic physics followed by these two and the one used in this work, are same. However, there exists various significant differences in the treatment of the of actual problem e.g., the choice of parameters, extent of SU(3) symmetry *used*, scalar-isoscalar mesons taken into account, responsible for the intermediate range attraction, form factor etc. In the following, these differences has been pointed out.

1. **Mesons**: The first difference between the other two and our one is the number of mesons being included. We are trying to follow SU(3) as much as we can, including all the **nonet mesons**, except the ϕ one, which did not found to have much effect on the hyperon sector [46, 47]. Moreover, we do not include higher lying mesons except the lower ones. We do not have any other extra mesons in our models. On the other hand, the ESC-models although usually use all the SU(3) mesons yet they have a fictitious particle 'pomeron' in their model. Esc group also considers all the massive mesons in their models. In total the number of meson channels they have are way higher than ours. Concerning the Jülich models (no more in continuation), there are three versions available: 1989, 1994, and 2005 one. The first two being much similar, have octet mesons. Our model is quite similar to the early versions of Jülich models in this particular point. The latest Jülich one discarded the e scalar-isoscalar (σ) and the vector-isovector (ρ) completely and used $\pi\pi$ and $K\bar{K}$ exchange channels instead.

2. **Boson-exchange vertices**: The other important factor is the diagrams taken into account of the potential involved. We have only considered One–boson–exchange diagrams. Both ESC and Jülich groups have in some of their versions two-meson (usually ps) exchange diagrams and sometimes delta resonances

[47]. The very recent ESC model includes multi-pomeron channels.

3. **Parameters**: We have minimized the parameters by fixing them for a type of octet and using SU(3). Where as Jülich models have all their vertices as parameters for the all of their version. For ESC one, the parameter choice is similar to ours but with a major difference that they usually make different versions depending on the parameter values [50]. There fore, the parameters are not actually fixed.

4. **Cut-off**: The choice of form factor is also different. Ours is similar to Jülich one where as ESC group uses a Gaussian type form-factor.

5. **Momentum or Co-ordinate Space?**: We will write the potential and solve the scattering equation, to be discussed in next chapter, in momentum space similar to Jülich model. On the other hand, the Nijmegen group prefers the co-ordinate space version and solve the equation in r-space. This is just a matter of choice in which one is comfortable to deal the problem as the final physics should be independent of the choice of the solving procedure.

6. **Fitting Procedure**: Both the Jülich and ESC models starts from the nucleon sector. In order to have a good fit with the nucleon data, the SU(3) values are already modified specially for the vector mesons. On the other hand, in order to study the SU(3) symmetry in close attention, the nucleon values are not fitted by our parameters. On the contrary, in this work, the reverse approach is followed. We first fitted the hyperon sector and then used the parameters to the nucleon sector.

7. **SU(3) Flavor Octet Interaction**: As already mentioned, the basic interest of revising the OBE models is to study the SU(3) symmetry range of applicability in terms of octet interaction. We are allowing the breaking only via physical particle masses. The coupling constant relations are not disturbed. As discussed in the previous point, fitting the nucleon sector, the SU(3) is already broken by some extent for both the other models. Also the earlier Jülich model considered SU(6) symmetry and the latest one is more on the

phenomenological side. The ESC and Nijmegen ones are using SU(3) symmetry. However, they use explicit breaking terms and mesons outside the octet, that also does not preserve the SU(3).

2.5 Summary of the model

In the following a list is given with the key points of the One–boson–exchange model based on SU(3) symmetry used in this thesis

1. This is an *effective model* with boson-exchange effective interactions.
2. The bosons (mesons) used belong to the *SU(3) meson octet* and the respective singlets
   - Pseudo-scalar : π, η, η', K^0
   - Vector : ρ, ω, K^*
   - Scalar : $a_0, \epsilon, \kappa, \epsilon'$
3. Effective meson-baryon coupling constants are determined using *SU(3) relations.*
4. *Physical particle masses* according to PDG [16] are used to account for explicit symmetry breaking.
5. A *dipole form factor* is multi-plied to each $\mathcal{BB'M}$ vertex to control divergence.
6. The free parameters are fixed by *fitting to scattering data.*

Chapter 3

Scattering Theory and Formalism

> "Physicists have come to realize that mathematics, when used with sufficient care, is a proven pathway to truth."
>
> Brian Greene

Now since the model is defined in Chap. 2, the next step is to use it in real systems. Scattering is an important experimental tool for quantum systems. For microscopic physics, most of our knowledge is indebted to scattering experiments. For hyperon-baryon interactions, scattering is a powerful technique to gain understanding about the interaction. Here the test of the model is to be able to reproduce scattering data set when used as theoretical input. Therefore, it is worthwhile to spend few pages on describing the two-body scattering problem.

In Section 1, basic kinematics for two body scattering is described briefly. Section 2 and 3 are devoted on describing theoretical descriptions of scattering processes by describing Bethe-Salpeter and Lippmann-Schwinger equations. In Section 4, isospin basis formalism is discussed for the scattering channels in connection with isospin symmetry conservation. A special characteristics of the hyperon included baryon scattering channels, the coupled channel formalism is the topic for discussion in Section 5. The formation of the OBE potential amplitudes relevant to our model has been discussed in detail in Section 6.

3.1 Kinematics

The kinematics of a scattering process is described largely by the energy and momentum conservation laws without depending on the detailed dynamics involved in the process.

A scattering is called elastic when outgoing particles are identical as the incoming ones,

$$A + B \rightarrow A + B$$

In case of elastic collision, the particles only exchange kinetic energy and momentum between themselves. On the other hand, a collision is called inelastic when at least one of the particle changes its internal state after collision.

$$A + B \rightarrow A^* + B$$

Here A^* is a excited state of particle A. A scattering can also be a reaction where

$$A + B \rightarrow C + D + E...$$

C, D, E are the reaction products, which are not identical to the incoming particles. In this thesis we will restrict ourselves to the simplest case of two body scattering.

$$A + B \rightarrow C + D$$

3.1.1 Relativistic kinematics of Two-particle Scattering

For a particle having energy E and three-momentum $\vec{p}$, the relativistic four-momentum P is defined as

$$P^\mu = (P^0, \vec{p}) = (\frac{E}{c}, \vec{p}) \tag{3.1}$$

The relation between relativistic energy (E) and three-momentum is given by

$$E^2 = p^2c^2 + m^2c^4 \tag{3.2}$$

The four-momentum P_i of any particle i satisfies the relation (in natural unit $c = 1$, $\hbar = 1$)

$$P_i^\mu P_\mu^i = E_i^2 - p_i^2 = m_i^2 \tag{3.3}$$

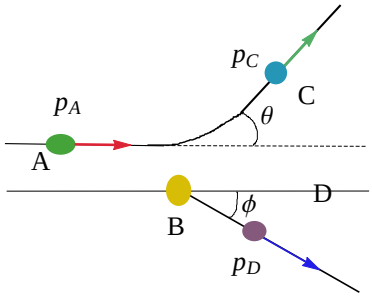

Figure 3.1: Two body scattering in laboratory frame

In this thesis we are interested in hyperon -baryon two body scattering reactions.

$$A + B \rightarrow C + D$$

where particle A of mass m_1 collides with particle B of mass m_2.

Usually in particle physics experiments, one particle remains at rest, known as the target, and the other one is made to collide with the target (called projectile or incident or beam particle). The reference frame in which the target particle is at rest is known as the laboratory (lab) frame as shown in Fig. 3.1. The center-of mass frame (CM) is the one in which total three momentum of the reaction is zero as in Fig. 3.2.

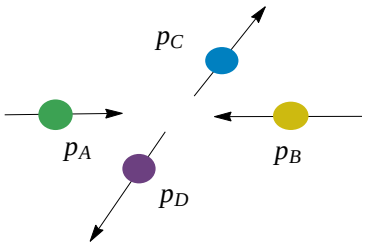

Figure 3.2: Two body scattering in center-of-mass (CM) frame

The usual convention is to consider the direction of beam particles along positive z axis. Let us consider the beam particle A has momentum $\vec{p_{lab}}$ in the laboratory (lab) frame along z axis. The outgoing particle C (mass m_3) and D (mass m_4) are detected in the lab frame at an angle θ having momentum $\vec{p}_3$ and at angle $\phi$with momentum $\vec{p}_4$ respectively with respect to the direction of travel of the projectile

$\vec{p_1}$ [Fig. 3.1]. Consider E_1, E_2, E_3 and E_4 are the energy of the particles A, B, C and D respectively in lab frame. Since the target is at rest in laboratory frame, we have,

$$\vec{p_2} = 0 \tag{3.4}$$

Now let us consider P_1, P_2, P_3, P_4 being the four-momenta of the particles A, B, C, and D respectively in the reaction under investigation. The total four-momentum is always conserved in any collision in any reference frame, hence

$$P_1 + P_2 = P_3 + P_4$$

Now in case of the target and beam scattering,i.e, for particles A and B in Fig. 3.1, we have, in lab frame,

$$P_1 = \begin{pmatrix} E_1(\vec{p}_{lab}) \\ \vec{p}_{lab} \end{pmatrix}, P_2 = \begin{pmatrix} E_1(\vec{0}) \\ \vec{0} \end{pmatrix}$$

In case of CM frame, considering the corresponding CM variables as asterisked ($P_i = P_i^*$), we have,

$$P_1^* = -P_2^*, P_3^* = -P_3^* \tag{3.5}$$

In relativity, the dot product of two four-vectors is a Lorenz invariant quantity and usually known as Lorenz scalar. Out of the possible invariant Lorenz scalars, e.g, $P_1.P_1$, $P_1.P_2$,$P_3.P_4$ etc., due to the constraints, only two are left as variables. Recalling the definitions of the Mandelstam variables,

$$s = (P_1 + P_2)^2 = (P_3 + P_4)^2 \tag{3.6}$$

$$t = (P_1 - P_3)^2 = (P_2 - P_4)^2 \tag{3.7}$$

$$u = (P_1 - P_4)^2 = (P_3 - P_2)^2 \tag{3.8}$$

we see they serve as a possible Lorenz scalar choice. It follows from these definitions that s- Mandelstam variable is square of the total CM energy where t is the four-momentum transfer squared between 1 and 3. It is straight forward to see that the

Mandelstam variables also satisfy

$$s + t + u = m_1^2 + m_2^2 + m_3^2 + m_4^2 = constant \tag{3.9}$$

Some useful formulas concerning scattering between CM and lab frame are summarized below:

$$p_{lab} = \sqrt{\frac{(s - m_1^2 - m_2^2)^2 - 4m_1^2 m_2^2}{4s}} \tag{3.10}$$

In terms of p_{lab}, the s mandelstam variable, the total energy squared of the system is given by

$$s = m_1^2 + m_2^2 + 2m_2\sqrt{p_{\text{lab}}^2 + m_1^2}. \tag{3.11}$$

3.2 Scattering Equations

The quantity we are interested in this kind of problems is the scattering amplitude. The time scale over which the particles interact are extremely short. Considering the time of interaction as t, then $-\infty \ll t \ll \infty$. For times long before and after the interaction, the incident particles are free. These two regions are known as the two asymptotic regions, one in distant past (t_{in}) and one in distant future (t_{out}). The scattering operator is defined mathematically as

$$\hat{S} \mid \Psi_i >= \mid \Psi_f > \tag{3.12}$$

Scattering matrix $\mathcal{S}$ measures the transition probability of state ψ_i to ψ_f.

$$\mathcal{S}_{fi} \equiv < \psi_f \mid \hat{S} \mid \psi_i > \tag{3.13}$$

3.2.1 Bethe-Salpeter Equation

In this thesis, we focus on hyperon (Y) -baryon (B) scattering problems.

$$\mathcal{B}_1(q_1) + \mathcal{B}_2(q_2) \rightarrow \mathcal{B}_3(q_3) + \mathcal{B}_4(q_4)$$

Particle physics scattering problems needs to be dealt not only from quantum mechanical but relativistic point of view. Therefore one can not start form the non-relativistic Schroedinger equation or it's counterpart Lippmann-Schwinger equation being a non-relativistic scattering equation. As far as nuclear physics is concerned, Bethe-Salpeter equation is the answer to the problem. Bethe-Salpeter equation (BSE) for a two-particle relativistic scattering in momentum space can be represented as [57]

$$\mathcal{T}(q', q \mid E) = \mathcal{V}(q', q \mid E) + \int d^4k \; \mathcal{V}(q', k \mid E) \; \mathcal{G}(k \mid E) \; \mathcal{T}(k, q \mid E) \tag{3.14}$$

where q', q, and k are final, initial, and intermediate relative four-momenta of the particles, respectively, E is implying constant energy, $\mathcal{T}$ is the total invariant two-particle scattering amplitude, $\mathcal{V}$ is the sum of all possible two-particle connected irreducible diagrams, and $\mathcal{G}$ is the relativistic two-particle free propagator, the Green function, which is represented in momentum space as

$$\mathcal{G}_{12}(q_1, q_2) = \mathcal{G}_1(q_1) \; \mathcal{G}_2(q_2) = \left(\frac{1}{\gamma^\mu q_\mu^1 - M_1 + i\epsilon}\right)\left(\frac{1}{\gamma^\mu q_\mu^2 - M_2 + i\epsilon}\right) \tag{3.15}$$

where M_1 and M_2 are the masses of particle 1 and 2. The diagrammatic representation of BSE is shown in Fig. 3.3. The more convenient way is to represent

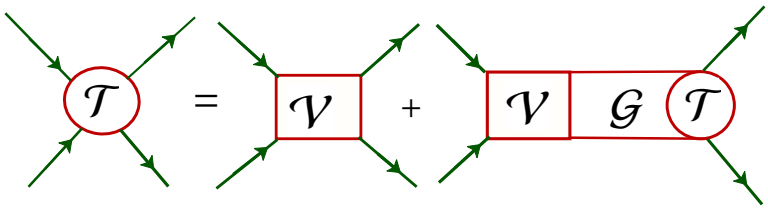

Figure 3.3: Diagrammatic representation of Bethe-Salpeter Equation

Bethe–Salpeter equation in the operator notation as following:

$$\mathcal{T} = \mathcal{V} + \mathcal{V} \; \mathcal{G} \; \mathcal{T} = \mathcal{V} + \mathcal{V} \; \mathcal{G} \; \mathcal{V} + \mathcal{V} \; \mathcal{G} \; \mathcal{V} \; \mathcal{G} \; \mathcal{V} + ... \tag{3.16}$$

This is a self-consistent equation. The first term $\mathcal{V}$ can be interpreted as a relativistic potential. The possible Feynman diagrams contained in $\mathcal{V}$ is shown in Fig. [3.4]. Considering only the highest (first term) order contribution to the kernel

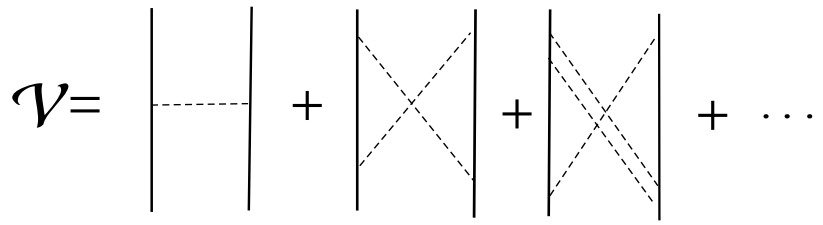

Figure 3.4: Irreducible Kernel V of Bethe-Salpeter Equation. The solid line represents the baryon and the dashed line is for meson.

$\mathcal{V}$, represented as $\mathcal{V}^0$, neglecting the crossed order contributions, then scattering amplitude $\mathcal{T}$ get the form as shown if Fig. 3.6. It is clear from Fig. 3.6 that

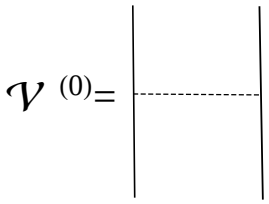

Figure 3.5: Highest order term of V of Bethe–Salpeter equations (Eq. 3.14)

various contributing terms to $\mathcal{T}$ looks like a ladder. Thus came the name *"ladder approximation"* for this truncation scheme. In this thesis, the one-boson exchange potential (OBE) used corresponds to the term $\mathcal{V}^{(0)}$ in Fig. 3.5. Here the dotted line represents the 'meson' acting as the force mediator between the baryons that are trying to interact with each other. Within the ladder approximation scheme, the crossed and other higher order terms are being neglected. The main reason behind this as a starting point are the facts that, first of all, a basic approach in physics is to start from the simplest interaction first then gradually adding the complexities. Following the same strategy, we for this time being, focused on $\mathcal{V}^{(0)}$ only. Secondly,

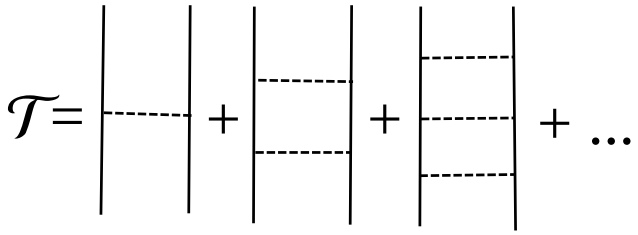

Figure 3.6: Bethe-Salpeter Scattering amplitude in ladder approximation

the order of magnitude of the higher order terms is much less as compared to the first one for this kind of two-body scattering problem as found already by various groups [11, 46, 49, 55, 62]. Whether this approximation is well enough or a crude one, that can be clear after the theoretical calculations are compared with the available date set. One important point to be worth mentioned here is that the way our model is build, if it is found at later stage that the higher order or crossed terms are unavoidable, they can be added conveniently to the scheme.

3.2.2 Lippmann-Schwinger Equation

The main difficulty with BSE is its 4-dimensional integral structure, which makes it difficult to solve. The usual way of making it workable is to reduce it to an equivalent 3-dimensional equation not affecting the covariant and relativistic elastic unitarity. The reduction scheme is not however unique. The reduction is done by considering an unknown operator U for the kernel that satisfies an analogous Bethe–Salpeter type equation with U defined as Eq. (3.17)

$$\begin{aligned} \mathcal{T} &= U + U\mathcal{G}\mathcal{T} \\ U &= \mathcal{V} + \mathcal{V}(\mathcal{G} - g)U \end{aligned} \tag{3.17}$$

Here g is a three-dimensional propagator. By method of insertion then it is straightforward to see that $\mathcal{T}$ is indeed the Bethe–Salpeter amplitude. For Eqs. (3.14) and (3.17) to be equivalent, g needs to be simple, ($\mathcal{G}$-g) needs to small, and $\mathcal{G}$ and g should have the same elastic unitarity cut in the physical region. Here in this thesis, the Blancenbekler-Sugar operator(BbS) [58] has been used as g for the reduction.

BbS reduction converts BSE to the following 3-D Lippmann-Schwinger type non-relativistic equation

$$T(\mathbf{q}', \mathbf{q} \mid E) = V(\mathbf{q}', \mathbf{q} \mid E) + \int d^3k \; V(\mathbf{q}', \mathbf{k} \mid E) \; G_{12} \; T(\mathbf{k}, \mathbf{q} \mid E) \tag{3.18}$$

Eq. 3.18 has formally the same form as BSE, an essential difference is that the integration is now over three dimension and T and V are defined now under the 'minimal relativity' condition, refers to considering the relativistic kinematics properly, taking only the positive-energy Dirac spinors into account. A detailed calculation of the derivation can be found in [59]. G is the non-relativistic two-particle propagator given by

$$G_{12} = \frac{2\mu_{12}}{q^2 - \mathbf{k}^2 + i\epsilon} \tag{3.19}$$

with μ_{12} being the reduced mass of the two interacting baryons

$$\mu_{12} = \frac{M_1 M_2}{M_1 + M_2} \tag{3.20}$$

By using Eq. 3.18 the full scattering matrix T is obtained by iterating over the term V, now the one-boson-exchange potential. We need to solve this equation to get various information about the hyperon-baryon scattering using out interaction. Before discussing about the numerical solution strategy, it is important to have a knowledge about the scattering channels. In next section, octet baryon-baryon channels are discussed.

3.3 Isospin Basis

In Chap. 2, we have discussed about the $J^P = \frac{1}{2}^+$ baryon octet that is our prime focus in this work. In Table 3.1 these baryons are listed with their observed spin, parity, charge and the quark content. It has been already discussed that SU(2) isospin symmetry is a subgroup of SU(3) flavor symmetry. Therefore, the effective interaction should be an isospin conserving one. In Eq. 2.31 the interaction is shown in one -way of isospin symmetry preserving manner using the baryon (N, Λ, Σ, Ξ) and meson (π, K, K_c) isospin multiplets defined via Eqs. 2.29 and 2.30. Considering

Baryon	Component	Isospin (I)	Isospin (I_3)	Charge (Q)
n	udd	$\frac{1}{2}$	$\frac{1}{2}^-$	0
p	uud	$\frac{1}{2}$	$\frac{1}{2}^+$	+1
Λ	uds	0	0	0
Σ^+	uus	1	1^+	+1
Σ^-	dds	1	1^-	-1
Σ^0	uds	1	0	0
Ξ^-	dss	$\frac{1}{2}$	$\frac{1}{2}^-$	-1
Ξ^0	uss	$\frac{1}{2}$	$\frac{1}{2}^+$	0

Table 3.1: $J^P = \frac{1}{2}^+$ Baryons with their quark component, isospin, third component of isospin (I_3), and charge (Q)

$SU_f(3)$ as an exact internal symmetry, the resonant particles must belong to the irreducible representations of $SU_f(3)$ introduced in the previous Chapter. On the other hand, for isospin to be a full symmetry, the particles in an isospin multiplet must have the same mass-spin-parity (space-time properties) of the one-particle states. A look on the baryon isospin multiplets (see Table. 3.2) shows that the individual particles of the multiplets differ by electric charge having same spin and almost same mass. This mass-splitting is due to an interaction that can distinguish the particles by some property, here as we can see by charge, hence it is the electromagnetic interaction. Therefore, if we neglect the electromagnetic interaction, the space-time properties of all particles of a multiplet are identical to each other. As for example the isospin multiplet of N, Λ, Σ, and Ξ baryon has one or more members with same spin, parity and slightly different masses as shown in Table. 3.2. The mesons also have this isospin symmetry inbuilt (see Table. 3.3). The multiplicity of the multiplets refer to the dimension of the irreducible representation we have discussed in previous chapter. The SU(3) isospin multiplets discussed about are consist of one-particle states. Our aim in this thesis is to study the hyperon-baryon interaction in connection with the two-body scattering. For that we need to understand the isospin transformations of the two baryon channels. Multi-particle states transform according to the direct product of the single-particle states representation that has been used earlier in Chapter 2 to derive the baryon and meson SU(3) traceless matrices (Eq. 2.4-2.7). Neglecting the electromagnetic and weak interaction and considering the isospin symmetry to be exact, the scattering matrix $\mathcal{S}$ and hence the T-matrix

Baryon	Strangeness(S)	Multiplet	Mass	Spin (J)	Parity (P)
N	0	$\begin{pmatrix} n \\ p \end{pmatrix}$	$\begin{pmatrix} 939.57 \\ 938.27 \end{pmatrix}$	$\frac{1}{2}$	+
Λ	-1	Λ	1115.683	$\frac{1}{2}$	+
Σ	-1	$\begin{pmatrix} \Sigma^+ \\ \Sigma^0 \\ \Sigma^- \end{pmatrix}$	$\begin{pmatrix} 1189.37 \\ 1192.64 \\ 1197.45 \end{pmatrix}$	$\frac{1}{2}$	+
Ξ	-2	$\begin{pmatrix} \Xi^0 \\ \Xi^- \end{pmatrix}$	$\begin{pmatrix} 1314.86 \\ 1321.71 \end{pmatrix}$	$\frac{1}{2}$	+

Table 3.2: Baryon isospin multiplets with their space-time properties*.

Meson	Multiplet	Mass	Spin	Parity
π	$\begin{pmatrix} \pi^+ \\ \pi^0 \\ \pi^- \end{pmatrix}$	$\begin{pmatrix} 139.57 \\ 134.97 \\ 139.57 \end{pmatrix}$	0	-
η	η	547.862	0	-
K	$\begin{pmatrix} \mathrm{K}^+ \\ \mathrm{K}^0 \end{pmatrix}$	$\begin{pmatrix} 493.677 \\ 493.677 \end{pmatrix}$	0	-

Table 3.3: Meson isospin multiplets with their space-time properties.

have diagonal form in isospin basis with respect to isospin I leaving the dynamics of the system unchanged for isospin rotations. This leaves total isospin I as conserved therefore we have

$$[\mathcal{S}, I] = 0, \quad [T, I] = 0 \tag{3.21}$$

This implies that the isospin can form a basis for the scattering problem. Correspondingly the T-matrix elements can be written now as an expansion in terms of isospin scattering amplitudes $T(I)$, scattering amplitude T for isospin I, an expansion in the *isospin basis*. For our two baryon scattering process $B_1B_2 \to B_3B_4$ the expansion is then given by

$$\langle B_3B_4|T|B_1B_2\rangle = \sum_I T(I)\Omega(I; B_1, B_2; B_3, B_4). \tag{3.22}$$

The element $\Omega(I; B_1, B_2; B_3, B_4)$ calculates the projection of T on a state of isospin I. By construction here each scattering amplitude $T(I)$ is isospin invariant. Formulating now the mentioned isospin expansion scheme to the octet SU(3) baryon channels, say B_8B_8 channels can be written in isospin basis. In Table 3.3 the B_8B_8

baryon channels have been tabulated accordingly in the isospin basis, defined in this case as channels grouped according to total strangeness (S) and isospin (I).

	I = 0	**I = $\frac{1}{2}$**	**I=1**	**I = $\frac{3}{2}$**	**I=2**
S=0	NN		NN		
S=-1		ΛN, ΣN		ΣN	
S=-2	$\Lambda\Lambda$, ΞN , $\Sigma\Sigma$		ΞN, $\Sigma\Lambda$, $\Sigma\Sigma$		$\Sigma\Sigma$
S=-3		$\Xi\Lambda$, $\Xi\Sigma$		$\Xi\Sigma$	
S=-4	$\Xi\Xi$		$\Xi\Xi$		

Table 3.4: Baryon-baryon channels in isopin basis

3.4 Coupled Channel Formalism

One new and interesting feature of the two baryon scattering problem appears when strangeness channels are included, the so called ***'coupled channel'*** behavior. The channels with only single entry is called as uncoupled. For example the ΣN, $I = \frac{3}{2}$ channel is a pure isospin-$\frac{3}{2}$ channel. Isospin conservation prohibits the coupling of this channel with any other. See in Table 3.3 that for channels $S \leq -1$, there are few isospin channels having more than one sub-channels. For example, consider the $S = -1, I = \frac{1}{2}$ subset, it has two BB channels : ΛN and ΣN as the elements. This means that these two channels together span the $S = -1, I = \frac{1}{2}$ subset. However, due to the mass difference between the 'physical particles', the massive particle channel ΣN opens has a higher threshold energy

$$E_{threshold} = \sqrt{s} = M_\Sigma + M_N. \tag{3.23}$$

Hence, ΣN channel will open at higher input momenta than the other member ΛN since $M_\Sigma - M_\Lambda > 0$ (see Table 3.3). In particular for this case the ΣN threshold pointing to the laboratory momenta at which the channel opens up is

$$p^{\text{th}}_{\text{lab}}(\Lambda N \to \Sigma N) = 643.8 \text{ MeV}/c. \tag{3.24}$$

In Fig. 3.7 total energy ($\sqrt{s}$) of $S = -1, I = \frac{1}{2}$ channels (orange: ΛN, blue(solid):

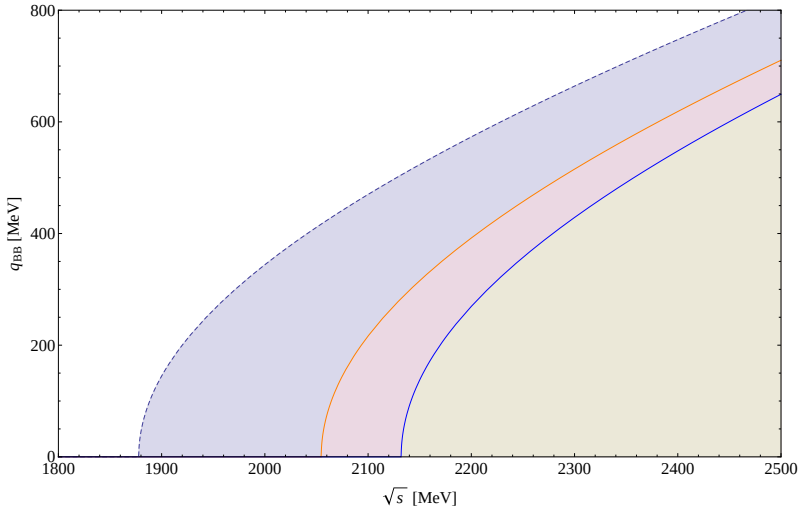

Figure 3.7: Center-of-mass momentum vs energy plot of NN (blue dashed), ΛN (orange) and ΣN (solid blue) channels showing ΣN channel opening at higher energies than ΛN

ΣN) along with the nucleon (dashed blue) has been plotted for varying center-of-mass momentum of the BB channels showing clearly the difference in threshold opening. Below the threshold energy, the corresponding q_{BB} is imaginary and the state act as a virtual one. At the threshold energy, the heavier channel opens up starts contributing to the physical observables. A very typical case is the 'cusp' effect when the cross section or phase shift of the lighter channel suddenly shows a 'kink' type structure at exactly the threshold energy. This cusp effect and more interesting phenomena related to the coupled behavior will be shown in the result section. To conclude this threshold behavior due to channel coupling is very special for the hyperon systems that should be taken care of while solving the scattering problem. While studying the system, one must therefore see as outcome this special coupled channel behavior of the baryon channels. In order to have the output right, therefore we must somehow set the input correctly to take care of this phenomena. This is done via the scattering equation by reformulating into a coupled channel version.

We define

$$\langle BB \rangle^{S,I}_{\alpha,\beta} \tag{3.25}$$

as a notation for each isospin basis subset where S, I is representing the isospin basis and α and β are the strangeness and isospin corresponding to the channel,

respectively. For two-baryon scattering $B_1B_2 \rightarrow B_3B_4$ the values α and β are defined as $\alpha = S_1 + S_2$ and $\beta = I_1 + I_2$. According to definition 3.25 then

$$\langle BB\rangle^{S,I}_{0,0} = NN, \quad \langle BB\rangle^{S,I}_{-4,0} = \Xi\Xi$$

and so on.

Now consider a isospin basis subset $\langle BB\rangle^{S,I}_{\alpha,\beta}$ with channel elements $Y_i{}^\dagger$, Y_j, and Y_k. The Lippmann-Schwinger equation for this coupled scattering system in operator notation is given by

$$T_{Y_i,Y_j} \equiv \langle Y_j|\ T\ |Y_i\rangle = V_{Y_i,Y_j} + \sum_{Y\in\langle BB\rangle^{S,I}_{\alpha,\beta}} V_{Y_i,Y}\ G_Y\ T_{Y,Y_j}. \tag{3.26}$$

This is called the coupled channel Lippmann–Schwinger equation[‡]. The second term of Eq. 3.26 takes care of the coupled channel behavior. For each channel element Y of the subset, T-matrix will have contribution from the other member elements too. $Y \in \langle BB\rangle^{S,I}_{\alpha,\beta}$ condition makes sure to include only those channels as the inter-mediate one which belong to the particular subset in use. It is important to note that in isospin basis (or any basis), two different subset elements are not mixed satisfying the orthogonality condition of any quantum mechanical basis. Therefore each subset is solved separately. For single member subsets, of course, one do not need the coupled equation. The non-relativistic Green function G_Y has the similar form as of Eq. 4.5 as

$$G_Y = \frac{2\mu_Y}{q_Y^2 - \mathbf{k}^2 + i\epsilon} \tag{3.27}$$

where μ_Y is the pertinent reduced mass of the inter-mediate YN channel. The on-shell momentum of the intermediate state Y ($= B_1B_2$) is defined as

$$q_{onshell} = \sqrt{s} = \sqrt{M_{B_1}^2 + q_Y^2} + \sqrt{M_{B_2}^2 + q_Y^2} \tag{3.28}$$

[†]Note that here each channel (Y) is a two-body scattering channel (e.g. ΛN).

[‡]It is important to note that Eq. 3.26 is in operator notation with Y_i, Y_j as BB scattering channels while Eq. 3.18 defined the T-matrix in integral form as a function of the respective momentum of the channel that is suppressed in operator notation.

that guarantees the threshold phenomena by making sure that the higher lying channel opens exactly at the physical threshold.

In order to get the physical output from the scattering equation, the potential, V, needs to written accordingly in the isospin basis keeping in mind the coupled channel formalism too. Consider the $\langle BB\rangle^{S,I}_{-1,\frac{1}{2}}$ subset, the ΛN and ΣN coupled scattering channel. Since they are coupled the input channel and output channel can be different, referring to inelastic scattering. Therefore, there exists four different T- matrix equations for this sub-channel. It is useful therefore to solve the system in matrix equation form for mathematical simplicity as below

$$\begin{pmatrix} T_{11} & T_{12} \\ T_{21} & T_{22} \end{pmatrix} = \begin{pmatrix} V_{11} & V_{12} \\ V_{21} & V_{22} \end{pmatrix} + \begin{pmatrix} V_{11} & V_{12} \\ V_{21} & V_{22} \end{pmatrix} \begin{pmatrix} G_{11} & G_{12} \\ G_{21} & G_{22} \end{pmatrix} \begin{pmatrix} T_{11} & T_{12} \\ T_{21} & T_{22} \end{pmatrix} \tag{3.29}$$

The explicit T,V, and G matrices are defined as for this coupled channel subset

$$\begin{pmatrix} T_{11} & T_{12} \\ T_{21} & T_{22} \end{pmatrix} = \begin{pmatrix} T_{\Lambda N\to\Lambda N} & T_{\Lambda N\to\Sigma N} \\ T_{\Sigma N\to\Lambda N} & T_{\Sigma N\to\Sigma N} \end{pmatrix} \tag{3.30}$$

$$\begin{pmatrix} V_{11} & V_{12} \\ V_{21} & V_{22} \end{pmatrix} = \begin{pmatrix} V_{\Lambda N\to\Lambda N} & V_{\Lambda N\to\Sigma N} \\ V_{\Sigma N\to\Lambda N} & V_{\Sigma N\to\Sigma N} \end{pmatrix} \tag{3.31}$$

$$\begin{pmatrix} G_{11} & G_{12} \\ G_{21} & G_{22} \end{pmatrix} = \begin{pmatrix} G_{\Lambda N\to\Lambda N} & 0 \\ 0 & G_{\Sigma N\to\Sigma N} \end{pmatrix} \tag{3.32}$$

Because the channels can mix, the off-diagonal terms are non-zero. Note that the Green function does not have any off-diagonal term associated. From Eqs. 3.29-3.32 it is then clear that the coupled-channel procedure is primarily depends on the potential matrix. If for a particular channel, there is no mixing between the channel elements, the off-diagonal terms of matrix V will be zero, hence going back to the uncoupled channel equation. Therefore it is important to allow channel mixing already in the stage of the potential by building what usually is called the "transfer potential".

Note that each of the T, V, and G matrix elements are functions of q', q which are

not explicitly shown here. Similar to Eq. 3.73, for each BB scattering channel subset of isospin basis (see Table 3.3), there exists a T-matrix equation with respective potential matrix of the system that needs to be solved for finding the scattering observables. In general coupled channel T-matrix equation, thus, can be written in the following form,

$$\boxed{T_{Y_i,Y_j} = V_{Y_i,Y_j} + \sum_{k=1,n} V_{Y_i,Y_k}\ G_{Y_k}\ T_{Y_k,Y_j}} \tag{3.33}$$

with "n" representing the number of channel element of the subset under investigation. From now on, any reference to scattering equation (or Lippmann–Schwinger equation) for the scattering process, will point to Eq. 3.33 in context of the octet baryon scattering we are working on this thesis. The numerical solving techniques of the same will be described in the next chapter.

3.5 Formation of the Potential

To have the proper coupled (as well as uncoupled) channel behavior of the octet baryons, the input potential should be appropriate. In Chap. 2 we have discussed about the effective interaction Lagrangian in detail. The potential used in this thesis is the one-boson-exchange potential. The different interaction Lagrangian terms for pseudoscalar(ps) , scalar (s), and vector (v) mesons has been shown in Eq. 2.16-2.17. The OBE potential (OBEP) is defined as a sum of one-boson-exchange diagrams as the following

$$V_{OBEP} = \sum_{x=ps,s,v} V_x^{OBE} \tag{3.34}$$

For iso-vector bosons, V_x^{OBE} contain an additional $\tau_1 \cdot \tau_2$ factor, τ^i being the Pauli matrices. The choice of the bosons, x, is entirely independent and that does not constraint the OBEP. The only important defining characteristics is the *one-particle-exchange* amplitudes. As fas as this work is concerned, the interaction model is *SU(3) OBEP*, exploring in addition to OBE the $SU_f(3)$ relations for finding the amplitudes. Other than that, the OBEP scheme is the same scheme as used in the nucleon sector by [10, 11, 62] or in the hyperon sector by [46, 47, 49, 50] when neg-

lecting the other the multi-particle exchange diagrams the others may have included. So for this thesis, the effective OBEP is

$$V_{\rm OBEP} = \sum_x V_x^{\rm OBE}, \quad x = \left\{ {\rm ps} : \pi, \eta, \eta', K^0 \right\}, \left\{ {\rm v} : \rho, \omega, K^* \right\}, \left\{ {\rm s} : a_0, \epsilon, \kappa, \epsilon' \right\} \quad (3.35)$$

3.5.1 OBEP Amplitudes

The one-boson-exchange amplitudes used in this thesis is based on the Bonn group developed version [62]. For defining the OBEP vertex, consider a a two-baryon scattering process

$$\mathcal{B}_1(q_1) + \mathcal{B}_2(q_2) \rightarrow \mathcal{B}_3(q_3) + \mathcal{B}_4(q_4)$$

with masses M_{B_i}, initial energy E_i, final energy E_i' and four-momentum $q_i = (E_i, \mathbf{q_i})$. We introduced already We define two momentum **p** and **k** for a channel with initial relative momenta **q**, final relative momenta **q'** as

$$\mathbf{k} = \mathbf{q}' - \mathbf{q}, \quad \mathbf{p} = \frac{\mathbf{q}' + \mathbf{q}}{2} \quad (3.36)$$

Consider the Feynman diagram in Fig. 3.8) representing one-boson-exchange scattering for The diagram is treated as the Born contribution to the scattering problem preserving the "**on-mass- shell**" condition for the baryons, referring that the baryons are real physical particles. The on-mass-shell condition points to the fulfillment of relativistic energy-momentum relation

$$E_i = \sqrt{M_i^2 + \mathbf{q_i}^2} \quad (3.37)$$

for each particle participating in the scattering. The scattering process is also energy conserving, hence satisfying the "**on-energy-shell condition**" : $E'(final) = E(initial) = E(say)$. For a beam-target type scattering process where one of the particle is used as target, the particle four-momenta in com frame satisfy relation Eq. 3.5 discussed in section 3.2. Under these conditions, we introduce now the Dirac spinors ($u_i(\mathbf{q}, \lambda)$) of the interacting baryons. The 4-component Dirac spinors of the

positive energy states of the free baryons in helicity basis are given by

$$u_1(\mathbf{q}) = \sqrt{\frac{(E+M_{B_1})}{E}} \begin{pmatrix} \chi(\lambda) \\ \frac{2\sigma_1\cdot\mathbf{q}}{E+M}\chi(\lambda) \end{pmatrix} \tag{3.38}$$

$$u_2(-\mathbf{q}) = \sqrt{\frac{(E+M_{B_2})}{E}} \begin{pmatrix} \chi(\lambda) \\ -\frac{2\sigma_2\cdot\mathbf{q}}{E+M}\chi(\lambda) \end{pmatrix} \tag{3.39}$$

Here σ_1, σ_2 are the spins of the particles. $\chi(\lambda)$ are 2-component Pauli -spinors which in the rest frame are given by

$$\chi(+\frac{1}{2}) = \begin{pmatrix} 1 \\ 0 \end{pmatrix}, \chi(-\frac{1}{2}) = \begin{pmatrix} 0 \\ 1 \end{pmatrix} \tag{3.40}$$

The Dirac spinors satisfy the following normalization condition

$$\overline{u_i}(\mathbf{q})\, u_i(\mathbf{q},) = \left(u_i^{\dagger}(\mathbf{q})\,\gamma^0\right) u_i(\mathbf{q}) = 1. \tag{3.41}$$

With these preliminaries, the general form of the OBE amplitude of the Feynman diagram in momentum space in center-of-mass (com) frame now can be introduced. In the Born approximation only tree level diagrams are included. A typical OBE Feynman diagram includes two interaction vertices, specifically, two baryon–baryon–meson vertices. Therefore, to cast the Lagrangian interactions discussed in last chapter, we need to transform the interaction vertex structure to the potential. Consider Fig. 3.8 as a general formulation of the OBE diagram under discussion, with two Feynman vertices, (say F_1 and F_2) with $\mathcal{B}\mathcal{B}'\mathcal{M}$ coupling constant being $g_1$and g_2, respectively, and Γ_1, Γ_2 being the corresponding Lorentz vertex structures. Our model picturizes the scattering process as an exchange of a boson(meson) of mass m_x between the two vertices, presented by the dotted line. Using the Feynman rules for the momentum space now we can read of the OBE amplitude ($\mathcal{A}$) of the process as of the following form

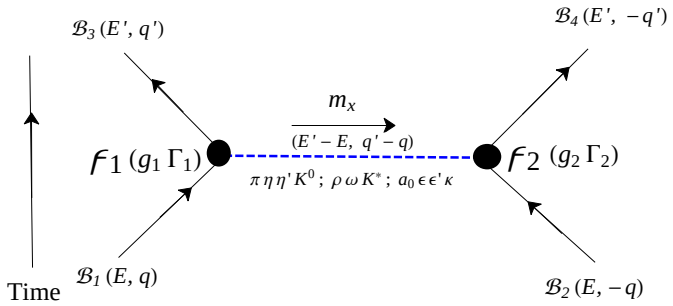

Figure 3.8: Feynman diagrams for OBE model contribution to baryon-baryon scattering in com frame. The solid lines denote baryons and the dashed line is the mediator meson with mass m_x.

$$\begin{aligned}
\mathcal{A} &= -iV_x(\mathbf{q}', \mathbf{q}) && (3.42)\\
&= F_1\ \mathcal{D}_x\ F_2 && (3.43)\\
&= [g_1\overline{u_1}(\mathbf{q}')\Gamma_1^x u_1(\mathbf{q})]\left[\frac{P_x}{q_x^2 - m_x^2}\right][g_2\overline{u_2}(-\mathbf{q}')\Gamma_2^x u_2(-\mathbf{q})]\,, && (3.44)
\end{aligned}$$

with $u_i(\mathbf{q})$ being the Dirac spinors represented in helicity suppressed notation. The factor $(-i)$ is the representative factor for momentum space Feynman diagrams. $\mathcal{D}_x$ is the meson propagator, representing the dashed line in Fig. 3.8. V_x are the "T-matrix" in Born-approximation. The momentum $\mathbf{q_x}$ in the denominator of $\mathcal{D}_x$ is the momentum carried by the meson, which is, under energy shell condition,

$$q_x = (E' - E)^2 - (q' - q)^2 = -(q' - q)^2. \tag{3.45}$$

This reduces the meson propagator to

$$\mathcal{D}_x = \frac{P_x}{-(q' - q)^2 - m_x^2} \tag{3.46}$$

For the simplest case of scalar mesons P_x=1. For vector mesons,

$$P_x = -g_{\mu\nu} + \frac{(q' - q)_\mu (q' - q)_\nu}{m_v^2} \tag{3.47}$$

Due to fact that vector mesons couple to a conserved baryon current, second term vanishes, reducing $P_x = -g_{\mu\nu}$. Next let us derive the OBE amplitudes for each meson type. The mesons differs from each other by three points: Lorentz structure (Γ), propagator ($\mathcal{D}$), and the mass (m). Using these three factors, we can calculate easily the potential for the respective mesons.

Pseudoscalar Meson ($J^P = 0^-$) Amplitude: Pseudo-scalar mesons corresponds to those meson field ϕ_{ps} that can switch sign under a space or time refection. The parity, spin, and isospin of the mesons is listed in Table 3.3. The required Lorentz structure to form a Lorentz scalar, has been shown in the Eq. 2.16 in Chap. 2 representing the interaction Lagrangian for meson. The resultant potential is then written as

$$V_{ps}(\mathbf{q}', \mathbf{q}) = -g_{13}^{ps} \;\; g_{24}^{ps} \;\; \frac{\bar{u_1}(q')i\gamma^5 u_1(q)\bar{u_2}(-q')i\gamma^5 u_2(-q)}{(q'-q)^2 + m_{ps}^2}. \tag{3.48}$$

We will solve the scattering equation in momentum space, as represented in Eq. 3.33, for which the potentials need to be represented in momentum space too. The general form functional form although is already represented in momentum space, however one can not insert these forms of the potentials straight into the scattering equation. To have the ready to be used in the numerical calculation format, each vertex has to evaluated completely, by some straight forward algebraic steps. Using the Dirac spinor definition, the left hand vertex for meson can be evaluated as follows, using the on-mass-shell condition,

$$\begin{aligned}
F_1 &= \bar{u_1}(q')i\gamma^5 u_1(q) \\
&= i\sqrt{\frac{(E'+M_{B_1})(E+M_{B_1})}{4E'E}} \begin{pmatrix} 1 & -\frac{\sigma_1\cdot q'}{(E'+M_{B_1})} \end{pmatrix} \begin{pmatrix} 0 & 1 \\ 1 & 0 \end{pmatrix} \begin{pmatrix} 1 & -\frac{\sigma_1\cdot q}{(E+M_{B1})} \end{pmatrix} \\
&= i\sqrt{\frac{(E'+M_{B1})(E+M_{B_1})}{4E'E}} \left[\frac{\sigma_1\cdot q}{(E+M_{B1})} - \frac{\sigma_1\cdot q'}{(E'+M_{B1})} \right] \\
&= \frac{i}{2E} \; [\sigma_1 \cdot (\mathbf{q} - \mathbf{q}')]
\end{aligned} \tag{3.49}$$

Similar calculation for the vertex Γ_2 will give

$$\Gamma_2 = \bar{u_2}(q')i\gamma^5 u_2(q) = \frac{i}{2E}\left[\sigma_2 \cdot (\mathbf{q}' - \mathbf{q})\right]. \tag{3.50}$$

Putting these back into Eq. 3.48, the explicit form of the pseudo-scalar meson potential in momentum space, we obtain

$$\boxed{V_{ps}(\mathbf{k}) = -\frac{g_{13}^{ps}\, g_{24}^{ps}}{4M_{B_1}M_{B_2}}\frac{(\sigma_1 \cdot \mathbf{k})\,(\sigma_2 \cdot \mathbf{k})}{k^2 + m_{ps}^2}.} \tag{3.51}$$

Here we have assumed $E' \approx M_{B'}$ and $E \approx M_B$. Another way to represent this equation by writing in terms of the tensor operator

$$S_{12} = \frac{3\,(\sigma_1 \cdot \mathbf{k})\,(\sigma_2 \cdot \mathbf{k})}{k^2} - (\sigma_1 \cdot \sigma_2). \tag{3.52}$$

Replacing the numerator of Eq. 3.51 using the definition of S_{12} leads to the following form

$$V_{ps}(\mathbf{k}) = -\frac{g_{13}^{ps}\, g_{24}^{ps}}{12M_{B_1}M_{B_2}}\frac{k^2}{k^2 + m_{ps}^2}\left\{\underbrace{S_{12}}_{\text{tensor}} + \underbrace{(\sigma_1 \cdot \sigma_2)}_{\text{spin-spin}}\right\} \tag{3.53}$$

arranged as a combination of *tensor* and *spin-spin* force component generated by the pseudo-scalar sector. The pion-nucleon-nucleon coupling constant is the octet coupling constant for the pseudo-scalar meson octet that in turn is connected to all the other meson couplings as shown in Table 2.6. The pion has three charge states, forming a isospin one state, the triplet. For this special property pion belongs to the pseudo-vector particle group with the interaction Lagrangian and correspondingly the potential differing from the one by having an additional isospin factor that we will discuss in relevance to each channel.

$$\begin{aligned} V_{pv}(\mathbf{q}', \mathbf{q}) &= \frac{f_{13}^{ps}\, f_{24}^{ps}}{m_{ps}^2}\frac{A_1^{ps} A_2^{ps}}{2\pi^3}\frac{1}{\left[(q'-q)^2 + m_{ps}^2\right]} \\ A_1^{ps} &= \left[\bar{u_1}(q')(\gamma^5 \cdot \gamma^\mu)i(q'-q)_\mu u_1(q)\right] \\ A_2^{ps} &= \left[\bar{u_2}(-q')(\gamma^5 \cdot \gamma^\mu)i(q'-q)_\mu u_2(-q)\right]. \end{aligned} \tag{3.54}$$

This can as well be worked out explicitly to find the momentum -space form, which we will not derive here. Apart form the amplitudes shown here, the one-pseudoscalar-meson exchange potential amplitudes needs to be multiplied with an isospin factor depending on the channel involved. The isospin factors for octet $\mathcal{BB}$ channels is shown in Table 3.5 in terms of the exchange flavor exchange operator P_f that is $+1$ for even-L singlet partial waves and -1 for odd-L triplet ones. For $\langle BB\rangle^{S,I}_{-2,2}$ subset owing to $\Sigma\Sigma$ scattering channel, the pseudoscalarexchange isospin factors are given by $(\Sigma\Sigma|\eta,\eta',\pi|\Sigma\Sigma) = \frac{1}{2}(1+P_f)$.

Scalar Meson ($J^P = 0^+$) Amplitude: Let us now turn to the scalar meson sector. Although the scalar mesons does not attain a clear 'particle' classification by many as discussed in the previous chapter under, namely the scalar meson puzzle, yet this is the simplest to work with as far as mathematics is concerned. They have the simplest interaction Lagrangian having requiring no extra Lorentz structure to form a scalar interaction contribution to the interaction. Having that in hand, keeping in mind they are the source of attractive interaction with a positive coupling strength, the OBE contribution can be easily written as

$$V_s(\mathbf{q}',\mathbf{q}) = g^s_{13}\; g^s_{24} \quad [\bar{u_1}(q')u_1(q)]\,\frac{1}{-\left(q'-q\right)^2 - m_s^2}\,[\bar{u_2}(-q')u_2(-q)]\,. \tag{3.55}$$

To have the explicit form, again, we need to evaluate the vertices. For the first one, we have

$$\begin{aligned}
\digamma_1 &= \bar{u_1}(q')u_1(q) \\
&= \sqrt{\frac{(E'+M_{B_1})(E+M_{B_1})}{4E'E}}\left(1 \quad -\tfrac{\sigma_1\cdot q'}{(E'+M_{B_1})}\right)\left(1 \quad -\tfrac{\sigma_1\cdot q}{(E+M_{B_1})}\right) \\
&= \sqrt{\frac{(E'+M_{B_1})(E+M_{B_1})}{4E'E}}\left\{1-\frac{(\sigma_1\cdot q')(\sigma_1\cdot q)}{(E'+M_{B_1})(E+M_{B_1})}\right\} \\
&= \sqrt{\frac{(E'+M_{B_1})(E+M_{B_1})}{4E'E}}\left\{1-\frac{p^2-\frac{k^2}{4}+i\sigma_1\cdot(\mathbf{k}\times\mathbf{p})}{(E'+M_{B_1})(E+M_{B_1})}\right\}
\end{aligned} \tag{3.56}$$

Similar expression can be evaluated for the right hand side vertex. Neglecting terms of second or higher order in momentum, the final momentum space scalar meson

$S=0$	$I=0$	$I=1$
$(NN\|\eta,\eta'\|NN)$	$\frac{1}{2}(1-P_f)$	$\frac{1}{2}(1+P_f)$
$(NN\|\pi\|NN)$	$-\frac{3}{2}(1-P_f)$	$\frac{1}{2}(1+P_f)$
$S=-1$	$I=\frac{1}{2}$	$I=\frac{3}{2}$
$(\Lambda N\|\eta,\eta'\|\Lambda N)$	1	0
$(\Sigma N\|\eta,\eta'\|\Sigma N)$	1	1
$(\Sigma N\|\pi\|\Sigma N)$	-2	1
$(\Lambda N\|\pi\|\Sigma N)$	$-\sqrt{3}$	0
$(\Lambda N\|K\|N\Lambda)$	P_f	0
$(\Sigma N\|K\|N\Sigma)$	$-P_f$	$2P_f$
$(\Lambda N\|K\|N\Sigma)$	$-P_f\sqrt{3}$	0
$S=-2$	$I=0$	$I=1$
$(\Lambda\Lambda\|\eta,\eta'\|\Lambda\Lambda)$	$\frac{1}{2}(1+P_f)$	0
$(\Xi N\|\eta,\eta'\|\Xi N)$	$\frac{1}{2}(1+P_f)$	1
$(\Sigma\Sigma\|\eta,\eta'\|\Sigma\Sigma)$	$\frac{1}{2}(1+P_f)$	$\frac{1}{2}(1-P_f)$
$(\Sigma\Lambda\|\eta,\eta'\|\Sigma\Lambda)$	0	1
$(\Xi N\|\pi\|\Xi N)$	-3	1
$(\Sigma\Sigma\|\pi\|\Sigma\Sigma)$	$-(1+P_f)$	$-\frac{1}{2}(1-P_f)$
$(\Lambda\Lambda\|\pi\|\Sigma\Sigma)$	$-\frac{1}{2}\sqrt{3}(1+P_f)$	0
$(\Sigma\Lambda\|\pi\|\Lambda\Sigma)$	0	P_f
$(\Sigma\Sigma\|\pi\|\Sigma\Lambda)$	0	$(1-P_f)$
$(\Lambda\Lambda\|K\|\Xi N)$	$1+P_f$	0
$(\Sigma\Sigma\|K\|\Xi N)$	$\sqrt{3}(1+P_f)$	$\sqrt{2}(1-P_f)$
$(\Xi N\|K\|\Sigma\Lambda)$	0	$\sqrt{2}; -P_f\sqrt{2}$
$S=-3$	$I=\frac{1}{2}$	$I=\frac{3}{2}$
$(\Xi\Lambda\|\eta,\eta'\|\Xi\Lambda)$	1	0
$(\Xi\Sigma\|\eta,\eta'\|\Xi\Sigma)$	1	1
$(\Xi\Sigma\|\pi\|\Xi\Sigma)$	-2	1
$(\Xi\Lambda\|\pi\|\Xi\Sigma)$	$\sqrt{3}$	0
$(\Xi\Lambda\|K\|\Lambda\Xi)$	P_f	0
$(\Xi\Sigma\|K\|\Sigma\Xi)$	$-P_f$	$2P_f$
$(\Xi\Lambda\|K\|\Sigma\Xi)$	$P_f\sqrt{3}$	0
$S=-4$	$I=0$	$I=1$
$(\Xi\Xi\|\eta,\eta'\|\Xi\Xi)$	$\frac{1}{2}(1-P_f)$	$\frac{1}{2}(1+P_f)$
$(\Xi\Xi\|\pi\|\Xi\Xi)$	$-\frac{3}{2}(1-P_f)$	$\frac{1}{2}(1+P_f)$

Table 3.5: Isospin factors for the various octet baryon-baryon channels for different total strangeness and isospin. P_f is the flavor exchange operator. [49]

potential has the following form ,

$$\boxed{V_s(\mathbf{k},\mathbf{p}) = -\frac{g^s_{13}\ g^s_{24}}{\mathbf{k}^2+m_s^2}\left[\underbrace{1}_{\text{attractive central}} + \underbrace{\frac{-i\ S\cdot(\mathbf{k}\times\mathbf{p})}{2M_{B_1}M_{B_2}}}_{\text{spin-orbit}}\right]} \tag{3.57}$$

with $S = \frac{1}{2}(\sigma_1+\sigma_2)$, the total spin operator. The first term of the scalar meson potential V_s is a strong attractive*central -force* component while the second term is referring to the *spin-orbit* force.

Vector Meson ($J^P = 1^-$) Amplitude: The vector mesons are defined as spin one particle with negative parity. The vector mesons have in a way similar force carriers like photons, another spin one mediator we know. They are represented by a four vector field. Being a four field vector, the corresponding Lorentz structure required to form a scalar is achieved by using the four γ matrices shown in Eq. 2.18. Using the structure defined in Eq. 2.18, the OBE contribution for the vector mesons has the following representation

$$V_v(\mathbf{q}',\mathbf{q}) = g^v_{13}\ g^v_{24}\ \ [\bar{u_1}(q')\gamma_\mu u_1(q)]\ \ \frac{-g_{\mu\nu}}{(q'-q)^2+m_v^2}\ \ [\bar{u_2}(-q')\gamma_\nu u_2(-q)] \tag{3.58}$$

For the first vertex we considering the term containing γ_0 , at this moment, we get

$$\begin{aligned} \digamma_1 &= \bar{u_1}(q')i\gamma^0 u_1(q) \\ &= \sqrt{\frac{(E'+M_{B_1})(E+M_{B_1})}{4E'E}}\begin{pmatrix}1 & -\frac{\sigma_1\cdot q'}{(E'+M_{B_1})}\end{pmatrix}\begin{pmatrix}1 & 0\\ 0 & -1\end{pmatrix}\begin{pmatrix}1 & -\frac{\sigma_1\cdot q}{(E+M_{B1})}\end{pmatrix} \\ &= \sqrt{\frac{(E'+M_{B_1})(E+M_{B_1})}{4E'E}}\ \left[1+(\sigma_1\cdot\mathbf{q}')\,\frac{(\sigma_2\cdot\mathbf{q})}{(E'+M_{B_1})(E+M_{B_1})}\right] \end{aligned} \tag{3.59}$$

Performing similar evaluation for terms with other γ matrices, the final vector OBE momentum potential can be written as

$$V_v(\mathbf{k},\mathbf{p}) = \frac{g^v_{13}\ g^v_{24}}{k^2+m_v^2}\left[\underbrace{1}_{\text{repulsive central}} - \underbrace{\frac{3\,[S\cdot(-i\mathbf{k}\times\mathbf{p})]}{2(M_{B_1}+M_{B_2})}}_{\text{spin-orbit}}\right] \tag{3.60}$$

with a *strong central force* (first term) and *spin-orbit force* component (second term), quite similar to the scalar case but with a repulsive central force and 3 times stronger spin-orbit force than the respective contribution by scalar meson.

In addition to the pure vector coupling, the 'vector' bosons also exhibit to have a 'tensor' coupling analogous to the magnetic dipole coupling of the photons to the electrons. In the vector meson -baryon interaction Lagrangian (Eq. 2.18), the second term represents the tensor coupling. Including that part to the OBE potential leads to tensor force contribution to the OBE potential, given by

$$
\begin{aligned}
V_t(\mathbf{k},\mathbf{p}) &= -\frac{f^t_{13}\, f^t_{24}}{4_B M_{B'}}\left[\frac{(\sigma_1\times\mathbf{k})\cdot(\sigma_2\times\mathbf{k})}{k^2+m_v^2}\right] && (3.61)\\
&= -\frac{f^t_{13}\, f^t_{24}}{4M_B M_{B'}}\frac{1}{k^2\left(k^2+m_v^2\right)}\left[(\sigma_1\cdot\sigma_2)-\left(\sigma_1\cdot\hat{k}\right)\left(\sigma_2\cdot\hat{k}\right)\right] && (3.62)\\
&= -\frac{f^t_{13}\, f^t_{24}}{4M_B M_{B'}}\frac{1}{k^2\left(k^2+m_v^2\right)}\left[(\sigma_1\cdot\sigma_2)-\frac{S_{12}+\sigma_1\cdot\sigma_2}{3}\right] && (3.63)\\
&= -\frac{f^t_{13}\, f^t_{24}}{4M_B M_{B'}}\frac{1}{k^2\left(k^2+m_v^2\right)}\left[\underbrace{\frac{2}{3}(\sigma_1\cdot\sigma_2)}_{spin-spin}-\underbrace{S_{12}}_{tensor}\right] && (3.64)
\end{aligned}
$$

where $\hat{k}$ is the unit vector in direction of $\mathbf{k}$. Combining these two potentials together we get the vector OBE , that after a few mathematical steps reduced to the following form

$$
\begin{aligned}
&V_v(\mathbf{k},\mathbf{p}) = \frac{1}{k^2+m_v^2}\\
&\Big\{\frac{g^v_{13}\, g^v_{24}}{2M_B M_{B'}}[2M_B M_{B'}+3p^2-\frac{k^2}{4}+3iS\cdot(\mathbf{k}\times\mathbf{p})-\frac{k^2\,(\sigma_1\cdot\sigma_2)}{2}+\frac{(\boldsymbol{\sigma_1}\cdot\mathbf{k})\,(\boldsymbol{\sigma_2}\cdot\mathbf{k})}{2}]\\
&+\frac{\sqrt{g^v_{13}\, g^v_{24}}\,\sqrt{f^t_{13}\, f^t_{24}}}{2M_B M_{B'}}\left[-k^2+4iS\cdot(\mathbf{k}\times\mathbf{p})-(\sigma_1\cdot\sigma_2)\,k^2+(\sigma_1\cdot\mathbf{k})\,(\sigma_2\cdot\mathbf{k})\right]\\
&+\frac{f^t_{13}\, f^t_{24}}{4M_B M_{B'}}\left[-(\sigma_1\cdot\sigma_2)\,k^2+(\sigma_1\cdot\mathbf{k})\,(\sigma_2\cdot\mathbf{k})\right]\Big\} \qquad (3.65)
\end{aligned}
$$

This is the input in our scattering equation in case of vector meson-baryon interaction potential.

To summarize, we first build an effective interaction Lagrangian as meson exchange forces in Chap. 2, and used that to derive the corresponding OBE potential

amplitudes. In Chap. 1, we had discussed about the features of strong interaction that should be an important base point for any kind of baryon force model to fulfill. In Table 3.6, each meson and their contribution towards the strong force type is listed verifying that the essential properties has been taken care of by the model.

Meson Coupling	Force Contribution
Pseudoscalar	tensor (S_{12}) , spin-spin ($\sigma_1 \cdot \sigma_2$)
scalar	attractive central, spin-orbit ($L \cdot S$)
vector	repulsive central, spin-orbit ($L \cdot S$)
tensor	spin-spin ($\sigma_1 \cdot \sigma_2$), tensor (S_{12})

Table 3.6: Various mesons and their contribution to strong force.

3.5.2 Potential Matrix in Isospin Basis

The OBEP amplitudes derived in last section are the general forms exclusive to the meson type. For practical purposes we need to form the total effective potential amplitudes in connection to each $\mathcal{BBM}$ vertex combining the relevant single meson amplitudes, as defined in Eq. 3.34. For example consider the following scattering process: $\Lambda N \to \Lambda N$. The mesons that can mediate the interaction for this channel are the once that pass through the isospin conservation at each vertex. The isospin of each octet and meson has been shown in Table 3.2, 2.3. Λ has isospin 0 while nucleon is with $I = \frac{1}{2}$. Consequently for the non-strangeness exchange $\Lambda\mathcal{M}\Lambda$ vertex, only these mesons having zero isospin can contribute, namely the η, ε, and ω meson. These mesons being of zero isospin, of course can couple to $N\mathcal{M}N$ vertex too. On the other hand for the strangeness exchange scattering vertex, in this case, the $\Lambda\mathcal{M}N$, the allowed meson should have isospin $\frac{1}{2}$. As a result K^0, κ, and K^* are the mesons giving rise to this interaction. The resultant Feynman diagrams are shown in Fig. 3.5.2. Finally the OBE amplitude for the $\Lambda N \to \Lambda N$ is given by

$$V_{\Lambda N \to \Lambda N} = \sum_{\eta,\varepsilon,\omega,K^0,\kappa,K^*} V_x^{OBE} \tag{3.66}$$

$$= V_{\eta,K^0}^{ps} + V_{\varepsilon,\kappa}^{s} + V_{\omega,K^*}^{v} \tag{3.67}$$

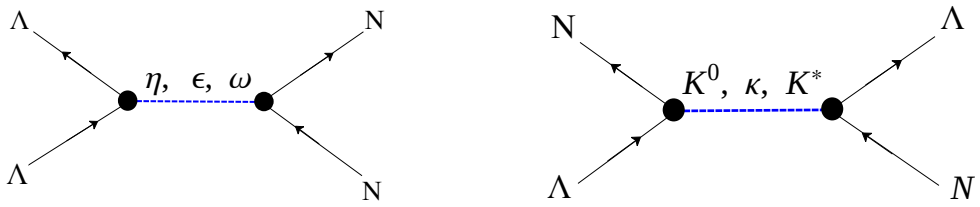

Figure 3.9: Feynman diagrams for $\Lambda N \to \Lambda N$ scattering.

where the OBE amplitudes for the meson now needs to be added correspondingly according to respective Lorentz structure as described earlier in detail. Different

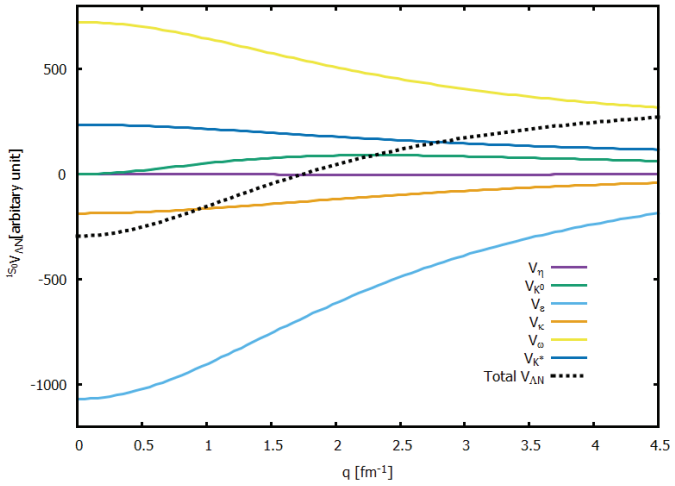

Figure 3.10: Various meson OBE amplitudes for ΛN in $^1S_0$ partial wave is shown b different colored solid lines. Total potential is represented by the dashed line.

meson OBE amplitude contribution in arbitrary unit for ΛN in $^1S_0$ partial wave is shown in Fig. 3.10 (solid lines). The total contribution is the dashed line that is obtained by summing up the individual ones. Likewise using similar arguments the effective total OBE amplitude can be formed for each scattering channel owing to isospin conservation. We will discuss more about the respective potentials in result section.

3.6 Introduction to Particle Basis

The interaction model in discussion here being a SU(3) invariant one is worth using to describe scattering, decays, and production processes between SU(3) mul-

tiplets. Hence the potential amplitudes derived in the last section can be inserted in place of the Born term in the scattering equation (Eq. 3.33). In order to treat the channel coupling between various scattering channels in a consistent manner, the potential should be written in a form that allows different channels to form the subset together. We have already discussed about the isospin basis in Sec. 3.3 and described the coupled channel Lippmann–Schwinger equation in isospin basis. The isospin basis is useful in writing the interaction in a isospin preserving manner, an underlying symmetry of the baryons that has to be maintained. A drawback associated with the isospin basis is its underlying multiplet structure of the particles. For example, the physical three physical Sigma ($\Sigma^{0,\pm}$) baryons belongs to the $\mathbf{\Sigma}$ isospin triplet. Then any calculation in isospin formalism then does not take into account the physical charged states of the particle. This charge blind property needs to be tackled in context of the hyperon-baryon scattering process in order to account the physical observables. In order to deal with the problem we need an operator that can distinguish each physical particle. One obvious choice is the charge (Q) operator here that as can be seen, can mark each particle separately in the isospin multiplet. The final check is to verify the commutation relation with scattering and T- matrices. Charge being a good quantum number commutate with both of them satisfying

$$[\mathcal{S}, Q] = 0, \quad [T, Q] = 0. \tag{3.68}$$

Therefore solving the scattering equation in particle basis is a good strategy by grouping the particles according to total strangeness (S) and charge (Q) subsets (Table 3.7), quite similar to isospin basis, but now replacing isospin (I) by charge (Q). In particle basis the T-matrix elements are expressed as a sum of different scattering amplitude elements T with charge Q. For the two-baryon scattering problem we are dealing with the T-matrix is then

$$\langle B_3 B_4 | T | B_1 B_2 \rangle = \sum_I T(Q) \Omega(Q; B_1, B_2; B_3, B_4) \tag{3.69}$$

with $\Omega(Q; B_1, B_2; B_3, B_4)$ being the projection of T on a state of charge Q. Like in isospin basis, some of the particle basis subsets are also have more than one

	Q=-2	**Q=-1**	**Q=0**	**Q=1**	**Q=2**
S=0			nn	np	pp
S= -1		$\Sigma^- n$	Λn $\Sigma^0 n$ $\Sigma^- p$	Λp $\Sigma^+ n$ $\Sigma^0 p$	$\Sigma^+ p$
S=-2	$\Sigma^-\Sigma^-$	$\Xi^- n$ $\Sigma^-\Lambda$ $\Sigma^-\Sigma^0$	$\Lambda\Lambda$ Ξ^0n Ξ^-p $\Sigma^+\Lambda$ $\Sigma^+\Sigma^0$	Ξ^0p $\Sigma^+\Lambda$ $\Sigma^+\Sigma^0$	$\Sigma^+\Sigma^+$
S= -3	$\Xi^-\Sigma^-$	$\Xi^-\Lambda$ $\Xi^0\Sigma^-$ $\Xi^-\Sigma^0$	$\Xi^0\Lambda$ $\Xi^0\Sigma^0$ $\Xi^-\Sigma^+$	$\Xi^0\Sigma^+$	
S=-4	$\Xi^-\Xi^-$	$\Xi^-\Xi^0$	$\Xi^0\Xi^0$		

Table 3.7: Baryon-baryon channels for fixed strangeness S and total charge Q

scattering channel. We will represent the particle basis subsets by notation $\langle BB\rangle^{S,Q}_{\alpha,\beta}$ as introduced earlier for isospin basis the likewise notation $\langle BB\rangle^{S,I}_{\alpha,\beta}$. For particle basis β is now the total charge of the channel defined analogously as $\beta = Q_1 + Q_2$ for two-baryon scattering.

The coupled channel Lippmann–Schwinger scattering equation in particle basis is the same as describes in Eq. 3.33 in our case "n" being the number of elements in a particle basis subset $\langle BB\rangle^{S,Q}_{\alpha,\beta}$. Although we have chosen particle basis as our working space for solving the scattering equation, the isospin symmetry of the Lagrangian, of course, still have to be preserved. This can be done manually now. Instead of deriving a particle basis OBE potential version, we will insert the OBE isospin forms as isospin eigen states of the particle basis subsets.For example, considering the case of $\langle BB\rangle^{S,Q}_{-1,0}$. The full scattering T-matrix equation for this subset is given by

$$\langle T = V + VGT\rangle^{S,Q}_{-1,0} \tag{3.70}$$

$$T^{S,Q}_{1,0} = \begin{pmatrix} T_{\Lambda n\to\Lambda n} & T_{\Lambda n\to\Sigma^0 n} & T_{\Lambda n\to\Sigma^- p} \\ T_{\Sigma^0 n\to\Lambda N} & T_{\Sigma^0 N\to\Sigma^0 N} & T_{\Sigma^0 N\to\Sigma^- p} \\ T_{\Sigma^- p\to\Lambda N} & T_{\Sigma^- p\to\Sigma^0 N} & T_{\Sigma^- p\to\Sigma^- p} \end{pmatrix} \tag{3.71}$$

$$V_{1,0}^{S,Q} = \begin{pmatrix} V_{\Lambda n\to\Lambda n} & V_{\Lambda n\to\Sigma^0 n} & V_{\Lambda n\to\Sigma^- p} \\ V_{\Sigma^0 n\to\Lambda N} & V_{\Sigma^0 N\to\Sigma^0 N} & V_{\Sigma^0 N\to\Sigma^- p} \\ V_{\Sigma^- p\to\Lambda N} & V_{\Sigma^- p\to\Sigma^0 N} & V_{\Sigma^- p\to\Sigma^- p} \end{pmatrix} \tag{3.72}$$

$$G_{1,0}^{S,Q} = \begin{pmatrix} G_{\Lambda n\to\Lambda n} & 0 & 0 \\ 0 & G_{\Sigma^0 N\to\Sigma^0 N} & 0 \\ 0 & 0 & G_{\Sigma^- p\to\Sigma^- p} \end{pmatrix} \tag{3.73}$$

This is the general form likewise the isospin coupled equation and certainly easy to extend for any subset by including proper matrix elements. We want to solve this equation for T-matrix as a solution of the scattering process. Notably T is determined by solving a self-consistent Lippmann–Schwinger equation. In fact, as already mentioned earlier, T is especially controlled by the tree level diagrams, the OBE potential amplitudes, in our case. We have described how the total OBE amplitude can be derived for any scattering channel using isospin conservation in Sec. 3.5.2.

Next is to put together the total amplitudes for each channel to form the coupled channel V-matrix element that is the input required in prior of solving the scattering equation. Albeit we will solve the Lippmann–Schwinger equation for each particle basis subset, the isospin indeed needs to be conserved. That is to say we require the potentials to preserve isospin even though we are in particle basis. It is important to realize that the particle basis is just a choice of writing the rather solving the baryon-baryon scattering channel such that the physical mass breaking effect can be used directly and that in no way effect the underlying symmetry of the system. Henceforth the isospin symmetry should remain intact in the interaction Lagrangian, to be more specific through the potential amplitudes in the scattering equation. So as to keep isospin conservation manifested in the potential, rather than forming a new particle basis version of the potential, we will use the potentials of the isospin basis with additional changes required for applying in particle basis. Consider the isospin basis for $S = -1$ case, it has two subsets:

$$I = \frac{1}{2}: \qquad \Lambda N, \Sigma N$$

$$I = \frac{3}{2}: \qquad \Sigma N.$$

Corresponding particle basis subsets are:

$$\begin{aligned} Q = +2: &\qquad \Sigma^+ p \\ Q = +1: &\qquad \Lambda p, \Sigma^+ n, \Sigma^0 p \\ Q = \ \ 0: &\qquad \Lambda n, \Sigma^0 n, \Sigma^- p \\ Q = -1: &\qquad \Sigma^- n. \end{aligned}$$

In this case we need to map the isospin basis potentials to the particle basis subset. In case of isospin basis, there is only one uncoupled channel , ΣN . While in particle basis, there are two: $\Sigma^+ p$ (Q=+2) and $\Sigma^- n$ (Q=-1) . All things considered, it is obvious that the particle basis uncoupled channels correspond to the isospin basis uncoupled ΣN potential however with now the physical particle masses. Hence we have

$$V_{\Sigma^+ p \to \Sigma^+ p} = V_{\Sigma N \to \Sigma N}(m_\Sigma \to m_{\Sigma^+}, m_N \to m_p) \tag{3.74}$$

$$V_{\Sigma^- n \to \Sigma^- n} = V_{\Sigma N \to \Sigma N}(m_\Sigma \to m_{\Sigma^-}, m_N \to m_n). \tag{3.75}$$

Considering the coupled subsets, the V-matrix for the coupled isospin $I = \frac{1}{2}$ basis has been shown in Eq. 3.31. The corresponding potential input matrix for $\langle BB \rangle^{S,Q}_{-1,0}$ particle basis subset is obtained by an isospin rotation leading to the following form

$$V^{S,Q}_{-1,0} = \begin{pmatrix} V_{\Lambda\Lambda} & \sqrt{\frac{1}{3}} V_{\Lambda\Sigma} & -\sqrt{\frac{2}{3}} V_{\Lambda\Sigma} \\ \sqrt{\frac{1}{3}} V_{\Sigma\Lambda} & \frac{1}{3} V_{\Sigma\Sigma}(\frac{1}{2}) + \frac{2}{3} V_{\Sigma\Sigma}(\frac{3}{2}) & \frac{1}{3}\sqrt{2}\left[V_{\Sigma\Sigma}(\frac{3}{2}) - V_{\Sigma\Sigma}(\frac{1}{2})\right] \\ -\sqrt{\frac{2}{3}} V_{\Sigma\Lambda} & \frac{1}{3}\sqrt{2}\left[V_{\Sigma\Sigma}(\frac{3}{2}) - V_{\Sigma\Sigma}(\frac{1}{2})\right] & \frac{2}{3} V_{\Sigma\Sigma}(\frac{1}{2}) + \frac{1}{3} V_{\Sigma\Sigma}(\frac{3}{2}) \end{pmatrix} \tag{3.76}$$

where we have introduced the short hand notation $V_{\Lambda\Lambda}$ stands for $V_{\Lambda n \to \Lambda n}$ and like

wise for others elements. Similar evaluation for $\langle BB\rangle^{S,Q}_{-1,+1}$ gives

$$V^{S,Q}_{-1,+1} = \begin{pmatrix} V_{\Lambda\Lambda} & \sqrt{\frac{2}{3}}V_{\Lambda\Sigma} & -\sqrt{\frac{1}{3}}V_{\Lambda\Sigma} \\ \sqrt{\frac{2}{3}}V_{\Sigma\Lambda} & \frac{2}{3}V_{\Sigma\Sigma}(\frac{1}{2}) + \frac{1}{3}V_{\Sigma\Sigma}(\frac{3}{2}) & \frac{1}{3}\sqrt{2}\left[V_{\Sigma\Sigma}(\frac{3}{2}) - V_{\Sigma\Sigma}(\frac{1}{2})\right] \\ -\sqrt{\frac{1}{3}}V_{\Sigma\Lambda} & \frac{1}{3}\sqrt{2}\left[V_{\Sigma\Sigma}(\frac{3}{2}) - V_{\Sigma\Sigma}(\frac{1}{2})\right] & \frac{1}{3}V_{\Sigma\Sigma}(\frac{1}{2}) + \frac{2}{3}V_{\Sigma\Sigma}(\frac{3}{2}) \end{pmatrix} \tag{3.77}$$

(3.78)

In the same fashion, for each particle basis subset, the input V-matrix can be determined. We will discuss about the other V- matrices corresponding to each particle basis subset latter in the result sections of this thesis. We will describe in next chapter the numerical strategy used for solving the scattering equation in matrix form and also describe about the method of determining relevant physical scattering observables.

Chapter 4

Numerical Methods

> "We're always, by the way, in fundamental physics, always trying to investigate those things in which we don't understand the conclusions. After we've checked them enough, we're okay."
>
> Richard P. Feynman

In this chapter the formalism used for numerical calculations to solve the scattering equation is described. In section 1, we will introduce R-matrix formalism. In Section 2 partial wave decomposition of R-matrix elements is discussed. Section 3 is devoted to describe numerical method of solving the partial wave R-matrix element. In Section 4 details about extraction of physical scattering observables from R-matrix elements is discussed.

4.1 R-Matrix

The T-matrix amplitude is a complex number in general. For practical purposes it is easier to deal with real numbers, when dealing the problem numerically. The computation time is significantly less for real number algorithms. Therefore, we chose to follow the R-matrix formalism, defined as solving the scattering equation in terms of R- matrix (commonly known as K- matrix as well). The R-matrix is

defined by the following relation to T-matrix

$$T = \frac{R}{1 - iR} \tag{4.1}$$

and is related to the S-matrix via

$$S = \frac{1 + iR}{1 - iR}. \tag{4.2}$$

In both of these relations, R,S and T are dimensionless. Using the above definitions, T-matrix scattering Eq. 3.18 can be casted in the following R- matrix form in operator notation

$$R = V + \mathcal{P} \int VGR. \tag{4.3}$$

Here $\mathcal{P}$ is referring to the principal value of the integral, thus making R a real number. In momentum space representation the above equation is given by (as in [59]) for constant energy E

$$R(\mathbf{q_f}, \mathbf{q_i} \mid E) = V(\mathbf{q_f}, \mathbf{q_i} \mid E) + \sum_n \mathcal{P} \int d^3k_n \; V(\mathbf{q_f}, \mathbf{k_n} \mid E) \; G_{12}(\mathbf{k_n}, \mathbf{q_i}) \; R(\mathbf{k_n}, \mathbf{q_i} \mid E) \tag{4.4}$$

where we have introduced $\mathbf{q_f}$, $\mathbf{q_i}$, $\mathbf{k}$ as the final, initial, and relative momenta, V is the potential. We will use this different notation in this Chapters. The Green function $G_{12}(\mathbf{k}, \mathbf{q_i})$ given as

$$G_{12} \;\; (\mathbf{k}, \mathbf{q_i}) = \frac{2\mu_{12}}{q_i^2 - \mathbf{k}^2 + i\epsilon} \tag{4.5}$$

with μ_{12} being the reduced mass of the channel. This equation is required to solve to find on-shell scattering observables.

4.2 Representation in Partial Wave Basis

The next step is to write the R-matrix element in an appropriate basis. For this kind of nuclear physics problems involving baryons, there are two choices for the basis: the helicity basis and partial wave basis. The helicity basis is useful for particles with non-zero spin. On the other hand, the partial wave decomposition is

relevant to compare with experimental data. In this work, we describe the partial wave basis representation. For comparison the helicity basis representation, a sample case for NN case is described in Appendix E.

In the literature, various formulations of the partial wave decomposition are found extending the standard approach used for NN scattering to the more complex conditions of SU(3) baryon-baryon scattering. Here, we follow the presentation of [106, 113, 114]. For comparison in Appendix D the NN case is reviewed.

The scattering between the baryons preserves angular momentum J and parity $\mathcal{P} = (-1)^L$, thus, $J^{\mathcal{P}}$ is preserved. Due to the underlying angular momentum symmetry, a description in terms of the partial wave amplitude enable to understand different interaction region of the interaction in more detail. The standard representation for a channel in LSJM basis is given in ${}^{2S+1}L_J$. Mixing between different partial wave states belonging to total J, can couple with each other. For J = 0, we have the uncoupled state ${}^1S_0$, with J = L = S = 0, commonly known as the singlet even (SE) state. We introduce the following notation for the R- matrix elements in LSJM basis

$$ {}^{L,L'}R_J = \langle L'SJM|R_J|LSJM\rangle \tag{4.6}$$

and the + for $L, L' = J + 1$ and − for $L, L' = J - 1$.

4.2.1 Partial Wave Amplitude

Since hyperons are unstable particles, beam to beam collision is not feasible. The type of collisions that are being considered here are fixed target-beam experiment. In such cases, for an incident beam of particles scattering at a localized potential $V(\mathbf{x})$, the potential serves either as a nucleus in some solid target or a particle in colliding beam. For fixed target experiments interaction with a single nucleus is of prime focus.

It is convenient to consider center-of-mass frame with the potential having form of V(r) where $r = |\mathbf{x}|$ and choosing the propagation axis along z-axis. Consider the asymptotic incident wave as a plane wave $\Psi_{in} = e^{ikz}$ with momentum $p = \hbar k$, then

the final wave can be decomposed as

$$\Psi_{out} = \Psi_{in} + \Psi_{scat} \tag{4.7}$$

$$= e^{ikz} + \Psi_{scat} \tag{4.8}$$

where Ψ_{scat} corresponds to the wave function of scattered particles. Quantum mechanically, x and y being delocalized, far from the potential, the scattered wave function can be parametrized in terms of scattering amplitude $f(k, \theta, \phi)$ in spherical polar coordinates (r, θ, ϕ) as

$$\Psi_{scat} \approx f(k, \theta, \phi) \, \frac{e^{ikr}}{r} + \mathcal{O}(\frac{1}{r^{\alpha}}) \tag{4.9}$$

representing an outward radial flow of particles. Here θ is the polar angle between z axis and scattered wave. The differential cross section is defined in terms of scattering amplitude as

$$\frac{d\sigma}{d\Omega} = |f(k, \theta, \phi)|^2 \tag{4.10}$$

Thus the whole process of scattering process is pinned down to the determination the scattering amplitude $f(k, \theta, \phi)$.

In the special case of central spherical symmetry, true for nuclear potentials, $V(\mathbf{x}) = V(r)$ and the main consequence being orbital angular momentum (L) preservation. This in turn preserves the incident and outgoing probability current for each L independently. For azimuthal symmetry, L^2 and L_Z are conserved quantities with eigen values $l(l+1)\hbar^2$ and 0 respectively. The incident wave here is therefore azimuthally symmetric, $f(k, \theta, \phi) \rightarrow f(k, \theta)$ and eigenfunction of L_Z. Mathematically the calculations can be made simpler for this cases exploiting rotational invariance by means of an expansion of in terms of spherical harmonics (Y_l^m). The wave function for this kind potentials are separable solutions of radial and angular functions. The incident wave in terms of spherical harmonics Y_l^m can be expressed in the asymptotic region as

$$e^{ikz} = \sum_{l=0} \sum_{m=-l}^{l} C_{lm} i^l F_l(kr) Y_l^m(\theta) \tag{4.11}$$

where radial part of the wave function is given in terms of spherical Bessel function $F_l(kr)$. For scattering in z-direction $Y_l^m = Y_l^0$, the scattering amplitude now can be expanded into a series of Legendre polynomials for the interval $-1 < \cos\theta < 1$ as

$$f(k,\theta) = \sum_{l=0}^{\infty}(2l+1)f_l(k)P_l(\cos\theta) \tag{4.12}$$

where we introduced the *partial wave scattering amplitude* $f_l(k)$.

So far we have discussed about scattering process between spinless particles. For spin-$\frac{1}{2}$ baryons there are some modifications. Considering the scattering from unpolarized spin-$\frac{1}{2}$ particles, we have $J_z = M_S = \pm\frac{1}{2}$ depending on the spin orientation. For parity conserving systems, these two states will correspond to same differential scattering cross section. During collision, the spin orientation can change, but due to conservation of J_z, L_z will also change simultaneously but in reverse manner. Thus for spin flip $\Delta M_S = \pm 1$, there must be $\Delta L_z = \mp 1$. Therefore we need to have an extra function taking care of the spin flip contribution of the particles. For this the Legendre polynomial in Eq. 4.12 is replaced by associated Legendre polynomial having different angular dependence and capable of reflecting spin affects of the scattered particles. The spin-flip states are orthogonal to the normally scattered waves, and hence are independent of each other. The contribution appears as distinguishable intensity. The incident wave now is defined as

$$e^{ikz}\chi(S,M_S) = \sum_{l,M_S}\sum_{m=-l}^{l} C_{l\ M_S\ m}^{L\ S\ J} i^l F_l(kr)Y_l^m(\theta)\chi(S,M_S) \tag{4.13}$$

As discussed in Chapter 2, the baryon-baryon potential have spin-orbit and tensor force components in addition to central force. Thus the commuting operators here are H, J^2, and J_z. Thus here L is not a conserved quantity but J is. To illustrate this point, different angular momentum states of a spin -$\frac{1}{2}$ - spin-$\frac{1}{2}$ system is tabulated in Table. 4.1.

Consider the states for J=1: $^3S_1$, $^1P_1$, and $^3D_1$ with parity +, -, and + respectively. If in between two states L is not conserved but J and parity is conserved,

State	$^1S_0$	$^3S_1$	$^1P_1$	$^3P_0$	$^1D_2$	$^3D_1, 2, 3$
L	0	0	1	1	2	2
S	0	1	0	1	0	1
J	0	1	1	0,1,or 2	2	1,2,or 3
Parity	+	+	-	-	+	+

Table 4.1: Different angular momentum states of a spin-$\frac{1}{2}$ -spin-$\frac{1}{2}$ system

partial wave transition can occur, for example here

$$^3S_1 \rightleftharpoons ^3 D_1 \tag{4.14}$$

This transition is playing a crucial role for ΛN- ΣN transition [48, 50, 106] for S = -1 coupled channel. For a special case of NN, the conservation of isotopic spin prevents the transition between opposite symmetry states.

For baryon-baryon system we redefine the momentum space spherical wave functions as [113]

$$\mathcal{Y}_{LS}^{JM}(\hat{k}, s) = (\hat{k}, s|JM; LS) = \sum_{M_L, M_S} C^{LSJ}_{M_L\ MS\ M} Y_L^{M_L}(\hat{k}) \chi^S_{M_S}(s) \tag{4.15}$$

$$= \sum_{M_L, M_S} \langle LSM_LM_S|JM\rangle Y_L^{M_L}(k)|SM_S\rangle \tag{4.16}$$

where with quantum numbers J, L, M, and S. Note that here we have changed the notation of the expansion co-efficients slightly to follow the standard one used by other hyperon groups; however the meaning of the co-efficients are same as well as for the spherical harmonics. Here s is the spin variable of baryons denoting the projection of the spin along the normal $\hat{n}$ to the scattering plane, or along z-axis. $\chi^S_{M_S}(s)$ is representing the baryon spin wave function, in this case, $\chi^S_{M_S}(s) = \delta_{s,M_S}$. Here the second equation is in abstract notation. Thus the incident baryon wave function in partial wave decomposition reads [97]

$$\Psi_B(k) = \sum_{LL'M} i^{L-L'} \Psi_{LL'}(k) \langle LSM_LM_S|JM\rangle \mathcal{Y}_{LS}^{JM}|TT_3\rangle \tag{4.17}$$

where for baryons we need to take into account the additional isospin symmetry as well given by $|TT_3\rangle$.

4.2.2 Partial Wave Projection of Potential Elements

Incorporating rotational invariance and parity conservation we finally expand the 2X2 Pauli-spinor T matrix and V matrix into a complete set of Pauli-spinor invariants (see [117, 118, 120]) as

$$T = \sum_{\alpha=1}^{8} T_\alpha(\mathbf{q}_f^2, \mathbf{q}_i^2, \mathbf{q}_i.\mathbf{q}_f)\ P_\alpha\ . \tag{4.18}$$

Introducing

$$\mathbf{q} = \frac{1}{2}(\mathbf{q_f} + \mathbf{q_i}), \quad \mathbf{k} = (\mathbf{q_f} - \mathbf{q_i}), \quad \mathbf{n} = \hat{\mathbf{q}}_\mathbf{i} \times \hat{\mathbf{q}}_\mathbf{f} = \frac{\mathbf{q} \times \mathbf{k}}{|\mathbf{q} \times \mathbf{k}|} \tag{4.19}$$

We choose the following set 8 spinor invariants P_α in spin-space in accordance with the potential amplitudes defined in Chap. 2 [106, 115]:

$$\begin{aligned}
P_1 &= 1, \\
P_2 &= \sigma_1 \cdot \sigma_2 \\
P_3 &= (\sigma_1 \cdot \mathbf{k})(\sigma_2 \cdot \mathbf{k}) - \frac{1}{3}(\sigma_1 \cdot \sigma_2)k^2, \\
P_4 &= \frac{i}{2}(\sigma_1 + \sigma_2) \cdot \mathbf{n} \\
P_5 &= (\sigma_1 \cdot \mathbf{n})(\sigma_2 \cdot \mathbf{n}), \\
P_6 &= \frac{i}{2}(\sigma_1 - \sigma_2) \cdot \mathbf{n} \\
P_7 &= (\sigma_1 \cdot \mathbf{q})(\sigma_2 \cdot \mathbf{k}) + (\sigma_1 \cdot \mathbf{k})(\sigma_2 \cdot \mathbf{q}), \\
P_8 &= (\sigma_1 \cdot \mathbf{q})(\sigma_2 \cdot \mathbf{k}) - (\sigma_1 \cdot \mathbf{k})(\sigma_2 \cdot \mathbf{q})
\end{aligned} \tag{4.20}$$

We neglect in our work the potential forms of $P_{5,7,8}$ and the dependence on $(\mathbf{k} \cdot \mathbf{q})$. Thus, the OBE potential is expanded into a 5-component representation using these 5-spinor invariants given as

$$V = \sum_{i=1,5} V^i(\mathbf{q_f}^2, \mathbf{q_i}^2, \mathbf{q_f}, \mathbf{q_i}) P_\alpha(q_f, q_i) \tag{4.21}$$

Scattering states of the baryon-baryon system are therefore tagged by total an-

gular momentum J and total orbital angular momentum L, and total spin S. For a spin half particle of fixed J, like the baryons, L can have $J \pm \frac{1}{2}$ values. Representing the partial wave with parity $\mathcal{P}_- = (-1)^{L_-=J-\frac{1}{2}}$ and $\mathcal{P}_+ = (-1)^{L_+=J+\frac{1}{2}}$ as short hand notation - and +, we can write the potential matrix elements in the LSJM basis as following

$$\langle q_f L' J' M' | V |\ q_i L J M \rangle^{-,L_+} \ = \ 4\pi\, V^{J,L_+}\ (L', L) \delta_{J'J}\ \delta_{L'L}\ \delta_{M'M} \qquad (4.22)$$

$$\langle q_f L' J' M' | V |\ q_i L J M \rangle^{-,L_-} \ = \ 4\pi\ V^{J,L_-}(L', L)\ \delta_{J'J}\ \delta_{L'L}\ \delta_{M'M} \qquad (4.23)$$

Since strong interaction preserves parity, the L_+ and L_- states are decoupled and mixing between states with different total angular momentum is prohibited. Most general expansion of the potential in LSJM basis is given by

$$V(k|k') = \sum C'_{M_L M_S}\ i^{L-L'} V_{LL'}(k|k')\ \mathcal{Y}_{LS}^{JM-}(k_0)\ \mathcal{Y}_{LS}^{JM+}(k')\ P_T \qquad (4.24)$$

as an operator in spin and isospin space and P_T is the isospin projection operator with k_0 referring to on-shell momenta. Rotational invariance implies

$$V_{LL'}(k|k') = V_{L'L}(k'|k) \qquad (4.25)$$

The sum is over allowed states by Pauli exclusion principle, i.e., S+L+T = odd integer.

Different partial wave matrix elements of $V^i(q_f, q_i)\ P_\alpha(q_f, q_i)$ of Eq. 4.21 is written in Appendix B.

4.2.3 Partial Wave Integral Equation

Ultimately we need to solve the scattering equation. For this reason we cast the scattering Eq. 4.4 in the plane wave basis states that reads now with energy-states $s_{i,f}$ with total energy E

$$\begin{aligned}\langle \mathbf{q_f}, s_f|R(E)|\mathbf{q_i}, s_i\rangle &= \langle \mathbf{q_f}, s_f|V|\mathbf{q_i}, s_i\rangle \\ &+ \mathcal{P}\sum_n \int \frac{d^3k_n}{(2\pi)^3}\ \langle \mathbf{q_f}, s_f|V|\mathbf{q_i}, s_i\rangle \\ &\quad G_{12}(\mathbf{k_n} \mid E)\ \langle \mathbf{q_f}, s_f|R(E)|\mathbf{q_i}, s_i\rangle \end{aligned} \tag{4.26}$$

We define the partial wave R-matrix by

$$R_{L',L}(\mathbf{k}', \mathbf{k_i}) = \langle \mathbf{k}', L'SJM|R(E)|\mathbf{k}, LSJM\rangle \tag{4.27}$$

Eq. 4.27 is independent of $J_Z = M$ due to rotational invariance. Connecting the partial wave element to plane wave basis element we get

$$\begin{aligned}R_{L',L}(\mathbf{q_f}, \mathbf{q_i}) &= \mathcal{P}\sum_{s_f,s_i}\int \frac{d^3q'_f}{(2\pi)^3}\int \frac{d^3q'_i}{(2\pi)^3}\langle q_f, L'; JM|\mathbf{q}'_\mathbf{f}, s_f\rangle \\ &\quad \langle \mathbf{q_f}, s_f|R(E)|\mathbf{q_i}, s_i\rangle\langle \mathbf{q}'_\mathbf{i}, s_i|q_i, L; JM\rangle. \end{aligned} \tag{4.28}$$

The corresponding completeness relation is given by

$$\sum_{L,J,M} \mathcal{Y}^J_{L,S}(\hat{\mathbf{q}}_\mathbf{f}, s_f)\mathcal{Y}^{J*}_{L,S}(\hat{\mathbf{q}}_\mathbf{i}, s_i) = \delta(\hat{\mathbf{q}}_\mathbf{f} - \hat{\mathbf{q}}_\mathbf{i})\delta_{s_f,s_i} \tag{4.29}$$

and the corresponding for $|q, L; JM\rangle$-state reads

$$\sum_{L,J,M}\int_0^\infty \frac{q^2dq}{(2\pi)^3}|q, L; JM\rangle\langle q, L; JM| = 1 \tag{4.30}$$

And for the Green's function one can easily verify the following relation

$$\begin{aligned}&\sum_{s_n}\int \frac{d^3k_n}{(2\pi)^3}|\mathbf{k_n}, s_n\rangle G_{12}(\mathbf{k_n} \mid E) \\ &= \sum_{L,J,M}\int_0^\infty \frac{k_n d^2k_n}{(2\pi)^3}|k_n, L; JM\rangle \\ &\quad G_{12}(\mathbf{k_n} \mid E)\langle k_n, L; JM| \end{aligned} \tag{4.31}$$

Since Green's functions are diagonal in the spin and rotational invariant, they are

also diagonal in L and J. Using the above definitions finally we can write the integral equation for the partial wave amplitude as the following

$$\begin{aligned} R_{L',L}(q_f, q_i|E) &= V_{L',L}(q_f, q_i|E) + \\ &\quad \mathcal{P}\sum_n \int_0^\infty \frac{k_n d^2 k_n}{(2\pi)^3} V_{L',L}(q_f, q_n|E) \\ &\quad G_{12}(\mathbf{k_n} \mid E) R_{L',L}(q_n, q_i|E) \end{aligned} \tag{4.32}$$

4.3 Numerical Formalism for R-matrix Solution

Next is to determine the partial wave R-matrix elements. Our final requirement are the on-shell matrix elements to extract scattering observables out of them. From Eq. 4.32, we can see that we not only need to solve the integration equation but also a self-consistent equation of R-matrix amplitude too. Consider the R-matrix equation in operator notation

$$R = V + \mathcal{P}\int VGR \tag{4.33}$$

where in addition we have explicitly shown the integration suppressing the momentum arguments and principal value specification ($\mathcal{P}$). Rearranging this equation we can write

$$R - \mathcal{P}\int VGR = V \Rightarrow (1 - \mathcal{P}\int VG)\ R = V \tag{4.34}$$

This implies if we can form a matrix equation, then R-matrix can be determined easily by solving the matrix equation. Important here is to realize these are not numbers in general, except for the uncoupled case, where R and V are one order matrices, hence a number. But in general cases, all these are matrices of order of the number of scattering channels involved. In addition we have the integration to solve.

The integration we solve numerically using Gaussian quadrature method [121]. For a function f(x) to be integrated in the range $-1 < x < 1$ Gaussian quadrature

method of integration is defined as

$$\int_{-1}^{1} f(x)dx \simeq \sum_{k=1}^{N} w_k f(x_k). \tag{4.35}$$

Here the points (x_k) at which the function are to be evaluated are called *abscissa* or *grid points* and the corresponding coefficients (w_k) are called the *weights*. The advantage of Gaussian method is the possibility of choosing unequally distributed points over the range. This is specifically of importance for computational physics problems as this allows to choose densely populated points for a short interval that require thorough investigation than other. In connection to this thesis, the Gaussian method was specifically preferred for studying the channel opening threshold with denser points. For a coupled channel problem of order 2, Eq. 4.34 is modified to suppressing the integration now

$$\begin{pmatrix} 1-\mathcal{P}\int V_{11}G_{11} & -\mathcal{P}\int V_{12}G_{22} \\ -\mathcal{P}\int V_{21}G_{11} & 1-\mathcal{P}\int V_{22}G_{22} \end{pmatrix} \begin{pmatrix} R_{11} & R_{12} \\ R_{21} & R_{22} \end{pmatrix} = \begin{pmatrix} V_{11} & V_{12} \\ V_{21} & V_{22} \end{pmatrix} \tag{4.36}$$

This can be as well expanded for higher order coupled channel problems as well.

The requirement is therefore, for a range of incident on-shell momentum q_i, q_f, we first solve the integration term in Eq. 4.34 using Gaussian quadrature method and then determine R-matrix by solving matrix equation. Considering Eq. 4.4, the Green's function has a singularity. The Haftel-Tabakin matrix inversion method [97] is employed to deal with this singularity. The partial wave decomposed R-matrix matrix equation reads after executing the angular distribution for uncoupled channel

$$\begin{aligned} R_{L',L}(\mathbf{q_f}, \mathbf{q_i} \mid E) &= V_{L',L}(\mathbf{q_f}, \mathbf{q_i} \mid E) \\ &+ \mathcal{P}\int \frac{k^2 dk}{2\pi^2} V_{L',L}(\mathbf{q_f}, \mathbf{k} \mid E) \\ &\quad \frac{2\mu_{12}}{q_i^2 - \mathbf{k}^2}\, R_{L',L}(\mathbf{k}, \mathbf{q_i} \mid E) \end{aligned} \tag{4.37}$$

Following [97], a zero value term is subtracted from the integration, having the

same pole and residue as the integrand to remove the singularity. This way the integration becomes smooth and of principal-value integral as demanded by R-matrix giving

$$\begin{aligned} R(\mathbf{q_f},\mathbf{q_i} \mid E) &= V(\mathbf{q_f},\mathbf{q} \mid E) \\ &+ \mathcal{P}\int \frac{k^2 dk}{2\pi^2} \\ &\Big\{V(\mathbf{q_f},\mathbf{k} \mid E)\ \frac{2\mu_{12}}{q_i^2-\mathbf{k}^2}\ R(\mathbf{k},\mathbf{q_i} \mid E) \\ &-\frac{q_i^2}{q_i^2-k^2}R(\mathbf{k},\mathbf{q_i} \mid E)\Big\} \end{aligned} \tag{4.38}$$

Rearrangement of terms leads to

$$\begin{aligned} R(\mathbf{q_f},\mathbf{q_i} \mid E) - \mathcal{P}\int \frac{k^2 dk}{2\pi^2}\big[V(\mathbf{q_f},\mathbf{k} \mid E)\ \frac{2\mu_{12}}{q_i^2-\mathbf{k}^2}\ R(\mathbf{k},\mathbf{q_i} \mid E) \\ -\frac{q_i^2}{q_i^2-k^2}R(\mathbf{k},\mathbf{q_i} \mid E)\big] = V(\mathbf{q_f},\mathbf{q} \mid E) \end{aligned} \tag{4.39}$$

This integration has a finite limit. There is a pole in the Green's function for $q_i = \mathbf{k}$. The goal is to solve Eq. 4.37 excluding points like $q_i = \mathbf{k}$. For the integration we use N grid points, the abscissas. The Gaussian interval (-1,1) is mapped to the momentum range of integration by mapping to the following grid points

$$q_j = q_{cut}\tan[\frac{\pi}{4}(x_j+1)] \tag{4.40}$$

$$\omega'_j = q_{cut}\frac{\pi}{4}\frac{w_j}{\cos^2\frac{\pi}{4}(x_j+1)} \tag{4.41}$$

with a q_{cut} value of 2000 MeV. In order to avoid the singularity, all integration points q_j are needed to be unequal to $\mathbf{k}$. The integration converts the integration equation to a matrix equation. Calling the on-shell momenta say q_0 as the momenta at N+1 point, q_{N+1}, Eq. 4.37 now can be written in the following matrix formulation

$$V_{L'L}(q_i|q_{N+1}) = \sum_{j=1}^{N+1} F_{L'L}(q_i|q_j)R_{L'L}(q_i|q_{N+1}) \tag{4.42}$$

where we define $F_{L'L}$ as

$$F_{L'L}(q_i|q_j) = \delta_{ij} + \omega'_j \;\; V_{L'L}(q_i|q_j) \tag{4.43}$$

with co-efficients

$$\omega'_j = \begin{cases} \frac{2\mu_{12}}{2\pi^2} \frac{q_j^2 \omega_j}{q_j^2 - q_0^2} & \text{for} \;\; j \leq N \\ -\frac{2\mu_{12}}{2\pi^2} \sum_{t=1}^{N} \frac{q_o^2 \omega_t}{q_t^2 - q_0^2} & \text{for} \;\; j = N+1 \end{cases} \tag{4.44}$$

This way the singularity of matrix $F_{L'L}$ is avoided as the on-shell point is exclusively at N+1 point. Thus, on and off shell R-matrix element can be determined by inversion method as

$$R_{L'L}(q_i|q_{N+1}) = \sum_{j=1,N+1} F^{-1}_{L'L}(q_i|q_j) V_{L'L}(q_j|q_{N+1}) \tag{4.45}$$

This is straight forward to extend to coupled channel problems, for example for a two channel problem the matrix dimensions would be (2N+2) X (2N+2) where each element R_{ab} (say) is of dimension (N+1) and satisfies

$$R_{(2N+2)X(2N+2)} = \begin{pmatrix} R^{aa} & R^{ab} \\ R^{ba} & R^{bb} \end{pmatrix} \tag{4.46}$$

where each R_{ab} element is now have the following form

$$R^{ab}_{L'L}(q_i|q_{N+1}) = \sum_{j=1,N+1} [F^{ab}_{L'L}(q_i|q_j)]^{-1} V^{ab}_{L'L}(q_j|q_{N+1}). \tag{4.47}$$

4.3.1 Extraction of T-matrix from R-matrix

The R-matrix is used solely for the numerical benefit. The physical scattering observables are defined in terms of the T-matrix (or equivalently S matrix) elements. Hence finally we need to transform the R-matrix to T-matrix (or equivalently to S) via Eq. 4.1 and 4.2 keeping in mind that the S-matrix should conserve unitarity.

For uncoupled channels, on-shell R-matrix element is a real number, R_{un} (say).

The corresponding T-matrix can be written as

$$T_{un} = \frac{R_{un}}{1 - iR_{un}} \tag{4.48}$$

For multi-channel problems the extraction of T-matrix elements is much more involved. For a coupled problem, T-matrix elements can be determined by solving a complex matrix equation of the following form

$$(1 - iR)\, T = R \tag{4.49}$$

as T matrix elements are complex quantities in general. However there is an important point to mention. Although mathematically Eq. 4.49 is true for the full R-matrix defined in Eq. 4.45, from physics point of view, the T-matrix elements we are interested in for scattering processes, requires to fulfill certain extra conditions. The T-matrix determined using Eq. 4.49 are only meaningful when we have on-shell R-matrix elements as components. This is because for any scattering processes the S-matrix, defined in Eq. 4.2 has to be unitary, means

$$SS^{\dagger} = I. \tag{4.50}$$

Remembering the relation between S-matrix and T-matrix as $S = 1 - 2iT$, the unitarity is not satisfied for off-shell R-matrix elements. Therefore to use Eq. 4.49 to extract on-shell T-matrix elements, the input R-matrix here is different than in Eq. 4.45.

We describe a two-channel problem here for illustration purposes. Consider a two-body coupled channel problem with two channels denoted as A, B. In order to derive the T-matrix, we first need to form a 2x2 matrix with on-shell R-matrix elements for each points. For a two-channel problem the on-shell R-matrix can be written as

$$R_{on} = \begin{pmatrix} R^{on}_{AA} & R^{on}_{AB} \\ R^{on}_{BA} & R^{on}_{BB} \end{pmatrix} \tag{4.51}$$

where each element corresponds to the on-shell element of the sub-block, i.e, $R^{on}_{AA} \equiv$

$R(N+1,N+1)$, $R^{on}_{AB} \equiv R(N+1,2(N+1))$ and so on. Using R_{on} Eq. 4.49 , the 2X2 complex matrix equation needs tp solved not for T. We have used LAPACK [104] math kernel library subroutine ZGESV for solving Eq. 4.49. The ZGESV is a subroutine that can efficiently solve complex matrix equations with multiple right hand sides. For more details about ZGESV, we refer to the user guide of LAPACK library [104].

4.4 Determination of Observables

Ultimate aim of the mathematical and numerical formalism described here is to determine the scattering observables.

4.4.1 Cross Section

For scattering processes the most important physical quantity is the scattering cross section. The total cross section for a two-baryon scattering process with orbital angular momentum components L as

$$\sigma_{tot} = \int d\Omega |f_l(k,\theta)|^2 \tag{4.52}$$

$$= 2\pi \int_{-1}^{+1} d(\cos\theta) f_l^*(k,\theta) f_l(k,\theta) \tag{4.53}$$

Using the orthogonality of Legendre polynomials

$$\int_{-1}^{+1} d(\cos\theta) P_l(\cos\theta) P_{l'}(\cos\theta) = \frac{2}{2l+1}\delta_{ll'} \tag{4.54}$$

the cross section reduced to

$$\sigma_{tot} = \sum_{l=0}^{\infty} 4\pi(2l+1)|f_l(k)|^2 = \sum_{l=0}^{\infty} \sigma_l \tag{4.55}$$

The T-matrix is related to the on-shell scattering amplitude $f_l(k)$ suppressing the angular dependence as

$$f_l(k) = \frac{-\mu}{2\pi} T_l(k) \tag{4.56}$$

with reduced mass μ.

For $\theta = 0$, we get the optical theorem

$$\sigma_{tot} = \frac{4\pi}{k}\mathrm{Im}f_l(k, \theta = 0) \tag{4.57}$$

In terms of S-matrix, the total elastic cross section is defined as

$$\sigma_{elastic} = \frac{\pi}{k^2}\sum_{jl}(J + \frac{1}{2})|S_{jl} - 1|^2 \tag{4.58}$$

The definition of reaction cross section is

$$\sigma_{reac} = \frac{\pi}{k^2}\sum_{jl}(J + \frac{1}{2})(1 - |S_{jl}|^2) \tag{4.59}$$

with total cross section as

$$\sigma_{tot} = \frac{2\pi}{k^2}\sum_{jl}(J + \frac{1}{2})(1 - Re(S_{jl})) \tag{4.60}$$

These equation can be as well converted in terms of T-matrices with proper conversions used for replacing S by T.

4.4.2 Phase Shift

Another interesting observable is the phase shift to have a closer look on the interaction behavior near the core. However, the phase shift is not an experimental observable. It needs to be extracted from other measurable quantities. On the other hand, from theoretical point of view, the phase shift are easy (not form a mathematical point of view although) to obtain as the S (or T) matrix elements are in hand already. For an uncoupled channel of angular momentum J, the phase shift δ is related to the corresponding S-matrix element by

$$S_J = e^{2i\delta_J} \tag{4.61}$$

For the simplest case of uncoupled SE partial wave, the cross section is then,

$$\sigma_J = \frac{4\pi}{q^2} \sin^2 \delta_J \tag{4.62}$$

For a coupled channel problem, there are more than one phase shifts, each corresponding to each channel or each partial wave depending on the the problem, which can be parametrized in terms of the T-matrix or S-matrix by different conventions. The S-matrix element is defined as following [125]

$$S_J^{L,L'} = \sum_{i=1,2} A_J^{L'i} \exp(2i\delta_J^i) A_J^{iL} \tag{4.63}$$

choosing [14]

$$A_{L'i}^J = \begin{pmatrix} \cos(\varepsilon_J) & \sin(\varepsilon_J) \\ -\sin(\varepsilon_J) & \cos(\varepsilon_J) \end{pmatrix} \tag{4.64}$$

where ε_J is the mixing parameter. Another standard parametrization used seldom is the Stapp parametrization [99]. According to that, for a two-channel coupled system, the S-matrix is,

$$\begin{pmatrix} {}^0S_+^J & {}^{12}S^J \\ {}^{21}S^J & {}^1S^J \end{pmatrix} = e^{i\bar{\delta}_1^J} e^{-2i\gamma^J \sigma^1} e^{i\bar{\delta}_1^J} \tag{4.65}$$

where the phase shift matrix comprises of eigen phase shifts ${}^0\delta^J$ and ${}^1\delta^J$ corresponding to the channels with $\bar{\delta}_1^J = \begin{pmatrix} {}^0\delta^J & 0 \\ 0 & {}^1\delta^J \end{pmatrix}$, σ^1 is the mixing between the channels, and γ^J is the inelasticity parameter Equivalent type of parametrization exists for T-matrix elements too. Any of these conventions can be used for multi-channel scattering systems to extract the eigen phase shifts from T or S matrices.

4.4.3 Low-Energy (LE) Parameters

The low energy behavior of the scattering process is an important and convenient measure of the interaction, specially for the baryon sector, where the known information about the core is negligible. For this purpose, the effective-range (ER)

expansion is used to find two important observables, the scattering length, a_s and the effective range, r_e of the interaction. For the region where q is close to zero, $q \to 0$, the low energy S-wave scattering, $q \cot \delta$ can be expanded as a function of q as

$$\lim_{q\to 0} \frac{q}{\tan \delta} = q \cot \delta \approx -\frac{1}{a_s} + \frac{1}{2} r_e q^2 \tag{4.66}$$

The usual convention is, for a positive a_s, there exist a bound state. The scattering length is related to the cross section by

$$\lim_{q\to 0} \sigma = 4\pi a_s^2 + \mathcal{O}(q^2) \tag{4.67}$$

Therefore the scattering length gives information about the low energy cross section of the interaction.

The LE parameters can be calculated either from the phase shifts or from the T-matrix elements by method of least squares by fitting to a polynomial of q^2 given by,

$$f(x) = \sum_n z_n x^n, \quad x = q^2, n = 0, ..., N \tag{4.68}$$

where comparing this equation to Eq. 4.67 the first co-efficient of order zero we can determine the scattering length a_s and from the second the effective range r_e can be obtained. Here the fit order N must be higher than two, at least three.

The advantage of using T-matrix elements over phase shifts is that for coupled channel problems, T being a complex number, information regarding the inelasticity part of the interaction can be accessed via the imaginary part T-matrix element. The corresponding relations for LE parameters in terms of T-matrix is given below:

$$\frac{q}{T_{aa}} + iq = -\frac{1}{a_s} + \frac{1}{2} q^2 r_e \tag{4.69}$$

$$(\frac{q}{T_{aa}} + iq) = -q\frac{\mathrm{Im}(T_{aa})}{|T|^2} + q = -Im(\frac{1}{a_s}) + \frac{1}{2} q^2 Im(r_e) \tag{4.70}$$

$$Re(\frac{q}{T_{aa}} + iq) = qRe(T_{aa})/|T|^2 = -Re(\frac{1}{a_s}) + \frac{1}{2} q^2 Re(r_e) \tag{4.71}$$

For coupled channel problems the T- matrix is more straight forward than the phase shift one, as for the latter, one first needs to parametrize the T (or S) matrix elements

to the phase shift formulations and then can use to calculate the LE parameters, where as the T- matrix method is readily accessible. In our calculation, for uncoupled channels, we used the phase shift method, and for the coupled channel, the T-matrix one is used.

Chapter 5

Vacuum Hyperon-Baryon Interactions

"Two paradoxes are better than one;
they may even suggest a solution."

Edward Teller

In this chapter we present various free space baryon -baryon (BB) scattering results.

5.1 Sensitivity of Parameters

In order to calculate various BB scattering matrix element by solving the 3D - reduced Bethe-Salpeter equation [Eq. 3.18], first of all the *free parameters* needs to be fixed. We have in total 15 parameters [see Table 2.10] corresponding to the three meson nonets (ps, s, v) . The goodness of any effective model rely heavily on how best fitted the parameters are to the experimental sector. This can also be viewed in terms of the preciseness of the parameter values. As a general rule, it can be concluded that the higher is the ratio between the number of data to the number of fit parameters , the more precise the parameters will be, hence making the model more reliable and predictive. The parameters of an effective model have to be taken typically from outside sources, either theoretical or experimental ones. For our approach, this is the case for the meson-baryon coupling constants and vertex form factors which are determined by phenomenology. The fitting to data therefore has an immense importance for the OBE based phenomenological models in nuclear

physics. On the other hand, the effectiveness of the fitting procedure is directly dependent on the quality of data. For example, in the nucleon sector, the available scattering data set is far more richer ($\sim$ 1000 scattering cross section points) for the three channel (nn, np, pp) problem and hence making the OBE based nucleon models to be precise and highly successful [10, 11, 62]. On the other hand, the present experimental data set for the strangeness sector is mostly available for these two $S = -1$ scattering channels: $\Sigma^+ p$ and Λp, comprising in total 35 cross section data points [66–74, 80] up to 700 MeV/c laboratory momenta however with large error bars [Fig. 5.1, 5.2].

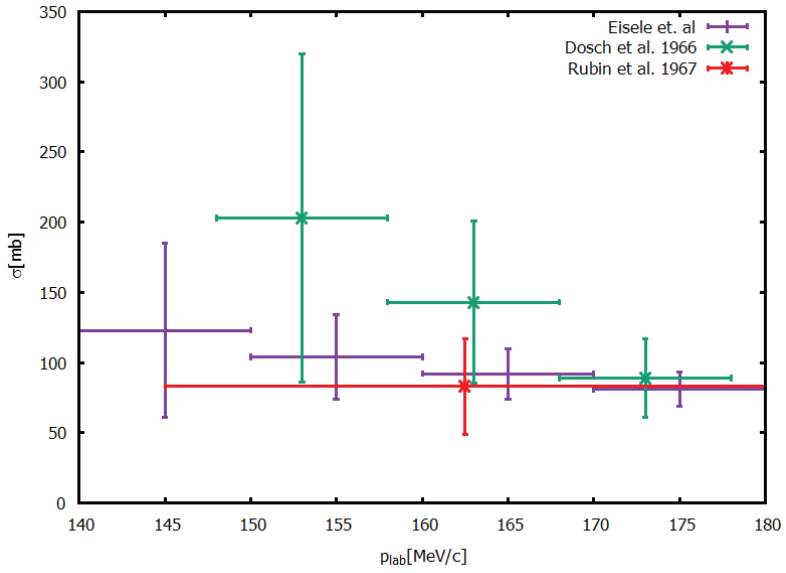

Figure 5.1: Available experimental $\Sigma^+ p$ total elastic cross section shown as a function of laboratory momentum p_{lab} in MeV/c [66, 67, 73].

Thus, strange OBE models are rather difficult to be well constrained in terms of parameter values comprising of 32 particle basis and 15 isospin basis baryon-baryon channels. As a way out of this uncertainty, different groups avail different strategies in terms of fixing the parameters, based on what physics aspects they want to more emphasize on to [48–50]. Thus comes found as the ambiguities between different strange OBE models in many aspects.

As a solution regarding the uncertainties coming from the insufficient quality and amount of data and free parameters, $35/15 \approx 2.33$, our primary strategy was to identify and then drop the less sensitive *free parameters* to optimize for the remaining

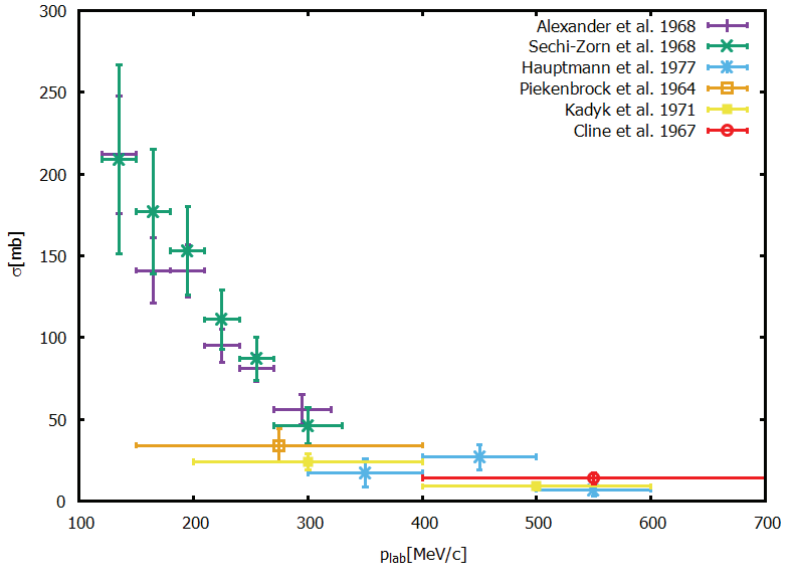

Figure 5.2: Available experimental Λp total elastic cross section shown as a function of laboratory momentum p_{lab} in MeV/c [68–72, 74, 80].

parameter set the fit to the data. Under this aspect, we scrutinized the strategies followed by different groups over the past years from 1973 till today [46–51, 78, 79].

5.1.1 Fitting Procedure

In Table 5.1 we have made a compilation of the range of parameter values used for the three types of mesons by the nuclear physics community so far. As can be seen, the meson model has a large uncertainty in terms of the parameter values. Having this as the long standing scenario, it is important to understand the strength of each of the 15 different parameters of our model first. Remembering that the main research interest of our work is to study the medium effect with a consistent vacuum interaction, we want to have a model that is reliable enough qualitatively, not paying much attention to the accountability.

Therefore we decided to do separate test on each parameter having the aim to reduce the number of fit parameters, thus getting a better result out of the scarce data set. In the final step, we will use these reduced set of parameters as fitting arguments. We will use MINUIT algorithm [103] provided by CERN that apart from any other χ^2 fitting routine allows to provide the limit in which one wants the parameter to be dwell in. In our case the ranges mentioned in the Table is a good

	$\frac{g_8}{\sqrt{4\pi}}$	$\frac{g_1}{\sqrt{4\pi}}$	α	θ	Λ_c
ps	**3.567 - 3.795**	2.08 - 4.16	**0.355** - 0.491	-10 or **-23**	1.2 - 1.4
s	0.76 - 1.395	3.17 - 4.598	0.841-1.285	37.05 - 54.75	0.988-2
v	.68-1.18	2.529-3.762	**E:1** M : 0.275 – 0.4447	**35.26**, 37.56	1.07-2

Table 5.1: Parameter values used by OBE based hyperon potential models over the years [46–51, 78, 79]. Bold characters are referring to the parameters that are fixed by theory or experiment.

set of limits already provided by the past investigations in this subject. Therefore, our interest now is to mark those parameters that are unavoidable to fix without a fit and the ones that we can be fixed from other strategies, if available.

Pseudo-scalar meson First let us take a look on the pseudoscalar sector. The octet coupling constant used by various groups over the last 40 years is quite precise, in particular ~ 3.6. This is because the pseudoscalar octet coupling constant is pion

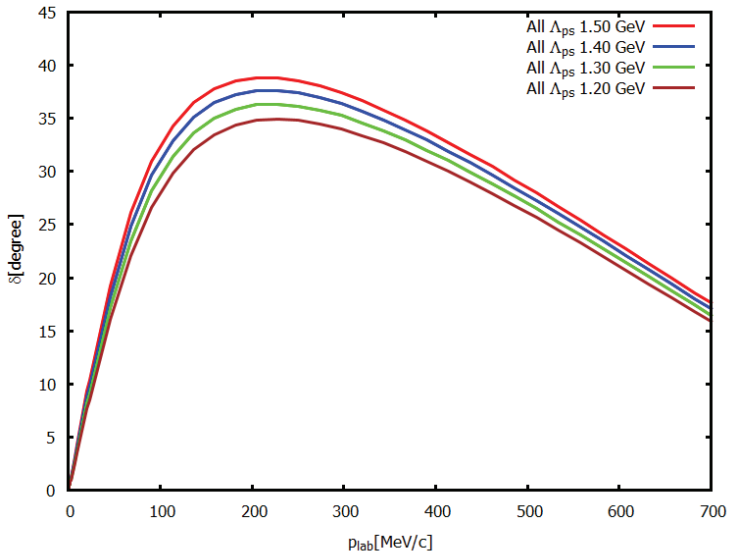

Figure 5.3: Variation of $\Sigma^+ p$ $^1S_0$ phase shift with different pseudoscalar meson cut-off mass (Λ_{ps}).

nucleon coupling, which is well determined from pion nucleon scattering data as $\frac{g^2_{\pi NN}}{4\pi} = 14.6$, thus in turn also fixing up all the other pseudoscalar meson octet coupling constants via SU(3) relations as shown in Table.2.6.

On the contrary, different groups are not in agreement for the singlet pseudo-

scalar coupling constant, as can be seen in Table 5.1, this having a wide range of values. Hence, this is mainly used as a free model parameter. Instead we decided to use a constant value of it as the effect of singlet pseudo-scalar coupling is not quite important for this sector. Moreover, since we already have octet η coupling fixed, the contribution from singlet will not affect the result much. In our calculation, we used a constant value of 0.1913 [50] , which we found to be a better estimation.

For the F/F+D ratio of pseudoscalar meson, the standard choice for a SU(3) based model is 0.355 coming from the Cabibbo theory of the weak interactions and the Goldberger-Treiman relation, the one we will also use in our case, hence not using it as a fit parameter. Another value seldom used for α_{ps} is 0.42, determined from $\bar{p}p \to \bar{\Lambda}\Lambda$ reaction [81]. For SU(6) symmetry based models [46–48], the value is 0.4.

There are two mixing angles (see Eq. 2.11) for $\eta - \eta'$, -10° and -23°, used by the groups. These are derived from Gell-Mann-Okubo mass formula, the linear one giving -23° (usually preferred) and -10° from the quadratic one. We in our case, following the usual strategy, will use -23° for θ_{ps}.

In Fig. 5.4 the variation of pseudoscalar cut-off mass Λ_{ps} (Eq. 2.34) for the $\Sigma^+ p$ $^1S_0$ is shown with other parameter values being fixed. The pseudoscalar mesons contribute to the long range part of the interaction. Fig. 5.4 showing the sensitivity of the interaction is not much, thus we choose a value of 1.3 GeV for all the pseudoscalar meson vertices. To sum up, for pseudoscalar meson, we do not have any free parameters, thus reducing the free parameters from 15 to 10.

Scalar Meson A quick glance on the second row of Table. 5.1 shows the large range of values being used for all the scalar meson model parameters. This also emphasizes the discussed "scalar meson puzzle" in Chap. 2. The scalar mesons not having very well accepted particle properties already has the underlying uncertainty that in a sense is portrayed by these large set of values. One point to mention is that all that values listed here are actually fitted values. These mesons are responsible for the intermediate range attraction which is a crucial part of the interaction to have a realistic result. Therefore, one can not ignore it in spite of the uncertainties. On the other hand the quality the available data is not helping much to overcome the puzzle.

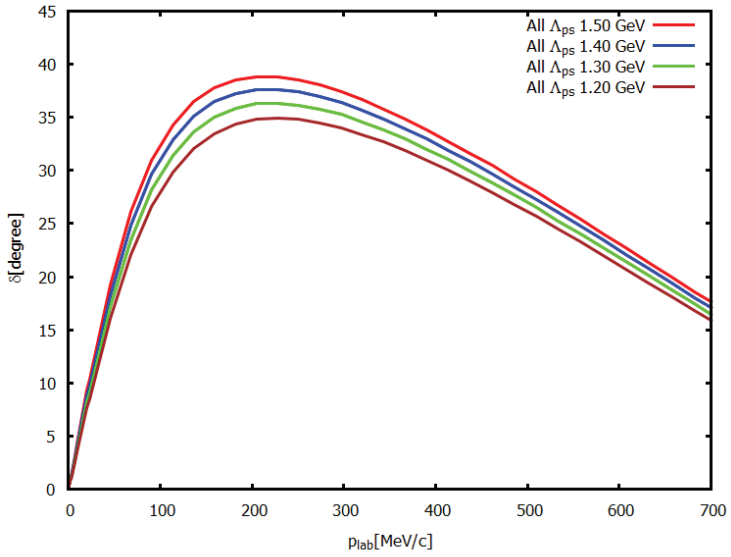

Figure 5.4: Variation of $\Sigma^+ p\ ^1S_0$ phase shift with different pseudoscalar meson cut-off mass.

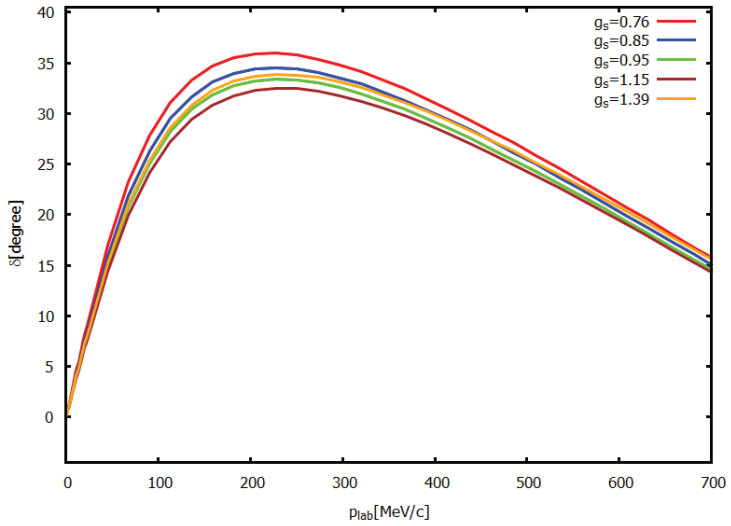

Figure 5.5: $\Sigma^+ p\ ^1S_0$ phase shift with the octet scalar meson coupling constant g_s^8, represented as simply g_s here.

In future, if more good data quality is achieved from the planned experiments at FAIR, J-PARC, and J-LAB in near future, that will not only help the strangeness sector but more effectively also to solve the *scalar meson puzzle*.

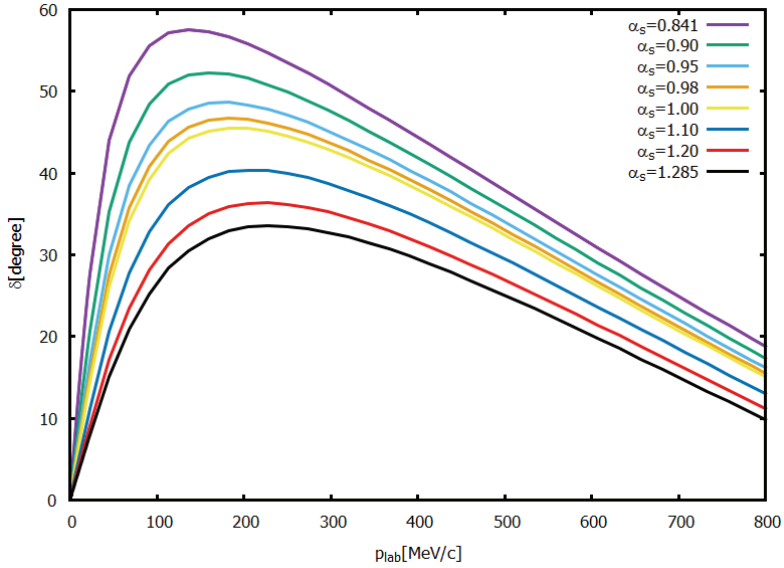

Figure 5.6: ${}^1S_0$ phase shift of $\Sigma^+ p$ as a function of p_{lab} for different values of $\alpha_s = \frac{F}{F+D}$ shows that the hyperon-nucleon interaction is very sensitive to α_s.

In Fig. 5.5 the effect of different values of scalar meson octet coupling constant (g_s) used by different groups is shown, red curve being the lowest value used (0.76) and yellow refers the strongest one (1.39). Notice that when the scalar octet coupling is varied, it affects the intermediate range of the interaction. Also the peak values of the phase shift gets changed, in general lower the coupling strength, higher the peak value. However the effect is not linear, for example, see in Fig. 5.5 that the phase shifts for $g_s = 1.39$ (yellow) is actually higher than $g_s = 1.15$ (brown) and comparable to $g_s = 0.95$ (green) near the peak position. The reason behind this is possibly originating from the interplay between other intermediate interactions resulting from vector and pseudoscalar mesons that is leading to this complex effect with stronger scalar coupling constant, at least for this channel. All in all, due to this important effect and unavailability of other input from either theoretical or experimental side for fixing the coupling strength precisely enough, g_s^8 must be determined from the fit.

As a matter of fact, the most sensitive parameter among the whole parameter

set is the scalar $\frac{F}{F+D}$ ratio, the α_s, as evident from Fig. 5.6. Here in Fig. 5.6 one can notice how within a range of 50% increase (0.84 - 1.285), the resulting hyperon-nucleon interaction gets affected in a much stronger scale than that of the other parameters discussed above. This is a bit surprising because both g_s^8 and α_s enter the coupling constant formulas in the same manner [Table. 2.3.5]. Therefore the stronger effect of α_s over g_s^8 on the interaction is somewhat puzzling however can not be ignored at all. This particular stronger effect can only be exclusive to $\Sigma^+ p$ channel as well. No wonder why the Nijmegen group has different versions of their models with different values of α_s [49, 50]. In our case, we will rely on the χ^2 fit derived value. One point should not be overlooked here is that the strong α_s dependency is also attributed the channel involved, for other channels it can happen that g_s^8 lead over α_s. In any case, this is referring to the strong sensitivity of scalar meson octet in hyperon interaction.

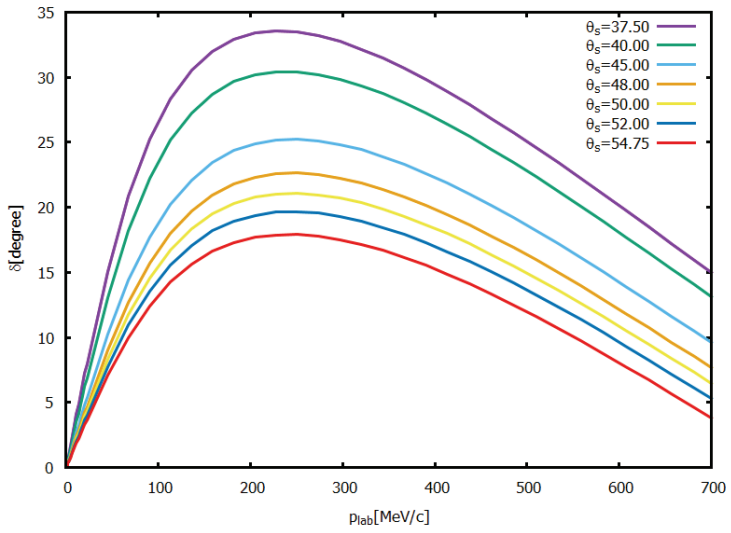

Figure 5.7: $^1S_0$ phase shift of $\Sigma^+ p$ as a function of p_{lab} for different values of θ_s.

In Table 5.1 one can notice a diverse range of values being used for the scalar mixing angle. The common strategy is to treat that angle as a free fit parameter. It is found to affect strongly the interaction especially in the $\Sigma^+ p$ $^1S_0$ channel, as seen for the phase shift shown in Fig. 5.7. However we decided to drop θ_s from free parameter list. As seen from Fig. 5.7 the best results are obtained for $\theta_s \sim 37.5°$ which is the value obtained for *ideal mixing* in the vector nonet. Following the

usual practice of favoring a stronger repulsion for $\Sigma^+ p$ [46–48, 50, 106], we are using $\theta_s \sim 37.5°$ value throughout the calculation.

Since the scalar mesons are heavy, their dependency on the cut-off mass parameter is also more than other meson groups. Look for example in the Fig. 5.8 that shows the dependency on cut-off mass even more stronger than the octet coupling constant itself. However apart from directly deriving the best cut off value, we give

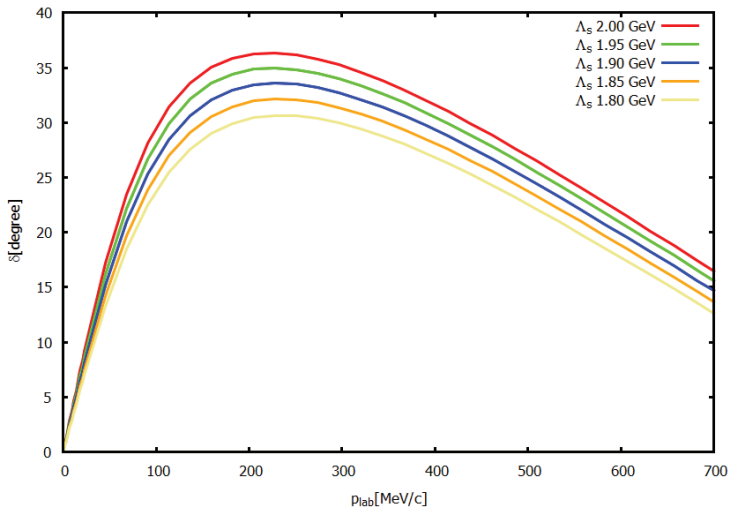

Figure 5.8: ${}^1S_0$ phase shift of $\Sigma^+ p$ as a function of p_{lab} for different values of Λ_s.

more preference in reducing the number of free parameters and using those as free only that are actually not possible to fix without fit at any cost. Hence after checking the variation with different values of the cut-off, we concluded that it is the cut-off for the ϵ meson that is mainly playing affecting the interaction in a crucial manner compared to others as pointed out in Fig. 5.9. The result of using a single cut-off for all scalar meson vertices with $\Lambda_s = 1.85$ GeV is equivalent to the choice of $\Lambda_\epsilon = 1.80$ GeV keeping other fixed at 2 GeV. Therefore, in order to reduce the parameters, we used a constant value of $\Lambda_s = 2$ GeV making sure it is higher enough than the massive scalar mesons to fulfill the convergence criteria. Concerning the Λ_ϵ, we will keep using the value 2 GeV preferring the reduction of free fit parameter number, but for some channels may reduce if the reduction in seen to play a major role however without fit. Therefore, we reduced now the fit parameters from 15 to 7.

Vector Meson In Table 5.1 the range of vector meson parameter set is shown in the third row. Although vector mesons are having a standard particle feature with a comparatively sharper width, unlike the scalar mesons, however these mesons are not having any source either for fixing the couplings.

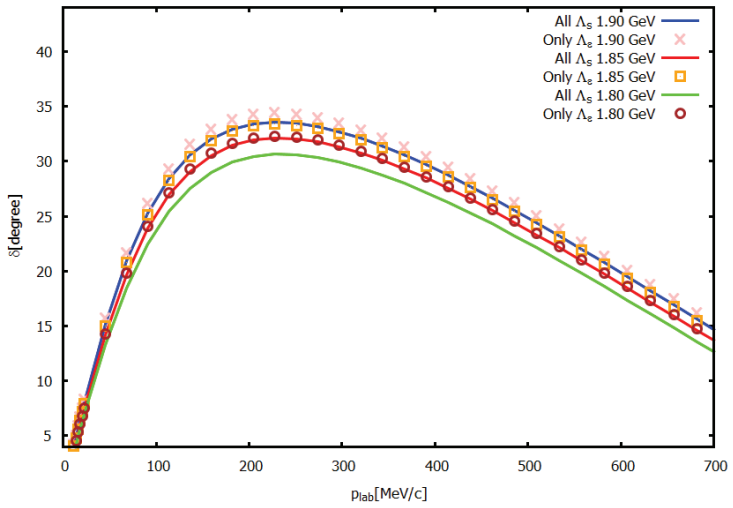

Figure 5.9: $^1S_0$ phase shift of Σ^+p as a function of p_{lab} for different values of Λ_s and Λ_ϵ.

Moreover, the vector mesons taken into account in this thesis, the $\omega(782)$, $\rho(775)$, and $K^*(892)$, are playing an important role in the interaction by taking care of the short-range part as clear from their large mass values. Thus, fitting the corresponding parameters will fix the core part of the interaction. As an illustration, the $^1S_0$ phase shift of Σ^+p for different values of g_v^8 is presented in Fig. 5.10. For any value less than 0.88, the phase shift starts from a value around 180 degree, thus pointing towards a bound state, experimentally which is not supported for $^1S_0$. The usual practice is to consider Σ^+p as a repulsive interaction [46–50], hence in our case we set the minimum limit to this value as an extra requirement used in χ^2 fit in addition to the data. The final value of g_v^8 is of course there after obtained from the fit within this limit.

The singlet coupling constant g_v^1 is also in a true sense a free parameter, however following the scalar meson strategy, we did not include it to the χ^2 fit parameter set. The supporting logic is singlet couplings together with the octet one together produce the physical effective coupling of the meson (Eq. 2.11). Therefore the octet coupling value obtained from the fit can as well serve the purpose. Therefore

we decided not to include the parameter in to the fit parameter and fixed to the Nijmegen group [49]. For the vector meson mixing angle we choose the universal

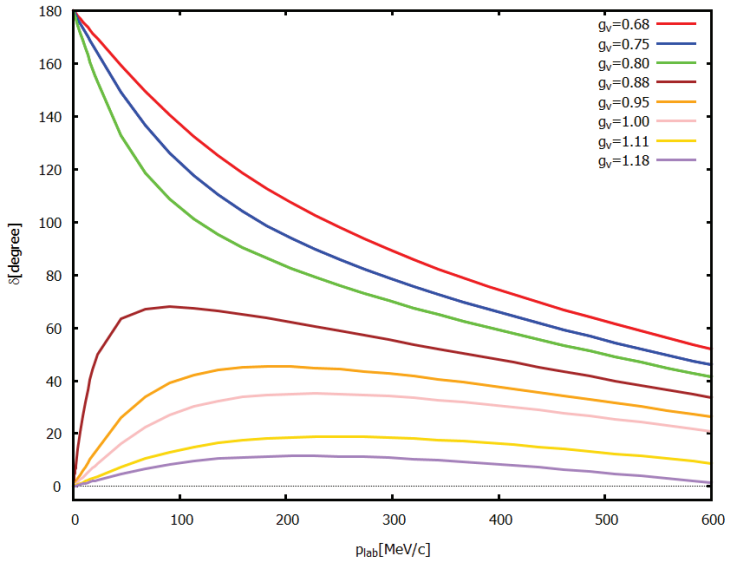

Figure 5.10: Variation of $\Sigma^+ p$ $^1S_0$ phase shift with different octet vector coupling constant (g_v^8) values shown as a function of p_{lab}.

coupling condition, given by, $\tan\theta = \frac{1}{\sqrt{2}}$ and use the value of 35.26°, the ideal mixing angle for vector mesons. Ideal mixing for vector mesons signify that one of the states is pure or mostly $|s\bar{s}\rangle$ where s is the strange quark. The universal condition simultaneously fixed the α_v to 1. For the magnetic one, we chose the Jülich group model value [46, 47].

The variation of the cut-off mass dependence for vector mesons is shown in Fig. 5.11. The difference being not strong as compared to other parameters, we fixed the vector cut-off mass to 1.7 GeV for the rest of the purpose, thus leaving from the fitting set of parameters.

We summarize our parameter values that are fixed prior fitting to data in Table 5.2 with the dashed ones referring to the ones used as free parameters, as an updated version of our list of free parameters shown in Table 2.10.

One point should be mentioned here about the sensitivity of parameters. For illustration purpose of the general influence of OBE based model parameters on hyperon interaction, we have picked up $\Sigma^+ p$ channel as an example. Although the general nature of dependency of the BB interaction over the parameters are same for

	$\frac{g_8}{\sqrt{4\pi}}$	$\frac{g_1}{\sqrt{4\pi}}$	α	θ	Λ_c
pseudoscalar	3.795	0.1913	0.355	-23	1.3
scalar	—	3.5434	—	37.05	2
vector	—	3.4431	1.0	35.26	1.7

Table 5.2: Set of parameter values used in this thesis. The dashed ones are to be obtained by χ^2 fit to data.

all channels, meaning the affect on the region of interaction is similar for all channels, the actual strength of the parameters that produces a repulsion or attraction (as here $g_v^8 \geq 0.88$ for avoiding bound state) or the order of sensitivity is also channel dependent. Therefore, the channel which is being dealt with is also playing a role on the sensitivity of the parameters. This is making the OBE scheme non-trivial and arising added uncertainty for any OBE based hyperon model [48, 49, 79]. In brief, the extra channel dependency makes a simultaneous good fit of different strangeness channels non-trivial.

5.2 Result of Fit

To obtain the best fit parameters, a FORTRAN source capable of calculating the scattering cross section for the Λp and $\Sigma^+ p$ channels are compiled parallel with MINUIT [103] χ^2 package. The χ^2 distribution is for a set of n experimental data points for an observable O (say) is defined as,

$$\chi^2 = \sum_{i=1,n} \frac{[O_{\rm ex}(i) - O_{\rm th}(i)]^2}{O_{\rm err}(i)^2} \tag{5.1}$$

where $O_{\rm ex}(i)$ is experimentally measured value with error $O_{\rm err}(i)$ and $O_{\rm th}(i)$ is the corresponding theoretical value.

We want to get the best fit values of the g_v^8, g_s^8, and α_s parameters. Following the standard practice by the Nijmegen group, J{ü}lich group, and χEFT group in their investigations [36, 40, 46–50], we fitted 12 experimental Λp cross sections [68, 74] and four $\Sigma^+ p$ cross sections [66]. As a starting point, we fitted the data with $^1S_0$ partial wave. For this kind of low energy scattering experiments, the most dominant contribution is coming from the $^1S_0$ partial wave. However, there is a significant difference in our and their fitting method. The other groups usually fit

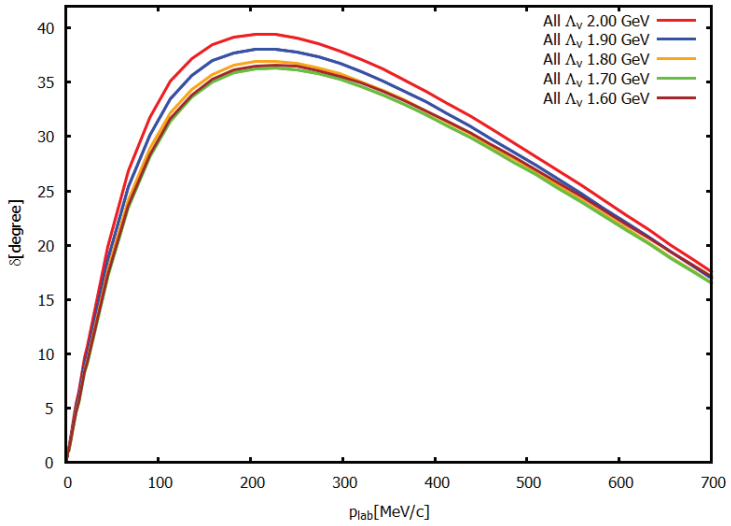

Figure 5.11: Variation of $\Sigma^+ p$ $^1S_0$ phase shift with different Λ_v values.

simultaneously total 36 YN data points, including 6 cross section data points for $\Sigma^- p \to \Lambda n$ [68], 6 cross section data points for $\Sigma^- p \to \Sigma^0 n$ [75] , 7 cross section data points for $\Sigma^- p \to \Sigma^- p$ [66] along with the inelastic capture ratio at rest [76, 77]. The reason we did not include the other 24 data points to our fit as these are coming from mainly the $\Lambda N - \Sigma N$ coupled channel system. The $\Lambda N - \Sigma N$ transition is primarily caused by the $^3S_1 - ^3D_1$ tensor-coupled partial wave (PW) transition [47, 48, 50, 106], which at these moment, we did not include in our calculations. We have decided to include only diagonal channels into the fitting procedure and to use the obtained parameter values to predict observables for non-diagonal reaction channels like $\Lambda N - \Sigma N$. Once this first stage of the model gives satisfactory result, one can always include partial wave coupling. Needless to say, for a full solution to the problem, the total cross section should include higher partial wave contributions as well, however as a first hand solution of the problem, $^1S_0$ PW is adequate for this type of low energy scattering problems. thus is sufficient for understanding the underlying physics.

In Fig. 5.12 the theoretical integrated cross section (solid lines) is shown calculated with the MINUIT[103] determined parameter values for Λp and $\Sigma^+ p$. A good reproduction of the empirical data we have achieved. The MINUIT package is capable of fitting the function with two minimization procedures, simplex [111],

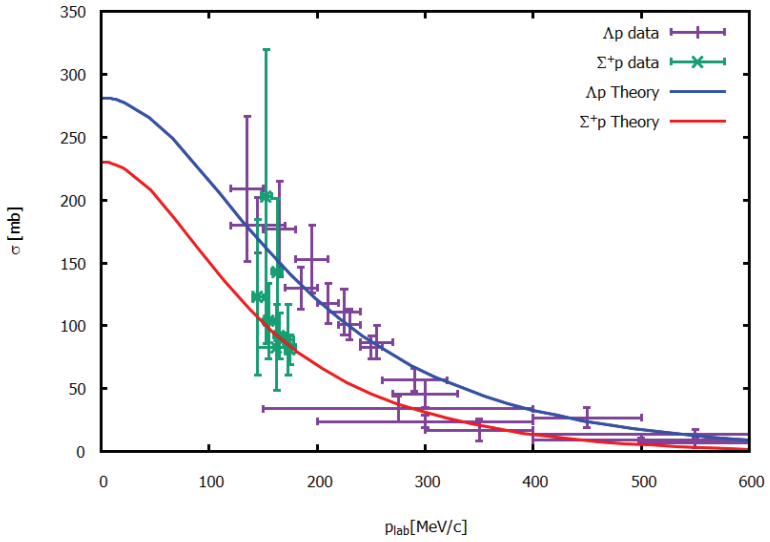

Figure 5.12: Free space Λp and $\Sigma^+ p$ scattering cross section for $^1S_0$ partial wave χ^2 fitted to world data as a function of laboratory momentum resulting in g_s^8 : 1.2274, g_v^8 : 1.1566, α_s : 0.9603 with a total $\chi^2 = 6.68$ for the 16 data points.

and migrad [112] minimization processes. In Fig. 5.12, the migrad values were used. The migrad minimization is more efficient as it evaluates the derivative of the fit function (here the χ^2) too. We report here the parameter sets evaluated by these methods. Apart form the MINUIT fit run, we also did a manual evaluation, based on the study discussed in Section 1, the obtained set of parameters we will call here after as *manual fit*. These three sets of parameter values are presented in Table 5.5 with the respective errors. For the manual fit values, we used in addition, a reduced cut-off value for Λ_ϵ= 1.85 GeV.

One can notice that the migrad minimization being more sophisticated, has much less error associated compared to the simplex one. One interesting point to note is that the errors associated with different parameter is different, thus in a sense, referring towards the sensitivity of the parameter. The error pointing towards the

Parameter	Migrad	Error	Simplex	Error	Manual Fit
g_s^8	1.2274	0.00032	1.2188	0.1	0.92
g_v^8	1.1566	0.00001	1.162	0.1	1.11
α_s	0.96053	0.00012	1.0280	0.1	1.05
χ^2	6.68	–	10.84	–	11.07
$\frac{\chi^2}{data}$	0.42	–	1.54	–	1.44

Table 5.3: χ-square fit result of the model.

uncertainty associated with the corresponding parameter. Supporting our investigation in last Section about the vector meson, the comparatively negligible error emphasizes the fact the vector coupling constant should be this strong. From the

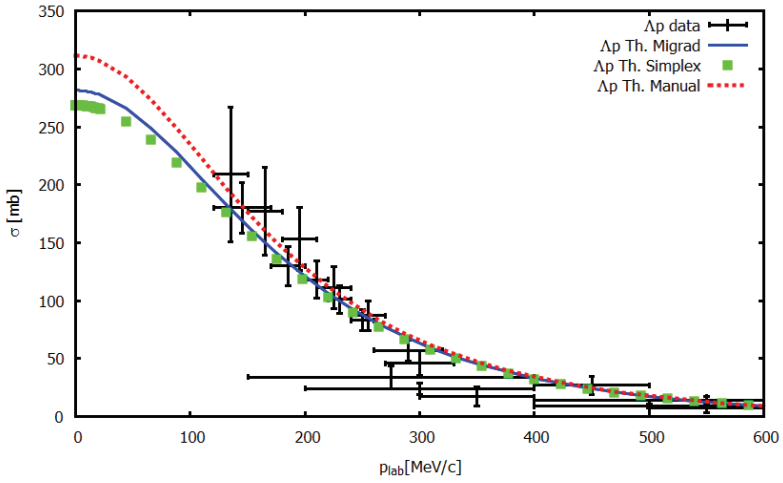

Figure 5.13: Free space Λp cross section for $^1S_0$ partial wave χ^2 fitted to world data as a function of laboratory momentum. Migrad fit (blue solid), simplex fit (green box), and manual fit (red dotted) are the three theoretical results.

Table. 5.5 therefore we can conclude the scalar sector has a larger uncertainty associated with than the vector, the octet coupling being more sensitive than the α. In our discussions in last section over scalar meson parameters, the α was guessed to be more sensitive than the octet constant. Instead the migrad minimization pointed out the sensitivity of octet constant slightly higher than the α. This implies the fact of channel dependency of the parameters. The incorporation of Λp channel changed the overall sensitivity. The theoretical cross sections are plotted in Figure 5.14 for

$p_{lab}^{\Sigma^+}$[MeV/c]	σ_{ex}[mb]	σ_{th}^{mig}[mb]	σ_{th}^{manu}[mb]
145	123± 62	106.6	135.23
155	104±30	98.5	117.28
165	92± 18	91.0	124.68
175	81± 12	84.0	114.91
	χ^2_{mig}:0.220		χ^2_{manu}:3.15

Table 5.4: Comparison of χ^2 fit theoretical result to the experimental $\Sigma^+p \to \Sigma^+p$ cross section data.

Σ^+p and Figure 5.13 for Λp for all three sets of parameters.

There is an important point to notice in these two Figures: for the Σ^+p the two

χ^2 minimization results, migrad (blue solid) and simplex (green box), are having a significant amount of difference in the region of low energy where as for the Λp channel the difference is small. This points towards different sensitivity of these two S= -1 channels to the scalar and vector meson. The main qualitative difference between these two sets of parameters are in the scalar meson strength. On the other hand, the manual one having a less strong scalar strength than the vector one. One point to remember here is the difference in Λ_ϵ value between the χ results to the manual one. Due to a comparatively low cut-off mass, the weaker scalar strength could reproduce the same result as with strong scalar strength with higher Λ_ϵ. Therefore, we can conclude that the ΣN potential is more sensitive towards the scalar strength than the ΛN channel.

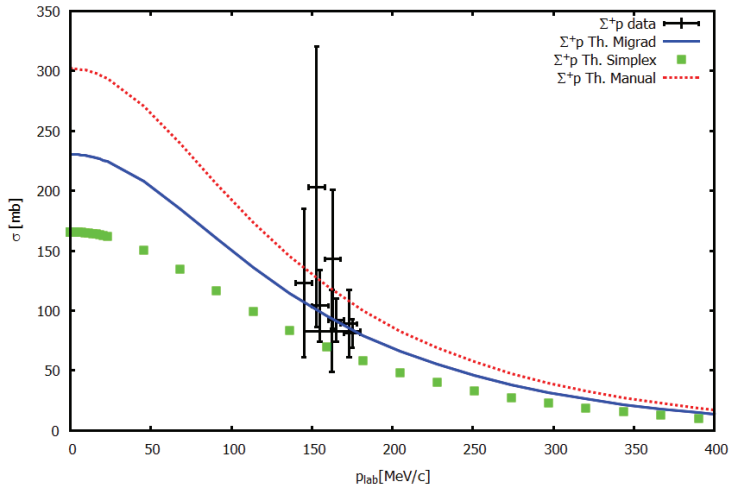

Figure 5.14: Free space $\Sigma^+ p$ scattering cross section for $^1S_0$ partial wave χ^2 fitted to world data as a function of laboratory momentum. Three theoretical results are reported: migrad fit (green solid),simplex fit (cross points), and manual fit (red dotted)

The manually derived one although have a comparable χ^2 value with the other too, the effect on the scattering length and the core behavior is different, the manual one having a slightly stronger core repulsion. Nevertheless, due to the equivalence between the migrad and simplex method parameter values, we will use the migrad set of values for further use in this thesis as the parameters has less errors associated compared to the simplex one. Nevertheless, the simplex one is equally good if not better and so as the manual one.

The parameters being set, now we can test the SU(3) limit of the baryon octet

p^{Λ}_{lab} [MeV/c]	σ_{ex} [mb]	σ^{mig}_{th}[mb]	σ^{manu}_{th}[mb]
145	180± 22	169.1	181.79
185	130± 17	132.6	141.19
210	118± 16	113.1	119.84
230	101± 12	99.5	104.95
250	83± 9	87.4	91.87
290	57± 9	67.4	70.41
135	209± 58	179.1	193.05
165	177± 38	150.1	160.53
195	153± 27	124.5	132.27
225	111± 18	102.7	108.50
255	87± 13	84.6	88.86
300	46± 11	63.1	65.89
χ^2_{mig}:6.49		χ^2_{manu}:7.92	

Table 5.5: Comparison of theoretical and experimental data for $\Lambda p \to \Lambda p$.

sector. The full OBE parameter set is listed in Appendix A. One point to realize here is although the χ^2 values are impressive, one should not have too much expectation form the fit parameters. First, since the fit was made to a set of points with large errors, thus reducing the χ^2 value, not overlooking that there lies a rather large uncertain region. Second, keeping in mind the complexity of the problem, the fit function in this case, the χ^2, does not have a single minimum. Rather the minimum depends in the initialization. The set of values obtained in this fit were made with a set of initial values that we could have guessed by the knowledge from the discussions made in Section 1. For an initial set of minimum values presented in Table 5.1, the MINUIT evaluated best fit value is different, giving $\{0.848, 1.1724, 0.89\}$ for example. In spite of these uncertainties, the model does result into a reliable one as from the Figure 5.12 evident. Keeping this in mind, we can definitely conclude our model was able to reproduce the data pretty well, and hence, it is now interesting to see how the model gives the results of the other baryon-baryon channels.

5.3 Free Space Result

We have now constructed a realistic OBE model for the hyperons using the χ^2 fit. The next step is to check the applicability over whole octet baryons. From non-strange NN to strange channels within $J^P = \frac{1}{2}^+$ octet, can now be investigated

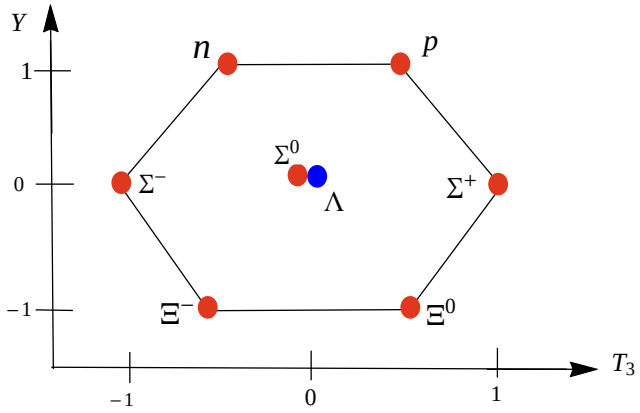

Figure 5.15: $J^P = \frac{1}{2}^+$ Baryon Octet

with the model. Contrary to Nijmegen, Jülich, and χEFT groups, we do not require any necessary modification to deal with higher or lower strangeness channels. An investigation within this strict SU(3) symmetry, will be helpful for understanding the validity of SU(3) in the octets.

5.3.1 S = 0 Results

We did not fit our data to the nucleon sector to preserve SU(3) within the model as fitting to NN data demands modification not fulfilled by SU(3) [46, 50]. However, in order to check whether the model satisfies the SU(3) conditions, it is important to evaluate the NN result since the nucleons are also part of the baryon octet, the basis of our model.

There are two isospin channels for nucleons, one with I=0 and I=1. For I=0 isospin, $^1S_0$ partial wave is prohibited due to Pauli exclusion principle. In Fig. 5.16 phase shifts evaluated by our model with the χ^2 and manual fit parameters has been shown. For I=1 channel, the manual fit model has a comparatively weak repulsion than the χ^2 one, due to much stronger scalar and vector coupling. The extracted phase shift for the SE wave from experimental data is much sharper than the one achieved here, shown in Fig. 5.18.

This rather high discrepancy is quite expected from our model for nucleons. We set our limit to SU(3), under which the ideal mixing condition between vector

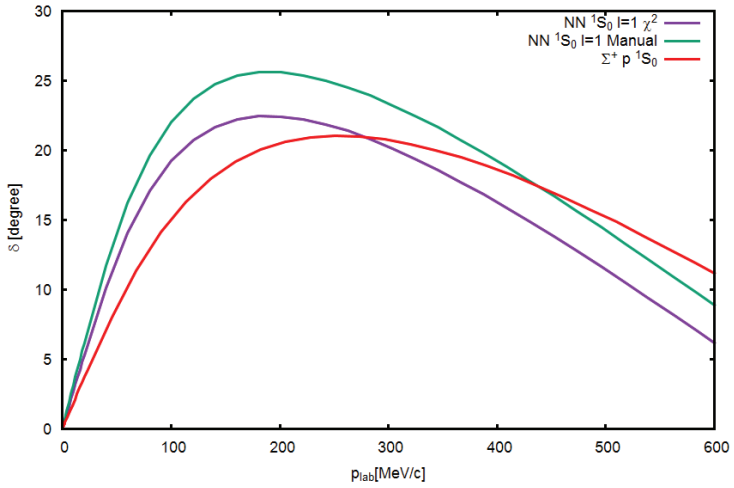

Figure 5.16: Theoretical NN free space $^1S_0$ phase shift for T=1 calculated with the χ^2 fit parameter (solid violet) and the manual parameter set (red box). The NN phase shift is plotted here with the respective Σ^+p phase shift.

mesons that demands $g_{\phi NN}$ to be zero and a lower ω nucleon coupling. However as the data is concerned, in order to have a proper description of the data, the nucleon meson models [62] had to increase the ωNN coupling effectively by more than two factor. This increase in ω coupling effectively contributes to sharp peak, compared to the pure SU(3) limit. Thus, without bothering much about the experimental data, it is better to look in to the SU(3) aspects. For the baryon octet, one can only have six independent representation, that is also satisfied by the $SU(3)_f$ potentials,

$$V_{\mathbf{8}} \oplus V_{\mathbf{8}} = V_{\mathbf{27}} \oplus V_{\mathbf{10}} \oplus V_{\mathbf{10}_*} \oplus V_{\mathbf{8}_s} \oplus V_{\mathbf{8}_a} \oplus V_{\mathbf{1}} \tag{5.2}$$

In terms of partial wave decomposition this is summarized Table 5.6. The $^1S_0$ NN

Isospin	Spin State	BB Channel	SU(3) Representation
1	$^1S_0$	NN	$V_{\mathbf{27}}$
$\frac{3}{2}$	$^1S_0$	ΣN	$V_{\mathbf{27}}$
1	$^1S_0$	ΞN	$V_{\mathbf{8}_s}$,$V_{\mathbf{27}}$
2	$^1S_0$	$\Sigma\Sigma$	$V_{\mathbf{27}}$
$\frac{1}{2}$	$^1S_0$	ΣN, ΛN	$V_{\mathbf{27}}$, $V_{\mathbf{8}_s}$

Table 5.6: SU(3) content of different baryon-baryon interaction channels.

with I=1 and $I = \frac{3}{2}$ Σ^+p belongs to the 27-plet $V_{\mathbf{27}}$ potential, and is a source of strong

repulsion. Therefore, the phase shifts and the potential should be qualitatively similar. In Fig. 5.16, the Σ^+p phase shifts for $^1S_0$ channel is compared to the nucleons. The similar repulsive interaction trends in Fig. 5.16 for NN and Σ^+p verify the SU(3) nature of our model. There is of course some difference in magnitude and peak positions which is obvious due to the mass difference of the particles and different particles involved, accounting for the SU(3) breaking. Another difference between these two systems is the mesons involved in the interaction. The hyperons with $S \neq 0$,will have strange meson exchange vertices in addition to the non-strange ones responsible for NN. As an illustration, we have shown the NN potential, the

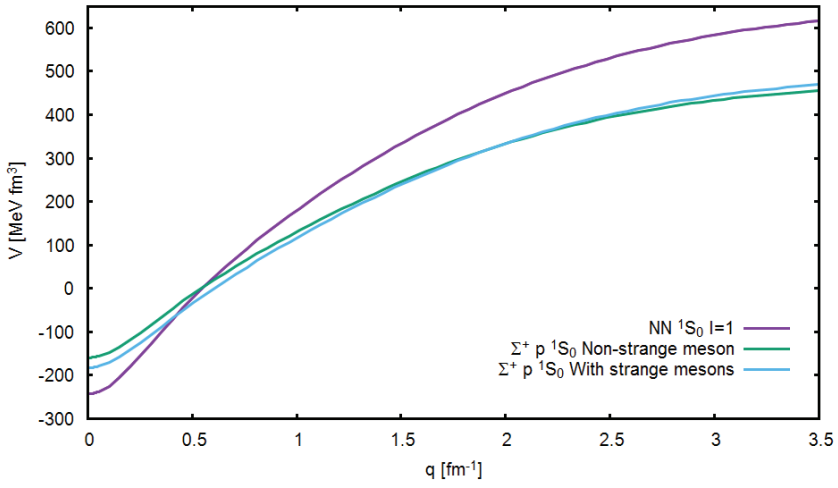

Figure 5.17: NN and Σ^+p potential originated from our model is shown as a function of the input center-of-mass momentum.

Σ^+p potential with and without strange mesons involved in the interaction, in Fig. 5.17 where the effect of inclusion strange mesons is not differing much to the non-strange counter part. The cross sections of the corresponding channels are shown in Fig. 5.18. Since our model produces a stronger NN interaction than the Σ^+p, the low energy cross section for the nucleons are also at a higher value than the Σ^+p channel. Scattering lengths and effective range for NN channels are shown in Table 5.7. The

Channel	$a_s(fm)$	$r_s(fm)$
NN (I=1)	-2.31	5.26

Table 5.7: Low-energy parameters of NN channel within SU(3) constraint.

value is far from the experimental values of -23.7 (I=1) fm. This deep repulsion is

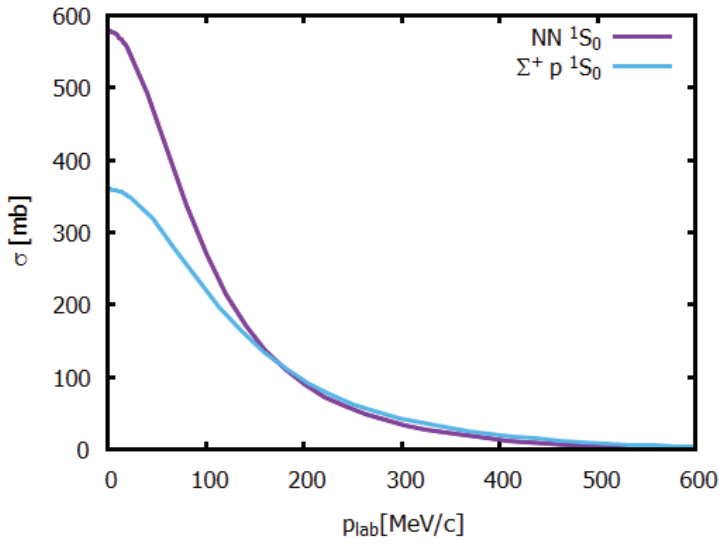

Figure 5.18: Theoretical NN cross section for $^1S_0$ compared with the SU(3) partner $\Sigma^+ p$ $^1S_0$ channel.

theoretically achieved by high-precision OBE models [10, 62, 64] that fit a large set of parameters to rich nucleon data set. The best fit values that can reproduce the correct NN scattering length, is only possible by considering SU(3) breaking effects already in the nucleon sector. Our model within SU(3) limit, therefore is expected to have a value comparable to the SU(3) partner $\Sigma^+ p$.

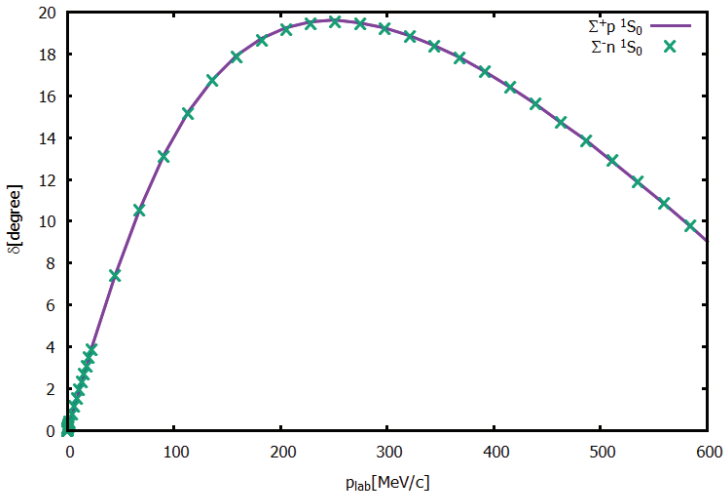

Figure 5.19: $^1S_0$ Phase shifts for $\Sigma^- n$ and $\Sigma^+ p$ channels.

As a summary of the S=0 results, we can conclude that our model has proved to be constrained by SU(3) symmetry, thus can be applied consistently to the whole

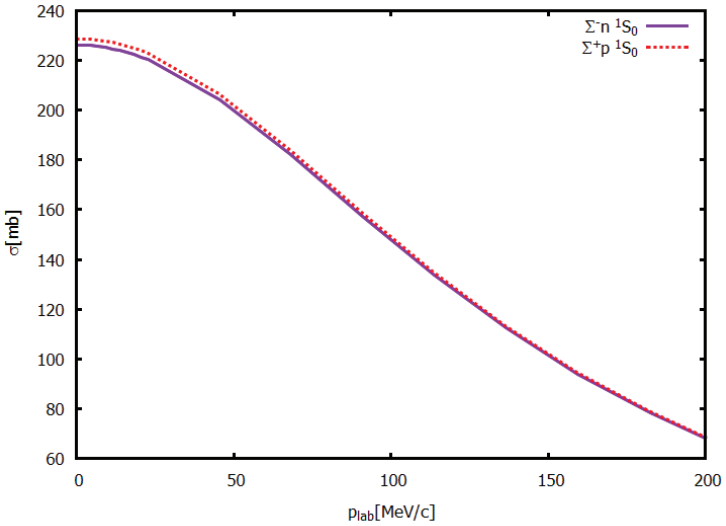

0.45

Figure 5.20: ${}^1S_0$ Phase shifts for $\Sigma^- n$ and $\Sigma^+ p$ channels.

baryon octet. The far off NN phase shift and LE parameters calculated by our model is a consequence of $SU(3)$ symmetry. Obviously, this is pointing towards SU(3) breaking in nucleon sector. On the other hand we are interested in hyperons, which seem to have a better SU(3) preserving sector from the results obtained. Next let us discuss the results of hyperon channels.

5.3.2 S = -1 Results

The different isospin and particle basis channels for S=-1 sector is listed in Table 5.8. There are two isospin basis BB channels: ΛN and ΣN. The potential we calculate in the isospin basis. The coupling of neutral pion to Λ hyperon is included in our model to account for the $\Lambda - \Sigma^0$ mixing, which is only included when the calculation is done in physical particle basis.

Isospin	**I = 0**	**I = $\frac{1}{2}$**	**I=1**	**I = $\frac{3}{2}$**	**I=2**
S=-1		ΛN, ΣN		ΣN	
Particle	**Q=-2**	**Q=-1**	**Q=0**	**Q=1**	**Q=2**
S= -1		$\Sigma^- n$	Λn $\Sigma^0 n$ $\Sigma^- p$	Λp $\Sigma^+ n$ $\Sigma^0 p$	$\Sigma^+ p$

Table 5.8: Isospin and particle basis channels for $S = -1$.

5.3.2.1 Uncoupled Channels

Connecting the isospin channels to four particle basis charged channels, it is evident that $I = \frac{3}{2}$ ΣN potential is responsible for the two uncoupled particle basis channels: $\Sigma^- n$ and $\Sigma^+ p$. An appropriate isospin transformation will give the potential in particle basis formalism. In addition the average mass values needs to be replaced by physical particle masses. for example, for $\Sigma^- n$ and $\Sigma^+ p$, the particle basis potentials are

$$V_{\Sigma^+ p} = V_{\Sigma N}(M_\Sigma \to M_{\Sigma^+}, M_N \to M_p) \tag{5.3}$$

$$V_{\Sigma^- n} = V_{\Sigma N}(M_\Sigma \to M_{\Sigma^-}, M_N \to M_n) \tag{5.4}$$

A mass breaking effect of about 4 MeV (Table 5.9) for the Σ's, thus has been incorporated referring to explicit SU(3) mass breaking. This is the only point where quark mass difference effect of $\delta m = (m_s - m_{u/d} \sim 3)$ MeV is taken into account. In Fig. 5.19 SE phase shifts of the two uncoupled channels has been shown, and as

Particle	Mass in Particle Basis	Mass in Isospin basis
n	939.57	939.42
p	938.27	
Λ	1115.68	1115.68
Σ^+	1189.37	
Σ^0	1192.64	1193.12
Σ^-	1197.45	

Table 5.9: Masses in isospin and particle basis for S = -1 channels.

obvious, they are identical due to same potential involved (Eq. 5.4). Similar is the case for cross sections shown in Fig. 5.20 with a slight modification near zero momenta. The masses in the two bases being negligible compared to the particle mass scale, the channels inherit identical properties. The low energy (LE) parameters too being same, not shown explicitly for these channels, but in general for $I = \frac{3}{2}$, ΣN in Table 5.10.

Our model, similar to other groups, predicts a repulsive ΣN interaction for $^1S_0$; however,with weaker strength. Because of the existing scarce and inaccurate data set, a unique partial wave analysis for hyperons is not possible. Therefore, models

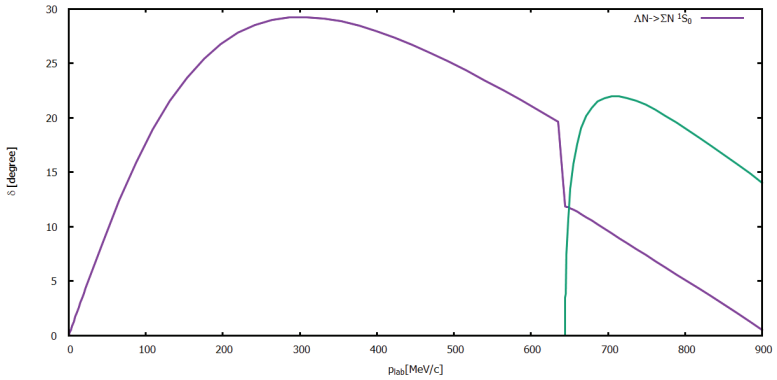

Figure 5.21: $^1S_0$ Eigen phase shifts for ΛN (violet) and ΣN channel (green).

dealing with different parameters (in OBE) as well as frameworks (LQCD, χEFT), predict different results. Special cases are the OBE based Nijmegen and Jülich groups, having significant differences in many points, pointed out in Chapter 2, differing quantitatively with our values. Furthermore, both these and the χEFT groups, incorporates Coulomb interaction in their calculations, that for charged channels can affect the cross sections by $100-150$ mb. Being extensions of NN based OBE models, both Nijmegen and Jülich models, take into account phenomenological affects coming from the nucleon sector, accounting for a stronger ω-nucleon coupling, for example. We, on the other hand, inclined more towards investigating the in-medium properties, did not include Coulomb at this stage, remembering this will not alter the strong interaction properties. Moreover, Coulomb, being a long range force, for the lowest partial wave, $^1S_0$, has less effect than for a higher energy calculation.

5.3.2.2 Coupled Channels

There is one coupled channel (CC) for $I = \frac{1}{2}$ in the isospin basis and two in particle basis for Q = 0 and Q = 1 (Table 5.8). The CC T-matrix equation for isospin basis has been shown in Eq. 3.29, that we solve numerically in R-matrix formalism. We introduce the following notation (similar to Nijmegen one) for CC systems of S = -1, ΛN-ΛN : $\Lambda\Lambda$; $\Sigma N - \Sigma N$: $\Sigma\Sigma$; $\Lambda N - \Sigma N$: $\Lambda\Sigma$ and similarly for

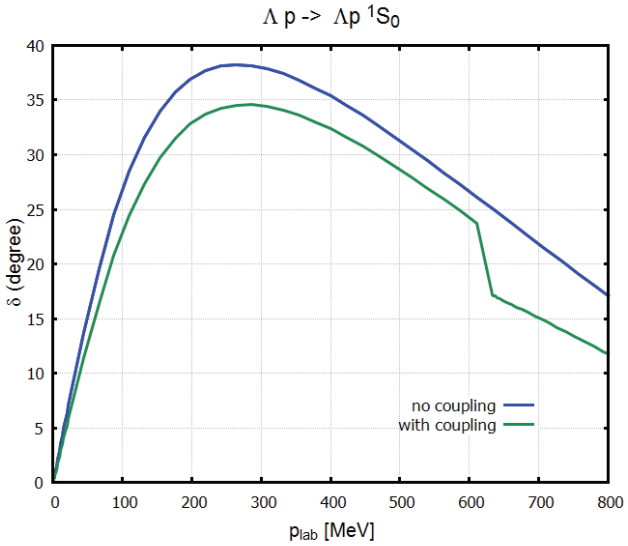

Figure 5.22: ${}^1S_0$ Phase shifts for Λp channel with or without coupling.

others. With this formalism, the CC R-matrix equation for isospin basis reads,

$$\begin{pmatrix} R_{\Lambda\Lambda} & R_{\Lambda\Sigma} \\ R_{\Sigma\Lambda} & R_{\Sigma\Sigma} \end{pmatrix} = \begin{pmatrix} V_{\Lambda\Lambda} & V_{\Lambda\Sigma} \\ V_{\Sigma\Lambda} & V_{\Sigma\Sigma} \end{pmatrix} + \begin{pmatrix} V_{\Lambda\Lambda} & V_{\Lambda\Sigma} \\ V_{\Sigma\Lambda} & V_{\Sigma\Sigma} \end{pmatrix} \begin{pmatrix} G_{\Lambda\Lambda} & 0 \\ 0 & G_{\Sigma\Sigma} \end{pmatrix} \begin{pmatrix} R_{\Lambda\Lambda} & R_{\Lambda\Sigma} \\ R_{\Sigma\Lambda} & R_{\Sigma\Sigma} \end{pmatrix} \tag{5.5}$$

which needed to be solved. Numerically we solve this integral equation using 64 Gaussian quadrature grid points. Rearrangement of Eq. 5.5 gives

$$\begin{pmatrix} 1 - V_{\Lambda\Lambda}G_{\Lambda\Lambda} & V_{\Lambda\Sigma}G_{\Sigma\Sigma} \\ V_{\Sigma\Lambda}G_{\Lambda\Lambda} & 1 - V_{\Sigma\Sigma}G_{\Sigma\Sigma} \end{pmatrix} \begin{pmatrix} R_{\Lambda\Lambda} & R_{\Lambda\Sigma} \\ R_{\Sigma\Lambda} & R_{\Sigma\Sigma} \end{pmatrix} = \begin{pmatrix} V_{\Lambda\Lambda} & V_{\Lambda\Sigma} \\ V_{\Sigma\Lambda} & V_{\Sigma\Sigma} \end{pmatrix} \tag{5.6}$$

Each term in first matrix of LHS is an integration. This matrix equation is solved for R by matrix inversion method using Gauss elimination LAPACK [104] routine. T-matrix elements are obtained from R-matrix with on shell elements (R_{on}) via ZGESV LAPACK package available for solving complex matrix equation by solving the following matrix equation for T

$$AX = B \Rightarrow (1 + iR_{on})^{-1}T = R_{on}. \tag{5.7}$$

The derived T-matrix elements are the input for determining the CC phase shifts, cross sections, and LE parameters. The special feature of the hyperon-nucleon interaction is different physical thresholds. The more massive particle channel, in this case, ΣN, does not contribute to the asymptotic flux unless the physical threshold for the channel opening is reached, below that point the other partner channel behaves like a uncoupled one.

Beyond threshold, the flavor mixing between channels starts, as the lower massive channel gets converted to the higher one. This is visible in observable level usually as a kink on the threshold point, commonly known as the 'cusp' effect. The channel opening is taken care of by the Green function in the scattering equation. For the ΛN - ΣN channel, the threshold value ΣN channel 'opening' is at

$$p^{\Lambda}_{lab}(\Lambda N \rightarrow \Sigma N) = 644.23 \quad \text{MeV/c} \tag{5.8}$$

The three different potentials of this CC channel are shown in Fig. 5.25. The ΛN potential is less repulsive compared to ΣN near the core region and gradually becomes attractive with higher incident momentum. The ΣN always is repulsive and has a saturation kind of point like NN. The transfer potential starts from a repulsion force to end up being attractive.

Isospin Basis S = -1 Coupled Channel Results: First we discuss the isospin basis result. In Figure 5.21, the $^1S_0$ eigen phase shifts for ΛN(violet) - ΣN (green) coupled channel is shown. The 'cusp' effect is visible as the kink appearing at the threshold value of p^{Λ}_{lab} where ΣN channel opens (see Eq. 3.28). An interesting aspect is to see how the channel mixing affects the interaction in Fig 5.22 where Λp $^1S_0$ (S= -1, Q=1 CC channel) phase shift is plotted with the coupling on(violet) and off (green), thus putting off-diagonal terms to as it is and zero in Eq. 5.5. For that we have in Figure 5.22. As can be seen, the phase shift for uncoupled channel is higher than the actual CC channel. This is because for a CC scattering system, although the higher channel opens at threshold, there is still off-shell conversion to ΣN channel going on, not visible on on-shell of course explaining the reduction. For CC case, there is a kink appearing on the phase shift exactly at the channel opening

Channel	Model	$a_s(fm)$	$r_e(fm)$
ΣN $(I=\frac{3}{2})$	χLO[101]	-1.80	1.76
	NSC97f[49]	-4.35	3.16
	J94[47]	-2.26	5.22
	J04[48]	-4.71	3.31
	Our Model	**-1.44**	**5.18**
ΛN	χLO	-1.91	1.40
	NSC97f	-2.60	2.74
	J94	-1.56	1.43
	J04	-2.56	2.75
	Our Model	**-1.52**	**2.34**
ΣN $(I=\frac{1}{2})$	J04	0.90	-4.38
	Our Model	**0.96-i0.96**	**-3.38-i0.08**

Table 5.10: Low-energy parameters of different isospin basis channels derived using this model compared to other existing model derived values.

threshold. From this point a part of ΛN starts converting into ΣN on on-shell level, reflecting on the observables.

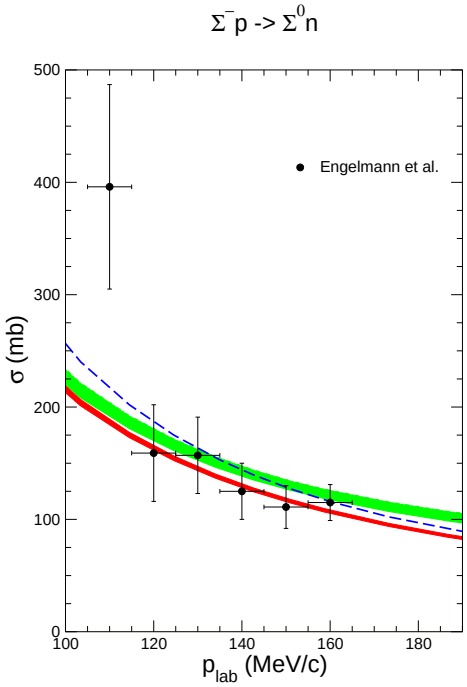

Figure 5.23: $\Sigma^- p \to \Sigma^0 n$ integrated cross section calculation by χEFT group. Figure taken from [101].

The investigation from other groups confirmed the tensor-coupled ${}^3S_1 - {}^3D_1$ partial wave predominantly controlling ΛN -ΣN transition [48, 50]. The partial wave coupling not included into our calculation, the cusp is not visible in cross section scale at present. Nevertheless, the threshold phenomena is visible on the phase shifts, as can be seen in Fig 5.21. Regarding the ΣN channel, it appears on-shell beyond threshold as pointed out by the green phase shift curve in Fig. 5.21.

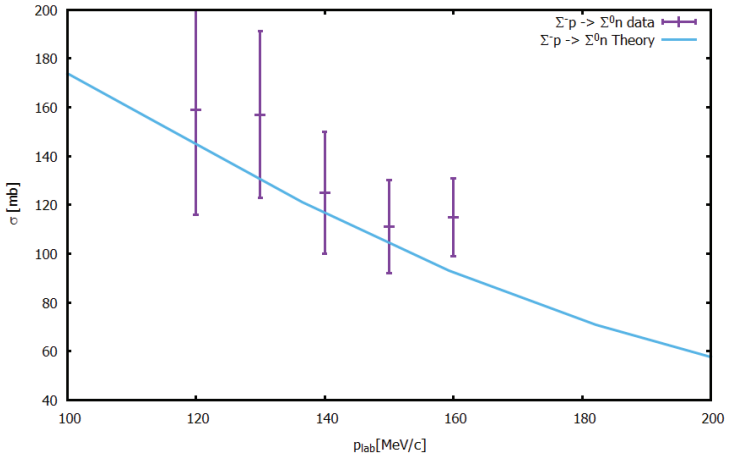

Figure 5.24: $\Sigma^- p \to \Sigma^0 n$ integrated cross section plotted with experimental data points [75].

The LE parameters for different isospin S=-1 channels has been listed in Table 5.10 with the results obtained by other groups. There are two ΣN channel parameters, one for uncoupled $I = \frac{3}{2}$ and $I = \frac{1}{2}$ responsible for CC. For all three of the three isospin BB channels, we agree on the type of interaction to others with quantitative difference of course. Our values are much weaker in strength compared to the OBE based models (NSC97f, J04, J89) where as much closer to χLO results. The reason behind this similarity can be due to the similarity in following SU(3) and not fitting NN for both of the two. Similar to χLO, which is then systematically improved to NLO, our model also can be improved by including more partial waves and partial wave couplings. As a whole, our model sufficiently reproduced the YB interaction.

Particle Basis S = -1 Coupled Channel Results: In order to calculate for particle basis channels, we need to apply the isospin transformation to the potential, (unlike uncoupled channels, where only mass value substitution was enough), as discussed in Chapter 3, and then solve the scattering equation in particle basis.

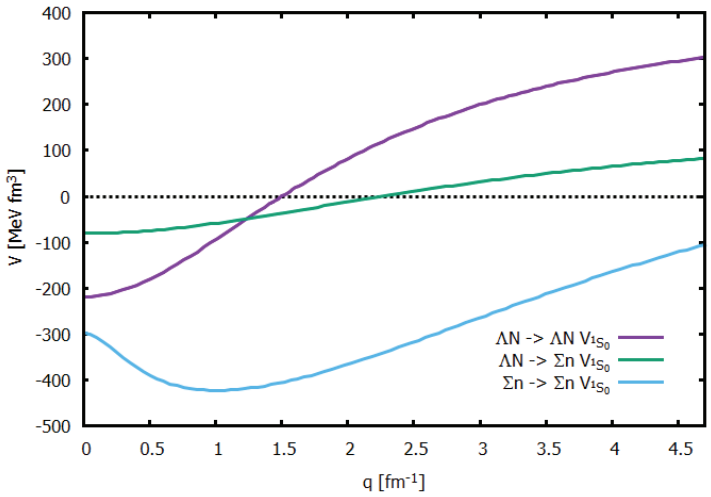

Figure 5.25: $^1S_0$ Potentials for CC ΛN -ΣN channel.

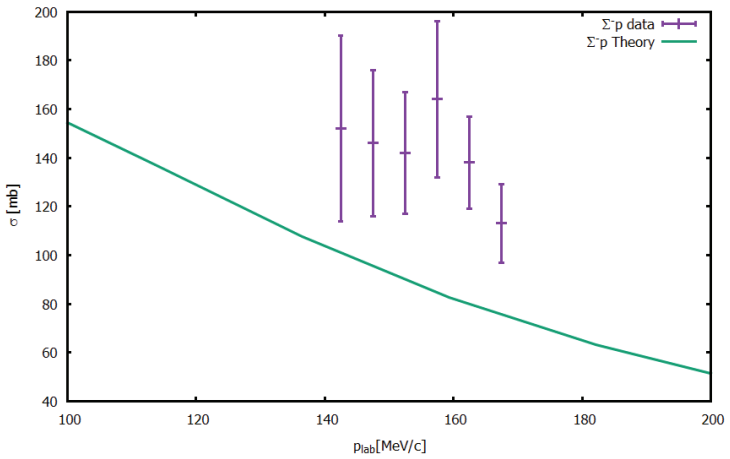

Figure 5.26: $\Sigma^- p \to \Sigma^- p$ integrated cross section plotted with experimental data points [66, 67].

On the contrary to isospin basis, the two CC particle basis sub-elements has three members each. Therefore, the R-matrix equation defined for isospin basis is of order 3X3 in particle basis. The potential transformation matrices for Q = 0 and Q = 1 has been shown in Chapter 3 in Eq. 3.78 and Eq. 3.76. With those transformed potential matrix elements, the R-matrix equation for Q = 0 sub-element is in operator notation,

$$R = V + VGR \tag{5.9}$$

$$R(Q=0) = \begin{pmatrix} R_{\Lambda\Lambda} & R_{\Lambda\Sigma^0} & R_{\Lambda\Sigma^-} \\ R_{\Sigma^0\Lambda} & R_{\Sigma^0\Sigma^0} & R_{\Sigma^0\Sigma^-} \\ R_{\Sigma^-\Lambda} & R_{\Sigma^-\Sigma^0} & R_{\Sigma^-\Sigma^-} \end{pmatrix} \tag{5.10}$$

$$V(Q=0) = \begin{pmatrix} V_{\Lambda\Lambda} & V_{\Lambda\Sigma^0} & V_{\Lambda\Sigma^-} \\ V_{\Sigma^0\Lambda} & V_{\Sigma^0\Sigma^0} & V_{\Sigma^0\Sigma^-} \\ V_{\Sigma^-\Lambda} & V_{\Sigma^-\Sigma^0} & V_{\Sigma^-\Sigma^-} \end{pmatrix} \tag{5.11}$$

$$G(Q=0) = \begin{pmatrix} G_{\Lambda\Lambda} & 0 & 0 \\ 0 & G_{\Sigma^0\Sigma^0} & 0 \\ 0 & 0 & G_{\Sigma^-\Sigma^-} \end{pmatrix} \tag{5.12}$$

Similar kind of equation exists for Q=1 with only exception in the potential given by

$$V(Q=1) = \begin{pmatrix} V_{\Lambda\Lambda} & V_{\Lambda\Sigma^+} & V_{\Lambda\Sigma^0} \\ V_{\Sigma^+\Lambda} & V_{\Sigma^+\Sigma^+} & V_{\Sigma^+\Sigma^0} \\ V_{\Sigma^0\Lambda} & V_{\Sigma^0\Sigma^+} & V_{\Sigma^0\Sigma^0} \end{pmatrix} \tag{5.13}$$

The explicit transformed elements are shown in Eq. 3.78 and Eq. 3.76. Forming the matrix equations, next steps are similar to that described for isospin basis, now for a 3X3 matrix equation instead.

The cross sections of various particle basis channels for S=-1 are shown in Fig. 5.24 to 5.26. The calculated integrated cross sections are plotted along with scattering data. Point to note is these are not fitted to data, hence are pure predictions of our model, and as can be seen, the quality is not bad. Our result for $\Sigma^- p \to \Sigma^- p$ is around $\pm$ 100 mb lower than the data. $\Sigma^- p$ being a charged channel, Coulomb

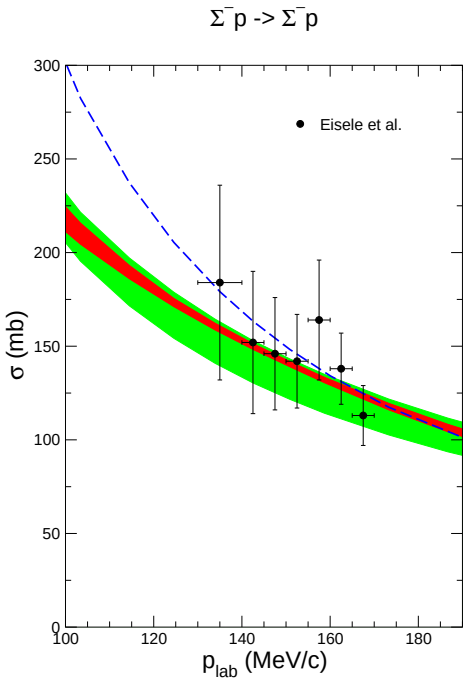

Figure 5.27: $\Sigma^- p \to \Sigma^- p$ integrated cross section calculation by χEFT group. [101]

interaction is playing a role, which we did not include. Therefore, the quality of our result with this difference, still can be considered quite good. Moreover, our interaction is similar to the χEFT calculation as can be seen in Fig. 5.27.

For the Q = 0 $\Sigma^- p \to \Sigma^0 n$ channel, the cross section fits satisfactorily with the data. $\Sigma^0 n$ is a neutral channel, hence without Coulomb, our model prediction matches pretty well to the data, emphasizing the quality of our nuclear potential. When compared to the χEFT calculations, out result is similar in behavior over change in energy as to theirs. The cross sections for these channels for even higher energies are shown in Fig. 5.30 and 5.31.

For S = -1, the Q= 0 $\Sigma^- p \to \Lambda n$ channel too has few data points. The calculated cross section is shown in Fig. 5.29, however without data. The data for this channel is around 150 mb. Our model predicts the cross section around 0.5 mb, insignificant too the data scale. However the trend is similar to the χEFT one, of course having a 100 times better magnitude (Fig. 5.28). The discrepancy too is due the tensor coupling. For $\Lambda - \Sigma$ mixing, the coupling between $^3S_1 - ^3D_1$ partial wave [47–

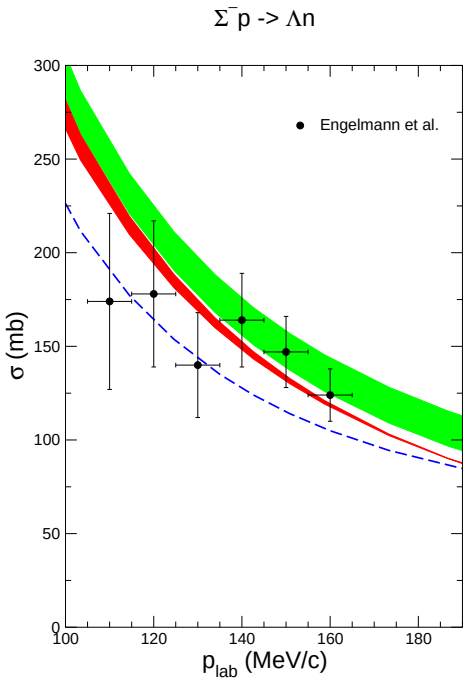

Figure 5.28: $\Sigma^- p \to \Lambda n$ integrated cross section calculation by χEFT group. Figure taken from [101].

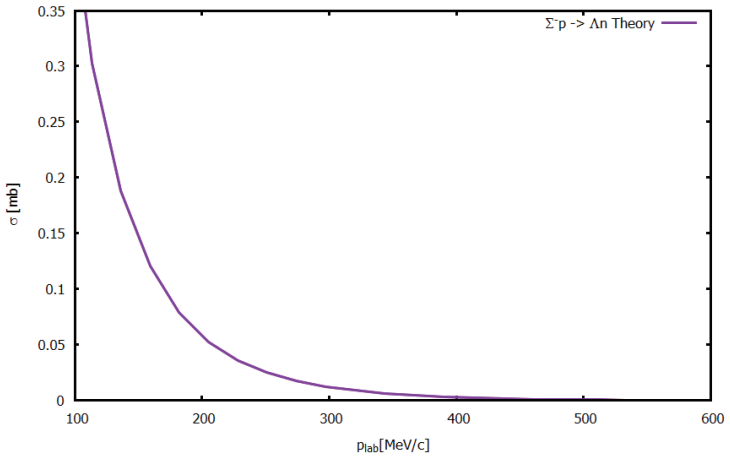

Figure 5.29: $\Sigma^- p \to \Lambda n$ integrated cross section for higher energies.

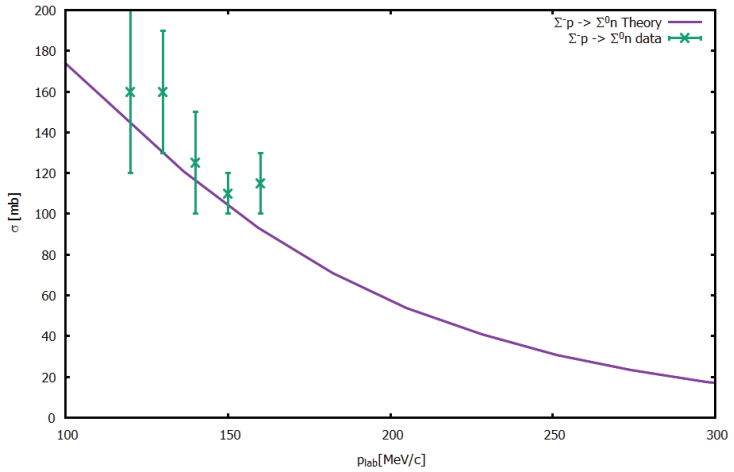

Figure 5.30: $\Sigma^- p \to \Sigma^0 n$ integrated cross section for higher energies. Data taken from [75].

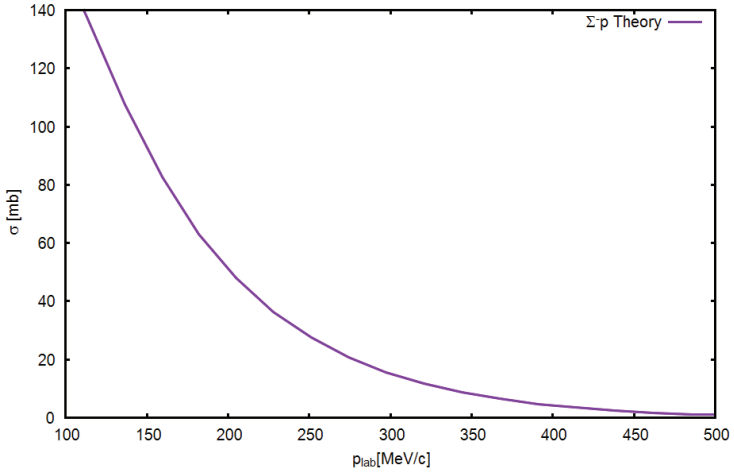

Figure 5.31: $\Sigma^- p \to \Sigma^- p$ integrated cross section for higher energies.

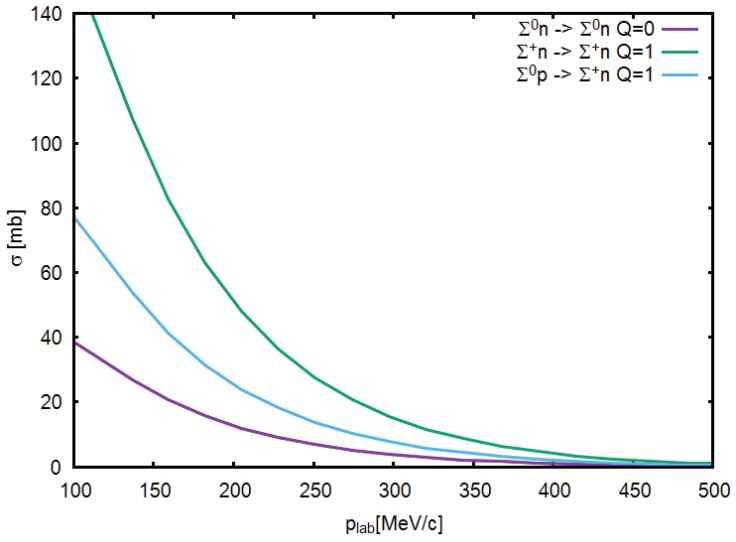

Figure 5.32: $\Sigma^0 n \to \Sigma^0 n$ (violet), $\Sigma^+ n \to \Sigma^+ n$ (green), and $\Sigma^0 p \to \Sigma^+ n$ (sky blue) integrated cross section for higher energies.

50, 101, 102] is required. That being ignored at present, the transition strength is much less, hence the magnitude problem occurred.

Another observable to consider here is the inelastic capture ratio at rest defined as

$$R = \frac{1}{4}\frac{\sigma_s(\Sigma^- p \to \Sigma^0 n)}{\sigma_s(\Sigma^- p \to \Sigma^0 n) + \sigma_s(\Sigma^- p \to \Lambda n)} + \frac{3}{4}\frac{\sigma_t(\Sigma^- p \to \Sigma^0 n)}{\sigma_t(\Sigma^- p \to \Sigma^0 n) + \sigma_t(\Sigma^- p \to \Lambda n)} \tag{5.14}$$

with s representing the singlet even ${}^1S_0$ and t is for triplet even ${}^3S_1$ partial wave. Following the standard procedure, we calculated the capture ratio at $p_{lab} = 10$ MeV/c, close enough to rest, and obtained a value of 0.25. This is 50% less compared to the experimental value of 0.47 [76] and 0.474 [77]. This dissimilarity in magnitude is expected due to the error coming from $\Sigma^- p \to \Lambda n$ of our model. One may argue why it can not reproduce a good value even when the parameters determined are effective in nature with a good fit. The point to mention is that data points that were fitted were below $\Lambda N - \Sigma N$ threshold, hence can not be expected to overcome by mere parameter values the tensor force effect owing to that coupling.

In Fig. 5.32, various particle basis $\Sigma N - \Sigma N$ channel cross sections are shown. We have seen that the uncoupled ΣN particle basis channels do not differ from each other. On the other hand, all the channels here belong to CC systems. The isospin

transformed potentials for these channels are

$$V_{\Sigma^0 n\to\Sigma^0 n} = \frac{1}{3}V_{\Sigma\Sigma}^{\frac{1}{2}} + \frac{2}{3}V_{\Sigma\Sigma}^{\frac{3}{2}} \tag{5.15}$$

$$V_{\Sigma^+ n\to\Sigma^+ n} = \frac{2}{3}V_{\Sigma\Sigma}^{\frac{1}{2}} + \frac{1}{3}V_{\Sigma\Sigma}^{\frac{3}{2}} \tag{5.16}$$

$$V_{\Sigma^0 p\to\Sigma^+ n} = \frac{\sqrt{2}[V_{\Sigma\Sigma}^{\frac{3}{2}} - V_{\Sigma\Sigma}^{\frac{1}{2}}]}{2} \tag{5.17}$$

which are clearly different. As a consequence, cross sections differ as in Fig 5.32.

The LE parameters of the CC particle basis channels are shown in Table 5.11. The scattering length for all along on-shell present ΛN system in particle basis channels are similar to the isospin basis values ≈ -1.5 fm. The channel mixing is observed to influence the ΣN sector, as expected. For two particle basis CC systems, the LE parameters for ΣN channels are different, coming from different interaction potential, pointed out in Eq. 5.17.

System	Channel	a_s[fm]	r_e[fm]
Q=0	$\Lambda n \to \Lambda n$	-1.50	2.17
	$\Sigma^0 n \to \Sigma^0 n$	-1.24	3.28
	$\Sigma^- p \to \Sigma^- p$	0.87	-14.25
Q=1	$\Lambda p \to \Lambda p$	-1.49	2.28
	$\Sigma^+ n \to \Sigma^+ n$	0.79	5.98
	$\Sigma^0 p \to \Sigma^0 np$	-1.29	7.02

Table 5.11: Low-energy parameters for CC particle basis channels.

5.3.3 S = -2 Results

We calculated the uncoupled $\Sigma\Sigma$ channels for S = -2 only at present, leaving the complicated multi-channels for future applications. Similar to S = -1, there are two particle basis channels, $\Sigma^+\Sigma^+$ and $\Sigma^-\Sigma^-$ for one isopin basis channel $\Sigma\Sigma$ with I = 2. Calculated phase shifts for $\Sigma^+\Sigma^+$ and $\Sigma^-\Sigma^-$ are shown in Fig. 5.33. Belonging to same isospin group, the phase shifts are obviously obtained as identical.

The cross sections for $\Sigma^+\Sigma^+$ is shown in Fig. 5.34. Due to lack of experimental data, for comparison purpose, we have shown the χEFT result. We can notice that the shape of the two results are similar, both predicting repulsion, except the

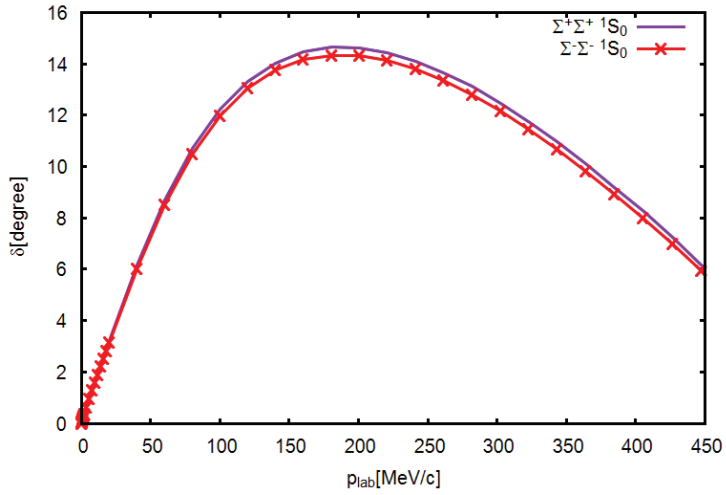

Figure 5.33: $^1S_0$ Phase shift for Σ^+ -Σ^+ and Σ^- -Σ^- channel for S = -2.

difference in magnitude.

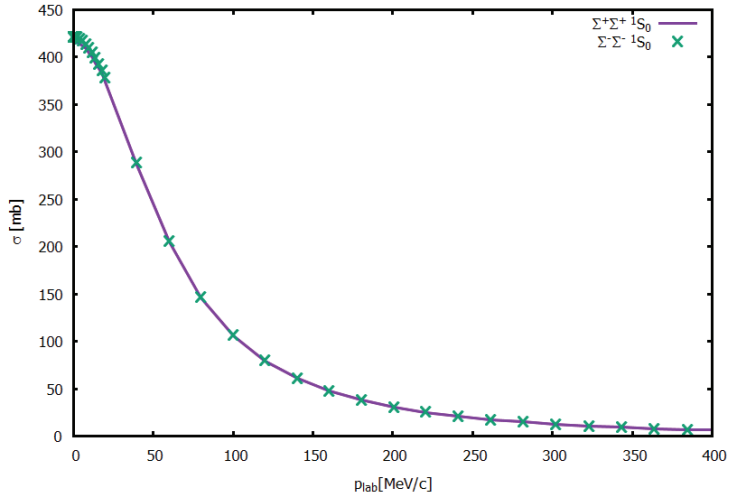

Figure 5.34: $^1S_0$ $\Sigma^+\Sigma^+$ and Σ^- -Σ^- integrated cross sections as a function of lab momenta.

The Nijmegen group investigated about the $\Sigma^+\Sigma^+$ channel and has shown that inclusion of Coulomb changes the interaction significantly [49].

The corresponding scattering lengths for the channels are listed in Table 5.12 predicting repulsion similar to the order of ΣN however with a higher effective range, ours being similar in order to χLO, as also in S = -1. Obviously, the LE parameters for Σ^+ Σ^+ and $\Sigma^-\Sigma^-$ are similar.

Channel	Model	$a_s(fm)$	$r_s(fm)$
$\Sigma^+\Sigma^+$	χLO[106]	-6.23	2.17
	Our Model	-5.75	1.94
$\Sigma^-\Sigma^-$	***Our Model***	-5.79	1.92

Table 5.12: $\Sigma^+\Sigma^+$ and $\Sigma^-\Sigma^-$ scattering length and effective range parameters for $^1S_0$ partial wave.

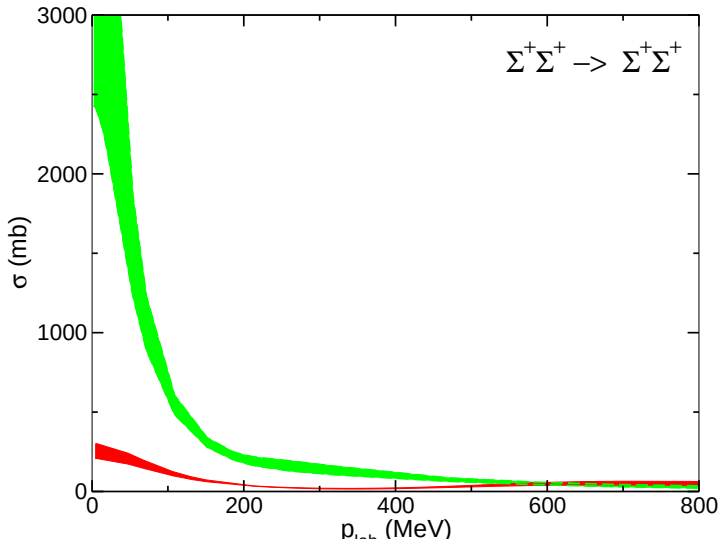

Figure 5.35: Σ^+ Σ^+ integrated cross section calculation by χEFT group. Figure taken from [102].

5.4 Dependence of the LE Parameters on the Coupling Constants

One interesting theoretical investigation we did as a side aspect is to see how the scattering length, i.e. the interaction, of different channels depend on the scalar and vector coupling constant. The result is shown in Fig. 5.36 for vector octet coupling constant and Fig. 5.37 for scalar octet coupling constant. The vector coupling is seen to be more crucial for Σ^+p and $\Lambda\Lambda$ (S = -2) channels, showing a steeper plot for the range of 1-1.2 of g_v^8. While the S = -2 uncoupled $\Sigma^+\Sigma^+$ channel found to be less sensitive over the change of vector octet coupling constant.

For the scalar coupling, both S = -1, -2 Σ channels are showing much less sensitivity compared to the $\Lambda\Lambda$ channel, for which the dependency is much stronger, as evident from Fig. 5.37. Thus, we conclude that it will be meaningful to explore

which baryon-baryon scattering system could possibly serve as a filter for particular interaction channels.

5.5 Summary of Free Space Interaction

Although our hyperon-interaction model is constructed with an impressively low $\frac{\chi^2}{data}$ value of 0.42, it is important to realize this is not a trivial task to obtain such a good fit simultaneously for $\Lambda p \to \Lambda p$, $\Sigma^+ p \to \Sigma^+ p$ channels with a good reproduction of $\Sigma^- p \to \Sigma^0 n$ and $\Sigma^- p \to \Sigma^- p$ data set with large statistical errors involved. Even a high end source fitting code like MINUIT [103] produce initialization dependent parameter values due to the physical differences between the channels and large error bars which is not sufficient to fix the parameter sets at partial wave level.

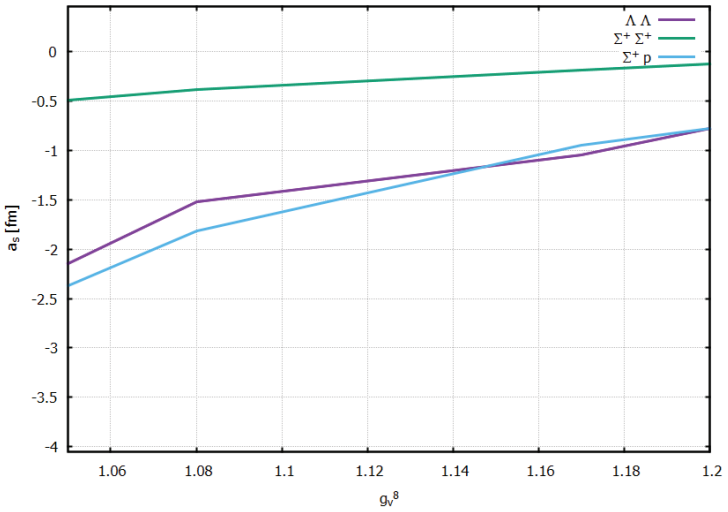

Figure 5.36: Variation of various S = -1, -2 channel scattering length with vector octet coupling constant.

With this being the case, we did a prior check of setting a good initialization for the problem. Reducing the number of free parameters was also one of our major goal. As discussed in Section 1, in this version of meson-exchange hyperon model, we have significantly reduced the free parameter numbers by prior investigation about their effects on the interaction. The three parameter sets we have presented are equally good having slightly different properties on a more detailed level as the incomplete and limited data set can not unambiguously determine hyperon interaction. We

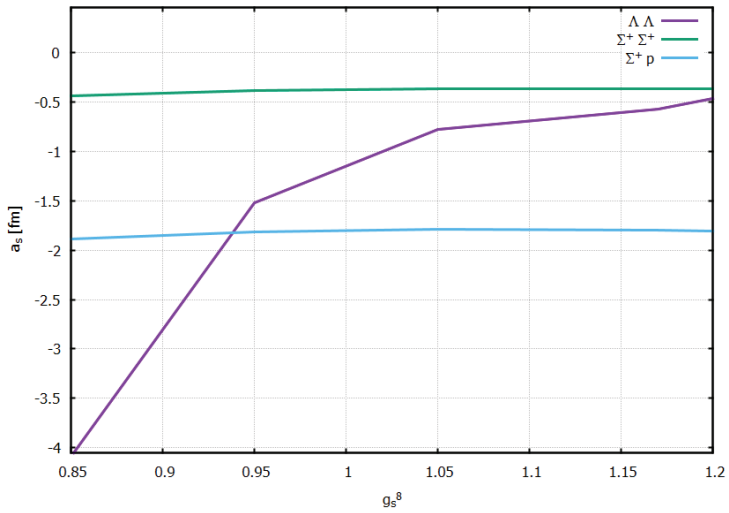

Figure 5.37: Variation of various S = -1, -2 channel scattering length with vector octet coupling constant.

choose to stick to the MINUIT migrad evaluated set of values because of the less error involved emphasizing the point that this values do not need to be modified for different channels and strangeness.

The factor that caused to have such a good fit is mainly because for Σ^+p channel the contribution of $^3S_1$ and higher partial waves are negligible, $^1S_0$ being the most dominant contributor. The resonance of $^1P_1$ partial wave at higher energies is already confirmed by previous investigations [79]. Hence a model with fit parameters for $^1S_0$ Σ^+p channel has been proven to be sufficient to obtain realistic results for other channels too. Another point to note here is the quoted experimental cross sections could not take into account the large Coulomb contribution at forward angles, thus adding another factor to obtain a good fit.

Concerning Λp channel, the tensor coupling did not affect much in obtaining a good fit as the region of data points was below ΣN threshold. For p_{lab} less than ΣN threshold, the tensor coupling coming from $^3S_1$-$^3D_1$ partial wave insignificantly influence the cross sections coming from $^1S_0$ that dominates the low-energy region. The cusp effect occurring due to $\Lambda N - \Sigma N$ channel coupling has been observed in phase shift scale. To see this effect on cross section scale, the $^3S_1$ contribution is mandatory, as found by other groups [48, 49]. However, since the cusp occurs over a very small momentum range, as can be seen in Fig. 5.21, it is very hard to

detect without high precision detection technology experimentally. Moreover, the large error bars coming form the old bubble -chamber data can not identify any cusp effect. All in all, the major constraint at this stage is non-inclusion of partial wave coupling specially $^3S_1$ -$^3D_1$ that is necessary to have a good reproduction of $\Sigma^- p \to \Sigma^- p$ data points.

One point to note here is that most of our results are similar to χLO results. Although the framework is different, still this qualitative agreement of the results is a good concluding point about the quality of our version. The χLO also considers one-meson exchange forces for their long-range part, similar to ours. For the short-range interactions, the EFT contact terms are fitted to data, equivalent to the three free parameters in our case. Unlike other meson exchange models, both our model and χLO are not including SU(3) breaking effects. With this being the similarity and dissimilarities, obtaining results in the same direction is giving confidence in the use of SU(3) symmetry constraints for hyperon interaction.

All things considered, constructing a reliable and predictive hyperon model for complete baryon octet as a whole is a non-trivial task. Many other groups are still trying to construct a single set parameter model covering the complete SU(3) octet. Our model being an effective one, the conclusiveness of the derived results is naturally much dependent on the quality of the input data which is not of a quality yet for stringent constraints. Within these limitations, we have been able to construct a new version of hyperon interaction describing interactions in free space to a satisfactory level.

The main characteristic of our model compared to other meson-exchange ones are that we have a **single parameter set** well- constrained by SU(3) (except the physical mass values) that is applicable to complete BB interaction without any modification [129–132]. The results obtained by such a model is useful to give an idea about the extent up to which SU(3) is still well-maintained. The good quality results for S = -1 channels and uncoupled S = -2 channel, we have presented here, implies that SU(3) is a 'good' symmetry for the strangeness sector. The model is constructed in a way that allow to add SU(3) breaking effects if necessary to obtain better reproduction of data for any channel under investigation. Concerning the

non-inclusion of higher partial waves and partial wave couplings, the basic physics of the interaction is not dependent on the number of partial waves included except improving the quantity of the observables which for this kind of low-energy dominant interactions, can be effectively reproduced by a lower order wave, as has been done in our case, aiming for a qualitative study. On the other hand, remembering our main interest on having a working model to study in-medium properties, we did not spend more effort on improving the quantitative feature of our model at the present time.

To sum up, we have been able to build a realistic model for hyperon-baryon interaction that can reproduce the free-space interaction in a reliable and qualitative manner. Being a model based on SU(3) flavor symmetry, this in principle is applicable for the whole strangeness sector without any modification for qualitative studies. There exists some discrepancies over the magnitude of some channel interactions, which, keeping in mind the large uncertainty coming from the errors, can be overlooked at this stage for our purpose of building the model: to apply medium effect on the vacuum behavior. Thus, we will impose medium effect on our vacuum results to investigate about the in-medium properties in next Chapter.

Chapter 6

In-Medium Effect

"Sometimes attaining the deepest familiarity with a question is our best substitute for actually having the answer."

Brian Greene

Infinite nuclear matter is a rich laboratory for investigation of many body baryon-baryon interaction. For diverse theoretical study ranging from few-body calculation, hyper-nuclear structure to equation of state of exotic neutron star, hyperon stars, many body interaction is unavoidable. On the experimental front, for heavy ion experiments involving hyperons, there is a good dense background present, which calls for taking into account the medium interaction to the bare one. In this Chapter we will investigate how presence of nuclear medium affects the free space result obtained in last chapter. In Section 1, theoretical description for studying medium effect microscopically on bare interaction is described. In-medium Bethe Golstone and Pauli projector operator is described in detail on this context. Section 2 is devoted in describing hyperon mean field. In Section 3, in medium effect on free space phase shift and cross section is presented. In Section 4 discussing medium effect on low energy parameters. A comparative study on medium effect and OBE parameter effect is presented in Section 5 finally summarizing the findings in Section 6.

6.1 Baryon-Baryon Interaction in Infinite Nuclear Matter

Having a good quality vacuum interaction model covering the complete SU(3) sector in hand, the in-medium scattering can now be described incorporating the bare potential in a microscopic calculation of dense matter. The framework we will follow here is to solve the Bethe-Goldstone equation, discussed in next section in more detail.

6.1.1 In-Medium Bethe-Goldstone Equation

The basic idea of the Bethe Goldstone equation is based on Pauli blocking. In addition, correlation between single particle energies are also taken into account in the presence of a dense medium. The Bethe-Goldstone equation is readily achieved on R-matrix level (equivalently for T-matrix) by multiplying the Green's function by the Pauli projector operator (Q_F) (Eq. 6.2). The in-medium coupled channel Bethe-Goldstone scattering equation in momentum space representation and after a partial wave decomposition, is expressed as,

$$\begin{aligned} R_{AB}(\mathbf{q}',\mathbf{q}) &= V_{AB}(\mathbf{q}',\mathbf{q}) \\ &\quad + \sum_C \int \frac{dkk^2}{2\pi}\, V_{AC}(\mathbf{q}',\mathbf{k})\; Q_F(k,k_{F_C})\; G_C(\mathbf{q}',\mathbf{k})\; R_{CB}(\mathbf{k},\mathbf{q}) \end{aligned} \tag{6.1}$$

where A and B represents the interacting channels with C as the intermediate one with $\mathbf{q}'$, $\mathbf{q}$, $\mathbf{k}$ representing final, initial and intermediate relative momenta. The medium effect is determined by the function Q_F, defined by,

$$Q_F = \Theta(k_1 - k_{F_1})\Theta(k_1 - k_{F_2}). \tag{6.2}$$

where $k_{F_{1,2}}$ are the nucleon Fermi momentum. This is a step function of nucleon Fermi momentum (in our case) k_F with the Pauli exclusion principle inherited in mathematical formulation. The Bethe-Goldstone equation is also known as G-matrix calculations.

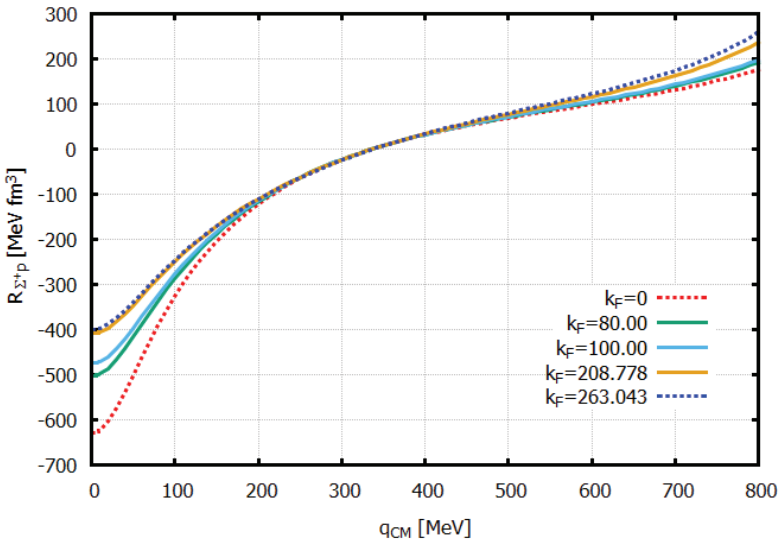

Figure 6.1: R matrix of $\Sigma^+ p \to \Sigma^+ p$ channel as a function of initial relative center-of-mass momentum at different nucleon Fermi momentum.

For nuclear matter calculations, nucleon density is more familiar quantity. The nucleon saturation density (ρ_{sat}) is at 0.16 fm^{-3}, a special region of interest in nuclear matter investigations. The Fermi momentum is related to the medium density, ρ, as

$$\rho(k_F) = \frac{k_F^3}{3\pi^2} \tag{6.3}$$

$$k_F(\rho) = \sqrt[3]{3\pi^2\rho} \tag{6.4}$$

In this Chapter we present the results in terms of k_F, Q_F being a function of this. On the other hand, for convenience of interpretation result, we will frequently present the results in terms of nuclear density. In the following Table the corresponding values are listed for few nucleon densities. For symmetric nuclear matter, proton

Density(ρ)	Fermi Momentum (k_F) fm^{-3}¿fm^{-3} [MeV/c]
0.08	208.778
0.16	263.043
0.32	417.555
0.64	526.086

Table 6.1: Values of Fermi momentum for corresponding nucleon total densities.

density and neutron density is equal, thus $\rho_p = \rho_n = \frac{\rho_{tot}}{2}$.

In Fig. 6.1, R-matrix at different nucleon Fermi momentum is plotted for $\Sigma^+ p$ interaction. The bare interaction ($k_F = 0$) is shown by the red curve and blue dotted one for symmetric nuclear matter saturation density. With increasing medium density (i.e. k_F), the R-matrix is observed to decrease. However, interesting to note that over an incident center-of-mass momentum range of $\approx$ 250-400 MeV/c, the R-matrix is independent of the medium density. Perhaps for this range of momentum, the final scattering states are always above Fermi sea, irrespective of the nucleon Fermi momentum, a special point to keep in mind of course. The system

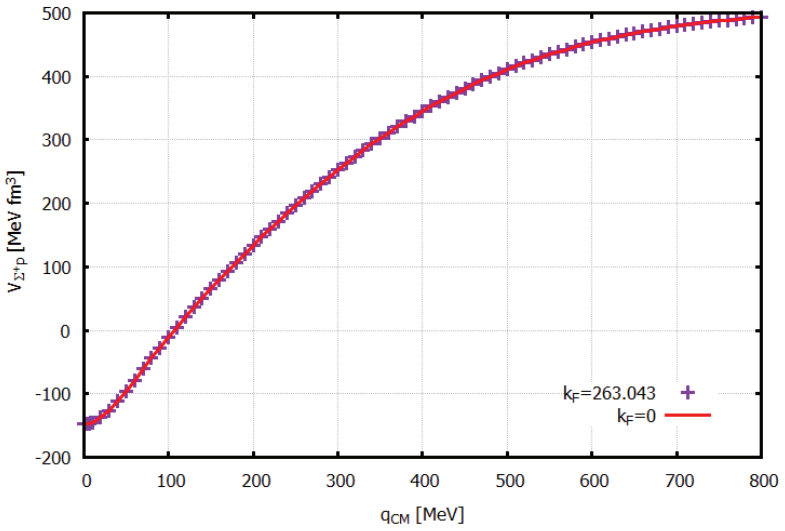

Figure 6.2: Bare and nuclear matter $\Sigma^+ p \to \Sigma^+ p$ OBE potential as a function of initial center-of-mass (relative) momentum.

does not get affected by any background for this range. Moreover, beyond this range the system again experiences medium influence as can be seen by the separation of R-matrix elements for different k_F. Although clear form Eq. 6.1, still to illustrate, we have plotted the bare and nuclear matter potential for this channel, which are same.

6.1.2 Pauli Projector Operator

The Pauli operator being the governing factor for the investigation of nuclear-medium effect, it is better to have more understanding about its properties. The Pauli exclusion principle for fermion states that two identical fermions can not oc-

cupy state with same quantum numbers, fulfilling the anti-symmetric condition under particle exchange for fermions. Keeping in mind that baryons are fermions, multiplying the Green function with Q_F is imposing Pauli principle to the scattering process besides the strong interaction symmetries. This makes sure each final scattering states (k_1, k_2) are outside already blocked Fermi sphere of nucleon Fermi momentum $k_{F_{1,2}}$. The number of step functions in Pauli projector definition correspond to each particle present in the medium. For the symmetric nuclear matter case, we have both Q_{F_p} and Q_{F_n} and for infinite neutron matter, we will have, Q_{F_n} or Q_{F_p}, and going back to free space for $Q_F = 1$. Thus, the Pauli projector can be thought of as following the particle motions during the whole scattering process to prevent scattering on occupied momentum states.

6.1.3 Transformation to Center-of-Mass Frame

We solve the scattering equation in momentum space and in center-of-mass frame, hence we need to rewrite the Pauli projector accordingly, as a function of total energy and relative momentum ($\mathbf{k}$). Following [60], we rewrite the relation between laboratory and center-of-mass momentum via x_i as

$$\mathbf{k_1} = \mathbf{k} + x_2\mathbf{P}, \quad \mathbf{k_2} = -\mathbf{k} + x_1\mathbf{P} \tag{6.5}$$

where $\mathbf{k}$ is the three-momenta component of a purely space-like relative momentum that is orthogonal to $\mathbf{P}$, total conserved center-of-mass momentum of the scattering defined as

$$\mathbf{P} = \mathbf{k_1} + \mathbf{k_2} = \mathbf{k'_1} + \mathbf{k'_2} \tag{6.6}$$

$$k = x_1\mathbf{k_1} - x_2\mathbf{k_2} \tag{6.7}$$

Here k is constructed by taking Lorentz invariant weight x_i satisfying

$$x_1 + x_2 = 1 \tag{6.8}$$

$$x_1\mathbf{k_1^0} - x_2\mathbf{k_2^0} = 0 \tag{6.9}$$

$$\rightarrow x_{1,2} = \frac{k^0_{1,2}}{P_0} \tag{6.10}$$

For 3D reduced Bethe-Salpeter equation P_0 is chosen to be the total energy to maintain symmetric on(off)-shell condition. Since in particular we are solving the T-matrix equation with on-shell condition, P_0 is set to $\sqrt{s}$, thus fixing the weights to [60, 82],

$$x_1 = \frac{1}{2}(\frac{M_2^2 - M_1^2}{s}) + 1, \qquad x_2 = \frac{1}{2}(\frac{M_1^2 - M_2^2}{s}) + 1 \tag{6.11}$$

with s being the s-mandelstam variable. For center-of-mass frame this implies that physical particles in asymptotic on-shell states. The appropriate conversion relations being introduced, now we can rewrite Q_F in center-of-mass frame in a covariant way, skipping the intermediate steps, worked out in [60],

$$Q_F = \Theta(k^2 + x_2^2P^2 - k_{F_1}^2 + 2x_2kP\cos\beta) \;\; \Theta(k^2 + x_1^2P^2 - k_{F_2}^2 + 2x_1kP\cos\beta) \tag{6.12}$$

We introduce a new quantity $Z_{1,2}$ defined as

$$Z_1 = \cos\beta_1 = \frac{k^2 + x_2^2P^2 - k_{F_1}^2}{2x_2Pk}; \quad Z_2 = \cos\beta_2 = \frac{k^2 + x_1^2P^2 - k_{F_2}^2}{2x_1Pk} \tag{6.13}$$

to simplify Eq. 6.12 into the following form

$$Q_F = \Theta(Z_1 - \cos\beta) \;\; \Theta(Z_2 - \cos\beta) \tag{6.14}$$

The angle β represents the angular dependence of the baryon propagators. To satisfy both $Z_{1,2} \geq \cos\beta$ simultaneously, the conditions are $k \geq x_1P + k_{F_1}$ and $k \geq x_2P + k_{F_2}$. On the other hand, for $k^2 < k_{F_1}^2 - x_1^2P^2$ or $k^2 < k_{F_2}^2 - x_2^2P^2$, both the inequalities are not satisfied simultaneously. These altogether set the following restriction on angle β,

$$\cos\beta > -Z_1 \equiv -\cos\beta_1 \tag{6.15}$$

$$\cos\beta < Z_1 \equiv \cos\beta_2 \tag{6.16}$$

The definition of Pauli projector now reads

$$\begin{aligned} Q_F &= 1, \quad if \quad k \geq \max[x_1 P + k_{F_1}, x_2 P + k_{F_2}] && (6.17) \\ &= 0, \quad if \quad k^2 < \max[k_{F_1}^2 - x_1^2 P^2, k_{F_2}^2 - x_2^2 P^2] && (6.18) \\ &= \min \ [\cos\beta_1, \cos\beta_2], \quad \text{otherwise} && (6.19) \end{aligned}$$

Since we solve the scattering equation in partial wave decomposition, it is convenient to use angular averaged Pauli projector $(Q_F(k,P))$, to avoid the mixing between the partial waves due to this additional angular dependence introduced by Pauli operator.

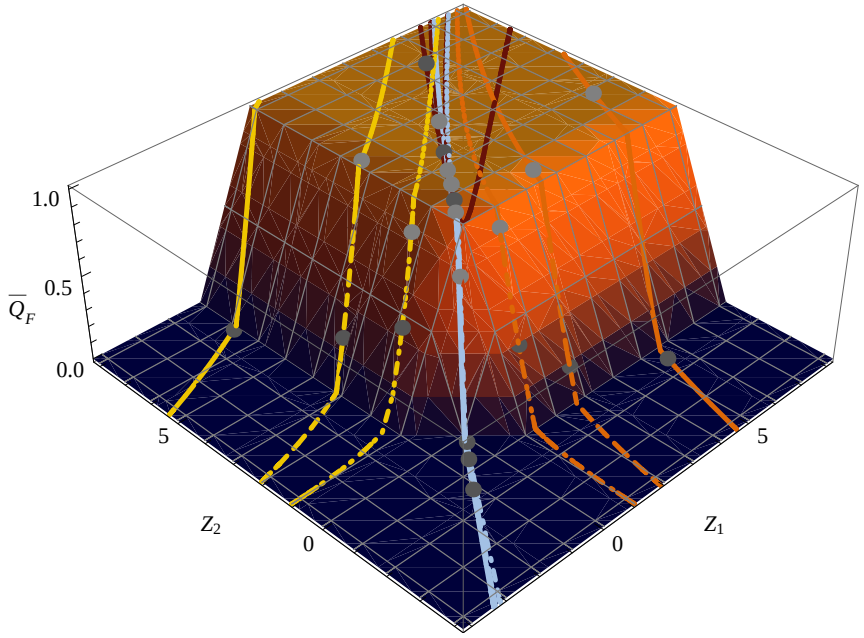

Figure 6.3: $Q_F(k,P)$ is plotted as function of Z_i, Figure taken from [82].

Hence, for a partial wave decomposed R-matrix equation, the angle-averaged Pauli projector is a better input. The angular average is obtained by integrating over a unit sphere [83], given as, integrating the angle $\beta(s,\mathbf{q})$ over,

$$\begin{aligned} Q_F(k,P) &= \frac{1}{4\pi}\int Q_F d\Omega \\ &= \frac{1}{2}\int_{-1}^{1} Q_F \ d\cos\beta \\ &= \frac{1}{2}\Theta(Z_1+Z_2)\Theta(1+Z_1)\Theta(1+Z_2) \end{aligned}$$

$$[2\Theta(-1+Z_1)\Theta(1+Z_2)+(1+Z_2)\Theta(1+Z_1)\Theta(1-Z_2)$$
$$+ \quad (Z_1+Z_2)\Theta(1-Z_1)+\Theta(1-Z_1)\Theta(-1+Z_2)] \tag{6.20}$$

In Fig. 6.3, taken from [82], $Q_F(k,P)$ is plotted as function of Z_i. This is basically showing the step function feature now in a four dimensional plane. For different set of $k_{F_{1,2}}$, $Q_F(k,P)$ has different patterns, crossing each other in the Z-planes shown in Fig. 6.4 [82]. More detailed discussion about Pauli projector operator dependence on it's arguments can be found at [60, 82].

The angle averaged Pauli projector has a straight forward density dependence incorporated as given by [93],

$$\begin{aligned} Q_F(k,P,k_F) &\approx 1-\frac{k_F^2}{kP}+\mathcal{O}(k_F^4) \\ &= 1-(3\pi^2)^{\frac{2}{3}}\frac{\rho^{\frac{2}{3}}}{kP}+\mathcal{O}(\rho^{\frac{4}{3}}) \end{aligned} \tag{6.21}$$

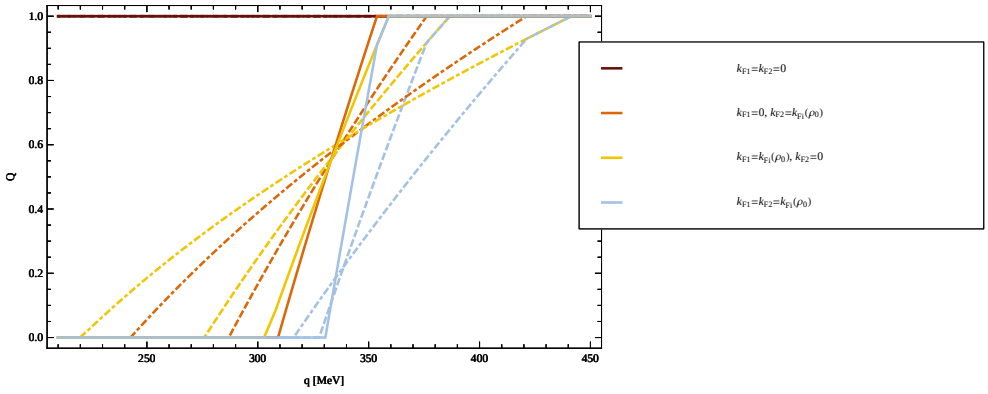

Figure 6.4: $Q_F(k,P)$ is plotted as function of Z_i, Figure taken from [82].

where we have used Eq. 6.5 in last line of Eq. 6.21. Thus the Pauli projector dominantly affects the low-density behavior of the in-medium interaction. The density dependence feature of the medium influences the self-energies of the particles as well, giving rise to medium-modified self-energies and effective masses. Thus, medium-effect introduced here can as well be used to study the self-energy modification, not considered in this work.

6.2 Hyperon Mean Fields

The Bethe-Goldstone equation defines the R (and T) matrix in partial wave representation, often referred to as the singlet-triplet or even-odd formalism. For nuclear matter calculations, the spin-isospin is a more convenient representation related by an orthogonal transformation to the partial wave one. This results into for each isospin doublet for N, Ξ, and Λ, or for Σ -isotriplet with proper isospin factor $\tau_B \to T_\Sigma$, the following R-matrix formulation

$$\begin{aligned} R^{AB}(\xi, k_F) &= \sum_{S,I=0,1} R^{AB}_{SI}(\xi, k_F) \left(\sigma_A \cdot \sigma_B\right)^S \left(\tau_A \cdot \tau_B\right)^I \\ &+ \sum_{I=0,1} \left(R^{AB}_{LI}(\xi, k_F)\mathbf{L}\cdot\mathbf{S} + R^{AB}_{TI}(\xi, k_F)\mathbf{S_{12}}\right)\left(\tau_A \cdot \tau_B\right)^I \end{aligned} \tag{6.22}$$

along with spin-orbit and rank-2 tensor terms. Here the amplitudes are functions of either in momentum space ($\xi = \{\mathbf{k_1}, \mathbf{k_2}\}$) or in coordinate space ($\xi = \{\mathbf{r_1}, \mathbf{r_2}\}$) in cases where static potential picture is an acceptable approximation which can get canceled from other contributions. With this now we can define the hyperon- mean fields in a single-hyperon spin-saturated nucleus as

$$U^{YA} = U^{YA}_0 + U^{YA}_{L0}\ell_Y \cdot \sigma_Y + \left(U^{YA}_1 + U^{YA}_{L1}\ell_Y \cdot \sigma_Y\right)\tau^0_Y \tag{6.23}$$

where $U^{YA}_{0,1}(\rho_{0,1})$ are the central isoscalar and isovector potentials, obtained from isoscalar and isovector nuclear densities, $\rho_{0,1} = \rho_n \pm \rho_p$, respectively. Spin-orbit mean-field expressions are defined in similar manner. Particular case of interest is infinite nuclear matter where hyperon potentials are mainly determined by the singlet and triplet scattering lengths. For example, for Λ hyperon, in infinite nuclear matter, the R-matrix can be expressed in terms of singlet and triplet spin-projectors $P_{1,3}$ and the $N\Lambda$ reduced mass $\mu_{N\Lambda}$ as given below

$$R_{\Lambda N}(q, k_F) \simeq \frac{4\pi\hbar^2}{2\mu_{N\Lambda}}\left\{a^{SE}_{\Lambda N}(k_F)P_1 + a^{TE}_{\Lambda N}(k_F)P_3\right\} \tag{6.24}$$

Therefore the nuclear matter hyperon potential becomes

$$U_\Lambda(\rho) = \frac{4\pi\hbar^2}{2\mu_{N\Lambda}}\left(\frac{1}{4}a^{SE}_{\Lambda N}(\rho) + \frac{3}{4}a^{TE}_{\Lambda N}(\rho)\right)\rho_N, \tag{6.25}$$

for a total nucleon density ρ. Determination of the in-medium singlet and triplet scattering lengths therefore will give information about the nuclear matter potential.

6.3 In-medium Phase Shift and Cross Section

First we discuss the effect of background nuclear medium on phase shift and cross sections of various BB scattering channels. In this Chapter we refer to the effect of background nuclear medium with density ρ_{sat} : k_F = 263.043 MeV/c as nuclear matter, and half saturation density as 'half nuclear matter' with k_F = 208.778 MeV/c. With this terminology, various phase shift and cross sections of BB channels are shown from Fig. 6.5 to Fig. 6.17.

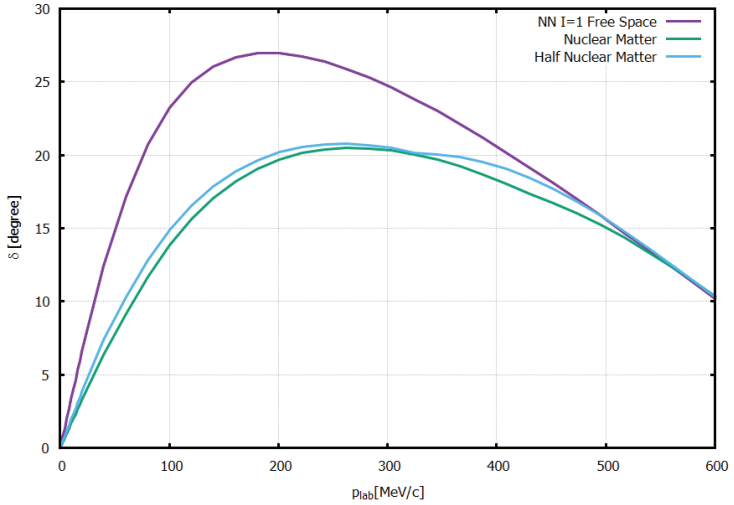

Figure 6.5: Theoretical NN phase shift in nuclear saturation density (ρ_{sat}) and half nuclear saturation density $\frac{\rho_{sat}}{2}$ as a function of laboratory momenta.

In- Medium Effect on Uncoupled Channels: Consider the uncoupled channels from S = 0 to S = -2: NN, ΣN, and $\Sigma^+\Sigma^+$. The effect of the nuclear medium being similar to the channels ranging from S = 0 to S = -2, we describe the effect collectively. In Fig. 6.5, the medium effect on our model calculated free space NN $^1S_0$ phase shift is shown. The medium effect appears as a decreasing factor in phase shift and cross section 6.5. Regarding the two nuclear densities, the difference is small in phase shifts, a bit more in cross section scale up to 100 MeV for S = 0 and S = -1 uncoupled channels, and coinciding beyond. For S = -2 uncoupled channel, even in cross section scale, the nuclear matter and half nuclear matter are completely

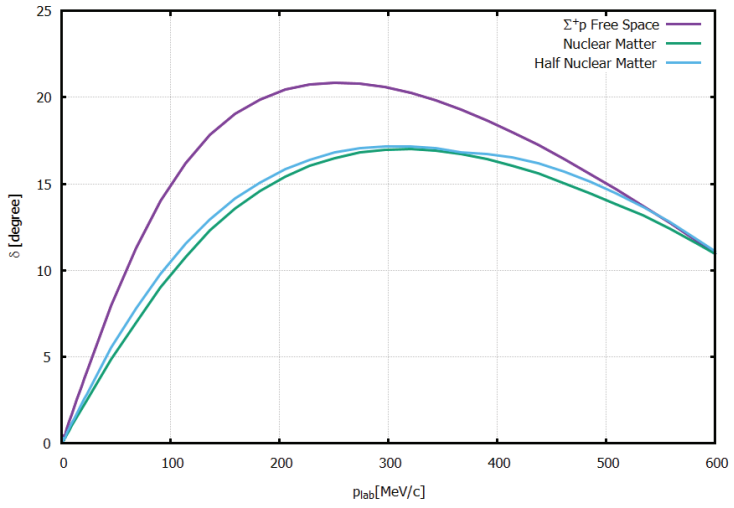

Figure 6.6: In-medium $^1S_0$ phase shift for Σ^+p is shown in nuclear saturation density (ρ_{sat}) and half nuclear saturation density $\frac{\rho_{sat}}{2}$ as a function of laboratory momenta.

indistinguishable (Fig. 6.9). A magnified look only is revealing a difference between the two results (Fig. 6.10).

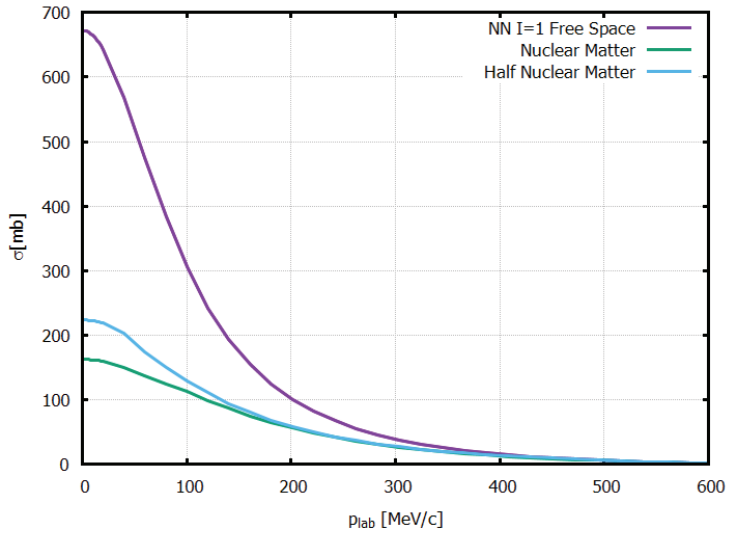

Figure 6.7: NN cross section as a function of nucleon lab momenta for different nucleon density.

The phase shift and cross section of the other uncoupled channels for S = -1 ($\Sigma^- n$), -2 ($\Sigma^-\Sigma^-$) being identical, are not shown explicitly. In summary, the vacuum interaction weakens due to Pauli-blocking and other medium effect, observed as a general phenomenon for the T-matrices in all octet channels.

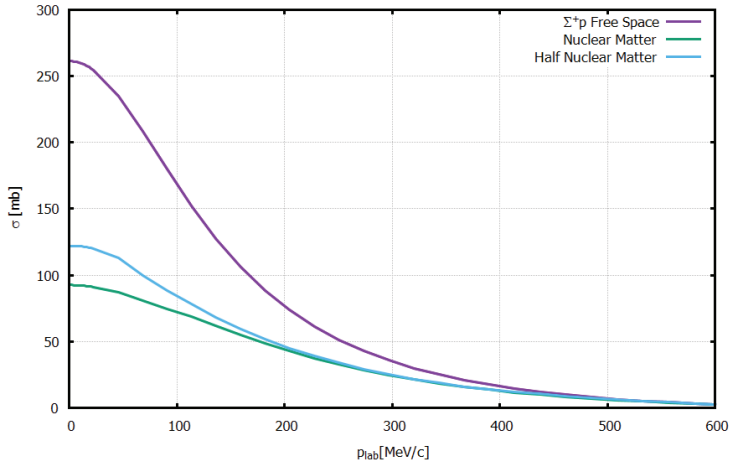

Figure 6.8: Theoretical integrated $\Sigma^+ p$ cross section for nuclear saturation density and half saturation density as a function of lab momenta.

In-Medium Effect on Coupled Channels: Talking about the effect of medium on the CC vacuum interaction, there is, of course decreasing effect in phase shift and cross section, in addition the medium effects the channel mixing. Considering the CC $\Lambda p \to \Sigma^+ n$ system, in Fig. 6.11, the medium is seen to affect the cusp. The

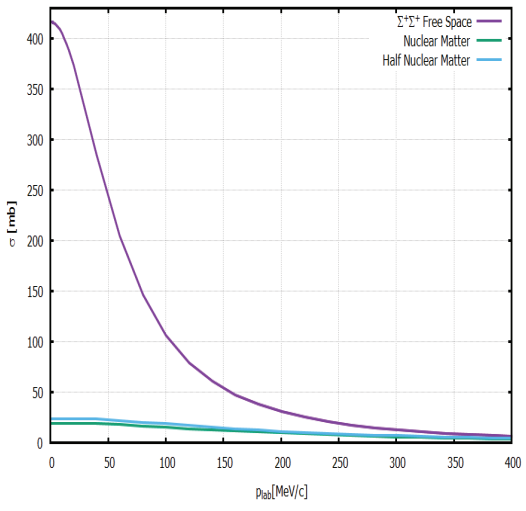

Figure 6.9: $\Sigma^+\Sigma^+$ $^1S_0$ phase shift at zero, nuclear matter, and half nuclear matter shown as a function of laboratory momentum.

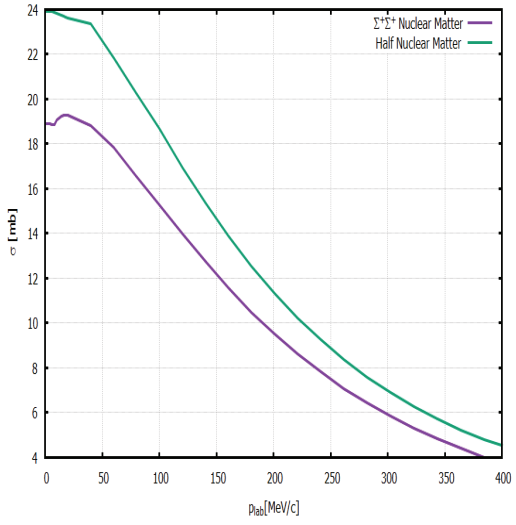

Figure 6.10: $\Sigma^+\Sigma^+$ $^1S_0$ phase shift at nuclear matter, and half nuclear matter shown as a function of laboratory momentum.

cusp is less pronounced in nuclear matter. This implies that the channel opening gets suppressed by the medium. This is more prominent when seen in terms of the mixing angle (Fig. 6.12), where the mixing is seen to be affected by the medium.

Point to note is that since the magnitude of the mixing angle for $^1S_0$ partial wave is pretty less, the difference between vacuum and medium effect compared to the scale, is pretty strong.

Similar to the $\Lambda N \to \Sigma N$ coupled problem, the medium affects the $\Sigma N \to \Sigma N$ CC channels available in the particle basis, in equivalent way (see Fig. 6.13 and 6.14).

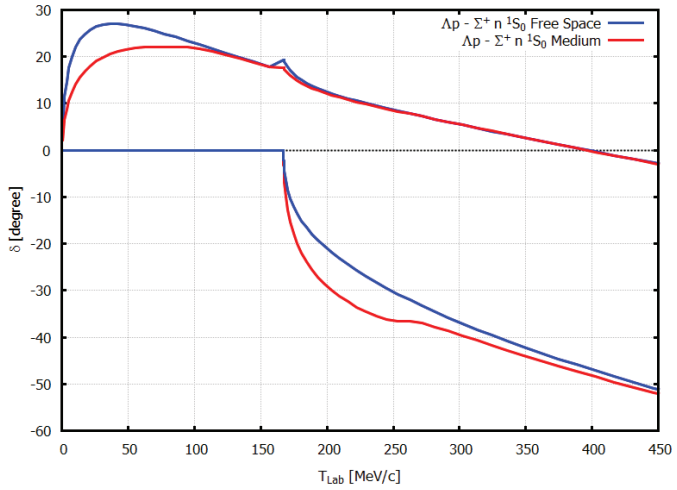

Figure 6.11: $\Lambda p \to \Sigma^+ n$ $^1S_0$ phase shift CC in vacuum and nuclear matter shown as a function of laboratory kinetic energy (T_{lab}) in MeV/c.

In terms of cross section for the CC channels, the magnitude is decreased significantly, pointing towards a weaker strength at low energies, as shown in Figures 6.15,

Fig. 6.16 and 6.15, the effect of nuclear medium is shown for CC $\Sigma^- p \to \Sigma^0 n$ and $\Sigma^- p \to \Sigma^- p$ channels respectively. In both of these Figures, the vacuum cross section (violet) is decreased by a factor of 10. The nuclear matter and half nuclear matter cross sections are almost on top of each other for both as can be seen. Fig. 6.17 is a magnified version of Figure 6.16 to understand the difference between nuclear matter and half nuclear matter results for $\Sigma^- p \to \Sigma^0 n$, as an equivalent case for the other $\Sigma^- p \to \Sigma^- p$. Thus, on there exists a small deviation between the nuclear matter and half nuclear matter results that is can not be understood for in large scale. Nevertheless, similar decreasing feature of cross sections found for uncoupled channels is observed for the coupled channels too. We did not show

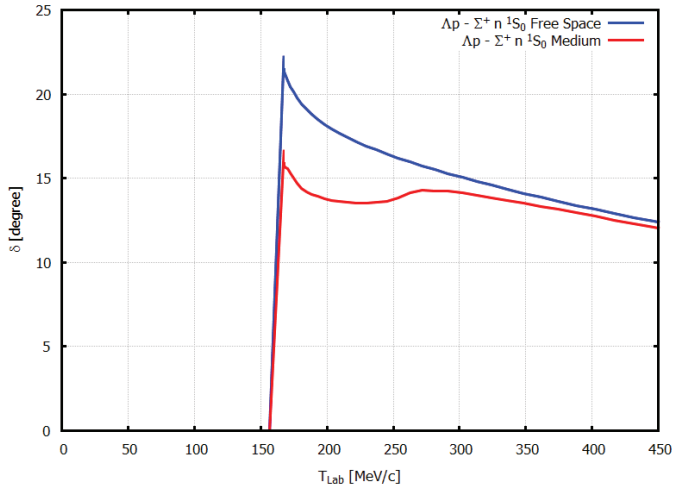

Figure 6.12: $\Lambda p \to \Sigma^+ n$ mixing in vacuum and nuclear matter shown as a function of laboratory kinetic energy (T_{lab}) in MeV/c.

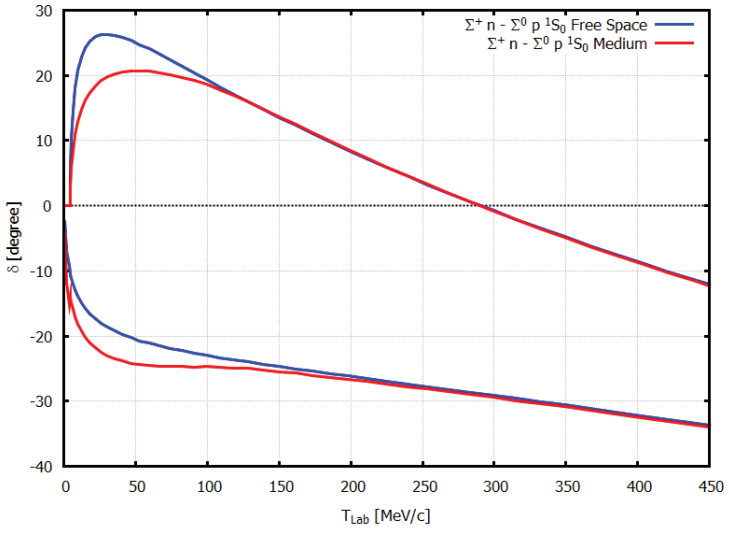

Figure 6.13: $\Sigma^- p \to \Sigma^0 n$ $^1S_0$ eigen phase shifts in vacuum and nuclear matter shown as a function of laboratory kinetic energy (T_{lab}) in MeV/c.

the off-diagonal CC channel elements, $\Lambda N \rightarrow \Sigma N$ here. Those, being very small in magnitude already for vacuum case, is diminished to vanishing amplitude in medium, hence skipped.

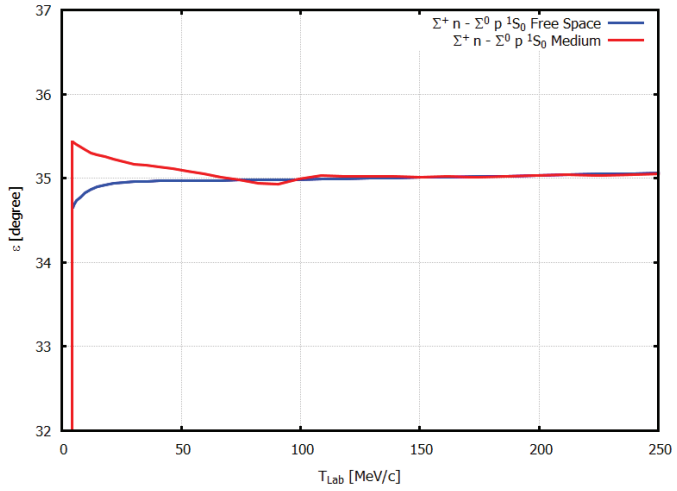

Figure 6.14: $\Sigma^- p \rightarrow \Sigma^0 n$ mixing in vacuum and nuclear matter shown as a function of laboratory kinetic energy (T_{lab}) in MeV/c.

To conclude, the nuclear medium is playing significant role in altering the vacuum hyperon interaction, seen here as weakening effect.

6.4 In-medium Low-Energy Parameters

The effect of medium is easy to interpret when described in terms of the LE parameters. The values of LE parameters in vacuum and nuclear saturation density for S = 0, -1, and -2 channels are listed in Table 6.2. The vacuum scattering lengths observed to change by about 50% for S= 0, -1 sector whereas for S = -2 the change is near about 80%, implying a stronger medium effect on higher strangeness channels that was not prominent enough from previous section results.

In Fig. 6.18, NN (I= 1) and $\Sigma^+ p$ scattering lengths are plotted against the nucleon Fermi momentum, k_F (MeV/c). These reveal the density dependence feature of the interaction. As density increases, the scattering length starts changing, with a steep slope in the range of 30-70 MeV/c of k_F, attaining a saturation value at nuclear saturation. Physically this means as the system is put inside more condensed background, the saturation is achieved, where as in low-density region, the medium

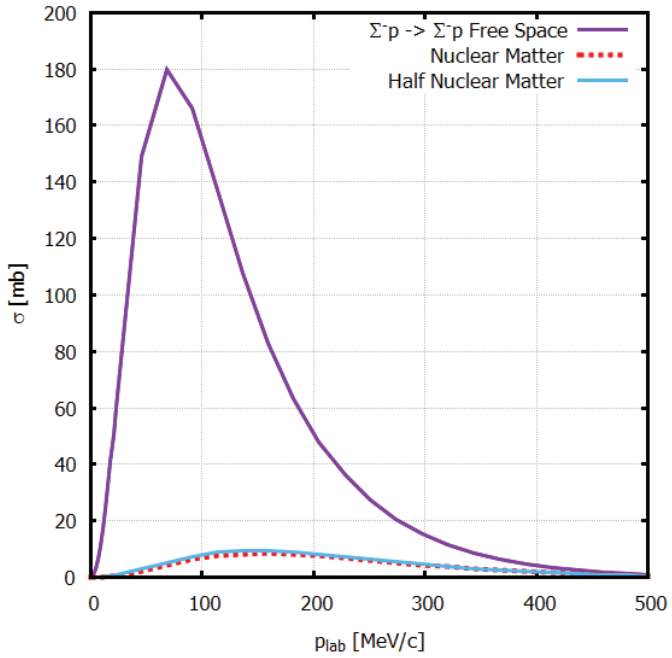

Figure 6.15: In-medium cross section for $\Sigma^- p \to \Sigma^- p$ coupled channel at saturation density and half saturation density.

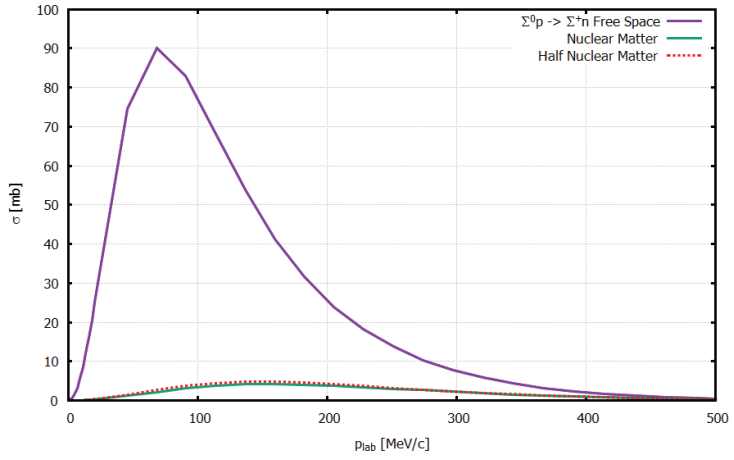

Figure 6.16: $\Sigma^- p \to \Sigma^0 n$ $^1S_0$ vacuum cross section affected by nuclear medium.

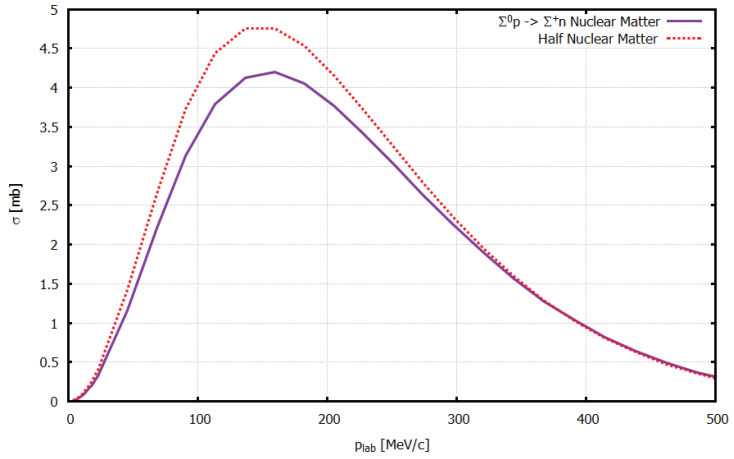

Figure 6.17: $\Sigma^- p \to \Sigma^0 n\ ^1S_0$ integrated cross section affected by nuclear matter saturation, and half nuclear matter saturation density as a function of laboratory momentum.

Channel	Free Space		Nuclear Saturation	
	$a_s(fm)$	$r_s(fm)$	$a_s(fm)$	$r_s(fm)$
NN(I=1)	-2.31	5.26	-1.14	5.80
$\Lambda n \to \Lambda n$	-1.50	2.34	-0.76	2.01
$\Sigma^+ p$	-1.44	5.18	-0.86	5.34
$\Sigma^0 n \to \Sigma^0 n$	-1.24	3.28	-0.637	2.12
$\Sigma^- p \to \Sigma^- p$	0.87	-14.25	0.68	-6.20
$\Lambda p \to \Lambda p$	-1.49	2.28	-0.74	2.52
$\Sigma^+ n \to \Sigma^+ n$	0.79	5.98	1.59	-1.35
$\Sigma^0 p \to \Sigma^0 p$	-1.29	7.02	-0.64	2.51
$\Sigma^+\ \Sigma^+$	-5.75	1.94	-1.23	2.78
$\Sigma^-\ \Sigma^-$	-5.79	1.92	-1.23	2.78

Table 6.2: Low-energy parameters of different baryon channels in free space and nuclear matter.

effect is found to be dominant. This satisfies the expected behavior as predicted by Eq. 6.21, as Pauli projector is incorporating the medium effect in the system. In Fig. 6.19, NN (I=1), Λn, $\Sigma^+ p$, and $\Sigma^+\Sigma^+$ scattering lengths are plotted as a function of nucleon Fermi momentum. The Figure points towards the sensitivity channels to medium density dependence. The slope of the scattering length curves are different, depending on the density dependent nature of the channel.

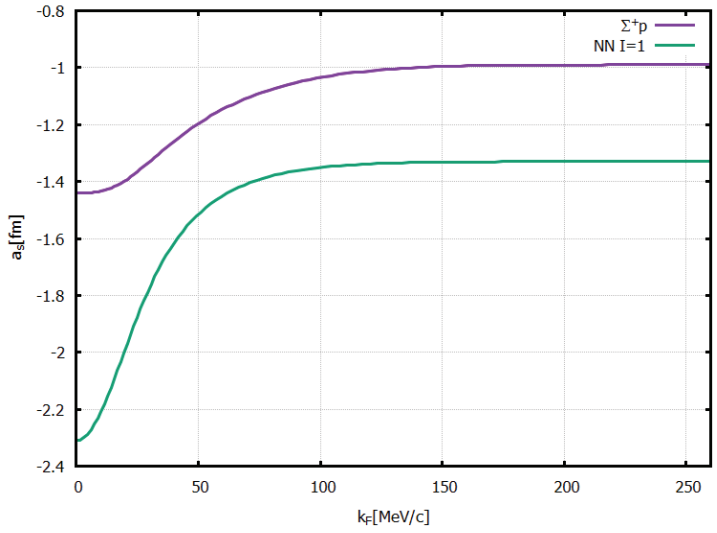

Figure 6.18: Variation of S=0 NN (I=1) and $\Sigma^+ p$ scattering length with nucleon Fermi momentum.

The density dependence of the effective range parameter for the channels under discussion, are shown in Fig. 6.21 and 6.20. Unlike the scattering length, the effective range is found not to have low-density predominance effect. For all the channels, from S = 0 to -2, the effective range parameter varies with density in all the channels in an equivalent manner, given by constant slope all over the density region, as shown in Fig. 6.20. In the Λn channel, the effective range is seen to gradually decrease with increasing density, thus indicating a reduction of the momentum dependence in nuclear matter.

One point we would like to mention here, for k_F values around 40-70 MeV/c, the numerical artifact for more or less all coupled channels in our calculation were found to be large occurring the low-energy expansion sub-routine. In particular for effective range parameter values were found fluctuating on ranges of 10^4 for some cases. For this huge instability of values, more sophisticated effective range routine

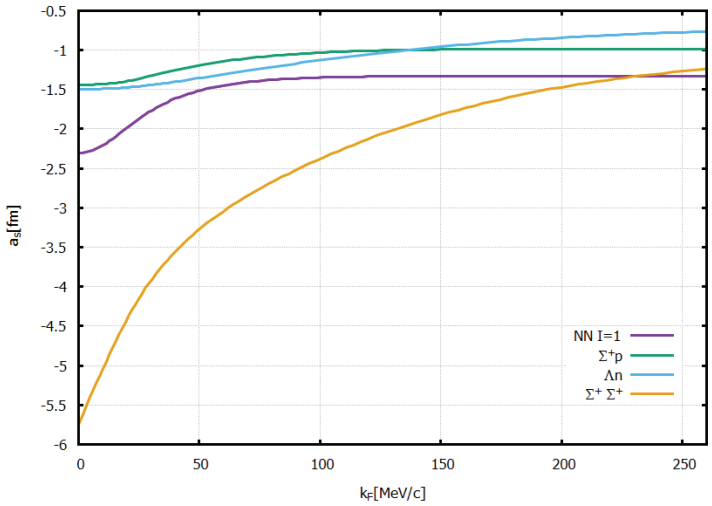

Figure 6.19: Variation of NN (I=1), Σ^+p, Λn, and $\Sigma^+\Sigma^+$ channel scattering length with nucleon Fermi momentum. Different strangeness channels showing different density dependence with a similar trend of reaching a a constant value as approaching the saturation point.

can evaluate a more accurate value, or remove the artifact completely. Nevertheless, this sudden instability may point to something turbulent going on to the system that needs further investigation before making concluding remarks. For the time being, we skipped values for this range in the low-energy plots presented here.

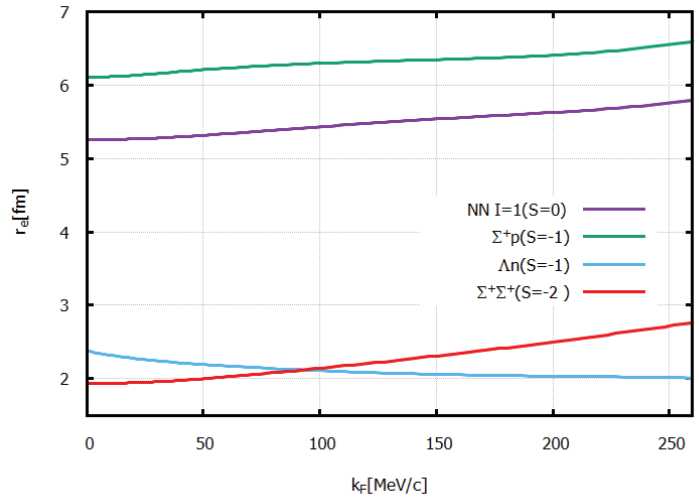

Figure 6.20: Variation of NN (I=1), Σ^+p, Λn, and $\Sigma^+\Sigma^+$ channel effective range with nucleon Fermi momentum.

6.5 Medium Effect vs. Parameter Variation

In Chapter 5 we have discussed how different parameters our OBE model effects differently the "hyperon interaction in terms of phase shift variation. On the other hand, here we have found out that the medium decreases the phase shift. Observing both, it is interesting to see how these differ from each other as far as hyperon interaction is concerned.

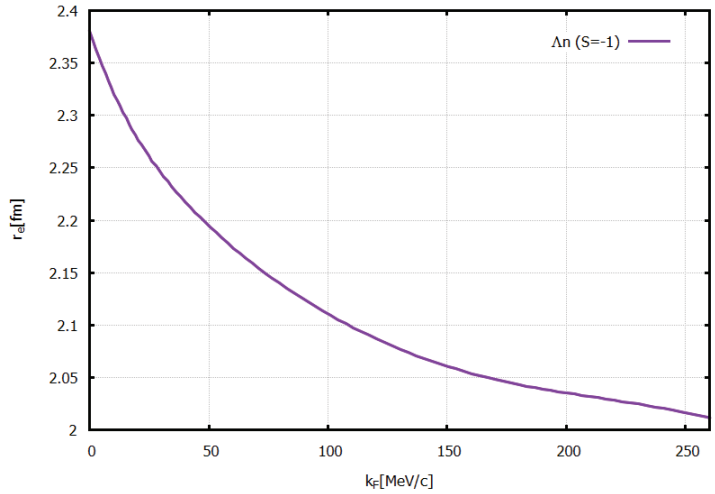

Figure 6.21: Variation of Λn effective range with nucleon Fermi momentum.

To understand the difference we have studied the effect of nuclear matter on parameter variation plots. The plots we will show here, are calculated with arbitrary model parameter values, not with the χ^2 evaluated set and also not the exact ones shown on Section 1 of Chap. 5, but similar. In Fig. 6.22, 6.23, and 6.24, the red dotted curve corresponds to nuclear matter phase shifts. In all of the Figures, we can see the qualitative difference between the effect of medium and over the effect of variation of parameters. In Fig. 6.22 representing scalar octet coupling constant (g_s^8) variation, the medium affects complete interaction region, where as by virtue, the scalar mesons are responsible for intermediate region interaction. Fig. 6.24 shows the same kind of effect for ϵ cut- off mass Λ_ϵ. Here also the medium effect is quality wise different form that cut-off mass dependence of the interaction. Thus, the medium properties can not be replicated by changing the parameter values, both being responsible for different physics involved. A bit of equivalent effect is

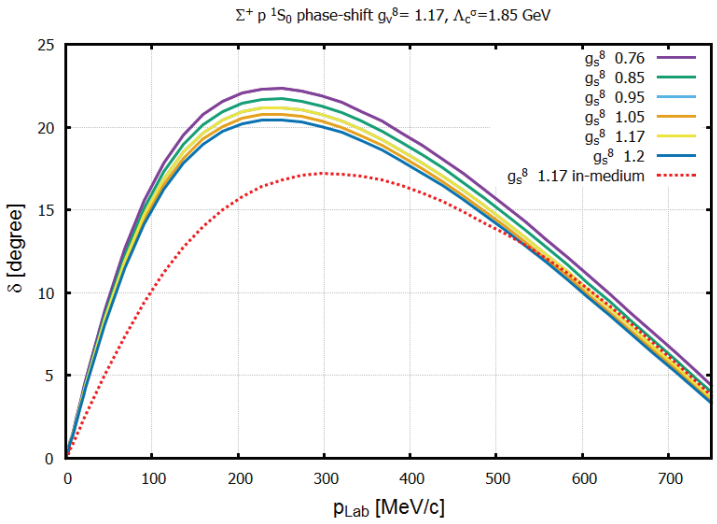

Figure 6.22: Difference between medium effect and scalar octet coupling constant (g_s^8) parameter dependence on hyperon interaction channel shown for $\Sigma^+ p$ phase shift for $^1S_0$ as a function of laboratory momentum.

observed for vector coupling variation as shown in Fig. 6.23, although not 100% equivalent. This is because both medium and vector mesons are affecting the low-energy interaction region predominantly, hence the effect on the interaction is in line.

These comparisons confirm the need of a relevant medium effect framework in order to investigate medium properties, as even for an effective interaction, the effective set of parameters alone can not reproduce the medium properties.

6.6 Conclusion

Our investigation on in-medium properties via Pauli projector operator on the vacuum hyperon-baryon interaction revealed the special density dependent nature of the octet interaction. With available consistent realistic bare interaction model valid for all SU(3) octet baryons, we have been able to find the medium properties microscopically [130, 131]. We have found out that the density dependence of the interaction is also a channel characteristics, some channel are more affected by the nuclear medium than others.

The low-density medium has a stronger influence on the medium than high dense part. We have found out the scattering length and effective ranges are showing

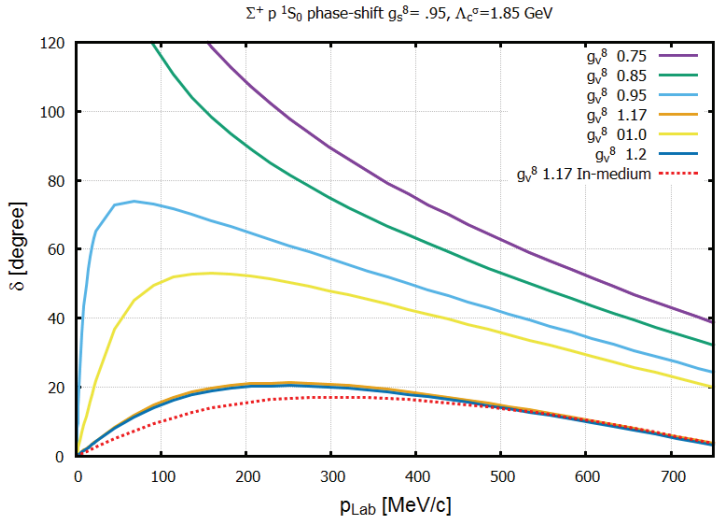

Figure 6.23: Difference between medium effect and vector octet coupling constant (g_v^8) parameter dependence on hyperon interaction channel shown for $\Sigma^+ p$ phase shift for $^1S_0$ as a function of laboratory momentum.

different sensitivity towards density of the medium. Another interesting fact was the saturation of scattering length while the density approaches the saturation value.

From observables to LE parameters, the medium is found to play a crucial role. In our investigations we have found a special instability of the low-energy parameters for nucleon Fermi momentum values between 40-70 MeV/c specially for coupled channels. Whether this is originating from some numerical artifact or hidden physics, that needs further thorough investigation. If a channels has a bound state in the physical region already for bare interaction, (for example, $\Lambda p \to \Lambda p$ interaction reported by earlier Jülich model [46, 47] had a bound state near physical threshold), in presence of medium this can approach towards more lower energy region, causing instability to the result. Since experimentally no such bound states has been observed, we tried to avoid that by sufficient checks also not to influence our medium results. However, since we do not have any other constraints apart form scattering data for our bare interaction, the χ^2 fit parameter may originate some unphysical bound state for some channels that in principle then influence our in-medium results.

A very interesting quantity often derived from this kind of G-matrix calculation is the potential in nuclear matter (U_Y). Due to the instability coming from 40-70 MeV/c region, we at this moment did not calculate the nuclear mater potentials.

However, this is in principle possible from our model and the framework. We have

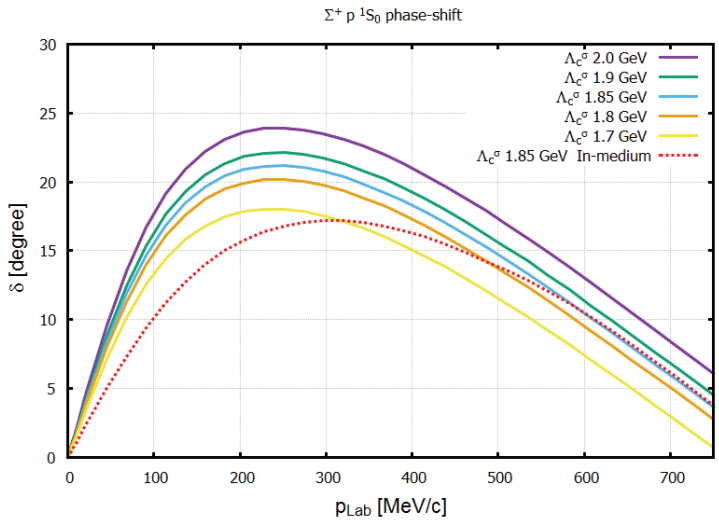

Figure 6.24: Difference between medium effect and vector cut-off mass (Λ_c) parameter dependence on hyperon interaction channel shown for $\Sigma^+ p$ phase shift for $^1S_0$ as a function of laboratory momentum.

solved Bethe-Goldstone equation for symmetric nuclear matter in this thesis. The Bethe-Goldstone equation can also be applied to symmetric as well as asymmetric medium with any number of particles with proper modifications. A particular interesting case would be to extend this for neutron star core calculations with density dependent vertices.

The medium is observed to play an important role in threshold region by hindering the channel opening. In general, for any usual experiments, there is always some background present, that needs to take care of while analyzing the data. Our model, at present, incorporating the nuclear effect, can determine this effect.

We have successfully introduced a revised OBE model for free space baryon interaction, which in turn was used to calculate interactions also in nuclear matter. In either case, the Born series was fully resummed to all orders by deriving the T-matrix from a Lippmann-Schwinger equation. To sum up, we have been investigating in-medium modifications on bare hyperon interaction. Already at low densities the resummed T-matrix interactions are changed considerably. Within the proper framework, our model can be used for hypernuclear structure and neutron star investigations.

Chapter 7

Summary and outlook

"Physicists like to think that all you have to do is say, these are the conditions, now what happens next? "

Richard P. Feynman

For many decades meson exchange picture provided the only conventional picture for nucleon-nucleon interactions, as well as hyperon-baryon interaction, until other alternatives have been discovered. Several authors have successfully extended the nucleon scheme to hyperon via SU(3) flavor symmetry, hence a good reproduction of data with the present model is not surprising.

The revised version of OBE hyperon model presented here is 'renewed' in many aspects [130, 131]. First, we have constrained ourselves to SU(3) flavor symmetry. Second, any fictitious particle like Pomeron by Nijmegen group or effective particle like ω' were not included in our model to reproduce a better agreement with data or additional low-energy attraction. We have only included one-boson-exchange diagrams in our calculation. The mesons considered are only those belonging to SU(3) flavor nonents. Both short and long range contribution are generated by meson-exchange between the baryons. We have shown a very good reproduction of available data set was achieved by our model. With a significant effort, we have been successfully introduced a OBE model with a single parameter set applicable for complete baryon octet. Moreover, a satisfactory reproduction of the date set

that were not fitted with the χ^2 fit parameters was also achieved. The only slight disagreement coming from $\Sigma^- p \rightarrow \Sigma^- p$ data is due to not incorporating tensor-triplet coupling to our model at this stage. In addition we do not have Coulomb interaction included that may affect the results for charged channels. However, the qualitative nature of $\Sigma^- p \rightarrow \Sigma^- p$ cross section was very well reproduced. Both uncoupled and coupled channel calculation results are shown here with a satisfactory level qualitative agreement with other investigations. In particular, the similarity of our results with χLO derived ones, emphasizes the success of our model construction. As of now, up to S = -2, we found SU(3) is well maintained by the baryon octet. Therefore, in future, this model can be well applicable for complete BB octet to obtain theoretical predictions of vacuum interactions.

There are certain points that can improve the quality of our model as a future outlook. First it will be interesting to see how inclusion of higher partial wave in fitting influence the result presented here with singlet even partial wave. To mention, we did a manual check with fitting partial waves up to J = 2 that did not significantly changed our results for $^1S_0$, hence we carried out our calculations with $^1S_0$ fit parameters. Solving the Lippmann-Schwinger equation including partial wave couplings is another possible improvement that may quantitatively improve S = -1 coupled channel results. For charged channels, calculations including Coulomb interaction, usually by Vincent Phatak method by other groups [107], would be interesting to be studied as well.

The in-medium effects on our vacuum interaction are the result of a pure theoretical prediction. We have found in our investigations that the vacuum interactions are modified significantly by the nuclear medium background. T-matrices and correspondingly the cross sections are reduced in magnitude. For coupled channels, the medium was found to influence the channel opening and the threshold behavior. An important in-medium property with far reaching consequences was revealed in terms of the density dependence of scattering lengths and effective range parameters. These results put questions marks on the widely used assumption that free space interactions are a good leading order approximation for nuclear studies. Our G-matrix interactions, obtained by solving the Bethe-Goldstone equation, show

that the incorporation of the Pauli exclusion principle is the major source for in-medium modifications, already affecting the effective interaction significantly at low -densities.

As a future prospectus, the scheme can be readily used to calculate hyperon mean field potential in nuclear matter. The corresponding quantity is important in particular to know at what baryon density hyperons can appear in exotic dense neutron stars. The methodology used here for finding in-medium properties are not applicable to neutron star densities. However, it will be interesting to see, in view of the present 'hyperon puzzle', how our version of hyperon interaction model predicts for neutron star mass value. An useful scheme for this purpose could be the density dependent relativistic field theory (DDRH) [93] keeping in mind the density dependent nature originated by medium on bare interaction as observed here. Our vacuum interaction can be mapped to DDRH to investigate neutron star core that will in turn can be an important step forward towards solving the 'hyperon puzzle'.

Our vacuum model as well as the in-medium results are directly relevant in analyzing various strangeness experiment data ongoing or to be performed in J-PARC (JAPAN), CLAS12 at J-LAB (USA), PANDA (Germany) , KaoS at MAMI (Germany), SUPERFRS at FAIR (Germany) and FINUDA and DAΦNE (Italy).

To conclude, we have successfully investigated the hyperon interaction in both free space and nuclear matter.

Appendices

Appendix A

Coupling Constant Values

Full set of baryon-baryon-meson coupling constants of our model is presented here. All the values are of $\frac{g_{\mathcal{B}\mathcal{B}'\mathcal{M}}}{\sqrt{4\pi}}$ here, where we suppressed the denominator.

Vector Meson Coupling Constants		
$g_{NN\rho}$= 1.1566	$g_{NN\omega} = 3.4698$	$g_{\Lambda NK^*} = -2.0033$
$g_{\Xi\Xi\rho} = 1.1566$	$g_{\Xi\Xi\omega} = 1.1569$	$g_{\Xi\Lambda K^*} = 2.0033$
$g_{\Lambda\Sigma\rho} = 0.00$	$g_{\Sigma\Sigma\omega} = 2.3133$	$g_{\Sigma NK^*} = -1.1566$
$g_{\Sigma\Sigma\rho} = 2.3132$	$g_{\Lambda\Lambda\omega} = 2.3133$	$g_{\Xi\Sigma K^*} = -1.1566$
$f_{NN\rho} = 3.0011$	$f_{NN\omega} = 0.1287$	$f_{\Lambda NK^*} = 1.1390$
$f_{\Xi\Xi\rho} = 1.1566$	$f_{\Xi\Xi\omega} = 1.1569$	$f_{\Xi\Lambda K^*} = 2.0033$
$f_{\Lambda\Sigma\rho} = 0.00$	$f_{\Sigma\Sigma\omega} = 2.3133$	$f_{\Sigma NK^*} = -1.1566$
$f_{\Sigma\Sigma\rho} = 2.3132$	$f_{\Lambda\Lambda\omega} = 2.3133$	$f_{\Xi\Sigma K^*} = -1.1566$
Pseudo-scalar Meson Coupling Constants		
$g_{NN\pi} = 3.795$	$g_{NN\eta} = 0.1913$	$g_{\Lambda NK} = -3.7467$
$g_{\Xi\Xi\pi} = -1.1006$	$g_{\Xi\Xi\eta} = -1.6322$	$g_{\Xi\Lambda K} = 0.9202$
$g_{\Lambda\Sigma\pi} = 2.8264$	$g_{\Sigma\Sigma\eta} = 0.9361$	$g_{\Sigma NK} = 1.1006$
$g_{\Sigma\Sigma\pi} = 2.6944$	$g_{\Lambda\Lambda\eta} = -1.2726$	$g_{\Xi\Sigma K} = -3.7950$
Scalar Meson Coupling Constants		
$g_{NNa_0} = 1.1274$	$g_{NN\epsilon} = 3.5434$	$g_{\Lambda N\kappa} = -2.0725$
$g_{\Xi\Xi a_0} = 1.1349$	$g_{\Xi\Xi\epsilon} = 1.0526$	$g_{\Xi\Lambda\kappa} = 2.0191$
$g_{\Lambda\Sigma a_0} = 0.0534$	$g_{\Sigma\Sigma\epsilon} = 2.3468$	$g_{\Sigma N\kappa} = -1.1349$
$g_{\Sigma\Sigma a_0} = 2.3623$	$g_{\Lambda\Lambda\epsilon} = 2.2817$	$g_{\Xi\Sigma\kappa} = -1.2274$

Appendix B

Partial Wave Potential Matrix Elements

The derived the partial wave potential matrix elements are based on convention used in [106].

Introducing an index η for paruty factor defined as

$$\mathcal{P} = \eta(-)^J \tag{B.1}$$

where $\mathcal{P} = +(-)^J$ contain spin-singlet and triplet-uncoupled states , and $\mathcal{P} = -(-)^J$ contain spin-triplet coupled states. Considering only non-zero matrix elements the elements are given below:

1. *central* $P_1 = 1$:

$$\begin{aligned}(q_f; L'S'J'M'|V^{(1)}P_1|g_i; LSJM) &= 4\pi\,\delta_{J'J}\,\delta_{M'M}\,F_1^{J,\eta}(L'\ S', L\ S)\ , \qquad \text{(B.2)}\\ \text{with}\quad F_1^{J,\eta}(L'\ S', L\ S) &= \delta_{L'L}\,\delta_{S'S}\,V_L^{(1)}(x)\end{aligned}$$

2. *spin-spin* $P_2 = \boldsymbol{\sigma}_1 \cdot \boldsymbol{\sigma}_2$:

$$\begin{aligned}(q_f; L'S'J'M'|V^{(2)}P_2|g_i; LSJM) &= 4\pi\,\delta_{J'J}\,\delta_{M'M}\,F_2^{J,\eta}(L'\ S', L\ S)\ , \qquad \text{(B.3)}\\ \text{with}\quad F_2^{J,\eta}(L'\ S', L\ S) &= \delta_{L'L}\,\delta_{S'S}\,[2S(S+1)-3]\,V_L^{(2)}(x)\end{aligned}$$

3. *tensor* $P_3 = (\boldsymbol{\sigma}_1 \cdot \mathbf{k})(\boldsymbol{\sigma}_2 \cdot \mathbf{k}) - \frac{1}{3}(\boldsymbol{\sigma}_1 \cdot \boldsymbol{\sigma}_2)\mathbf{k}^2$:

$$(q_f; L'S'J'M'|V^{(3)}P_3|g_i; LSJM) = \frac{8\pi}{3}(q_f^2 + g_i^2)\,\delta_{J'J}\,\delta_{M'M}\,F_3^{J,\eta}(i,j)\ , \tag{B.4}$$

where $i = S'$ and $j = S$ for $\eta = +$, respectively $i = L'$ and $j = L$ for $\eta = -$.
(i) triplet uncoupled: $L = L' = J,\ S = S' = 1$

$$F_3^{J,+}(1,1) \ = \ \left[V_J^{(3)} - \frac{1}{2}\sin 2\psi\left(\frac{2J+3}{2J+1}V_{J-1}^{(3)} + \frac{2J-1}{2J+1}V_{J+1}^{(3)}\right)\right] \tag{B.5}$$

(ii) triplet coupled: $L = J \pm 1,\ L' = J \pm 1,\ S = S' = 1$

$$\begin{aligned}
F_3^{J,-}(J-1,J-1) &= \frac{J-1}{2J+1}\ \left[-V_{J-1}^{(3)} + \frac{1}{2}\sin 2\psi\cdot\right. \\
&\quad \left.\times\left\{\frac{2J-3}{2J-1}V_J^{(3)} + \frac{2J+1}{2J-1}V_{J-2}^{(3)}\right\}\right] \\
F_3^{J,-}(J-1,J+1) &= -3\frac{\sqrt{J(J+1)}}{2J+1}\ \left[-\sin 2\psi\ V_J^{(3)} + \right. \\
&\quad \left.+\left(\cos^2\psi V_{J-1}^{(3)} + \sin^2\psi V_{J+1}^{(3)}\right)\right] \\
F_3^{J,-}(J+1,J-1) &= -3\frac{\sqrt{J(J+1)}}{2J+1}\ \left[-\sin 2\psi\ V_J^{(3)} + \right. \\
&\quad \left.+\left(\sin^2\psi V_{J-1}^{(3)} + \cos^2\psi V_{J+1}^{(3)}\right)\right] \\
F_3^{J,-}(J+1,J+1) &= \frac{J+2}{2J+1}\ \left[-V_{J+1}^{(3)} + \frac{1}{2}\sin 2\psi\cdot\right. \\
&\quad \left.\times\left\{\frac{2J+5}{2J+3}V_J^{(3)} + \frac{2J+1}{2J+3}V_{J+2}^{(3)}\right\}\right]
\end{aligned} \tag{B.6}$$

where

$$\cos\psi = \frac{g_i}{\sqrt{q_f^2 + g_i^2}} \quad , \quad \sin\psi = \frac{q_f}{\sqrt{q_f^2 + g_i^2}} \tag{B.7}$$

4. *spin-orbit* $P_4 = \frac{i}{2}(\boldsymbol{\sigma}_1 + \boldsymbol{\sigma}_2) \cdot \mathbf{n}$:

$$(q_f; L'S'J'M'|V^{(4)}P_4|g_i; LSJM) \ = \ 4\pi\, q_f g_i \delta_{J'J}\,\delta_{M'M}\,F_4^{J,\eta}(i,j)\ . \tag{B.8}$$

(i) triplet uncoupled: $L = L' = J,\ S = S' = 1$

$$F_4^{J,+}(1,1) = -\left(V_{J-1}^{(4)} - V_{J+1}^{(4)}\right)/(2J+1) \tag{B.9}$$

(ii) triplet coupled: $L = J \pm 1,\ L' = J \pm 1,\ S = S' = 1$

$$\begin{aligned} F_4^{J,-}(J-1,J-1) &= \frac{(J-1)}{(2J-1)}\left(V_{J-2}^{(4)} - V_J^{(4)}\right) \\ F_4^{J,-}(J+1,J+1) &= -\frac{(J+2)}{(2J+3)}\left(V_J^{(4)} - V_{J+2}^{(4)}\right) \end{aligned} \tag{B.10}$$

5. *antisymmetric spin-orbit* $P_6 = \frac{i}{2}(\boldsymbol{\sigma}_1 - \boldsymbol{\sigma}_2)\cdot\mathbf{n}$:

$$(q_f; L'S'J'M'|V^{(6)}P_6|g_i; LSJM) = 4\pi\, q_f g_i \delta_{J'J}\,\delta_{M'M}\,F_6^{J,\eta}(S',S)\ . \tag{B.11}$$

(i) singlet-triplet uncoupled: $L = L' = J,\ S = 0,\ S' = 1$

$$F_6^{J,+}(1,0) = F_6^{J,+}(0,1) = \frac{\sqrt{J(J+1)}}{2J+1}\left(V_{J-1}^{(6)} - V_{J+1}^{(6)}\right)\ . \tag{B.12}$$

Using these matrix elements, the partial waves for the potentials can be calculated for the pseudo-scalar, the vector,and the scalar meson-exchange potentials. Following [116], henceforth the following short hand notation we will use for the potentials:
(i) $P = (-)^J$:

$$\begin{aligned} V_{0,0}^J &= V^{J,+}(0,0) \quad , \quad V_{0,2}^J = V^{J,+}(0,1) \\ V_{2,0}^J &= V^{J,+}(1,0) \quad , \quad V_{2,2}^J = V^{J,+}(1,1) \end{aligned} \tag{B.13}$$

(ii) $P = -(-)^J$:

$$\begin{aligned} V_{1,1}^J &= V^{J,-}(J-1,J-1) \quad , \quad V_{1,3}^J = V^{J,-}(J-1,J+1) \\ V_{3,1}^J &= V^{J,-}(J+1,J-1) \quad , \quad V_{3,3}^J = V^{J,-}(J+1,J+1) \end{aligned} \tag{B.14}$$

where q_f and q_i are the final and initial momenta. So $V_{0,0}^J = V_{0,0}^J(q_f,q_i)$ etc. Since

rotational invariance implies

$$V^J_{2,0}(q_f, q_i) = V^J_{0,2}(q_i, q_f) \quad , \quad V^J_{3,1}(q_f, q_i) = V^J_{1,3}(q_i, q_f) \tag{B.15}$$

the off-diagonal terms will be mentioned only for the explicit expressions like $V^J_{0,2}(q_f, q_i)$ and $V^J_{1,3}(q_f, q_i)$.

Appendix C

LSJM Representation Operators

In this Appendix, a description about LSJM operators is given following [106] in SYM convention [128]. In the SYM-convention the spherical wave functions in momentum space with quantum numbers J, L, S, is given by

$$\mathcal{Y}^M_{JLS}(\hat{\mathbf{p}}) = i^L \; C^{J\;\;L\;\;S}_{M\;\;m\;\;\mu} Y^L_m(\hat{\mathbf{p}}) \chi^S_\mu \tag{C.1}$$

where χ is the two-nucleon spin wave function. Here the configuration space basic JLS-states are $\mathcal{Y}^M_{JLS}(\hat{\mathbf{r}}) = C^{J\;\;L\;\;S}_{M\;\;m\;\;\mu} Y^L_m(\hat{\mathbf{r}}) \chi^S_\mu$. Transformation to momentum space results in (C.1). Then

$$\begin{aligned}(\mathbf{S}\cdot\hat{\mathbf{p}})\,\mathcal{Y}^M_{JLS}(\hat{\mathbf{p}}) \;\; = \;\; -\sqrt{6}\; i\; (-)^L \Bigg\{ & \sqrt{\frac{L}{2L-1}} \begin{bmatrix} L & S & J \\ 1 & 1 & 0 \\ L-1 & S & J \end{bmatrix} \mathcal{Y}^M_{JL-1S}(\hat{\mathbf{p}}) \\ & + \sqrt{\frac{L+1}{2L+3}} \begin{bmatrix} L & S & J \\ 1 & 1 & 0 \\ L+1 & S & J \end{bmatrix} \mathcal{Y}^M_{JL+1S}(\hat{\mathbf{p}}) \Bigg\}\end{aligned}$$

where the $9j$-symbols differ from [127], formula (6.4.4), in the replacement of the $3j$-symbols by the Clebsch-Gordan coefficients and by leaving out the m_{33}-summation

(see [133]). The calculation will lead to

$$\begin{aligned}
(\mathbf{S}\cdot\hat{\mathbf{p}})\,\mathcal{Y}^M_{JJ-11}(\hat{\mathbf{p}}) &= -i\;a_J\;\mathcal{Y}^M_{JJ1}(\hat{\mathbf{p}}) \\
(\mathbf{S}\cdot\hat{\mathbf{p}})\,\mathcal{Y}^M_{JJ+11}(\hat{\mathbf{p}}) &= \quad i\;b_J\;\mathcal{Y}^M_{JJ1}(\hat{\mathbf{p}}) \\
(\mathbf{S}\cdot\hat{\mathbf{p}})\,\mathcal{Y}^M_{J\;J\;1}(\hat{\mathbf{p}}) &= \quad i\;a_J\;\mathcal{Y}^M_{JJ-11}(\hat{\mathbf{p}}) - i\;b_J\;\mathcal{Y}^M_{JJ+11}(\hat{\mathbf{p}})\;,
\end{aligned} \tag{C.2}$$

where

$$a_J = -\sqrt{\frac{J+1}{2J+1}} \qquad , \qquad b_J = -\sqrt{\frac{J}{2J+1}}\;. \tag{C.3}$$

Using usual ordering of states $L = J-1,\; L = J,\; L = J+1$, the matrix form can be formed as

$$\left(\begin{array}{ccc|c|ccc} L &=& J-1 & & L &=& J-1 \\ & & J & \mathbf{S}\cdot\hat{\mathbf{p}} & & & J \\ & & J+1 & & & & J+1 \end{array}\right) = \left(\begin{array}{ccc} 0 & ia_J & 0 \\ -ia_J & 0 & ib_J \\ 0 & -ib_J & 0 \end{array}\right)\;. \tag{C.4}$$

Similarly, using for $-i(\hat{\mathbf{q}}_f\times\hat{\mathbf{q}}_i)\cdot\mathbf{S}$ for spherical components the formula

$$-\,i(\hat{\mathbf{q}}_f\times\hat{\mathbf{q}}_i)_n = -\frac{4\pi}{3}\sqrt{2}\;C^{111}_{kln}Y^1_k(\hat{\mathbf{q}}_f)Y^1_l(\hat{\mathbf{q}}_i)\;, \tag{C.5}$$

the partial wave matrix elements of the operator can be worked out.

These all together give the partial wave projections for the spin triplet states:

$$(L'1J|V(\mathbf{k}^2)\,(\mathbf{S}\cdot\hat{\mathbf{q}}_i)^2\,|L1J) = 4\pi\left(\begin{array}{ccc} a_J^2V_{J-1} & 0 & -a_Jb_JV_{J-1} \\ 0 & V_J & 0 \\ -a_Jb_JV_{J+1} & 0 & b_J^2V_{J+1} \end{array}\right)$$

$$(L'1J|(\mathbf{S}\cdot\hat{\mathbf{q}}_f)^2V(\mathbf{k}^2)|L1J) = 4\pi\left(\begin{array}{ccc} a_J^2V_{J-1} & 0 & -a_Jb_JV_{J+1} \\ 0 & V_J & 0 \\ -a_Jb_JV_{J-1} & 0 & b_J^2V_{J+1} \end{array}\right)$$

$$(L'1J|(\mathbf{S}\cdot\hat{\mathbf{q}}_f)V(\mathbf{k}^2)(\mathbf{S}\cdot\hat{\mathbf{q}}_i)|L1J) \;=\; 4\pi \begin{pmatrix} a_J^2 V_J & 0 & -a_J b_J V_J \\ 0 & a_J^2 V_{J-1} + b_J^2 V_{J+1} & 0 \\ -a_J b_J V_J & 0 & b_J^2 V_J \end{pmatrix}$$

and

$$(L'1J|-i(\hat{\mathbf{q}}_f\times\hat{\mathbf{q}}_i)\cdot\mathbf{S}\,V(\mathbf{k}^2)|L1J) = \frac{4\pi}{2J+1}\begin{cases} (J-1)\,(V_{J-2}-V_J) & , \quad L=L'=J-1 \\ -\,(V_{J-1}-V_{J+1}) & , \quad L=L'=J \\ -(J+2)\,(V_J-V_{J+2}) & , \quad L=L'=J+1 \end{cases}$$

Considering the identity

$$(\boldsymbol{\sigma}_1\cdot\mathbf{a})(\boldsymbol{\sigma}_2\cdot\mathbf{a}) = 2(\mathbf{S}\cdot\mathbf{a})^2 - \mathbf{a}^2 \;, \tag{C.6}$$

the tensor operator can be written as

$$\begin{aligned} P_3 \;=\; & (\boldsymbol{\sigma}_1\cdot\mathbf{k})(\boldsymbol{\sigma}_2\cdot\mathbf{k}) - \frac{1}{3}(\boldsymbol{\sigma}_1\cdot\boldsymbol{\sigma}_2) = \frac{1}{3}\left[g_i^2\,S_{12}(\hat{\mathbf{q}}_i) + q_f^2\,S_{12}(\hat{\mathbf{q}}_f)\right] \\ & -4\,(\mathbf{S}\cdot\mathbf{q}_f)\,(\mathbf{S}\cdot\mathbf{q}_i) + 2i\,(\mathbf{q}_f\times\mathbf{q}_i)\cdot\mathbf{S} + \frac{4}{3}\,(\mathbf{q}_f\cdot\mathbf{q}_i)\,\mathbf{S}^2 \end{aligned} \tag{C.7}$$

where the momentum-space tensor-operator S_{12} is defined in Eq. 3.52. From the formulas given in this appendix the partial wave projections of the several potential forms of scalar, pseudo-scalar , and vector mesons can be derived in a straightforward manner.

Appendix D

Partial Wave Decomposition of NN

We introduce the following notation for the R- matrix elements in LSJM basis

$$^{L,L'}R_J = \langle L'SJM|R_J|LSJM\rangle \tag{D.1}$$

and the + for L,L'= J+1 and − for L,L'= J-1. The partial wave elements can be obtained from the helicity basis elements by the following unitary transformations [59]

$$^{0}R^J = ^{0}\ R^J \tag{D.2}$$

$$^{1}R^J = ^{1}\ R^J \tag{D.3}$$

$$^{++}R^J = \tfrac{1}{2J+1}[(J+1)^{12}R^J + J\ ^{34}R^J - 2\sqrt{J(J+1)}(^{5}R^J + ^{6}\ R^J)] \tag{D.4}$$

$$^{--}R^J = \tfrac{1}{2J+1}[J^{12}R^J + J\ (J+1)^{34}R^J + 2\sqrt{J(J+1)}(^{5}R^J + ^{6}\ R^J)] \tag{D.5}$$

$$^{+-}R^J = -\tfrac{1}{2J+1}[\sqrt{J(J+1)}(^{12}R^J - ^{34}\ R^J) + 2(J+1)^{5}R^J - 2J\ ^{6}R^J] \tag{D.6}$$

$$^{-+}R^J = -\tfrac{1}{2J+1}[\sqrt{J(J+1)}(^{12}R^J - ^{34}\ R^J) - 2J^{5}R^J - 2(J+1)\ ^{6}R^J] \tag{D.7}$$

According to the transformation, the uncoupled spin singlet $^{0}R^J$ and the corresponding uncoupled spin triplet element $^{1}R^J$ are same in both the representations and in more explicit formulation is given by

$$^{0}R^J(\mathbf{q}',\mathbf{q}\mid E) = ^{0}\ V^J(\mathbf{q}',\mathbf{q}\mid E) + P\sum_i \int \frac{dk}{2\pi^2}\ ^{0}V^J(\mathbf{q}',\mathbf{k_i}\mid E)\ G(\mathbf{k_i},\mathbf{q_i})\ ^{0}R^J(\mathbf{k_i},\mathbf{q}\mid E) \tag{D.8}$$

$$ {}^1R^J(\mathbf{q}',\mathbf{q}\mid E) = {}^1V^J(\mathbf{q}',\mathbf{q}\mid E) + P\sum_i \int \frac{dk}{2\pi^2}\, {}^0V^J(\mathbf{q}',\mathbf{k_i}\mid E)\, G(\mathbf{k_i},\mathbf{q_i})\, {}^1R^J(\mathbf{k_i},\mathbf{q}\mid E) \tag{D.9} $$

For the coupled triplet state the elements are given by

$$ \begin{aligned} {}^{++}R^J(\mathbf{q}',\mathbf{q}\mid E) &= {}^{++}V^J(\mathbf{q}',\mathbf{q}\mid E) + \mathcal{P}\sum_i \int \frac{dk}{2\pi^2} \\ &\quad [{}^{++}V^J(\mathbf{q}',\mathbf{k_i}\mid E)\; G(\mathbf{k_i},\mathbf{q_i})\; {}^{++}R^J(\mathbf{k_i},\mathbf{q}\mid E) + \\ &\quad {}^{+-}V^J(\mathbf{q}',\mathbf{k_i}\mid E)\; G(\mathbf{k_i},\mathbf{q_i})\; {}^{-+}R^J(\mathbf{k_i},\mathbf{q}\mid E)] \end{aligned} \tag{D.10} $$

$$ \begin{aligned} {}^{--}R^J(\mathbf{q}',\mathbf{q}\mid E) &= {}^{--}V^J(\mathbf{q}',\mathbf{q}\mid E) + \mathcal{P}\sum_i \int \frac{dk}{2\pi^2} \\ &\quad [{}^{-+}V^J(\mathbf{q}',\mathbf{k_i}\mid E)\; G(\mathbf{k_i},\mathbf{q_i})\; {}^{+-}R^J(\mathbf{k_i},\mathbf{q}\mid E) + \\ &\quad {}^{--}V^J(\mathbf{q}',\mathbf{k_i}\mid E)\; G(\mathbf{k_i},\mathbf{q_i})\; {}^{--}R^J(\mathbf{k_i},\mathbf{q}\mid E)] \end{aligned} \tag{D.11} $$

$$ \begin{aligned} {}^{-+}R^J(\mathbf{q}',\mathbf{q}\mid E) &= {}^{-+}V^J(\mathbf{q}',\mathbf{q}\mid E) + \mathcal{P}\sum_i \int \frac{dk}{2\pi^2} \\ &\quad [{}^{-+}V^J(\mathbf{q}',\mathbf{k_i}\mid E)\; G(\mathbf{k_i},\mathbf{q_i})\; {}^{-+}R^J(\mathbf{k_i},\mathbf{q}\mid E) + \\ &\quad {}^{--}V^J(\mathbf{q}',\mathbf{k_i}\mid E)\; G(\mathbf{k_i},\mathbf{q_i})\; {}^{-+}R^J(\mathbf{k_i},\mathbf{q}\mid E)] \end{aligned} \tag{D.12} $$

$$ \begin{aligned} {}^{+-}R^J(\mathbf{q}',\mathbf{q}\mid E) &= {}^{+-}V^J(\mathbf{q}',\mathbf{q}\mid E) + \mathcal{P}\sum_i \int \frac{dk}{2\pi^2} \\ &\quad [{}^{++}V^J(\mathbf{q}',\mathbf{k_i}\mid E)\; G(\mathbf{k_i},\mathbf{q_i})\; {}^{+-}R^J(\mathbf{k_i},\mathbf{q}\mid E) + \\ &\quad {}^{+-}V^J(\mathbf{q}',\mathbf{k_i}\mid E)\; G(\mathbf{k_i},\mathbf{q_i})\; {}^{+-}R^J(\mathbf{k_i},\mathbf{q}\mid E)] \end{aligned} \tag{D.13} $$

In operator notation this reads

$$ \begin{pmatrix} {}^{++}R^J & {}^{+-}R^J \\ {}^{-+}R^J & {}^{--}R^J \end{pmatrix} = \begin{pmatrix} {}^{++}V^J & {}^{+-}V^J \\ {}^{-+}V^J & {}^{--}V^J \end{pmatrix} + \begin{pmatrix} {}^{++}V^J & {}^{+-}V^J \\ {}^{-+}V^J & {}^{--}V^J \end{pmatrix} \begin{pmatrix} G & 0 \\ 0 & G \end{pmatrix} \begin{pmatrix} {}^{++}R^J & {}^{+-}R^J \\ {}^{-+}R^J & {}^{--}R^J \end{pmatrix} \tag{D.14} $$

This is the general form that can be written accordingly inserting if necessary the partial wave couplings and flavor coupling.

Appendix E

Helicity State Basis Decomposition

The baryons being a spin-$\frac{1}{2}$ particles, the spin also need to be taken into account. In order to treat the spin accordingly, the helicity basis representation is a convenient method. Here we briefly describe the helicity basis representation used in our numerical calculation, for representation purposes. A more detailed description on the subject can be found in [59]. The helicity H of a particle is defined as in [59]

$$H = \frac{\mathbf{S} \cdot \mathbf{p}}{|\mathbf{S}| \cdot |\mathbf{p}|} \tag{E.1}$$

where S is the spin and p is the momentum of the particle. Physically it implies the projection of spin of the particle to the direction of the momentum, when the spin is parallel to momentum, the helicity is denoted by positive (+) sign and called "right-handed" , where as for anti-parallel motion, it is negative (−) and termed as "left-handed". For a spin-$\frac{1}{2}$ particle, the eigenvalue λ_i of the helicity operator (Eq. E.1) of particle i can have two possible values: $\pm\frac{1}{2}$. In the following, we denote, $\frac{1}{2}$ as + and $-\frac{1}{2}$ as - . The R-matrix equation in helicity basis, after partial wave decomposition for a state with total angular momentum J, is given by,

$$\begin{aligned}
&\langle \lambda_1' \lambda_2' | R^J | \lambda_1 \lambda_2 \rangle \\
&= \langle \lambda_1' \lambda' 2 | V^J | \lambda_1 \lambda_2 \rangle \\
&+ \sum_{h_1 h_2} P \int \frac{k^2 dk}{2\pi^2} \langle \lambda_1' \lambda_2' | V^J | h_1 h_2 \rangle \; G_{12} \; \langle h_1' h_2' | R^J | \lambda_1 \lambda_2 \rangle
\end{aligned} \tag{E.2}$$

The momentum dependence of R is suppressed here. Here the summation is over different helicity states h_i of particle 1 and 2. λ_1', λ_2' are the final and λ_1, λ_2 are the initial helicities of the particles involved in scattering. From now on we represent only the absolute value of the three-momenta denoted as $q = |\mathbf{q}|, q' = |\mathbf{q'}|$,and $k = |\mathbf{k}|$. Here the execution of the angle integration leaves Eq. 4.4 in one-dimensional form with a leading factor of $4\pi k^2$. We now re-write re-introduce the function Green's function G_{12} as G as following,

$$G \ \ (\mathbf{k}, \mathbf{q}) = \frac{2\mu_{12}k^2}{q^2 - \mathbf{k}^2 + i\epsilon} \tag{E.3}$$

and rewrite the above R-matrix equation in helicity basis as

$$\begin{aligned} \langle \lambda_1'\lambda_2'|R^J|\lambda_1\lambda_2\rangle \ &= \ \langle \lambda_1'\lambda_2'|V^J|\lambda_1\lambda_2\rangle \\ &+ \sum_{h_1h_2} \mathcal{P}\int \frac{dk}{2\pi^2}\langle \lambda_1'\lambda_2'|V^J|h_1h_2\rangle \ G \ \langle h_1'h_2'|R^J|\lambda_1\lambda_2\rangle \end{aligned} \tag{E.4}$$

where the k^2 is now not shown explicitly but taken care of of by G. This equation is a coupled integral equation. Ignoring antiparticles following [59] , there are 4X4=16 helicity amplitudes of R^J. Taking into account the conservation principle followed by the strong interaction, namely, parity, total spin, and time reversal, the number of independent amplitudes reduced to only six. Following Machleidt's convention [59], these can be represented as

$$^0R^J = \langle ++|R^J++\rangle - \langle ++|R^J--\rangle \tag{E.5}$$

$$^1R^J = \langle +-|R^J+-\rangle - \langle +-|R^J-+\rangle \tag{E.6}$$

$$^{12}R^J = \langle ++|R^J++\rangle + \langle ++|R^J--\rangle \tag{E.7}$$

$$^{34}R^J = \langle +-|R^J+-\rangle + \langle +-|R^J-+\rangle \tag{E.8}$$

$$^5R^J = \langle ++|R^J+-\rangle \tag{E.9}$$

$$^6R^J = \langle +-|R^J++\rangle \tag{E.10}$$

with $\pm$ representing $\pm\frac{1}{2}$ helicity states. For a more detailed derivation, one can look at [59]. Similar representation exists for the potential matrix elements $\langle \lambda_1'\lambda_2'|V(\mathbf{q}', \mathbf{q}\ |$

$E)|\lambda_1\lambda_2\rangle$. The R-matrix equation now can be solved in this form, however, The hyperon-model derived here is fitted to the partial wave analyzes of the hyperon-baryon scattering data. Hence the integral equation for the scattering amplitude defined above, must be solved in partial wave basis. Here we define the transformation of the integral equation on the plane wave basis of the integral equation to the partial wave basis, commonly referred to as the LSJM basis. In next section, we discuss the relation between these representations.

Bibliography

[1] M. Agniso et al. [FINUDA Collaboration], Nucl. Phys. A 881 (2012) 269.

[2] C. Rappold et al. [HypHI Collaboration], Phys. Lett. B 728 (2014) 543.

[3] C. Rappold et al. [HypHI Collaboration], On the measured lifetime of light hypernuclei ${}^{3}\Lambda_H$ and ${}^{4}\Lambda_H$, Phys. Lett. B 747 (2015) 129.

[4] N. Shah, Y. G. Ma, J. H. Chen and S. Zhang, Production of multistrange hadrons, light nuclei and hypertriton in central Au+Au collisions at $\sqrt{sNN} = 11.5$ and 200 GeV, Phys. Lett. B 754 (2016) 6.

[5] Z. L. She, G. Chen, H. g. Xu, T. t. Zeng and D. k. Li, Properties of light (anti)nuclei and (anti) hypertriton production in Pb-Pb collisions at $\sqrt{sNN} = 2.76$ TeV, [arXiv:1509.06493].

[6] Integrated Publishing, Inc.

[7] Paulo F. Bedaque, Andrew W. Steiner, Hypernuclei and the hyperon problem in neutron stars, Phys. Rev. C 92, 025803 (2015) [arXiv:1412.8686v1];
Y Lim, CH Hyun, K Kwak, CH Lee, Hyperon puzzle of neutron stars with Skyrme force models, Int. J. Mod. Phys. E 24, 1550100 (2015).

[8] M. Danysz, J. Pniewski, Phil. Mag. 44 (1953) 348.

[9] R. Machleidt, K. Holinde and Ch. Elster, The bonn meson-exchange model for the nucleon-nucleon interaction, Phys. Rep. 149, 1 (1987).

[10] W. N. Cottingham, M. Lacombe, B. Loiseau, J. M. Richard and R. Vinhman, Nucleon-Nucleon interaction from pion-nucleon phase-shift analysis, Phys. Rev. D 8, 800 (1973).

[11] V. G. J. Stoks, R. A. M. Klomp, C. P. F. Terheggen, and J. J. de Swart, Construction of high-quality NN potential models, Phys. Rev. C 49 (1994), 2950-2962.

[12] Murray Gell-Mann The Eightfold Way: A Theory of strong interaction symmetry, CTSL-20, TID-12608.

[13] Yuval Ne'eman, Derivation of strong interactions from a gauge invariance, Nucl. Phys. 26 (1961) 222-229.

[14] Murray Gell-Mann, A Schematic Model of Baryons and Mesons , Phys. Lett. 8 (1964) 214-215.

[15] G Zweig, An SU(3) model for strong interaction symmetry and its breaking, Feb 21, 1964, CERN-TH-401.

[16] K.A. Olive et al. (Particle Data Group), Chin. Phys. C, 38, 090001 (2014) and 2015.

[17] NN-online.org, May, 2016.

[18] Samuel S. M. Wong, Introductory Nuclear Physics, Second Edition, Wiley-VCH Verlag GmbH and Co. KGA, Weinheim, 2004.

[19] T. Furumoto, Y. Sakuragi, Y. Yamamoto, Hyperon-nucleus folding potentials in the complex G-matrix approach, Nucl. Phys. A 835, 362 (2010);
Yasuo Yamamoto, Toshio Motoba and Thomas A. Rijken, G-Matrix Approach to Hyperon-Nucleus Systems, Prog. Theor. Phys. Supplement 185 (2010) 72-105.

[20] M Naghdi, Nucleon-nucleon interaction: A typical/concise review, [arXiv:0702078];
R. Machleidt, I. Slaus, *The Nucleon-nucleon interaction*, J. Phys. G 27: R69-R108 (2001) [arXiv:0101056v1].

[21] Anwar Kamal, Nuclear Physics, Springer, United States, 2014.

[22] Peter Ring, Peter Schuck , The Nuclear Many-Body Problem, Springer, 1980.

[23] E. Hiyama, S. Ohnishi, M. Kamimura, Y. Yamamoto, Four-body structure of neutron-rich hypernucleus ${}^{6}\Lambda_{H}$, [arXiv:1304.0317v1].

[24] E. Hiyama, M. Kamimura, T. Motoba, T. Yamada, Y. Yamamoto, $\Lambda - \Sigma$ conversion in based on four-body calculation, Phys. Rev. C 65 (2002) 011301.

[25] Masahiro Isaka, Masaaki Kimura, Akinobu Dote, Akira Ohnishi, Deformation of hypernuclei studied with antisymmetirzed molecular dynamics, Phys.Rev.C83:044323,2011

[26] K. Miyagawa et al., Phys. Rev. C 74, 034002 (2006).

[27] D. Gazda, J. Mares , P. Navratil, R. Roth ,R. Wirth, No-Core Shell Model for Nuclear Systems with Strangeness, Phys. Rev. C 88, 035208 (2013) .[arXiv:1312.0478v1].

[28] J. S. Liang and H. Shen, Medium modifications of baryon properties in nuclear matter and hypernuclei, [arXiv:1304.4713v3].

[29] Y. Yamamoto, T. Furumoto, N. Yasutake, and Th.A. Rijken, Hyperon-mixed neutron star with universal many-body repulsion, [arXiv:1510.06099v1].

[30] R.O. Gomes, V.A. Dexheimer, S. Schramm, C.A.Z. Vasconcellos, Many-body forces in the equation of state of hyperonic matter, [arXiv:1411.4875v1].

[31] I. Vidana, Single-particle spectral function of the Λ hyperon in finite nuclei, [arXiv:1603.05635v1]

[32] Francesca Sammarruca, Effects of Λ hyperons on the nuclear equation of state in a Dirac-Brueckner-Hartree-Fock model, Phys. Rev. C 79 : 034301, 2009

[33] H. Chen, M. Baldo, G. F. Burgio, and H.-J. Schulze, Hybrid stars with the Dyson-Schwinger quark model, [arXiv:1107.2497v2].

[34] E. N. E. van Dalen, G. Colucci, and A. Sedrakian, Phys. Lett. B 734, 383 (2014).

[35] H. Lenske, C. Fuchs, Phys.Lett. B 345 355 (1995)

[36] S. Petschauer, J. Haidenbauer, N. Kaiser, Ulf-G. Meißner, W. Weise, Hyperons in nuclear matter from SU(3) chiral effective field theory, Eur. Phys. J. A (2016) 52: 15

[37] H. Togashi, E. Hiyama, Y. Yamamoto, and M. Takano, Equation of state for neutron stars with hyperons by the variational method, [arXiv:1602.08106].

[38] E E Kolomeitsev, K A Maslov, D N Voskresensky, Hyperon puzzle and the RMF model with scaled hadron masses and coupling constants, [arXiv:1509.06312v1].

[39] K. A. Maslov, E. E. Kolomeitsev and D. N. Voskresensky, Relativistic Mean-Field Models with Scaled Hadron Masses and Couplings: Hyperons and Maximum Neutron Star Mass, [arXiv:1509.02538v2].

[40] Ulf-G. Meißner, Johann Haidenbauer, Foundations of Strangeness Nuclear Physics derived from chiral Effective Field Theory, [arXiv:1603.06429v1].

[41] Diego Lonardoni, Alessandro Lovato, Stefano Gandolfi, and Francesco Pederiva, Hyperon Puzzle: Hints from Quantum Monte Carlo Calculations, Phys. Rev. Lett. 114, 092301 (2015) [arXiv:1407.4448v2].

[42] Tsuyoshi Miyatsu and Myung-Ki Cheoun, Equation of state for neutron stars with hyperons and quarks in relativistic Hartree-Fock approximation, [arXiv:1506.05552].

[43] I. Tews, S. Gandolfi, A. Gezerlis, A. Schwenk, Quantum Monte Carlo calculations of neutron matter with chiral three-body forces, Phys. Rev. C 93, 024305 (2016).

[44] Sinya Aoki, Takumi Doi, Tetsuo Hatsuda, Yoichi Ikeda, Takashi Inoue, Noriyoshi Ishii, Keiko Murano, Hidekatsu Nemura, Kenji Sasaki, Lattice QCD approach to Nuclear Physics, [arXiv:1206.5088].

[45] S. R. Beane, E. Chang, S. D. Cohen, W. Detmold, H.-W. Lin, T. C. Luu, K. Orginos, A. Parreno, M. J. Savage, A. Walker-Loud, Hyperon-Nucleon Interactions and the Composition of Dense Nuclear Matter from Quantum Chromodynamics, [arXiv:1204.3606].

[46] B. Holzenkamp, K. Holinde, and J. Speth, Nucl. Phys. A500, 485 (1989)

[47] A. Reuber, K. Holinde and J. Speth, Nucl. Phys. A 570 (1994) 543

[48] J. Haidenbauer, U.-G. Meißner, Phys. Rev. C 72 (2005) 044005

[49] V. G. J. Stoks and Th. A. Rijken, Soft-core baryon-baryon potentials for the complete baryon octet, Phys. Rev. C 59 (1999), no. 6, 3009-3020

[50] Th. A. Rijken, V. G. J. Stoks, and Y. Yamamoto, Soft-core hyperon-nucleon potentials, Phys. Rev. C 59 (1999), no. 1, 21-40

[51] Th.A. Rijken and Y. Yamamoto, Extended-soft-core Baryon-Baryon Model. II. Hyperon-Nucleon Interaction, Phys. Rev. C 73 , 044008 (2006).

[52] Hideki Yukawa, On the Interaction of Elementary Particles , Proc. Phys. Math. Soc. Jap. 17 (1935) 48.

[53] R. B. Wiringa, V. G. J. Stoks, and R. Schiavilla Phys. Rev. C 51, 38-51 (1995)

[54] V.G.J. Stoks, R.A.M. Klomp, C.P.F. Terheggen, J.J. de Swart, Construction of high-quality Nucleon-Nucleon potential models Phys.Rev.C49:2950-2962,1994

[55] R. Machleidt , The high-precision, charge-dependent Bonn nucleon-nucleon potential (CD-Bonn),Phys.Rev. C63 (2001) 024001

[56] J.J. de Swart, Rev. Mod. Phys. 35, 916 (1963); ibid. 37, 326(E) (1965)

[57] H. Bethe, E. Salpeter (1951), "A Relativistic Equation for Bound-State Problems", Physical Review 84 (6), 1232

[58] R. Blankenbecler and R. Sugar, Linear Integral Equations for Relativistic Multichannel Scattering, Phys. Rev. 142 (1966), 1051-1059

[59] R. Machleidt, "One-Boson Exchange Potentials and Nucleon-Nucleon Scattering", Computational Nuclear Physics 2: Nuclear Reactions, Springer- Verlag, New York, 1993

[60] Christoph Marcus Keil, Microscopic baryon-baryon interactions at finite density and hypernuclear structure, Ph.D. thesis, Justus-Liebig-Universität Gießen, unpublished (2004)

[61] K. Erkelenz, R. Alzetta, and K. Holinde, Momentum space calculations and helicity formalism in nuclear physics, Nuclear Physics A 176 (1971), no. 2, 413 - 432.

[62] R. Machleidt, K. Holinde, and Ch. Elster, Phys. Rep. 149, 1 (1987).
R. Machleidt, Adv. Nucl. Phys. 19, 189 (1989).

[63] E. Epelbaum, H.-W. Hammer, and Ulf-G. Meißner, Modern theory of nuclear forces, Rev. Mod. Phys. 81 (2009), 1773-1825

[64] R. B. Wiringa, V. G. J. Stoks, and R. Schiavilla Phys. Rev. C 51, 38-51 (1995)

[65] R. Machleidt, Computational Nuclear Physics 2-Nuclear Reactions, ch. 1, pp. 1-29, Springer, New York, 1993.

[66] F. Eisele, H. Filthuth, W. Foehlisch, V. Hepp, G. Zech, Phys. Lett. 37B (1971), 204.

[67] H.G. Dosch, R. Engelmann, H. Filthuth, V. Hepp, E. Kluge, Phys. Lett. 21 (1966), 236.

[68] G. Alexander, U. Karshon, A. Shapira, G. Yekutieli, R. Engelmann, H. Filthuth, W. Lughofer, Phys. Rev. 173 (1968), 1452.

[69] L. Piekenbrock, F. Oppenheimer, Phys. Rev. Lett. 12 (1964), 625.

[70] Thomas H. Groves, Phys. Rev. 129 (1963), 1372

[71] J.A. Kadyk, G. Alexander, J.H. Chan, P. Gaposchkin, G.H. Trilling,Nucl. Phys. B27 (1971), 13.

[72] J.M. Hauptmann, J.A. Kadyk, G.H. Trilling, Nucl. Phys. B125 (1977), 29.

[73] H.A. Rubin, R.A. Burnstein,Phys. Rev. 159 (1967), 1149.

[74] B. Sechi-Zorn, B. Kehoe, J. Twitty, R.A. Burnstein, Phys. Rev. 175 (1968), 1735.

[75] R. Engelmann, H. Filthuth, v. Hepp, G. Zech, Phys. Lett. 37B (1971) 204.

[76] V. Hepp and H. Schleich, Z. Phys. 214 (1968) 71.

[77] D. Stephen, Ph.D. thesis, University of Massachusetts, unpublished (1970).

[78] P. M. M. Maessen, Th. A. Rijken, and J. J. de Swart, Phys. Rev. C 40, 2226 (1989).

[79] M.M. Nagels, T.A. Rijken, and J.J. de Swart, Ann. Phys. (N.Y.) 79, 338 (1973)

[80] D. Cline, R. March, M. Sheaff, Phys. Lett. 25B (1967), 446.

[81] R.G.E. Timmermans, Th.A. Rijken, and J.J. de Swart, Phys. Lett. B 257, 227 (1991)

[82] Anika Obermann, Master Thesis, Universoty of Giessen, unpublished (2011).

[83] M.A. Preston and R.K. Bhaduri, Structure of the Nucleus, Westview Press, 1993.

[84] P.J. Ellis, R. Knorren and M. Prakash, Phys. Lett. B349, 11 (1995).

[85] J. Schaffner and I. Mishustin, Phys. Rev. C 53, 1416 (1996)

[86] S. Balberg and A. Gal, Nucl. Phys. A625, 435 (1997).

[87] H.-J. Schulze, A. Lejeune, J. Cugnon, M. Baldo, and U. Lombardo, Phys. Lett. B355, 21 (1995).

[88] H.-J. Schulze, M. Baldo, U. Lombardo, J. Cugnon, A. Lejeune, Phys. Rev. C57, 704 (1998).

[89] P.B. Demorest, T.T. Pennucci, S.M. Ransom, M.S.E. Roberts, J.W.T. Hessels, Nature 467, 1081 (2010).

[90] J. Antoniadis et al., Science 340, 1233232 (2013).

[91] Alessandro Drago et al., Phys. Rev. C90 (2014) no. 6,065809.

[92] David Blaschke et al., AIP COnf. Proc. 1701 (2016) 020013.

[93] H. Lenske, Density Dependent Relativistic Field Theory, Lect. Notes. Phys. 641, 147-174 (2004).

[94] S. Weissenborn, D. Chatterjee, and J. Schaffner-Bielich, Hyperons and massive neutron stars: Vector repulsion and SU(3) symmetry, Phys. Rev. C 85, 065802 (2012);
S. Weissenborn, D. Chatterjee, and J. Schaffner-Bielich, Hyperons and massive neutron stars: the role of hyperon potentials, Nucl. Phys. A 881, 62 (2012).

[95] Y. Yamamoto, T. Furumoto, N. Yasutake, and T. A. Rijken, Hyperon mixing and universal many-body repulsion in neutron stars, Phys. Rev. C 90, 045805 (2014).

[96] D. Lonardoni, A. Lovato, S. Gandolfi, and F. Pederiva, Phys. Rev. Lett. 114, 092301 (2015).

[97] M. I. Haftel and F. Tabakin, Nucl. Phys. A 158 (1970).

[98] V. G. J. Stoks and Th. A. Rijken, Phys. Rev. C 59 (1999) 3009-3020 [arXiv:9901028]

[99] H.P. Stapp, Phys. Rev. 103 (1956) 425

[100] J. Haidenbauer, U.-G. Meißner, A. Nogga, H. Polinder, Lect. Notes Phys. 724 (2007) 113;
J. Haidenbauer, U.-G. Meißner, Phys.Lett. B684 (2010) 275-280.

[101] J. Haidenbauer, S. Petschauer, N. Kaiser, U.-G. Meißner, A. Nogga, W. Weise, Nucl.Phys. A915, 24 (2013), [arXiv:1304.5339v1]

[102] J. Haidenbauer, Ulf-G. Meißner, S. Petschauer, Strangeness S = -2 baryon-baryon interaction at next-to-leading order in chiral effective field theory, [arXiv:1511.05859].

[103] MINUIT, CERN Program Library entry D506, CERN, Geneva.

[104] E. Anderson, Z. Bai, C. Bischof, L. S. Blackford, J. Demmel, J. Dongarra, J. Du Croz , A. Greenbaum, S. Hammarling, A. McKenney and D. Sorensen, LAPACK Users' Guide, Third Edition, Society for Industrial and Applied Mathematics, Philadelphia, PA, 1999.

[105] Y. Fujiwara, C. Nakamoto, Y. Suzuki, Phys. Rev. 54 (1996) 2180;
M. Kohno, et al., Nucl. Phys. A 674 (2000) 229;
Y. Fujiwara , Y. Suzuki , C. Nakamoto, Prog. Part. Nucl. Phys. 58 (2007) 439;
M. Oka, K. Shimizu and K. Yazaki, Prog. Theor. Phys. S137 (2000).

[106] H. Polinder, J. Haidenbauer and U.-G. Meißner, Nucl. Phys. A 779, 244 (2006);
H. Polinder, J. Haidenbauer and U.-G. Meißner, Phys. Lett. B 653, 29 (2007).

[107] C. M. Vincent, S. C. Phatak, Phys. Rev. C 10 (1974) 391.

[108] P.J. Ellis, R. Knorren and M. Prakash, Phys. Lett. B349, 11 (1995).

[109] J. Schaffner and I. Mishustin, Phys. Rev. C 53, 1416 (1996).

[110] E. Epelbaum, H. W. Hammer, and U.-G. Meiẗner, Rev. Mod. Phys. 81 (2009) 1773;
R. Machleidt and D. R. Entem, Phys. Rept. 503 (2011) [arXiv:1105.2919].

[111] Siegmund Brandt, Data Analysis: statistical and computational methods for scientists and engineers, Third Edition, Springer Publisher GMBH, New York, 1998. Statistical and Computational Methods for Scientists and Engineers

[112] F. James, MINUIT Function Minimization and Error Analysis: Reference Manual Version 94.1, CERN-D-506

[113] Hendrik Polinder, Strong Meson-Baryon Interactions, A soft-core model for low- and intermediate-energy π-nucleon and K^+-nucleon scattering, Ph.D. thesis, University of Nijmegen, 2004, ISBN 90-9017742-6.

[114] W. S. C. Williams, An Introduction to Elementary Particles, Second Edition, Academic Press, New York and London, 1971.

[115] P. M. M. Maessen, T. A. Rijken, J. J. de Swart, Phys. Rev. C 40 (1989) 2226.

[116] T. A. Rijken, Ann. Phys. (NY) 164, 1 and 23 (1985).

[117] J. J. de Swart, M. M. Nagels, T. A. Rijken, and P. A. Verhoeven, Springer tracts in Modern Physics, Vol. 60, 137 (1971).

[118] P.M.M. Maessen, T.A. Rijken, and J.J. de Swart, Phys. Rev. D 40, 2226 (1989).

[119] P. S. Signell and R. E. Marshak, Phys. Rev. 106, 832 (1957); 109, 1229 (1958).

[120] S. Okubo and R. E. Marshak, Ann. Phys. (NY) 4, 166 (1958).

[121] Tao Pang, An Introduction to Computational Physics, Cambridge University Press, Cambridge, UK, 2006.

[122] G. D. Rochester and C. C. Butler, Nature 160 (1947) 855.

[123] J. H. Christenson, J. W. Cronin, V. L. Fitch, and R. Turlay, Evidence for the 2π Decay of the K_2^0 Meson, Phys. Rev. Lett. 13, 138 (1964).

[124] O. Hashimoto, H. Tamura, Prog. Part. Nucl. Phys. 57 (2006) 564.

[125] Charles J. Joachain, Quantum Collision Theory, North-Holland Pub. Co., 1975.

[126] K.A. Olive et al. (Particle Data Group), Chin. Phys. C, 38, 090001 (2014) and 2015 update.

[127] A.R. Edmonds, Angular Momentum in Quantum Mechanics, (Princeton University Press, Princeton (1957)).

[128] H. P. Stapp, T. J. Ypsilantis, M. Metropolis, Phys. Rev. 105 (1957) 302.

[129] H. Lenske, M. Dhar, T. Gaitanos, SU(3) Approach to Hypernuclear Interactions and Spectroscopy, [arXiv:1602.08917].

[130] H. Lenske, X. Cao, M. Dhar, T. Gaitanos, R. Shyam, Production and Interactions of Hyperons and Hypernuclei, HYP 2015 Conference Proceedings, Sendai, Japan, Sept. 7-11, 2015, [arXiv:1603.00298].

[131] M. Dhar, H. Lenske, in preparation.

[132] H. Lenske, M. Dhar, N. Tsoneva, J. Willhelm, Exotic nuclear matter, EPJ Web Conf. 107 (1026) 10001.

[133] The explicit relation between $9j$-symbols used here and those in [127] Eq. (6.4.4) is the following

$$\begin{bmatrix} j_{11} & j_{12} & j_{13} \\ j_{21} & j_{22} & j_{23} \\ j_{31} & j_{32} & j_{33} \end{bmatrix} = (-)^{j_{31}+j_{13}-j_{32}-j_{23}} \; [(2j_{13}+1)(2j_{31}+1)(2j_{23}+1)(2j_{32}+1)]^{1/2} \times \begin{Bmatrix} j_{11} & j_{12} & j_{13} \\ j_{21} & j_{22} & j_{23} \\ j_{31} & j_{32} & j_{33} \end{Bmatrix}$$

Acknowledgment

First I want to express my deep gratitude towards to my supervisor Prof. Dr. Horst Lenske without whom this thesis would never have been possible. For the interesting research topic that he has suggested for the dissertation, for the fruitful discussions, help, and guidance throughout these years not only regarding physics but also for other related or irrelevant matters, I would like to sincerely thank him. I want to thank also for believing an international student and showing the trust that let me come and work with him in Germany. The days I spent here enriched me in many ways of my life helping me to grow. I am very much grateful to my supervisor for introducing me to the world physics community by recommending the conferences I should be attending. Last, a special mention should be on his immense help and support during the time when I had a leg fracture that provided me the strength to recover soon.

I would like to acknowledge HGS-HIRe for FAIR facility for providing the financial support for this work.

Next person contributing the most in this thesis is Prof. Johann Haidenbauer. I would like to thank him for providing important opinion on construction of the model, sharing his insights about the difficulties involved but always with a possible solution to that, replying to my e-mails with utmost care, all in all guiding me in achieving the proper results.

Prof. Dr. Christian Fischer is also someone whom I would like to express my deep gratitude too for providing the necessary support always, especially at the last stage of the work, regarding visa, defense, and more.

I would like to thank Prof. Terry Mart for providing the MINUIT source code and generously explaining how to use the facility.

Steffi, Rainer, Alessia, Christian, Jan Haas, Richard, Walter, Jan Lücker: I thank each of them for making my stay wonderful and enjoyable in Germany far from my family and friends. A big thanks to Rainer for always being there in crisis and Alessia for the lovely dinners we had, the lovely times we had spent, and for being the lovely friend she has been always. The lunches at the 'Tee-Küche' were the best parts of the stay.

I thank Christian, Alessia, and Richard wholeheartedly for helping me in submitting the thesis to prüfungsamt while I am away, and Rainer for providing the German translated abstract.

I would also like to thank Prof. S P Khastgir for actually introducing me to the world of 'real' physics, for those enlightening words that helped me to keep the enthusiasm for hard work, the true 'guidance' he always provided, for teaching in a way that can not get better, for always there being for any help and suggestion, and for the proof reading even in quick deadline. Prof. Sayan Kar, Prof. A K Singh, Prof. K L Panigrahi, and Prof. Anushree Roy are also acknowledged for always providing the inspiration for doing good work.

For indirect support, I would like to mention Somnathda for passing useful tips on writing thesis, Subhashishda for providing the thesis template, Stans also for the same, and Narayan for giving useful tips on hard times and for the quick proof reading.

I would like to thank the secretaries of Institute of Theoretical Physics, Uni Gießen, for taking care of the formal affairs efficiently.

A special bunch of thanks towards Ripanda, Binoy Sir, Debajyotida, Laxmanda, and Atishadi for providing relevant information in getting leave to finish the project.

Anumama is someone whom I would like to express my special gratitude for giving me the practical tips for finishing the project and all the relevant motivations he provided.

Last but not the least, I would like to thank my family for everything. I want to thank my mother for all the sacrifices she did for me, for all the trouble she took to

travel to Delhi along with me each time I fly to Frankfurt, for always motivating to do progress and finish the thesis, for teaching the principles of life, and for always being concerned about my health and well-being. My gratitude towards my mother can not be expressed in words. I also would like to thank my brother, who always inspired me to do good work, always provided positive vibes, being always there to take care of the family crisis so that I can concentrate in my work, and during the last phase kept me going. Thanks. My little nephew, Aarno, is also someone I would like to thank just for being here to make us happy. A special thanks to my sister-in-law too for taking care of the family.

Finally, I end by thanking my father, who, wherever today, is the reason for this thesis and everything I achieved in my life.

Declaration

I declare that I have completed this dissertation single-handedly without the unauthorized help of a second party and only with the assistance acknowledged therein. I have appropriately acknowledged and cited all text passages that are derived verbatim from or are based on the content of published work of others, and all information relating to verbal communications. I consent to the use of an anti-plagiarism software to check my thesis. I have abided by the principles of good scientific conduct laid down in the charter of the Justus Liebig University Giessen "Satzung der Justus-Liebig-Universität Gießen zur Sicherung guter wissenschaftlicher Praxis" in carrying out the investigations described in the dissertation.

Gießen, May 2016

Madhumita Dhar